Semiconductors, Vol. 37, No. 2, 2003, pp. 119–123. Translated from Fizika i Tekhnika Poluprovodnikov, Vol. 37, No. 2, 2003, pp. 129–133.
Original Russian Text Copyright © 2003 by Klevkov, Martovitskii, Medvedev.

Special Features of Structural Defects in Undoped CdTe Textured Ingots Produced by Free Growth from a Gasdynamic Vapor Flow

Yu. V. Klevkov*, V. P. Martovitskii, and S. A. Medvedev

Department of Solid-State Physics, Lebedev Physical Institute, Russian Academy of Sciences, Leninskiĭ pr. 53, Moscow, 119991 Russia

** e-mail: martov@okb.lpi.troitsk.ru*

Submitted May 7, 2002; accepted for publication June 17, 2002

Abstract—The structural features of undoped CdTe ingots grown in a gasdynamic flow at 620°C were studied by selective etching and X-ray diffractometry. It is found that the samples grown at a deposition rate of up to 500 μm/h consist of independently growing rods with both [111] *A* and [111] *B* directions. This indicates that the vapor composition in the growth region is almost stoichiometric. Both rod types exhibited transverse striations due to rotation twins. The twin boundaries in rods with the growth direction [111] *A* were shown to be also small-angle boundaries with additional misorientation of separate twins of 0.2°–0.3°. © *2003 MAIK "Nauka/Interperiodica".*

1. INTRODUCTION

The study of structural defects and their interactions with point defects in the CdTe semiconductor compound is of significant interest in relation to the production of crystals and films with reproducible properties. The reason for this is that the interaction of extended (dislocations, stacking faults, twin boundaries, and grain boundaries) and point defects is rather intricate and gives rise to various clusters responsible for deep electron states arising in the band gap. As a result, the electrical and optical properties of materials can be drastically changed. This is especially important in the case of CdTe, since its single crystals grown at high temperatures (≈1000°C) contain cadmium vacancies and tellurium inclusions over grain boundaries [1, 2]. According to the section through the *P*–*x* CdTe state diagram, the smallest possible deviations from the stoichiometry of bulk crystal under the congruent sublimation condition should be observed at a growth temperature close to 620°C. This study is concerned with the special features of structural defects in textured CdTe samples produced by free growth in a gasdynamic flow at this temperature.

2. EXPERIMENTAL

Cadmium telluride ingots up to 70 mm in diameter were grown on graphite bars at a temperature $T \approx 620$°C from a gasdynamic vapor flow. The mass transfer rate in dynamic vacuum was varied within 4–20 g/h. The vapor deposition rate at the bar, taking into account the condensation rate, was 250–750 μm/h. As the initial charge, we used purified polycrystalline CdTe with the smallest possible deviations from the stoichiometric composition. Some of the optical and electrical properties of the textured *p*-CdTe samples grown by us are given in [3, 4].

Three series ***A***–***C*** of CdTe samples produced at growth rates of 250, 500, and 750 μm/h, respectively, and treated in bromine–methanol polishing etchant were studied. The samples were cut out as parallelepipeds with sides of 3–8 mm along the growth direction. The polarity of separate single-crystal grains and their defect structure were revealed by *E*–Ag–1 selective etchant [1].

Structural studies were carried out using a DRON-2.0 X-ray diffractometer with a reflection-mode graphite monochromator. Each sample simultaneously contains a few crystalline grains, whose crystallographic [111] directions are misoriented with respect to each other up to 15° with the random azimuth angle of twisting around the normal to the growth surface. Therefore, a major problem in the study of such samples is the relation of an observed reflection to a particular grain. To solve this problem, we calculated all the probable reflections of the CdTe cubic phase, which can be observed using Cu X-rays in the mode of reflection from the (111) surface. When materials characterized by a high absorption of X-rays (to which CdTe is related) are studied in the aforementioned conditions, only the asymmetric reflections for which the Bragg reflection angle Θ_B is larger than the tilt angle φ_{hkl} of the reflecting plane with respect to the surface under study are observed. We calculated the angles with the [111] direction, which were formed by the normals to all of the probable reflecting planes. These normals, which

Fig. 1. Gnomonic projection of the twin with the common axis [111] deviated by a few degrees from the aggregation growth direction. A Boldyrev polar net is used. We show the components of the normals only to the planes, the reflections from which can be observed in the mode of reflection from the (111) surface when using K_α X-rays.

met the criterion $\Theta_B > \varphi_{hkl}$, were drawn on a gnomonic projection as a Boldyrev polar net, which is used when constructing pole figures of textured samples [5]. This net (see Fig. 1) is represented by concentric circles drawn with a misorientation interval of 10° from the normal to the sample surface; the angular distance between the nearest radial lines is 30°. Thus, a sample should be rotated by 30° about the normal to the surface under study so that each successive radial line is aligned horizontally and the planes, the normals to which lie in this horizontal line of the net, are aligned vertically. The filled circles in Fig. 1 are related to the normals of reflecting planes of a separate twin; the larger open circles correspond to twins of rotation around the general growth direction [111] of the same grain. We note that this direction does not coincide with the projection center.

Although the [111] direction of the studied grains is deflected by a few degrees from the normal to the sample surface, we will conditionally consider the reflections (333) or (444) as symmetric ($\varphi_{hkl} \approx 0°$), at which both twins of the cubic phase with a sphalerite structure and the hexagonal phase with a wurtzite structure reflect X-rays as a single crystal. The diffraction conditions are fulfilled for only one of the separate twins for most of the asymmetric reflections (except for the {153} system with $\varphi_{hkl} = 28.56°$); this factor can be used to separate them. A DRON-2.0 diffractometer can detect reflections only from vertical (or close to vertical) planes [6]. Therefore, to measure the dihedral angle between the (111) and asymmetric reflection planes, both planes should be aligned vertically. The fact that a given reflection was related to a particular grain was established as two criteria were simultaneously met: the Bragg angle coincided with the value calculated for this reflection, and the calculated and measured angles between the grain plane (111) and the reflecting plane were close.

To diminish the spreading of asymmetric reflection, an additional vertical slit 0.1 mm wide was placed immediately in front of the sample under study.

3. RESULTS

The treatment of all three samples in a selective etchant showed that the crystallite cross sizes decreased from several millimeters to fractions of a millimeter as the deposition rate increased from 250 to 750 μm/h. Samples ***A*** and ***B*** exhibited a conical axial texture [111] (with a misorientation of the axis [111] of each grain by a few degrees from the growth direction). Sample ***C***, in addition to grains {111}, contained grains with orientations {110} and {331} along the growth direction.

Another special feature of samples ***A*** and ***B***, revealed by selective etching, is the fact that grains with orientations {111}***A*** and {111}***B*** coexist along the growth direction. The tellurium grain surface in Fig. 2 (top micrograph) appears to be dull due to insoluble tellurium oxides [7]. The equiprobable growth of grains with both polarity directions confirms that the vapor composition above the growth surface is almost stoichiometric. This is also indicated by the absence of reflections in most of the twin grains (grain polarity change). At higher temperatures of II–VI crystal growth, rods of only one polarity grow preferentially, with equiprobable nucleation for both polarities [8]. The average dislocation density in a separate grain does not exceed 5×10^3 cm^{-2}.

The bottom micrograph of Fig. 2 displays the striated structure (caused by twin boundaries) in each separate grain in sample ***B*** cut normal to the growth direction. The number of twin boundaries and their contrast are significantly higher in the grains growing along the [111]*A* direction in comparison with [111]*B* grains. This can be caused by a minor cadmium deficiency, as well as by a higher mobility of α dislocations in comparison with β dislocations. A similar inference about the higher quality of epitaxy of CdTe films onto {111}*B* CdTe substrates was made in [9]. The rocking curves of sample ***B*** grains, measured in a diverging X-ray beam without an additional slit, showed that the grains can be classified into two groups with relative misorientations of 0.4°–0.5° and smaller than 0.15°. A careful comparison of the arrangement of separate grains in the etch pattern with the grain rocking curves for the same area allowed the conclusion to be made that the grains growing along the [111]*A* direction are characterized by a higher concentration of defects in comparison with [111]*B* grains. Since each group of grains has a random

azimuth angle of twisting around the normal to the growth surface, we managed to analyze separately the asymmetric reflections belonging to grains grown in the [111]*A* and [111]*B* directions using the algorithm described in Section 2.

The symmetric reflections (333) and (444) for both groups of grains for sample ***B*** are very narrow with well resolved $K_{\alpha 1}$ and $K_{\alpha 2}$ lines (Fig. 3 shows the curves for a grain growing in the [111]*A* direction). The lattice parameter calculated from the position of the reflection (444) peak ($2\Theta = 110.80°$) is 6.4835 Å. The asymmetric reflections at large sample rotation angles ($\Theta_B + \varphi_{hkl}$) are also very narrow and are always observed as two pairs: reflections (331) and (440) are detected for a separate single-crystal grain, whereas a pair of reflections (422) and (533) from another single-crystal grain is invariably observed. To pass from one pair of reflections to another in a single crystal, a sample should be rotated through 60° about the [111] axis (see Fig. 1). Since both pairs coexist, each studied grain is a twin with a common [111] axis nearest to the direction of grain growth. We emphasize that the intensities of asymmetric reflections in sample ***B*** from two separate twins are largely the same, taking into account the difference in structure factors for these reflections. Since the symmetry center is always involved in the diffraction pattern (the Friedel law) [10], it is impossible to distinguish between the rotation twin (rotation through 60° about the common triad axis with unchanged polarity in the growth direction) and the reflection twin (reflection in the (111) plane with changed polarities of growing grains). However, the selective etching patterns show mostly rotation twins. Reflection twins were also observed, but much less often than rotation twins, which were probably indicative of small local variations in the vapor composition stoichiometry.

Large-angle reflection spots (440) of one separate twin and (533) of the other are narrow with well resolved doublets, $K_{\alpha 1}$ and $K_{\alpha 2}$. Hence, it may be argued that the reflections are not appreciably spread due to microstresses or small X-ray coherent-scattering regions (CSR). No reflections from the hexagonal phase were observed. The data obtained allow an estimation of the lower thickness limit for each twinned interlayer no smaller than 1000 Å, since the reflections broaden in inverse proportion to the CSR size at smaller thicknesses [15].

The rocking curve for the symmetric reflection (444) of the grain grown along the {111}*A* direction consists of four separate peaks indexed as *1–4* in Fig. 4. The rocking curves of the asymmetric reflections (440) and (533) of two separate twins consist of two peaks. A comparison of the angular positions of the peaks and peak shapes in these rocking curves made it possible to ascertain which peaks in the rocking curve of a (444) reflection are related to one separate twin and which two peaks, to the other. Peak *4* in reflection (440) is approximately half as high as the peak in reflection

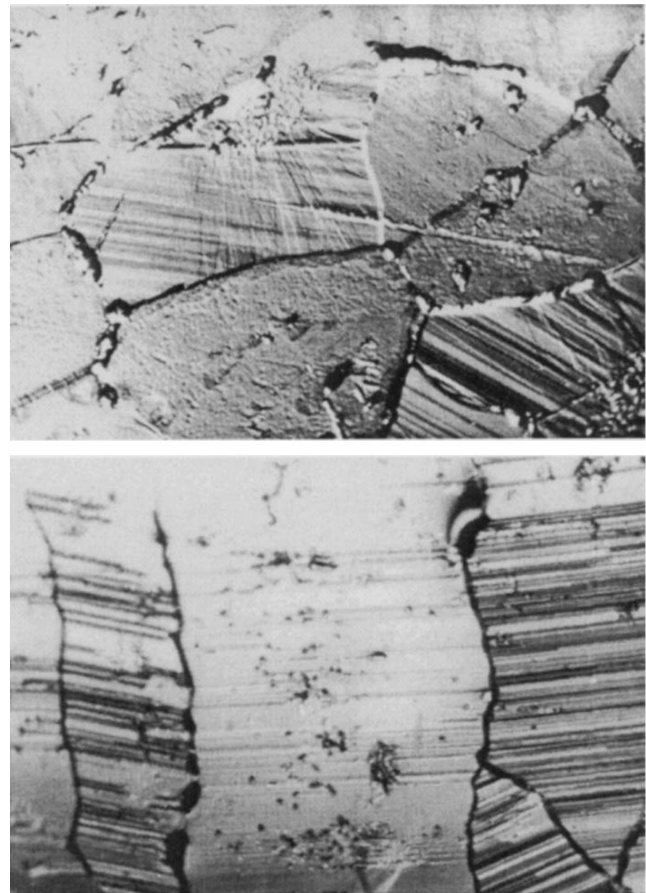

Fig. 2. Patterns of selective etching perpendicular (top) and parallel (bottom) to the growth direction.

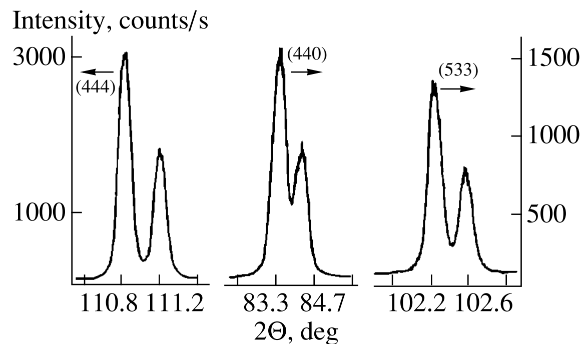

Fig. 3. Diffraction profiles of the symmetric reflection (444) common for twins and asymmetric reflections (440) and (533) of two separate twins. The left angle values on the scale of each reflection approximately correspond to the reflection maxima.

(444). This can be explained by different penetration depths of X-rays in the sample. Using the mass-absorption coefficients $(\mu/\rho)_{Cd} = 231$ cm^2/g and $(\mu/\rho)_{Te} = 282$ cm^2/g [11] of cadmium and tellurium for CuK_α X-rays, as well as the X-ray density of 5.85 g/cm^3 for cadmium telluride, the determined linear coefficient of

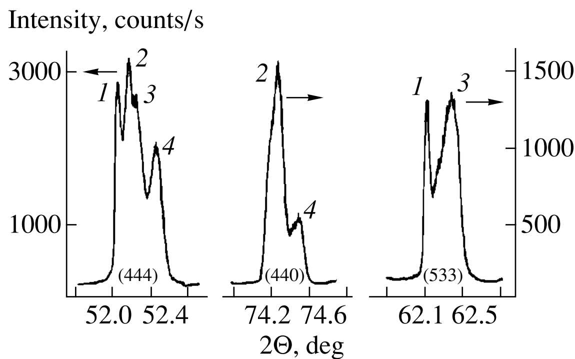

Fig. 4. Rocking curves of the symmetric reflection (444) common for twins and asymmetric reflections (440) and (533) of separate twins.

absorption $\mu = 1500\ \text{cm}^{-1}$ can be used to calculate the total penetration depth X of the wave into the sample for the symmetric reflection (444) and the asymmetric reflection (440) with a tilt angle φ (35.26°) to the reflecting surface [12, 13],

$$X_{444} = \frac{\sin(\Theta_{444})}{2\mu},$$

$$X_{440} = \frac{\sin(\Theta_{440}+\varphi)\sin(\Theta_{440}-\varphi)}{\mu[\sin(\Theta_{440}+\varphi)+\sin(\theta_{440}-\varphi)]}.$$

Since these formulas are employed for only a rough estimation of the X-ray penetration depth in the sample, we disregarded small (3°–5°) deviations of the [111] direction from the normal to the surface under investigation.

The X-ray penetration depth for the symmetric (444) and asymmetric (440) reflections are approximately 2.75 μm and a mere 0.75 μm. Thus, a decrease in the height of peak *4* in the rocking curve of reflection (440) can be caused by a deeper position of the twin interlayer in the sample and by an almost fourfold decrease in the X-ray penetration depth for this reflection. We note that such an appreciable change in the peak heights is not observed in the rocking curve of reflection (533) in comparison with the same peaks for reflection (444) due to comparable X-ray penetration depths for these reflections ($X_{533} = 2.41$ μm), since the tilt angle of the reflecting plane (533) is only 14.42°.

We measured the rocking curves of asymmetric reflections (335) and (044) from the side of small angles ($\Theta_B - \varphi_{hkl}$)). In this case, an intensity decrease was observed even for peak *3*. The data obtained allow the conclusion that interlayers *3* and *4* are located deeper in comparison with interlayers *1* and *2*. These data allow estimation of the upper limit of the twin interlayer thickness, which cannot exceed several tenths of a micrometer, so that the deepest twin interlayer at reflection (440) can be detected. The values determined conform well to the thicknesses of the interlayers detected by selective etching in the sample transverse section.

Although the (111) interface between twins is coherent, slight misorientations between separate twins suggest that the twins contain grain-boundary dislocations [14], which is confirmed by etch pits detected in the emergence traces of a twin boundary at the transverse cut of the sample.

A supersaturation decrease during the preparation of sample ***A*** does not radically change the pattern of the sample structure: several groups of grains are also observed (but in a smaller number). Each grain consists of twinned interlayers, whose boundaries are perpendicular to the [111] axis closest to the growth direction. However, the misorientation of the normal to the growth surface with respect to the [111] direction, which is common for two twins, can be as large as 15°, while the estimated interlayer thickness can be as large as several micrometers. This follows from the increase in the distance between twin striations in the etch pattern of the transverse cut, the increase in the ratio of intensities of reflections from twins with an angle of reflecting plane asymmetry (i.e., as the X-ray penetration depth decreases), and the total disappearance of the peaks of one of the twins at reflection (440).

An increase in supersaturation above a certain limit gives rise to grains with orientations close to [110] and [331] along the normal to the growth surface (sample ***C***). In this case, grains with the [111] orientation also exist. Such a change in the growth direction at high levels of supersaturation can be caused either by twinning over three other equivalent {111} planes or by the replacement of the layer growth mechanism by the normal (fibrous) mechanism [15]. Crystallites become so small and their total number becomes so great that it becomes impossible to attribute asymmetric reflections to any grain. The presence of twins during the layer growth of crystals can facilitate nucleation of new layers in the twin reentrant angle [15]. However, the twin boundaries terminating inside grains more likely count in favor of a deformational mechanism of grain formation.

4. CONCLUSIONS

Cadmium telluride samples grown in a gasdynamic flow at 620° at deposition rates of up to 500 μm/h were found to consist of rods with the ⟨111⟩ directions of both polarities close to the growth direction. This indicates that the vapor composition above growing crystallites is close to stoichiometric. Both grain types consist of rotation twins alternating perpendicularly to the growth axis, as well as, to a much lesser extent, reflection twins. The grains with the [111]*A* orientation along the growth direction are characterized by small-angle boundaries with a misorientation of several tenths of a degree at twin boundaries.

ACKNOWLEDGMENTS

We would like to thank V.S. Bagaev for his interest in this study.

This study was supported by the Russian Foundation for Basic Research (project nos. 01-02-16500, 02-02-17392, and 00-02-17335), as well as by the Federal Program for the Support of Leading Scientific Schools (project no. 00-15-96568).

REFERENCES

1. K. Durose, G. J. Russel, and J. Woods, J. Cryst. Growth **72**, 85 (1985).
2. K. Durose and G. J. Russel, J. Cryst. Growth **86**, 471 (1988).
3. V. S. Bagaev, V. V. Zaĭtsev, Yu. V. Klevkov, *et al.*, Fiz. Tverd. Tela (St. Petersburg) **43**, 1779 (2001) [Phys. Solid State **43**, 1853 (2001)].
4. Yu. V. Klevkov, S. A. Kolosov, S. A. Medvedev, and A. F. Plotnikov, Fiz. Tekh. Poluprovodn. (St. Petersburg) **35**, 1192 (2001) [Semiconductors **35**, 1139 (2001)].
5. S. S. Gorelik, L. N. Rastorguev, and Yu. A. Skakov, *X-Ray and Electron-Optical Analyses* (Metallurgiya, Moscow, 1970).
6. D. M. Kheĭker, *X-Ray Diffractometry of Single Crystals* (Mashinostroenie, Leningrad, 1973).
7. Y.-C. Lu, C. M. Stahle, R. S. Feigelson, and J. Morimoto, J. Appl. Phys. **62**, 4453 (1987).
8. H. Iwanaga, T. Yoshiie, T. Yamaguchi, and N. Shibata, J. Cryst. Growth **47**, 703 (1979).
9. P. D. Brown, K. Durose, G. J. Russel, and J. Woods, J. Cryst. Growth **101**, 211 (1990).
10. M. A. Poraĭ-Koshits, *Application-Oriented Course of X-Ray Analysis* (Mosk. Gos. Univ., Moscow, 1960).
11. *International Tables for X-Ray Crystallography* (Kynoch Press, Birmingham, 1983), Vol. 3.
12. A. I. Kitaĭgorodskiĭ, *X-Ray Analysis* (Gostekhizdat, Moscow–Leningrad, 1950).
13. B. D. Cullity, *Elements of X-Ray Diffraction*, 2nd ed. (Addison-Wesley, Reading, Mass., 1978).
14. *Atomic Structure of Grain Boundaries*, Ed. by A. N. Orlov (Mir, Moscow, 1978).
15. *Processes of Actual Crystal Formation*, Ed. by N. V. Belov (Nauka, Moscow, 1977).

Translated by A. Kazantsev

Semiconductors, Vol. 37, No. 2, 2003, pp. 124–130. Translated from Fizika i Tekhnika Poluprovodnikov, Vol. 37, No. 2, 2003, pp. 134–141.
Original Russian Text Copyright © 2003 by Vintsents, Zaitseva, Plotnikov.

ATOMIC STRUCTURE AND NONELECTRONIC PROPERTIES OF SEMICONDUCTORS

Self-Organization of Laser-Induced Point Defects at the Initial Stages of Inelastic Photodeformation in Germanium

S. V. Vintsents*, A. V. Zaitseva, and G. S. Plotnikov****

** Institute of Radio Engineering and Electronics, Russian Academy of Sciences (Fryazino Branch), pl. Vvedenskogo 1, Fryazino, Moscow oblast, 141120 Russia*

e-mail: alkeev@ms.ire.rssi.ru

*** Faculty of Physics, Moscow State University, Vorob'evy gory, Moscow, 119899 Russia*

Submitted June 13, 2002; accepted for publication June 18, 2002

Abstract—Atomic-force microscopy is applied to study the characteristic features of the relief forming on a germanium surface at the initial stages of multiple laser-induced deformation. Both elastic and inelastic strains can be induced in a semiconductor surface layer irradiated by scanning laser pulses. It is shown that the elastic deformation of the Ge surface does not affect its initial nanorelief, whereas inelastic deformation initiates a low-threshold formation of ordered nanostructures on the surface. Correlation between this phenomenon and the laser-induced generation of point defects near the inelastic-strain threshold is considered.
© 2003 MAIK "Nauka/Interperiodica".

INTRODUCTION

One of the most interesting phenomena induced by pulsed laser irradiation of solids is the appearance of strain and the related displacement of the surface layers [1, 2]. In conditions of multiple local irradiation of metals and semiconductors, nondestructive (elastic) shear strain $\varphi = dU_z/dr$ (where r is the coordinate along the laser beam radius) corresponds to effective normal surface displacements U_z on the order of subnanometers [3, 4]. Irradiation in the nanosecond mode ($\tau \leq 1$–100 ns) has been studied in detail because of acoustic [5, 6] and other fast processes that take place, for example, during the laser annealing of defects [7, 8].

Slower quasi-static ("photothermal", [9]) strain appears under single-mode irradiations, with the typical size of the light spot on the surface $\omega \approx 10$–100 μm and the exposure time $\tau \geq 0.1$–1.0 μs [10, 11]. Such quasi-static strain (if it is elastic or quasi-elastic) holds promise for the contactless local monitoring of thermal [12] and optical [13] parameters of surface layers and for studying the kinetics of the first-order phase transition in thin semiconductor films [14, 15], as well as for revealing and 3D analysis of special modes in the kinetics of local nondestructive surface displacement [10, 11]. Usually, a typical relaxation time of the discussed strain t ranges from 1 to 100 μs [3, 4].

During the development of pulsed photoinduced quasi-static strain in semiconductors (and metals), different channels of defect formation may be activated. Three main factors have traditionally been considered as those governing laser-induced defect formation in semiconductors: heating, energy transfer from photoexcited carriers to defects, and strain of the surface layer itself [16–19]. According to the electron-strain-thermal (ESH) theory of defect formation [16, 19], the processes of point defect formation prevail until the photoinduced heating is of below-threshold type (i.e., does not result in the short-term melting of the surface layers [7, 8]).

It was shown in previous studies [3, 20–22] that, in the conditions of multiple local irradiation of semiconductors, the elastic form of strain gives way to the inelastic one even at low shear strains, $10^{-5} < \varphi_0(W_0) < 10^{-4}$, where $W_0 \leq 0.1$ [J/cm^2] is the threshold energy density of submicrosecond laser pulses. It was also shown that, at least at the initial stages of inelastic deformation (with a moderate number of pulses $N \leq 10^3$), the amplitude of temperature inhomogenities over the surface reaches only a few tens of degrees. Under these conditions, the multiple deformation of semiconductor local regions (within a size of $\approx 2\omega$) may give rise to the so-called size effects [3, 20, 21] and enhance the influence of strain on the generation (and redistribution) of point defects [22–24].

The slow electron states (of fluctuation origin) in a thin insulating GeO_2 film [23] and the vacancies that are driven from the interface into the bulk [24] may be considered among the defects that are sensitive to the threshold $\varphi_0(W_0)$ in germanium. Note that the previously described [23, 24] contribution from the generation and accumulation of defects to changes in the relief on an actual Ge surface subjected to cyclic inelastic deformation has not yet been detected in experiments.

For the direct investigation of the initial stages of inelastic strain in germanium and the detection of corresponding residual displacements ΔU_z on a nanometer scale, we used atomic-force microscopy (AFM) to

1063-7826/03/3702-0124$24.00 © 2003 MAIK "Nauka/Interperiodica"

study the nanorelief produced on a germanium surface subjected to scanning pulsed laser irradiation ($N \leq 10^3$) in the vicinity of previously determined [3, 22–24] deformation thresholds $\varphi_0(W_0)$.

EXPERIMENTAL

Similar to [23, 24], the (111) surfaces of high-resistivity (ρ = 25–30 Ω cm) *n*-Ge:Sb single crystals etched in H_2O_2 were scanned by laser pulses in air at room temperature. A normal-incidence laser beam with λ = 0.53 µm was used for the scanning method, which is similar to that described in [22–24]: the repetition rate was $f \approx 10^4$ s^{-1}; a typical pulse duration was $\tau \approx$ 0.4–0.5 µs; the single-mode laser beam produced a Gaussian spot with a size of $2\omega \approx$ 70 µm on the surface; the velocity and the step of scanning were $v \approx$ 1–5 mm/s and $\delta \approx$ 5–10 µm, respectively.

Our method of overlapping the laser spots on the surface allowed us to obtain a spread no greater than 5–7% in the maximal incident-energy density W within each scanned area of ≈3 × 5 mm^2. Note that W[mJ/cm^2] = $E/\pi\omega^2$, where E is the measured total energy of the pulse [22–24]. The single-mode character of the laser beam should be emphasized: the dependence of the intensity of light on the radial coordinate r and time t (as in [10, 11, 20]) can be closely approximated by the formula $I(r, t) = W\exp(-r^2/\omega^2)(t/\tau^2)\exp(-t/\tau)$.

We considered the energy densities W in the range from 0 to 150 mJ/cm^2, which includes the previously determined inelastic-strain thresholds in germanium [3, 23, 24] $W_0 \approx$ 65–70 mJ/cm^2 and is essentially below the W_m values predicted for the melting thresholds upon long-term (submicrosecond) irradiation: $W_m \geq$ (1.2–1.5) J/cm^2 [7, 8].

Profiles of the surface nanorelief were measured and the topology of the surface was studied on a submicron scale with the use of a Nanoscope-111a-type atomic-force microscope (AFM) (Digital Instruments), which operated in air in the contact mode. Levers with a rigidity of ≈0.01–0.2 N/m provided a nondestructive mode for studying the relief on the Ge surface. Images of the surface regions after exposure to the scanning laser pulses were processed using specialized "FemtoScan-001" software [25].

RESULTS

Figure 1 shows the results of the AFM study of the actual germanium surface (*1*) before and after laser irradiation with W = (*2*) 50, (*3*) 85, (*4*) 110, and (*5*) 150 mJ/cm^2. According to our measurements, the average difference in height in the relief of the initial (unirradiated) surface is no larger than $\delta U_z \leq$ 2–5 nm (Fig. 1, *1*). In some areas, we observe scratches as deep as 10 nm, which apparently are traces from the mechanical grinding and remained after the chemical etching of the surface.

The situation is nearly the same in the region irradiated with W = 50 mJ/cm^2 (Fig. 1, *2*): the amplitudes of the random nanorelief δU_z remain as before and neither laser-induced residual strain nor additional displacement of the surface is revealed. This circumstance correlates with the data obtained previously [3, 23, 24] for the elastic mode of laser-induced deformation of Ge surface layers at $W < W_0$ = 65–70 mJ/cm^2. It is noteworthy that previous studies [23, 24] revealed an enhanced formation of point defects at the inelastic-strain thresholds $\varphi_0(W_0)$.

At the initial stages ($N \leq 10^3$) of inelastic laser-induced strain ($W \geq$ 85 mJ/cm^2 ≈ $1.2W_0$), it was only in separated uncoordinated surface spots (Fig. 1, *3*) with a diameter of several micrometers and a total area accounting for 5–10% of the scanned surface area that we observed the appearance of a threshold (with respect to W) for formation of nonoriented clusters (Fig. 2, *1*) and for self-organization of laser-induced point defects [22–24] into two-dimensional (2D) arrays of surface nanorelief (Fig. 2, *2*) with the amplitude of irreversible normal surface displacements $\delta U_z \approx$ 10–20 nm (Fig. 2, *3*). The size of nonoriented clusters was on the order of ≈100 nm, and the spacings in the emerging 2D array $a \approx$ 550–600 nm (perpendicular to the direction of scanning) and $b \approx$ 350–400 nm (along the crystallographic directions of [100] type (Fig. 2)). Note that these values are considerably smaller than the laser spot size ≈2ω and the scanning pitch δ (see above).

The presence of regions with a weak plastic strain in Fig. 1, *3* and the clearly defined horizontal sections (so-called "plateaus") in Fig. 2, *3* allows us to set a reference point along the z direction (normal to the surface) with an accuracy of $\approx\delta U_z/2$; in other words, we determined the zero level of the initial surface. As a result, regular elevations of nanorelief appearing in 2D submicron arrays are attributed to the transfer of material from well-developed circumferential "nanotrenches" around each of the "nanohills".

The stable formation of ordered (periodic) structures over the entire area of the irradiated surface is observed at an energy density $W \geq$ 110 mJ/cm^2 ≈1.5–$1.6W_0$. When W is much higher than W_0, separate hills merge into parallel ridges (Fig. 1, *4*); i. e., the 2D arrays give way to one-dimensional structures with a period ≈a and a height difference $\Delta U_z \approx$ 20–40 nm.

Irradiation of the germanium surface with $W \geq$ 150 mJ/cm^2 ≈ 2.2–$2.5W_0$ results in an essentially more complicated pattern of microplastic strain. For example, simultaneously with the growth of the amplitudes of irreversible displacements ΔU_z to 30–60 nm in the submicrometer arrays, we observed an additional generation of structures with a large (several micrometers) spatial period (Fig. 1, *5*). With a further increase in W, the evolution of multiple inelastic laser-induced strains in the germanium surface layer had mainly a destruc-

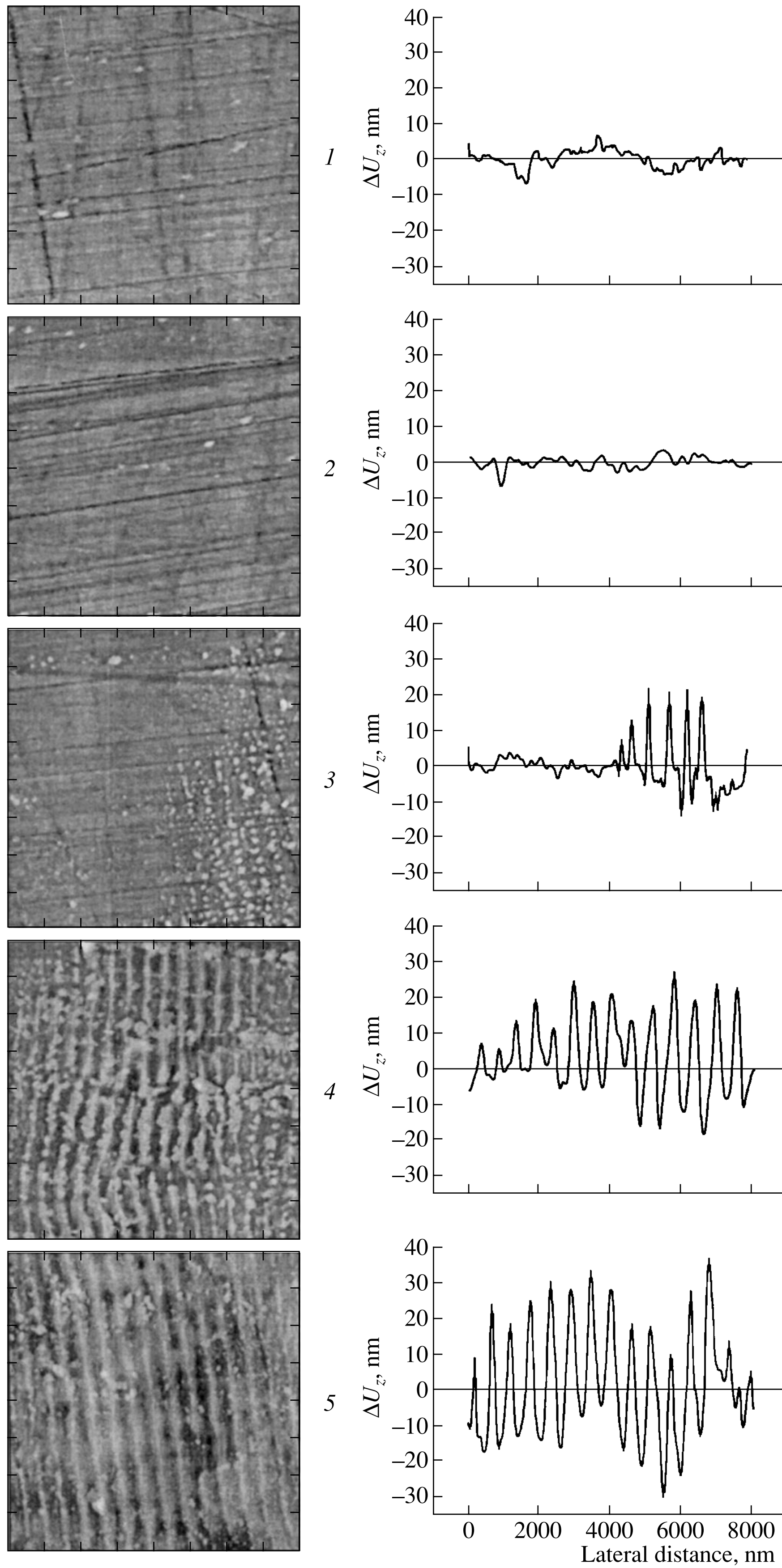
1
2
3
4
5
ΔU_z, nm
40
30
20
10
0
−10
−20
−30
0
2000
4000
6000
8000
Lateral distance, nm

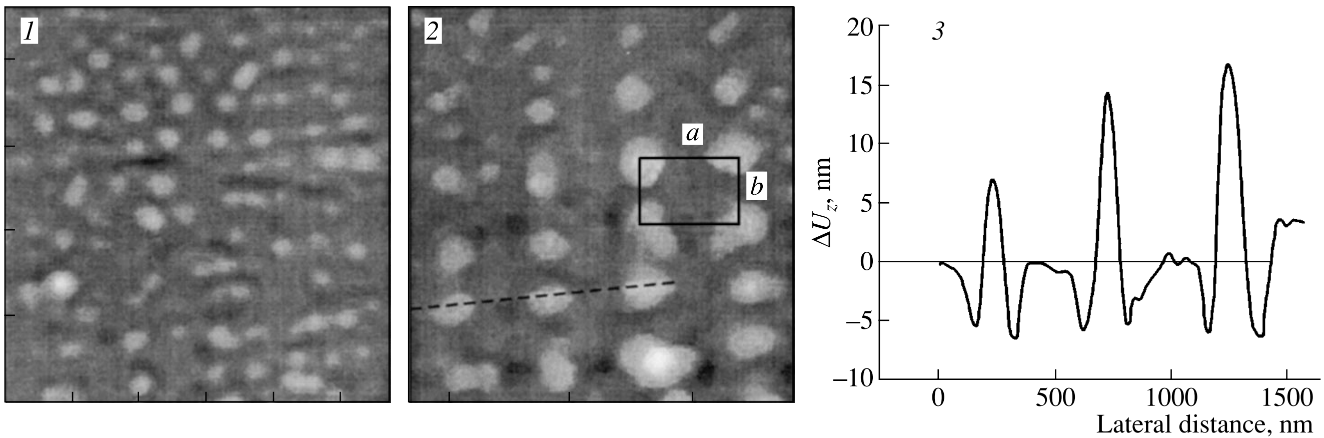

Fig. 2. AFM images at the initial stages of the formation of (*1*) nonoriented clusters and (*2*) 2D gratings; (*3*) vertical profiles of irreversible displacements ΔU_z at the germanium surface subjected to inelastic deformation near the thresholds $W_1 \approx 1.2–1.5W_0$. The size of images *1* and *2* is 2300×2300 nm^2.

tive character and fell outside the scope of this AFM study.

DISCUSSION

In what follows, we provide an interpretation of the most important results and present a number of estimates. Let us recall that the modes of multipulse local irradiation of semiconductors and metals have traditionally been divided (see, e. g., [3, 20–24] and references therein) into destructive ($W > W_d$) and nondestructive ($W < W_0$). The upper damage threshold W_d is usually defined by the onset of the formation of extended (on the order of micrometers) damaged sites, which are visible under a microscope, or by a pronounced drop in the mirror reflectivity of the scanning beam from the surface [3, 10, 26–29]. These final stages of degradation with the appearance of microcracks can be detected with the use of acoustic waves, among other methods [30, 31].

A detailed study of the changes induced at the initial stages of irradiation was performed by Vintsents et al. [20–24]. The corresponding lower thresholds W_0, below which no damage is produced on the solid surface even after exposure to a large number of focused laser pulses $N \geq 10^7–10^9$ [3, 4, 10–15], were determined. For the case $N \leq 10^3$, highly sensitive techniques were used: quasi-equilibrium field effect [23], molecular luminescence probes [24], photothermal deformation of the surface [20–24], as well as Raman (and diffuse) scattering of light [22, 24] are examples. As a result, it was established that the thresholds W_0 corresponding to the buildup of inelastic strain in Ge surface layers and changes related to the size effect [3, 20] should appear under the surface even at the earliest stages of irradiation [21]. With a further increase in W above W_0, a threshold growth of the concentration of defects was detected both in the thin GeO_2 oxide film [23] and in the deeper layers in the bulk of the material [24]. Similar low-threshold phenomena were also observed in Si and GaAs samples [22].

Thus, one might expect that the laser irradiation of solids at $W_0 \leq W \leq W_d$ in the inelastic mode of multiple local strain is mostly destructive. However, this statement appears to be true only for large N [3, 22]. The results of AFM studies (Figs. 1, 2) indicate the exact opposite situation at $N \leq 10^3$: at the initial stage of inelastic deformation, laser-induced point defects [22–24] are self-organized into periodic nanostructures on the germanium surface. In this case, the discussed energy interval may be considered as the range of controlled inelastic effects where, along with W, the governing parameters can also be N, ω, τ, and λ.

Periodic surface structures appearing as a result of the irradiation of solids have already been observed. The most thoroughly studied case is the formation of a surface periodic relief due to the instability that develops as a result of interference between incident and diffracted (surface) electromagnetic waves. The spatial orientation of such interference gratings (IG) should depend on the polarization and the angle of incidence of radiation, while their period strictly correlates with the wavelength and is proportional to λ [32–34].

In this study, the orientation of the observed gratings is defined mainly by the crystallographic symmetry (Fig. 2, *2*) or by the direction of scanning (Fig. 1, *5*). At normal incidence of the beam, the resulting structures had different periods (*a* and *b*), which were not closely

Fig. 1. AFM images and nanorelief profiles of the actual germanium surface irradiated with multiple ($N \leq 10^3$) laser pulses of submicrosecond duration for different energy densities W: (*1*) unirradiated sample, W = (*2*) 50, (*3*) 85, (*4*) 110, and (*5*) 150 mJ/cm^2. The size of images is 8×8 μm^2. Plots to the right show the displacement of surface ΔU_z along the vertical section of sample.

related to λ, ω, or δ (see above). The formation of gratings has a pronounced low-threshold character and takes place only within the energy range $W \geq W_1 \approx (1.2–1.5)W_0 < W_d \ll W_m$.

In this context, we believe that, at the initial stages (at $N \leq 10^3$) of inelastic ($W > W_0$) light-induced strain, i. e., far from the damage thresholds W_d [22, 26–29] and the calculated melting thresholds W_m [7, 8], the defect-diffusion microplasticity mechanism [36] (unrelated to dislocations [35]) is realized on the solid germanium surface. It is only in the inelastic mode of deformation that critical concentrations of defects can be attained due to the successive (from pulse to pulse) accumulation of laser-induced point defects [37] and the appreciable enhancement of this process at the strain thresholds $\varphi_0(W_0)$ [22–24]. According to the theory developed in [38], an increase in the concentration of defects above certain critical values initiates the transition of a system of laser-induced point defects to a spatially inhomogeneous state with a lower energy due to the formation of so-called defect-deformation (DD) surface structures [38, 39].

According to the present theoretical view [38], generation of DD structures stems from the development of the so-called generation-diffusion-deformation instability (GDDI). This instability can be related to defect–deformation interaction [40, 41] at which the generation or annihilation of defects implies a change in the volume (and the energy) of a crystal and an initial fluctuation of strain gives rise to deformation-induced defect fluxes and/or leads to modulation of their generation rate [38]. As a result, the inhomogeneous field of the defect concentration $n_d(r, t)$ produces forces that are proportional to the concentration gradients and increase the strain in a material. These forces enlarge the initial fluctuation up to the formation of autolocalized defect clusters (Fig. 2). At the early stages of self-organization (Fig. 2, *1*; Fig. 2, *2*), an angular selection of gratings [42, 43] occurs and the AFM-detected changes in the height of the nanorelief (Fig. 2, *3*) can be interpreted in terms of the theory of 2D gratings [38] as clusters of excess atoms in interstices (or as vacancy clusters).

Thus, the initial stages of inelastic deformation in germanium are characterized by generation of both vacancies [24] and interstitial defects, which then organize into small-scale (submicrometer) convex–concave DD structures. The rate of generation of these and some other [23] point defects under the submicrosecond irradiation of semiconductors is still low compared to nanosecond irradiation [7, 8]. We believe that these conditions provide for the realization of a special case of GDDI, i. e., a diffusion–deformation instability (DDI) [38]. The submicrometer (or micrometer) period d of such diffusion–deformation gratings is proportional to the thickness h of the defect-enriched surface region rather than to λ [38]. This circumstance indicates that the arising inhomogeneities in the concentration of defects are indeed fairly small-scale, $d \approx h$ [38], and are mainly due to deformation-induced defect fluxes, while spatial variations in the rate of defect generation or some other mechanisms (for example, the development of microcracks) [44] play only a secondary role in the conditions under consideration.

As was mentioned above, the combined effect of radiation-induced heating, transfer of the electron excitation energy to defects, and deformation of the surface layers causes the efficient formation of point defects under the uniform irradiation of the surface [16, 19]. In the conditions of local multiple irradiation, the effect of strain may become enhanced and, thus, give rise to "size" effects at the thresholds when W_0 values are proportional to ω [3, 20, 21]. In our opinion, this situation enables the low-threshold self-organization of defects into DD gratings at temperatures which are considerably lower than the melting point.

Indeed, the calculated laser-induced heating of a surface at the thresholds W_0 is still only moderate: $\Delta T_{max} < 100°C$ [3, 21, 22]; therefore, the thermal (quenching) mechanism [45] seems to be of minor significance for the pulse-to-pulse accumulation of vacancies (and other defects) at small N. However, in the conditions of appreciably greater N and $W > W_0$, additional heat release is possible due to the action of external forces (associated with the temperature gradients arising from thermal extension [10, 21]) during the accumulation of irreversible displacements of atoms [36].

At small N and $W \approx W_0$, our estimate of d from the length h of the low-temperature diffusion of defects produced near the surface into the bulk of the material (Ge, Si) in terms of the deformation-induced "vacancy pump" [36] is in good agreement with the predictions of theory [38].

When the alternating-sign contact loading of semiconductors is characterized by an asymmetric cycle (i. e., the extension strain exceeds the compression strain in every cycle), the role of vacancy sources is known to dominate over that of sinks [36]. In this case, the kinetics of escape of vacancies to the bulk sinks during compression lags behind the process of their escape from the surface during extension. A "hill" usually forms on semiconductor (or metal) surfaces subjected to local pulsed irradiation [3, 4, 10–13, 20, 21, 23]; i. e., quasi-static deformation in the surface layers of solids is mainly realized in the form of extension, and tensile (and shear) stresses are dominant. According to the vacancy-pump model [36], the thickness of the defect-enriched layer h (and the diffusion length) should be defined by the total time $N\tau_{1/2}$ of the stressed state of a semiconductor.

In the case of germanium, the half-time of relaxation of the photoinduced stresses $\tau_{1/2} \approx 10–15$ μs starting from the leading edge of each pulse (for every beam size 2ω, the time $\tau_{1/2}$ is different [10, 11]) can be estimated from the experiments with the kinetics of local quasi-static photoinduced strain [46] or from the instantaneous profiles of the surface displacements

[47]. As determined in [36], the largest values of $h_{max} \approx 2(D_v N\tau_{1/2})^{1/2} = 420$ nm, where $D_v \approx 4.3 \times 10^{-8}$ cm^2/s is the diffusion coefficient of vacancies in germanium extrapolated to room temperature ($D_v \approx 10^{-4}\exp(-0.2/kT)$ [48]) and $N \sim 10^3$ is the maximal number of photodeformation pulses used during the scanning irradiation.

Close correlation between the estimates $h \approx 420$ nm and the grating periods obtained in experiment, $d \approx$ 350–550 nm (*a* and *b* sections in Fig. 2, *2*), may be considered as further verification of the defect–deformation mechanism [38] for the formation of residual nanometer displacements ΔU_z at the initial stages of inelastic photoinduced deformation in germanium. A significant role in this process is apparently played by the point-defect generation (discovered previously [23, 24] at the deformation thresholds $\varphi_0(W_0)$) in the surface layer and at the Ge–GeO_2 interfaces. The maximal amplitudes $\delta U_z \approx 30$–60 nm in Fig. 1, *5* are also in good agreement with the estimate $\Delta U_z \equiv \xi_q \approx h/10 \approx 40$ nm obtained for the stationary state of gratings, i. e., after the completion of angle selection and the monochromatization of their spectrum [38].

In conclusion, we should note the 2D character of the structures generated near the thresholds of the grating formation $W_1 \approx 1.2$–$1.5W_0$ (Fig. 2, *2*) and their nonuniform distribution over the surface; in our opinion, the separate "spots" of generation may be interpreted as sites with an enhanced concentration of biographical defects in germanium (Fig. 1, *3*). In such regions, which, at first, are undistinguishable, the critical concentrations of point defects should be most readily attained under irradiation. This finding may be of use in revealing and outlining defect regions. At a considerable excess over the thresholds W_1, the inelastic photoinduced strain features a more uniform distribution over the surface; however, its identification becomes a challenge because of the additional generation of other structures with a larger period (Fig. 1, *5*). The possible influence of the direction of scanning on the merging of hills into ridges on the surface (Fig. 1, *4*) presents a topic for further investigation. In this context, we are pinning much hope on the future AFM study of semiconductors under local ($\omega \approx 10$–100 μm) inelastic ($W > W_0$) laser-induced deformation for a different number of pulses N when the position of a beam on the surface is fixed.

CONCLUSIONS

For the first time, we studied experimentally the formation of residual displacements ΔU_z on an actual germanium surface at the initial stages of inelastic quasistatic deformation induced in micrometer-sized ($\omega \le$ 10–100 μm) surface regions. It is shown that, at a fixed number of pulses, $N \le 10^3$, in the nondestructive (elastic) photodeformation range (i. e., at $W < W_0$), no effective accumulation of defects occurs and the surface relief remains random. At the very beginning of microplastic changes, at $W_0 < W < 1.2$–$1.5W_0$, an intense [23, 24] concealed (i. e., subsurface, latent) accumulation of point defects with a quasi-uniform distribution of their concentration over the surface prevails over the main part of the scanned area. As the microplastic strain increases (at $W \ge W_1 \approx (1.2$–$1.5W_0)$) we observe the low-threshold self-organization of light-induced defects [23, 24] into deformation–defect "convex–concave" nanostructures, which can be adequately explained in terms of existing theory [38]. The discovered mechanism for the formation of regular residual displacements of nanometer-size ΔU_z directly points to the defect–diffusion (unrelated to dislocations [35]) character of microplasticity in the germanium surface layers [36] irradiated by multiple laser pulses in the temperature range near the brittle point.

ACKNOWLEDGMENTS

We are grateful to V.B. Zaitsev for his useful comments.

REFERENCES

1. V. É. Gusev and A. A. Karabutov, *Laser Optical Acoustics* (Nauka, Moscow, 1991).
2. V. P. Zharov and V. S. Letokhov, *Laser Optical–Acoustic Spectroscopy* (Nauka, Moscow, 1984).
3. A. G. Barskov and S. V. Vintsents, Fiz. Tverd. Tela **36**, 2590 (1994) [Phys. Solid State **36**, 1411 (1994)].
4. S. V. Vintsents and S. G. Dmitriev, Zh. Tekh. Fiz. **67** (2), 105 (1997) [Tech. Phys. **42**, 216 (1997)].
5. S. A. Akhmanov and V. É. Gusev, Usp. Fiz. Nauk **162** (3), 3 (1992) [Sov. Phys. Usp. **35**, 153 (1992)].
6. L. M. Lyamshev, *Laser Thermoacoustic Generation of Sound* (Nauka, Moscow, 1989).
7. R. F. Wood, C. W. White, and R. T. Young, Semicond. Semimet. **23** (1984).
8. A. V. Dvurechenskiĭ, G. A. Kachurin, E. V. Nidaev, and L. S. Smirnov, *Pulsed Annealing of Semiconductor Materials* (Nauka, Moscow, 1982).
9. *Proceedings of 8th International Topical Meeting on Photoacoustic and Photothermal Phenomena* (Paris, 1994).
10. S. V. Vintsents, S. G. Dmitriev, and O. G. Shagimuratov, Fiz. Tverd. Tela **38** (4), 993 (1996) [Phys. Solid State **38**, 552 (1996)].
11. S. V. Vintsents, S. G. Dmitriev, and K. I. Spiridonov, Fiz. Tverd. Tela **39** (12), 2224 (1997) [Phys. Solid State **39**, 1985 (1997)].
12. S. V. Vintsents and V. B. Sandomirskii, Phys. Status Solidi A **133**, K7 (1992).
13. S. V. Vintsents, V. I. Mirgorodskiĭ, and Sh. S. Khalilov, Poverkhnost **9**, 157 (1990).
14. S. V. Vintsents, V. F. Kiselev, N. L. Levshin, and V. B. Sandomirsky, Surf. Sci. **241**, 225 (1991).
15. S. V. Vintsents and N. L. Levshin, Poverkhnost **2**, 67 (1993).
16. V. I. Emel'yanov and P. K. Kashkarov, Poverkhnost **2**, 77 (1990).

17. P. K. Kashkarov and V. F. Kiselev, Izv. Akad. Nauk SSSR, Ser. Fiz. **50** (3), 435 (1986).
18. V. A. Zuev, V. G. Litovchenko, G. A. Sukach, and N. M. Torchun, Ukr. Fiz. Zh. **21** (5), 752 (1976).
19. V. I. Emel'yanov and P. K. Kashkarov, Appl. Phys. A **55**, 161 (1992).
20. S. V. Vintsents and S. G. Dmitriev, Pis'ma Zh. Tekh. Fiz. **21** (19), 1 (1995) [Tech. Phys. Lett. **21**, 767 (1995)].
21. S. V. Vintsents, S. G. Dmitriev, and O. G. Shagimuratov, Pis'ma Zh. Tekh. Fiz. **22** (8), 8 (1996) [Tech. Phys. Lett. **22**, 602 (1996)].
22. S. V. Vintsents, A. V. Zoteev, and G. S. Plotnikov, Fiz. Tekh. Poluprovodn. (St. Petersburg) **36**, 902 (2002) [Semiconductors **36**, 841 (2002)].
23. S. V. Vintsents, S. G. Dmitriev, R. A. Zakharov, and G. S. Plotnikov, Fiz. Tekh. Poluprovodn. (St. Petersburg) **31**, 513 (1997) [Semiconductors **31**, 433 (1997)].
24. S. V. Vintsents, V. B. Zaĭtsev, A. V. Zoteev, *et al.*, Fiz. Tekh. Poluprovodn. (St. Petersburg) **36**, 947 (2002) [Semiconductors **36**, 883 (2002)].
25. A. S. Filonov and I. V. Yaminskiĭ, *User Manual for the Application Package Designed to Control a Sounding Microscope and Processing Images FemtoScan-001* (TsPT, Moscow, 1999).
26. C. S. Lee, N. Koumvakalis, and M. Bass, Appl. Phys. Lett. **41**, 625 (1982); Opt. Eng. **22**, 419 (1983).
27. S. S. Cohen, J. B. Bernstein, and P. W. Wyatt, J. Appl. Phys. **71**, 630 (1992).
28. P. M. Fauchet, Phys. Lett. A **93**, 155 (1983).
29. A. G. Barskov, S. V. Vintsents, G. G. Dvoryankina, *et al.*, Poverkhnost **3**, 79 (1995).
30. V. P. Veĭko, G. V. Dreĭden, Yu. N. Ostrovskiĭ, *et al.*, Zh. Tekh. Fiz. **60** (4), 162 (1990) [Sov. Phys. Tech. Phys. **35**, 499 (1990)].
31. I. A. Konovalov, K. S. Sklyarenko, and S. K. Sklyarenko, Pis'ma Zh. Tekh. Fiz. **20** (6), 26 (1994) [Tech. Phys. Lett. **20**, 226 (1994)].
32. A. M. Bonch-Bruevich, A. M. Kochengina, M. N. Libenson, *et al.*, Izv. Akad. Nauk SSSR, Ser. Fiz. **46**, 1186 (1982).
33. J. E. Sipe, J. F. Young, J. S. Preston, and H. M. van Driel, Phys. Rev. B **27**, 1141 (1983); Phys. Rev. B **27**, 1155 (1983).
34. S. A. Akhmanov, V. I. Emel'yanov, N. I. Koroteev, and V. N. Seminogov, Usp. Fiz. Nauk **147**, 675 (1985) [Sov. Phys. Usp. **28**, 1084 (1985)].
35. Yu. I. Golovin and A. I. Tyurin, Fiz. Tverd. Tela **42**, 1818 (2000) [Phys. Solid State **42**, 1865 (2000)].
36. V. P. Alekhin, *Physics of Strength and Plasticity of Surface Layers of Materials* (Nauka, Moscow, 1983).
37. B. L. Volodin, V. I. Emel'yanov, and Yu. G. Shlykov, Kvantovaya Élektron. (Moscow) **20** (1), 57 (1993).
38. V. I. Emel'yanov, Kvantovaya Élektron. (Moscow) **28** (1), 2 (1999).
39. V. I. Emel'yanov, P. K. Kashkarov, N. G. Chechenin, and T. Ditrikh, Fiz. Tverd. Tela **30**, 2259 (1988) [Sov. Phys. Solid State **30**, 1304 (1988)].
40. J. D. Eshelby, Solid State Phys. **3**, 79 (1956).
41. V. S. Vavilov, A. E. Kiv, and O. R. Niyazova, *The Mechanisms of Defect Formation and Migration in Semiconductors* (Nauka, Moscow, 1981).
42. V. P. Veĭko, I. A. Dorofeev, Ya. A. Imas, *et al.*, Pis'ma Zh. Tekh. Fiz. **10**, 15 (1984) [Sov. Tech. Phys. Lett. **10**, 6 (1984)].
43. V. P. Veĭko, Ya. A. Imas, M. N. Libenson, *et al.*, Izv. Akad. Nauk SSSR, Ser. Fiz. **49**, 1236 (1985).
44. F. Kh. Mirzoev, V. Ya. Panchenko, and L. A. Shelepin, Usp. Fiz. Nauk **166** (1), 3 (1996) [Phys. Usp. **39**, 1 (1996)].
45. N. V. Karlov, N. A. Kirichenko, and B. S. Luk'yanchuk, *Laser Thermochemistry* (Nauka, Moscow, 1992), Chap. 15.
46. S. V. Vintsents and V. I. Mirgorodskiĭ, in *Proceedings of IX All-Union Symposium on Electron Processes on Surface and in Thin Layers of Semiconductors* (Novosibirsk, 1988), Chap. 1, p. 87.
47. S. V. Vintsents, in *Technical Digest of XVI International Conference on Coherent and Nonlinear Optics* (Moscow, 1998), WM 23.
48. V. V. Voronkov, G. I. Voronkova, and M. I. Iglitsin, Fiz. Tekh. Poluprovodn. (Leningrad) **6**, 20 (1972) [Sov. Phys. Semicond. **6**, 14 (1972)].

Translated by A. Sidorova

Semiconductors, Vol. 37, No. 2, 2003, pp. 131–133. Translated from Fizika i Tekhnika Poluprovodnikov, Vol. 37, No. 2, 2003, pp. 142–144.
Original Russian Text Copyright © 2003 by Kurova, Ormont, Gromadin.

ATOMIC STRUCTURE AND NONELECTRONIC PROPERTIES OF SEMICONDUCTORS

Photoinduced Annealing of Metastable Defects in Boron-Doped *a*-Si:H Films

I. A. Kurova*, N. N. Ormont*^, and A. L. Gromadin**

** Moscow State University, Moscow, 119899 Russia*

^e-mail: scon282@phys.msu.su

*** State Research Institute for the Rare-Metals Industry, Moscow, 109017 Russia*

Submitted May 17, 2002; accepted for publication June 27, 2002

Abstract—The effect of illumination on the isothermal relaxation of slow photoinduced metastable defects (metastable electrically active impurity atoms) in boron-doped *a*-Si:H films has been studied. It was established that, under illumination, the kinetics of relaxation of these metastable defects is governed not only by their thermal annealing and photogeneration, but also by the process of photoinduced annealing. *© 2003 MAIK "Nauka/Interperiodica".*

Recently, photoinduced annealing of metastable dangling silicon bonds (MDB) in undoped *a*-Si:H films have been studied extensively. This process was first predicted theoretically. It was suggested in [1] that the kinetic equation must also include, in addition to the photoinduced formation of metastable defects and their thermal annealing, two symmetric processes: thermal formation and photoinduced annealing. Later, the occurrence of photoinduced annealing of MDB in undoped *a*-Si:H films, manifested in an increase in the rate of their annealing during the initial period of their relaxation, was demonstrated experimentally [2–4]. It was also established that the rate of MDB annealing at a given concentration N of these defects is proportional to the carrier generation rate G raised to a power γ coinciding with the exponent in the current–light characteristic. In the authors' opinion, this may indicate that photoinduced annealing of MDB is proportional to the concentration of free carriers and involves capture of a hole by a metastable center [4].

It is known that two kinds of metastable defects, fast and slow, are formed in doped *a*-Si:H films under illumination. MDB are fast defects, and metastable electrically active impurity atoms (MEAI) or complexes of these are slow [5, 6]. We are not aware of any observations of photoinduced annealing of MEAI. Therefore, we analyzed the effect of illumination on the isothermal relaxation of photoinduced MEAI in boron-doped *a*-Si:H films in order to study the process of photoinduced annealing.

With the concentration of MDB and MEAI changing as a result of their formation or relaxation, the position of the Fermi level in the energy gap changes and, consequently, so does the dark conductivity of the material. Provided that the density of states is constant within the range through which the Fermi level moves in the energy gap of *a*-Si:H, the variation of the dark conductivity with time reflects the manner in which the concentration of metastable states, $N(t)$, varies with time [7]:

$$|\ln(\sigma_d(t)/\sigma_{d0})| = |\Delta F(t)|/kT = N(t)/\rho_0 kT.$$

Here, σ_{d0} is the equilibrium dark conductivity, $|\Delta F(t)|$ is the magnitude of the Fermi level shift relative to the equilibrium position, and ρ_0 is the density of states in the range across which the Fermi level moves.

For study, we chose *a*-Si:H films lightly doped with boron. The total concentration of boron in the films, determined by SIMS, was $(3–4) \times 10^{17}$ cm^{-3}, and the Fermi level position was found to be 0.79 eV above the valence band top. In this case, the Fermi level lies within a rather wide dip in the density of states, in which $\rho(E)$ can be considered virtually constant and equal to ρ_0. In addition, the ρ_0 value in the material lightly doped with boron is small, compared with ρ_0 for a more heavily doped material [8]. This makes it possible to vary the dark conductivity more widely when the same concentration N of metastable states is generated and, consequently, to determine the $N(t)$ dependence with a higher precision.

Figure 1 shows how the dark conductivity of the studied *a*-Si:H films (doped with boron to 3×10^{17} cm^{-3}) varies with time after its preliminary illumination at T = 410 K for 10 min. It can be seen that the quantity $\ln(\sigma_d(t)/\sigma_{d0})$ varies nonmonotonically, which is due to relaxation of the photoinduced MDB and MEAI, whose energy levels lie, respectively, higher and lower than the Fermi level. Curve *3* fits the experimental points rather well. This curve can be regarded as the sum of two stretched exponentials with different $N(0)$, τ_0, and β (curves *1* and *2*). The exponentials, representing fast relaxation of MDB and slow relaxation of MEAI, are

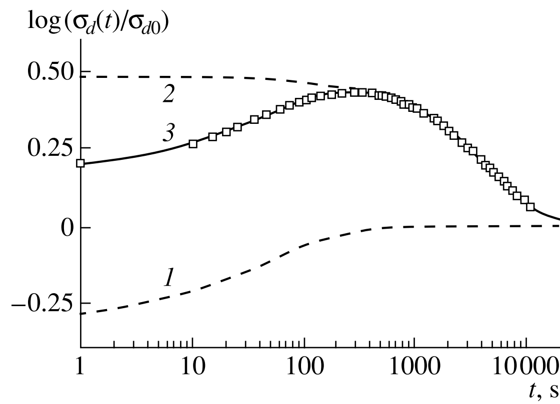

Fig. 1. Variation with time of the dark conductivity of an a-Si:H film with boron concentration $N_B = 3 \times 10^{17}$ cm^{-3} after its preliminary exposure to white light with an intensity of 90 mW cm^{-2} at $T = 410$ K for 10 min (experimental points). Curve *3* is described by a sum of two stretched exponentials (curves *1* and *2*) corresponding to isothermal relaxation in the dark of photoinduced ensembles MDB I and MEAI I. Parameters of stretched exponentials: (curve *1*): $N_1(0) = -0.3$, $\tau_{01} = 51$, and $\beta_1 = 0.66$; (curve *2*): $N_2(0) = 0.49$, $\tau_{02} = 4800$, and $\beta_2 = 0.85$.

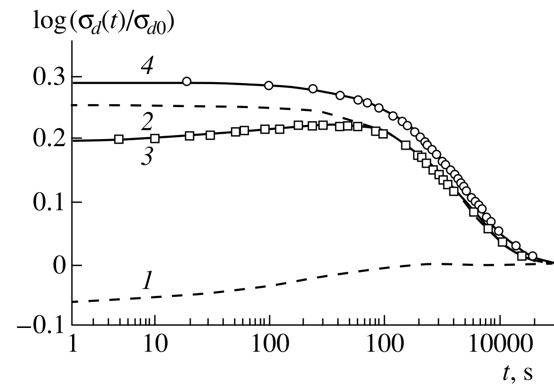

Fig. 2. Variation with time of the dark conductivity of the same a-Si:H(B) film after its preliminary illumination at $T = 410$ K for 10 min, followed by partial isothermal relaxation for 40 min in the dark (experimental points on curve *4*) or under weak illumination (experimental points on curve *3*). Curves *4*, *1*, and *2* represent stretched exponentials describing the isothermal relaxation in the dark of, respectively, ensembles MEAI II, MDB III, and MEAI III, with the following parameters: (curve *1*): $N_1(0) = -0.06$, $\tau_{01} = 240$, and $\beta_1 = 0.68$; (curve *2*): $N_2(0) = 0.25$, $\tau_{02} = 5200$, and $\beta_2 = 1$; (curve *4*): $N_2(0) = 0.29$, $\tau_{02} = 5700$, and $\beta_2 = 0.95$.

responsible for the increase in dark conductivity at short t and decrease in dark conductivity at long t:

$$\ln(\sigma_d(t)/\sigma_{d0}) = N_1(0)\exp[-(t/\tau_{01})^{\beta_1}] + N_2(0)\exp[-(t/\tau_{02})^{\beta_2}].$$

The indices *1* and *2* refer to, respectively, relaxation of MDB and MEAI. The parameters of the stretched exponentials are listed in the caption to Fig. 1.

The fact that the isothermal relaxation of metastable defects of the given type is described by a stretched, rather than simple, exponent means that we are dealing with a set of defects with different relaxation times τ. In this case, the parameters of a stretched exponential have the following meaning: $N(0)$ is the total initial concentration of metastable defects with a relaxation time distribution having a maximum at $\tau = \tau_0$ and a half-width characterized by the reciprocal of the parameter β. Thus, the parameters $N(0)$, τ_0, and β define an ensemble of metastable defects at the initial instant of annealing.

Correspondingly, with the aim of studying the photoinduced annealing, we determined the parameters

Table

MEAI ensembles	$N(0)$, rel. units	τ_0, s	β
I	0.49	4800	0.85
II	0.29	5700	0.95
III	0.25	5200	1

$N(0)$, τ_0, and β for the isothermal relaxation of three ensembles of MEAI and compared the results obtained. Ensemble I was obtained by exposing an annealed a-Si:H film to light with an intensity of 90 mW cm^{-2} at $T = 410$ K for 10 min. Ensembles II and III were obtained from the isothermal relaxation of ensemble I for the same time (40 min) in the dark and under weak illumination (8 mW cm^{-2}), respectively.

The variation in the dark conductivity of a film with time, associated with the relaxation of MEAI in ensemble I, is shown by curve *2* in Fig. 1. The parameters characterizing this ensemble at the initial instant of annealing are listed in the table. Figure 2 shows how the dark conductivity of a film varies with time as a result of relaxation of ensemble II (curve *4*). It can be seen that the relaxation of ensemble II is described by a single stretched exponent, corresponding to the relaxation of MEAI. Thus, virtually all MDB of ensemble I are annealed out, and ensemble MDB II is lacking. The parameters characterizing ensemble II are listed in the table. Comparison between the parameters for ensembles MEAI I and MEAI II shows that isothermal annealing of ensemble MEAI I in the dark leads to a decrease in the total concentration of MEAI in ensemble I (decrease in $N(0)$), a narrowing of the ensemble half-width (increase in β), and a rise in the effective relaxation time τ_0. This last fact is associated with the immediate annealing-out of MEAI with short times τ.

The manner in which the dark conductivity varies via the isothermal relaxation in the dark of metastable defects belonging to ensemble III produced by isothermal annealing of ensemble I under illumination is represented by curve *3* in Fig. 2. It can be seen that illumi-

nation in the course of annealing of ensemble I leads to formation of ensemble MDB III, together with ensemble MEAI III, and, consequently, to a nonmonotonic variation of the dark conductivity. Curve *3*, which is the sum of two stretched exponentials (curves *1* and *2*), fits the experimental points well. The parameters of the stretched exponential characterizing ensemble MEAI III are listed in the table.

A comparison between the parameters for ensembles MEAI II and III shows that illumination in the course of isothermal annealing makes the total concentration of MEAI lower (decrease in $N(0)$). This indicates that the photoinduced annealing of MEAI occurs, especially if account is taken of the additional photoinduced formation of MEAI under illumination. It can also be seen from the table that the parameter τ_0 for ensemble III is smaller than that for ensemble II, which indicates that photoinduced annealing is manifested in a decrease in the concentration of MEAI with long relaxation times τ. This may be due to the much lower rate of formation of MEAI with long relaxation times τ under illumination compared with the rate at which MEAI with short relaxation times τ are created, which is in accordance with the model of MEAI formation based on a three-level configuration diagram [9].

The relaxation of MEAI in the *a*-Si:H films under study is due to a structural rearrangement that consists of the transformation of a tetracoordinated electrically active impurity atom—an acceptor impurity of boron in the given case—into an electrically inactive complex composed of a tricoordinated boron atom and a hydrogen bonded to a silicon atom. Elucidating the mechanism by which the rate of this structural transformation increases under illumination requires further experimental and theoretical study.

ACKNOWLEDGMENTS

We thank I.P. Zvyagin for his helpful participation in discussions.

This study was supported by the program "Universities of Russia" and by the Scientific Program of the Giredmet (State Research Institute for the Rare-Metals Industry) State Scientific Center.

REFERENCES

1. D. Redfield, Appl. Phys. Lett. **52**, 492 (1988).
2. R. Meaudre and M. Meaudre, Phys. Rev. B **45**, 12134 (1992).
3. H. Gleskova, P. A. Morin, and S. Wagner, Appl. Phys. Lett. **62**, 2063 (1993).
4. H. Gleskova, S. N. Bullock, and S. Wagner, J. Non-Cryst. Solids **164–166**, 183 (1993).
5. X. M. Deng and H. Fritzsche, Phys. Rev. B **36**, 9378 (1987).
6. I. A. Kurova, É. V. Larina, N. N. Ormont, and D. V. Senashenko, Fiz. Tekh. Poluprovodn. (St. Petersburg) **31**, 1455 (1997) [Semiconductors **31**, 1257 (1997)].
7. J. K. Rath, W. Fuhs, and H. Mell, J. Non-Cryst. Solids **137–138**, 279 (1991).
8. S. Sheng, X. Liao, and G. Kong, Appl. Phys. Lett. **78**, 2509 (2001).
9. A. G. Kazanskii, I. A. Kurova, N. N. Ormont, and I. P. Zvyagin, J. Non-Cryst. Solids **227–230**, 306 (1998).

Translated by M. Tagirdzhanov

Semiconductors, Vol. 37, No. 2, 2003, pp. 134–139. Translated from Fizika i Tekhnika Poluprovodnikov, Vol. 37, No. 2, 2003, pp. 145–150.
Original Russian Text Copyright © 2003 by Lashkarev, Dmitriev, Baĭda, Kovalyuk, Kondrin, Pronin.

ELECTRONIC AND OPTICAL PROPERTIES OF SEMICONDUCTORS

Anomalies in Static and Dynamic Conductivity of Indium Monoselenide

G. V. Lashkarev*^, A. I. Dmitriev*, A. A. Baĭda*, Z. D. Kovalyuk*, M. V. Kondrin, and A. A. Pronin****

** Frantsevich Institute of Materials Science Problems, National Academy of Sciences of Ukraine, ul. Krzhizhanovskogo 3, Kiev, 03142 Ukraine*

^e-mail: lask@ips.kiev.ua

*** Institute of General Physics, Russian Academy of Sciences, ul. Vavilova 38, Moscow, 117942 Russia*

Submitted April 18, 2002; accepted for publication April 24, 2002

Abstract—Results of investigating the static and dynamic conductivity of an InSe single crystal in the temperature range from 4.2 to 300 K are reported. The measurements were performed for a temperature-variation rate of 0.2–0.8 K/min and for currents through a sample of up to 10 μA. Under such conditions, new states can be formed as a result of phase transitions and the dimensionality of the gas of carriers changes. Charge-density waves arising in this case do not penetrate the crystal under the action of an electric field. A substantial difference was observed between the properties of InSe single crystal in the static and dynamic modes. *© 2003 MAIK "Nauka/Interperiodica".*

1. INTRODUCTION

Indium monoselenide InSe is a prominent example of III–VI semiconductors. It has a layered structure in which each layer perpendicular to the *c* axis of the crystal contains a group of atomic planes, Se–In–In-Se, characterized by strong covalent bonds. In contrast, the neighboring layers are bonded by weaker Van der Waals forces, which are the cause of the characteristic mechanical properties of these crystals, specifically, their high cleavability in the layer plane. The formation energy for crystal-lattice defects in InSe is such that there exists the possibility of generating a significant concentration of electrons, for example, by means of self-intercalation with indium. This fact distinguishes InSe from other III–VI semiconductors in which defects compensating introduced electrically active impurities are generated.

The physical properties of InSe have been adequately investigated in a number of studies [1–9]. As a result of these investigations, the following reliable proofs were obtained for the two-dimensional (2D) localization of electron gas at low temperatures [1, 3]:

(i) the existence of regions in the dependence of the magnetoresistance (MR) on the magnetic-field strength where the MR is proportional to $\ln H$ in the magnetic field with an $\mathbf{H} \parallel \mathbf{c}$ that corresponds to concepts of the theory [10];

(ii) the possibility of observing quantum oscillations up to certain maximum angles of inclination for the magnetic-field vector with respect to the *c* axis;

(iii) the independence of the frequency of Shubnikov–de Haas oscillations on the magnetic-field component perpendicular to the plane of layers and the cylindrical shape of the Fermi surface [11];

(iv) a high coefficient of anisotropy of conductivity attaining a value of $K = 10^3$–10^5;

(v) a decrease in K for the temperature region (9–18 K) of the transition from 2D conductivity to three-dimensional (3D) conductivity;

(vi) the influence of superconducting lead precipitates on the 2D-to-3D-conductivity transition at $T < T_c$ [12];

(vii) the appearance of *N*-shaped portions in the current–voltage (*I–V*) characteristics, which is typical of 2D structures having superlattice properties;

(viii) the suppression of the *N*-shaped portions of the *I–V* characteristics for the case when InSe is intercalated with lead at $T < T_c$;

(ix) the MR-sign change from negative to positive when the sample is illuminated [3]; and

(x) the observation of the Mott semiconductor–metal transition when applying a quasihydrostatic pressure, due to an increase in the wave-function overlap for neighboring electrons [13].

Thus, the reversible transition from 2D to 3D conductivity can be attained by increasing temperature, intercalating with a superconductor (which is able to form precipitates), illuminating (with a photon energy exceeding a 2D-localized-state depth beneath the 3D percolation level), and by a pressure shifting of the 2D localized state into the conduction continuum.

The 2D nature of the electron gas in InSe is associated with two circumstances:

(i) the anisotropy of the chemical bond in the crystal lattice with a period scale;

(ii) the presence of planar extended defects, which are potential barriers for electrons, with a distance between them of ~1 μm [14] or ~500 lattice spacings.

The latter fact causes a drop in the crystal conductivity when the electron path along the *c* axis becomes comparable with the interbarrier spacing. Planar defects may also explain the high conduction-anisotropy coefficient.

However, in our opinion, the natural anisotropy of the chemical bond can independently and consistently explain all the special features of the properties of InSe.

In study [4], and then in [5], we advanced a hypothesis that explains a number of anomalous properties of indium selenide:

(I) an unusual temperature dependence of conductivity;

(II) special features of temperature dependences for the thermopower;

(III) the appearance of a narrow gap when the temperature decreases and the dependence of this gap on the current through the sample;

(IV) a change in the sign of the linear-expansion coefficient from positive to negative with decreasing temperature; and

(V) a change in the sign of the derivative in the temperature dependence of the nuclear-quadrupole-resonance frequency.

This hypothesis consists in realizing the Peierls structural phase transition with the formation of charge-density waves in an InSe layered crystal at a temperature below 80–100 K.

The formation of charge-density waves (CDW) as a result of the Peierls structural phase transition (PSPT) and their influence on the properties of layered dichalcogenides of transition metals with metallic conduction and also on the anisotropic semimetal oxide Mo_4O_{11} were investigated previously [15–18].

In contrast to metal-like dichalcogenides, the observation of effects associated with the formation of CDWs at the PSPT is difficult in InSe due to a low concentration of free carriers. Nevertheless, the aforementioned InSe anomalies investigated by us and observed in other studies indicate that the PSPT is possible in this crystal.

A modification of the spectra of electrons and phonons in InSe at the PSPT must certainly affect the spatial distribution and the energy spectrum of impurities and defects in the crystal. Since the indicated modification is realized in a time necessary for the diffusion processes to take place, the appearance of hysteresis phenomena should be expected when the temperature slowly decreases or increases under PSPT conditions. The presence of van der Waals gaps, to which the impurities and defects shift under certain conditions, can be the cause of the formation of new modifications in the periodic structures based on InSe layered crystal. This, in turn, can lead to new multiple phase transitions (PT) with new critical temperatures.

In addition, possible inhomogeneities of the crystal at the microlevel can explain why individual parts of the crystal experience PT at various temperatures; as a result, we can have multiple PTs.

The phenomenon of suppressing the CDW mode, which we previously observed when the electric current increased through the crystal and was accompanied by collapse of the gap that arose at the PSPT, must also affect the manifestation of CDW under various conditions.

The rigorous proof for the realization of PSPT can be obtained by means of structural analysis. This analysis is very difficult because the displacement of atomic positions from equilibrium is small, and a long-duration exposure is necessary for keeping the sample at a fixed low temperature.

Taking into account all of the reasons mentioned, we set ourselves the task of investigating the static and high-frequency conductivity of indium monoselenide in the temperature range of 4.2–300 K. For revealing the features of conductivity associated with the formation of CDWs, we performed measurements at a temperature-variation rate of 0.2– 0.8 K/min and with currents through the sample up to 10 μA. Such conditions were chosen in order to ensure that the phase arising as a result of the PT can be completely formed and that the CDW does not penetrate into the crystal under the action of an electric field.

2. EXPERIMENTAL

For investigations, we chose γ-polytype samples, whose unit cell contained a single InSe layer [1]. The crystal structure was assessed by measuring the X-ray diffraction and Raman spectra. The dc static conductivity was measured using the conventional four-point probe method. For preparing nonrectifying contacts, various methods were used: the deposition of current-conducting pastes with various compositions and the soldering of indium in a newly cleaved surface. The results of the measurements of $\sigma_{\|}$ and $\sigma_{\perp}$ were independent of the method for preparing the contact. The dynamic conductivities $\sigma_{\|}(\nu)$ and $\sigma_{\perp}(\nu)$ were measured in the range of ν = 1–500 MHz using an HP 4191A impedance analyzer. A high-frequency cable was used to provide a connection to the sample in the cryostat. The electrical length of the cable was instrumentally compensated using the facilities incorporated into the analyzer and by software processing of data, which allowed us to take into account more accurately the spurious contribution from the cable. For investigating the conductivity $\sigma_{\|}(\nu)$ in the frequency range $\nu \approx 100$ GHz, the quasi-optical procedure [6] was used. The current flowed through the sample in the cleavage plane.

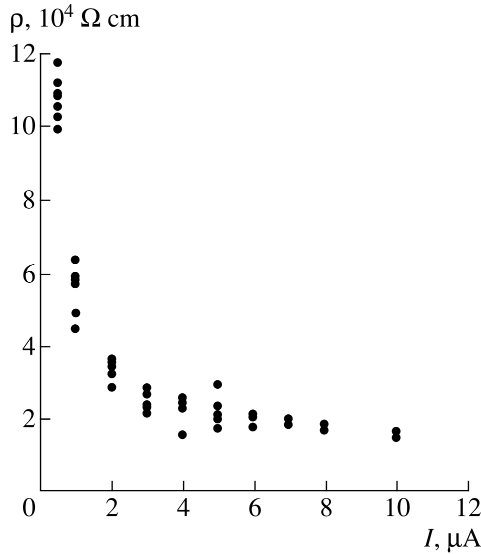

Fig. 1. Resistivity ρ as a function of a current through the InSe single-crystal sample at $T = 4.2$ K. The dots show the spread in the magnitude of ρ for a fixed current through the sample.

3. RESULTS

3.1. Static Mode

3.1.1. Low temperature-variation rates

The investigation of resistivity as a function of current through the sample (Fig. 1) shows that it decreases by six times when the current increases from 0.6 to 4 μA; a further increase in current up to 10 μA leads to a decrease in resistivity only by a factor of 1.3. This dependence tends to level off.

The maintenance of a fixed current through the sample leads to a substantial reduction in the resistivity. Such an instability in ρ (16%) is most pronounced for the lowest current. For 10 μA, the variation of ρ amounts to ~10%.

On cooling and heating the sample in the range from 9 to 130 K at a rate of ~(0.2–0.8) K/min and for a current $I = 10$ μA through the sample, we found jumps of ρ (Fig. 2) in the region of 150 K during cooling and at 200 K during heating. The $\rho(T)$ dependence forms a hysteresis loop with a maximum span of ~50% (or by more than 600 Ω cm).

The temperature dependence of electrical conductivity for a lower current $I = 1$ μA is much more complicated. In Fig. 3, we show the $\rho(T)$ dependence for a low heating rate after the preliminary cooling of the sample. The jumplike variations of the resistance can be seen at 15, 20, 45, 70, and 150 K (the last feature was observed also for a current of 10 μA). An especially large variation in ρ is 3000 Ω cm at 45 K.

3.1.2. High temperature-variation rates

We consider temperature dependences for the real part of conductivity σ'. The conductivity $\sigma'_{\perp}$ across lay-

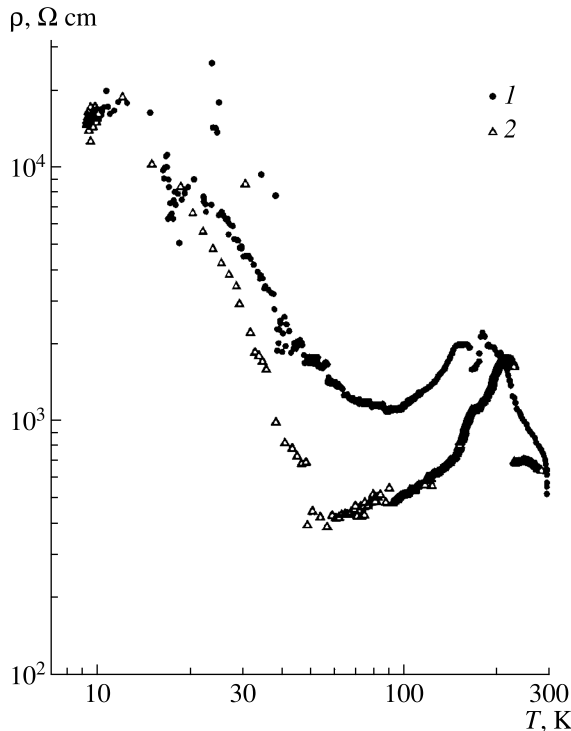

Fig. 2. Cyclic variation in the resistivity ρ as a function of temperature (*1*) during cooling and (*2*) during heating the InSe sample for a fixed current $I = 10$ μA.

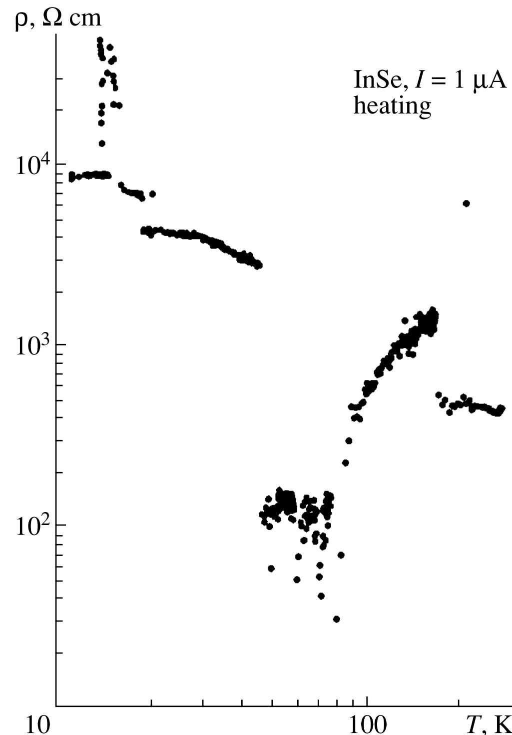

Fig. 3. Resistivity ρ as a function of temperature for the current $I = 1$ μA during low-rate heating after preliminary cooling of the sample.

ers decreases with temperature in the region of 150 K < T < 300 K. In the range of 50 K ≤ T ≤ 150 K, a tendency towards leveling off $\sigma'_{\perp}(T)$ is observed, while, for T < 50 K, a drop in $\sigma'_{\perp}$ increases again with decreasing T. A further reduction in temperature is accompanied by a leveling off of the dependence $\sigma'_{\perp}(T)$ at the level of (6–7) × 10^{-7} $(\Omega\ \mathrm{cm})^{-1}$ at $T \lesssim$ 10–20 K. It should be noted that the temperature dependence of $\sigma'_{\perp}$ for the frequency ν = 100 MHz is qualitatively similar; however, the steepness of variation in $\sigma'_{\perp}$ turns out to be much less as compared with the case of ν = 0 (Fig. 4, curves *1*, *1'*).

The temperature dependence of conductivity $\sigma'_{\parallel}$ along layers is more complicated. Similarly to $\sigma'_{\perp}$, $\sigma'_{\parallel}$ (ν = 0) increases with temperature for T > 150 K. In the region of $T \approx$ 150 K, a minimum is observed in the $\sigma'_{\parallel}(T)$ curve at ν = 0. A temperature decrease in the range of 50 K $\lesssim T \lesssim$ 150 K leads to an increase in $\sigma'_{\parallel}$ by a factor of 4, while the conductivity again abruptly decreases with temperature for $T \lesssim$ 50 K, and, at T = 4.2 K, it turns out to be approximately 30 times lower as compared with $\sigma'_{\parallel}$ at $T \approx$ 50 K. It is of interest that fluctuations are observed in the dependence $\sigma'_{\parallel}(T)$ in the region of 50 K $\lesssim T \lesssim$ 150 K at the level of $\Delta\sigma'_{\parallel}/\sigma'_{\parallel} \approx$ 10–20%.

3.2. Dynamic Mode

The results of measurements of temperature dependences for the real part of conductivity σ' for various frequencies and orientations of an electric field are summarized in Fig. 4. It was found that the conductivity both across and along layers substantially depends on the frequency, with σ' increasing with the frequency up to $\nu \approx$ 100 GHz in both cases. It can be seen that the conductivity increases 30–100 times for $\sigma'_{\perp}$ and $\sigma'_{\parallel}$ in the range of 0 < ν < 100 MHz, while the strongest variation in conductivity is observed at helium temperatures: $\sigma'_{\perp}(100\ \mathrm{MHz})/\sigma'_{\perp}(0) \approx 180$ and $\sigma'_{\parallel}(100\ \mathrm{MHz})/\sigma'_{\parallel}(0) \approx 250$.

Special features of the $\sigma'_{\perp}(T)$ dependences are substantially less pronounced for ν = 0 than in the case of ν = 100 MHz, and, at $T \lesssim$ 50 K, the rate of decrease of $\sigma'_{\perp}(T)$ turns out to be substantially lower for ν = 100 MHz than in the case of ν = 0 (Fig. 4). However, the temperature range of 50 K $\lesssim T \lesssim$ 150 K turns out to be anomalous (Fig. 5) also for the dynamic conductivity. In this temperature range, a pronounced temperature hysteresis is observed both for the real part $\sigma'_{\parallel}$ and for the imaginary part $\sigma''_{\parallel}$ of the conductivity, while the reproducibility of data for $\sigma'_{\perp}(T)$ and $\sigma''_{\parallel}(T)$ is attained only at $T \lesssim$ 50 K and $T \gtrsim$ 250 K (Fig. 5).

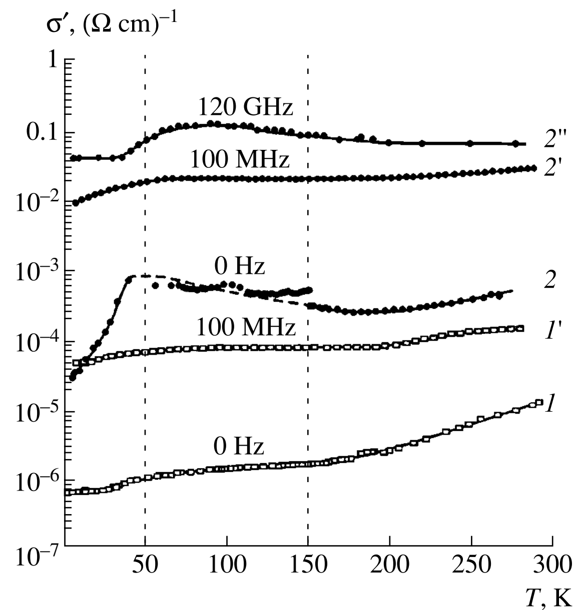

Fig. 4. Results of measuring the temperature dependences for the real part σ' of conductivity of InSe for the crystallographic directions (*1*, *1'*) $\sigma'_{\perp}$ across the layers and (*2*–*2"*) $\sigma'_{\parallel}$ along the layers. The conductivity was measured at the frequencies ν = (*1*, *2*) 0; (*1'*, *2'*) 10^8; and (*2"*) 1.2×10^{11} Hz.

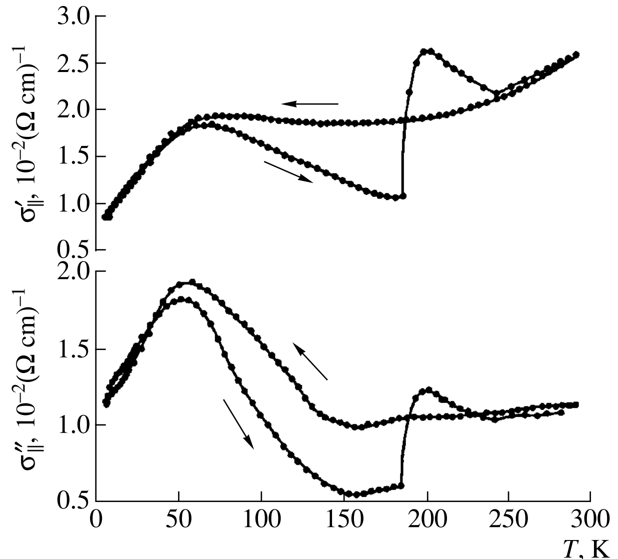

Fig. 5. Special features of $\sigma'_{\parallel}$ during a cyclic temperature variation and the measurements at a frequency of 100 MHz.

In the frequency region of $\nu \approx$ 120 GHz, the conductivity along layers measured by the quasi-optical

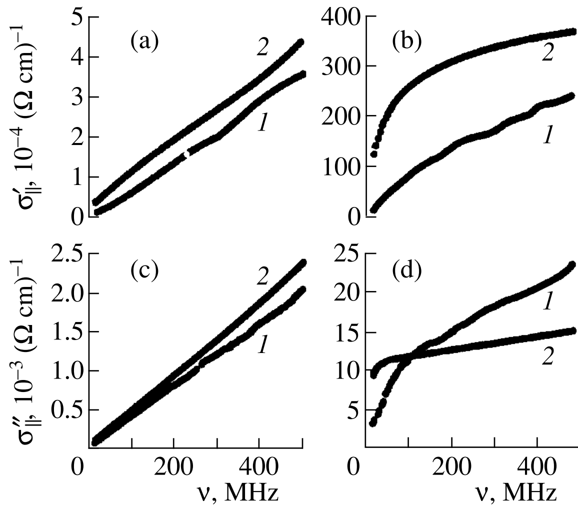

Fig. 6. Frequency dependences of (a, b) real and (c, d) imaginary parts of the conductivity at temperatures of 4.2 K (curves *1*) and 300 K (curves *2*). The conductivity was measured (a, c) ($\sigma'_{\perp}$, $\sigma'_{\parallel}$) across layers and (b, d) ($\sigma'_{\parallel}$, $\sigma''_{\parallel}$) along InSe layers.

method is highest in the region of 50 K $\lesssim T \lesssim$ 150 K and levels off at $T \lesssim$ 50 K (Fig. 4). It should be noted that the value of $\sigma(T)$ for $\nu \approx$ 120 GHz increases when the temperature decreases (Fig. 4) for $T \gtrsim$ 150 K, in contrast to the measurements at frequencies $\nu \approx$ 100 MHz and $\nu \approx 0$.

4. DISCUSSION

The InSe conductivity we considered in the previous section depends very unusually on frequency and temperature. First of all, it should be noted that there is a pronounced frequency dispersion of conductivity even at helium temperatures at which the electron gas in InSe is two-dimensional and degenerate. However, for a degenerate electron gas at $\nu \approx <$ 100 GHz, $\sigma'_{\parallel}$ must, first, depend weakly on frequency and, second, decrease with frequency instead of increasing as follows from the data in Fig. 4. Such behavior of $\sigma'(\nu)$ in degenerate systems is conventionally associated either with strong Fermi liquid effects or with generation of charge-density waves [19].

In order to clarify the possible nature of the dispersion of $\sigma'_{\parallel}$ and $\sigma'_{\perp}$, we consider the frequency dependences of the real and imaginary parts of the conductivity at T = 300 and 4.2 K for $\nu <$ 500 MHz (Fig. 6). In the case of conductivity across layers (Figs. 6a, 6c), $\sigma'_{\perp}(\nu)$ and $\sigma''_{\parallel}(\nu)$ increase almost linearly with the frequency, whereas the frequency dependences of the conductivity along InSe layers for $\sigma'_{\parallel}(\nu)$ and $\sigma''_{\parallel}(\nu)$ (Figs. 6b, 6d) are nonlinear and tend to level off at 300 K.

The simplest explanation can be given for the conductivity $\sigma_{\perp}$ across layers because the conductivity is controlled in this case by planar defects and by potential barriers related to them. It is well known [20] that these barriers can give rise to frequency dispersion of the conductivity beginning at low frequencies, which is apparently observed experimentally (Figs. 4, 6). If the space-charge relaxation time depends only slightly on temperature, the temperature dependence of high-frequency conductivity can be weaker than the thermally activated tunneling at the direct current (Fig. 4).

The presence of spatial inhomogeneities may be one of the possible causes of strong dispersion of the conductivity $\sigma_{\parallel}$ along layers. Such an assumption makes it possible to explain the similar shape of the curves $\sigma'_{\parallel}(\nu)$ at T = 300 and 4.2 K (Fig. 6b) in a natural way. At the same time, the form of the dependences $\sigma''_{\parallel}(\nu)$ turns out to be different for these cases (Fig. 6d), which indicates that it is necessary to take into account the frequency dependence of the relaxation time $\tau(\nu, T)$ arising due to interaction effects. It should be stressed that the necessity of taking into account the relaxation-time dispersion and the scattering anomalies related with it follows also from an analysis of the data for $\sigma'(\nu, T)$ at $T \gtrsim$ 150 K (Fig. 4), according to which $\partial\sigma'_{\parallel}/\partial T > 0$ for $\nu \lesssim$ 100 MHz and $\partial\sigma'_{\parallel}/\partial T < 0$ for $\nu \approx$ 100 GHz.

The behavior of $\sigma(\nu, T)$ is most complex in the range of 50 K $\lesssim T \lesssim$ 150 K, where a 3D-to-2D-conductivity transition occurs. The fluctuations observed for ν = 0 and also the hysteresis for ν = 100 MHz (Fig. 5) in the case of conductivity along layers can be explained by the presence of structural defects in InSe crystals under investigation; these defects act as traps for charge carriers. The relaxation processes (including long-duration ones) induced by the capture of electrons and by emptying these localized states are likely the cause of the anomalous behavior of the conductivity in the region of a 2D-to-3D-conductivity transition.

5. CONCLUSIONS

The obtained experimental data show conclusively that there is a substantial difference between the properties of InSe layered crystal in the static and dynamic modes.

In the static mode, we managed to prove that multiple phase transitions can occur in InSe layered crystal. Their characteristics (the critical temperatures and their large number, the presence of a hysteresis loop and its span, and the presence of unstable conductivity), as can be expected, depend on experimental conditions (the temperature-variation rate and current through the sample). The hysteresis loop indicates that a first-order PT, possibly associated with a transition between the states of commensurable and incommensurable charge-den-

sity waves, is realized. The effects discovered require further careful investigation.

If there is a superstructure (higher orders of periodicity) associated with interlayers of polytypes, the alternation of intercalated van der Waals gaps, or with other causes, the commensurability or incommensurability of CDWs must be considered relative to the periods of identity for a different dimension. Therefore, in this case, multiple phase transitions from the commensurable phase to the incommensurable one should be expected.

The multiple instabilities of the conductivities for the quasi-2D organic conductor (BEDT-TTF)$_3$Cl$_2$-2H$_2$O in the range of 4.2–300 K and also the hysteresis phenomena and bistabilities associated with the formation of CDWs were observed previously [21–23]. Thus, the phenomena described by us for InSe, instead of being unique, are characteristic of conducting materials with reduced dimensionality of the electron gas.

The experimental data obtained in this study show that the pronounced dispersion of high-frequency conductivity of InSe is also caused by structural imperfections of various nature. The fluctuations and the hysteresis in the temperature dependences of static and dynamic conductivity at comparatively low frequencies likely arise as a result of the interaction of charge carriers with structural inhomogeneities in the directions across and along layers and also with the superstructure caused by the formation of CDWs.

An important role is likely played by the modification of the spatial distribution and energy spectrum of impurities and defects in the crystal; this modification is related to the formation of charge-density waves.

ACKNOWLEDGMENTS

We are grateful to professor S.V. Demishev for his participation in discussions of experimental results.

This study was supported by the programs "Fundamental Spectroscopy" and "Physics of Microwaves" of the Ministry of Industry, Science, and Technology of the Russian Federation.

REFERENCES

1. A. I. Dmitriev, Z. D. Kovalyuk, V. I. Lazorenko, and G. V. Lashkarev, Phys. Status Solidi B **162**, 2B (1990).
2. A. I. Dmitriev, V. I. Lazorenko, G. V. Lashkarev, *et al.*, Solid State Commun. **75**, 465 (1990).
3. A. I. Dmitriev and G. V. Lashkarev, Indian J. Phys. A **66**, 301 (1992).
4. A. I. Dmitriev, G. V. Lashkarev, and D. A. Fedorchenko, in *Proceedings of XVIII International Conference on Infrared and Millimeter Waves* (Essex, UK, 1993), p. 226.
5. A. I. Dmitriev, G. V. Lashkarev, V. K. Kiseleyv, *et al.*, Int. J. Infrared Millim. Waves **16**, 775 (1995).
6. B. Gorshunov, A. Volkov, A. Prokhorov, *et al.*, Solid State Commun. **105**, 433 (1998).
7. A. Segura, B. Man, J. Martínez-Pastor, and A. Chevy, Phys. Rev. B **43**, 4953 (1991).
8. P. H. Houdy, Y. L. Maurice, J. M. Besson, *et al.*, J. Appl. Phys. **61**, 5267 (1998).
9. T. L. Belen'kiĭ, E. A. Vyrodov, and V. I. Zverev, Zh. Éksp. Teor. Fiz. **94** (12), 276 (1988) [Sov. Phys. JETP **67**, 2548 (1988)].
10. A. I. Larkin, Pis'ma Zh. Éksp. Teor. Fiz. **31** (4), 239 (1980) [JETP Lett. **31**, 219 (1980)].
11. N. B. Brandt, V. A. Kul'bachinskiĭ, Z. D. Kovalyuk, and G. V. Lashkarev, Fiz. Tekh. Poluprovodn. (Leningrad) **21**, 1230 (1987) [Sov. Phys. Semicond. **21**, 613 (1987)].
12. A. I. Dmitriev, Z. D. Kovalyuk, V. I. Lazorenko, and G. V. Lashkarev, Fiz. Tverd. Tela (Leningrad) **30**, 1246 (1988) [Sov. Phys. Solid State **30**, 725 (1988)].
13. A. I. Dmitriev, V. I. Lazorenko, G. V. Lashkarev, and A. I. Bykov, Fiz. Tekh. Vys. Davlenii **1**, 13 (1991).
14. A. A. Volkov, Yu. G. Goncharov, G. V. Kozlov, *et al.*, Infrared Phys. **25**, 369 (1985).
15. L. I. Bulaevskiĭ, Usp. Fiz. Nauk **116**, 449 (1975) [Sov. Phys. Usp. **18**, 514 (1975)].
16. L. I. Bulaevskiĭ, Usp. Fiz. Nauk **120**, 259 (1976) [Sov. Phys. Usp. **19**, 836 (1976)].
17. H. Guot, C. Shlenker, O. Fourcandot, and K. Konate, Solid State Commun. **54**, 909 (1985).
18. M. Ino, S. Ohara, and S. Horisaka, Phys. Status Solidi B **148**, 659 (1983).
19. G. Gruner, Rev. Mod. Phys. **60**, 1129 (1988).
20. P. T. Oreshkin, *Physics of Semiconductors and Insulators* (Vysshaya Shkola, Moscow, 1977).
21. W. Lubczynski, S. V. Demishev, J. M. Caulfield, *et al.*, J. Phys.: Condens. Matter. **8**, 6005 (1996).
22. S. V. Demishev, N. E. Sluchanko, N. A. Samarin, *et al.*, Ferroelectrics **176**, 329 (1996).
23. A. I. Dmitriev, Z. D. Kovalyuk, V. I. Lazorenko, and G. V. Lashkarev, Fiz. Tverd. Tela (Leningrad) **30**, 1246 (1988) [Sov. Phys. Solid State **30**, 725 (1988)].

Translated by V. Bukhanov

Semiconductors, Vol. 37, No. 2, 2003, pp. 140–144. Translated from Fizika i Tekhnika Poluprovodnikov, Vol. 37, No. 2, 2003, pp. 151–155.
Original Russian Text Copyright © 2003 by Brudnyĭ, Peshev.

The *U* Peak in the DLTS Spectra of *n*-GaAs Irradiated with Fast Neutrons and 65-MeV Protons

V. N. Brudnyĭ* and V. V. Peshev**

* *Kuznetsov Siberian Physicotechnical Institute, Tomsk, 634050 Russia*

** *Tomsk Polytechnical University, Tomsk, 634034 Russia*

e-mail: peshev@mail.2000.ru

Submitted April 23, 2002; accepted for publication May 22, 2002

Abstract—The origin of a broad *U* band in spectra obtained using deep-level transient spectroscopy (DLTS) of *n*-GaAs irradiated with fast neutrons and 65-MeV protons was investigated. It is believed that this band is presumably a superposition of two peaks related to two defects *P*2 and *P*3 which have been well documented in GaAs and reside within defect clusters. The DLTS spectra were calculated taking into account the nonuniform distribution of these defects in a sample and the built-in electric fields induced by corresponding inhomogeneities. © *2003 MAIK "Nauka/Interperiodica".*

1. INTRODUCTION

It is well known that a broad peak (referred to as the *U* band in previous publications) is observed in the spectra of deep-level transient spectroscopy (DLTS) of *n*-GaAs irradiated with ions or fast neutrons; this band manifests itself in the temperature range of 250–350 K, which is characteristic for the appearance of *E*4 and *E*5 peaks in the spectra of samples irradiated with gamma-ray photons or 1- to 2-MeV electrons. The *U* peak is presumably related to the presence of aggregates (clusters) of point defects in irradiated GaAs samples [1]. It has been attempted to relate this peak to the As_{Ga} antisite defect, which has an irradiation origin and is similar to a grown-in *EL*2 center with a level at E_c – (0.75–0.82) eV in the GaAs band gap. In fact, measurements of electron spin resonance indicate that this defect is efficiently generated in GaAs exposed to radiation [2]; at the same time, the intensity of the DLTS band corresponding to the *EL*2 center does not increase. Therefore, it has been assumed that the As_{Ga} radiation defect produced during the ion or neutron irradiation of GaAs is formed within a dense defect cluster. In addition, an unknown defect *X* with a shallower level is formed in the vicinity of the As_{Ga} defect. In this case, the emission of an electron from the As_{Ga} level to the conduction band occurs via the level of the *X* defect, which supposedly results in a shift of the corresponding DLTS peak to a lower temperature region of the spectrum [3]. Indeed, isochronous annealing of irradiated GaAs samples brought about a shift of the *U* peak to higher temperatures and a slight increase in the intensity of the *EL*2 peak, compared to its preirradiation value in the DLTS spectra, which was related to annihilation of the *X* defect. However, the above assumption was not corroborated by subsequent special investigations of this problem [4]. It was also noted that a decrease in the filling-pulse amplitude U_p (with the bias voltage U_b maintained unchanged) in *n*-GaAs samples irradiated with neutrons shifts the *U* peak to the higher temperature region of the spectrum. This phenomenon was related to the anomalously profound effect of the strength of an applied external electric field on the rate of emission of electrons from the traps that were involved in the formation of the *U* band [5]. Therefore, we suggest estimating the "true" position of the *U* peak by extrapolating the strength of the external electric field to zero.

2. RESULTS AND DISCUSSION

In this study, we assume that the *U* band is related to well-known point defects which are characteristic of GaAs irradiated with 1–2-MeV electrons or gamma-ray photons but are located within a defect cluster in the case of irradiation with ions or fast neutrons. It can then be expected that special features of the band under consideration are caused by the fact that electron emission from the above defects occurs in the region of a nonuniform electric field formed at the interface between a cluster and crystalline matrix. Indeed, since the Fermi level in irradiated GaAs is pinned at the limiting (stationary) position near $F_{\lim} = E_v + 0.6$ eV [6], the contact potential difference $\varphi_c = (E_g - F_{\lim} - F_0)/q$ appears between the cluster and the crystal matrix; this potential difference gives rise to a space-charge region (SCR) at the interface between the defect cluster and the crystal. Here, E_g is the semiconductor band gap; F_0 is the Fermi level, whose position is specified by the doping of initial material; and *q* is the elementary charge.

In order to gain insight into the factors that control the shape and the temperature position of the *U* band,

we studied the influence of the duration t_p and amplitude U_p of the filling pulse on the shape of the U peak in n-GaAs irradiated with pulsed-reactor neutrons (~1 MeV) and cyclotron protons (65 MeV). We subjected irradiated samples to isochronous annealing under conditions where a reverse-bias voltage was or was not applied to the structures. We then calculated the DLTS spectra of the samples under consideration taking into account the nonuniform distribution of radiation defects and the presence of built-in electric fields caused by these inhomogeneities.

We measured the DLTS spectra using Au–Ti–n-GaAs–n^+-GaAs–n^{++}-GaAs structures, where $n = (3–6) \times 10^{15}$ cm^{-3}, $n^+ \approx 2 \times 10^{17}$ cm^{-3}, and $n^{++} \approx 2 \times 10^{18}$ cm^{-3}. The n-type region under investigation contained $EL2$ and $EL3$ growth defects, whose concentrations were equal to about $(5–8) \times 10^{13}$ cm^{-3} and $\lesssim 2 \times 10^{12}$ cm^{-3}, respectively. The DLTS spectra of irradiated structures included the well-known peaks $E2$ (E_c – 0.16 eV) and $E3$ (E_c – 0.38 eV), and also a broad peak located in the temperature range of 250–350 K and referred to as the U band (Figs. 1a, 1b).

It follows from Figs. 1a and 1b that, as the duration of the filling pulse decreases from 20 μs (curves *1*, *1*') to 2 μs (curves *2*, *2*') with U_p = 6 V kept constant, the peak of the U band shifts to higher temperatures; this shift is mainly caused by a distortion of the band shape due to a decrease in the DLTS-signal amplitude at the low-temperature wing of the U band. This circumstance indicates that the traps which form the low-temperature wing of the U band have a smaller capture cross section compared to the traps responsible for the high-temperature wing of this band. In addition, a decrease in the amplitude of the filling pulse U_p from 6 to 2 V (for t_p = 2 μs) brings about a further shift of the peak of the band under consideration to higher temperatures due to similar distortion of its shape (curves *3*, *3*'). Presumably, this effect is caused by the fact that a decrease in the amplitude U_p of the filling pulse results in an increase in the ratio $\lambda/(W_1 - W_0)$. Here, W_0 and W_1 are the widths of the depletion layer when the filling pulse is or is not applied to the structure, respectively; and λ is the distance between the depletion-layer boundary and the point of intersection of the Fermi level for electrons with the level of a deep trap. The aforementioned effect brings about an increase in the contribution of slowly filled traps to the total number of traps in the region under investigation [7]. As a result, the contribution of traps with a smaller capture cross section (the low-temperature wing of the U band) to the DLTS signal decreases; consequently, the shape of the U band changes.

In order to clarify the cause of shift of the U-band peak to lower temperatures as the amplitude U_p decreased, we measured the DLTS spectrum at U_p = 2 V

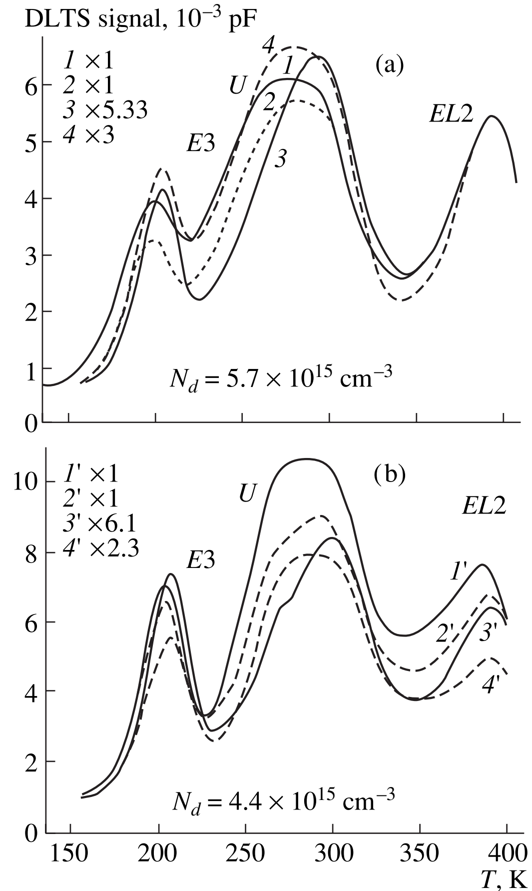

Fig. 1. The DLTS spectra of n-GaAs irradiated with (a) fast neutrons at a dose of 6.3×10^{13} cm^{-2} and (b) 65-MeV protons at a dose of 1.3×10^{13} cm^{-2}. The measurements were performed at (*1*, *1*') $U_b = U_p$ = 6 V and t_p = 20 μs (the conditions of almost complete filling of the U-band traps); (*2*, *2*') $U_b = U_p$ = 6 V and t_p = 2 μs (the conditions of incomplete filling of the traps); (*3*, *3*') U_b = 6 V, U_p = 2 V, and t_p = 2 μs (the conditions with an even lower degree of filling); and (*4*, *4*') U_b = 6 V, U_p = 2 V, and t_p= (*4*) 300 and (*4*') 100 μs (the conditions of almost complete filling of the traps). The time window $t_1/t_2 = 2 \times 10^{-3}/10^{-2}$ s/s.

with the filling-pulse duration increased to t_p = 300 μs (curve *4*) and 100 μs (curve *4*'). An increase in t_p leads to an almost complete recovery of both the temperature position of the U-band peak and the corresponding band shape. Hence, it follows that the main cause of the U-peak shift as the amplitude U_p decreases (at t_p = const) is the incomplete filling of the traps that form the low-temperature wing of the U band during the time t_p when the filling pulse is in effect. This circumstance indicates that, contrary to previous assumptions [5], the rate of emission of electrons from the traps, which form the U band, is virtually independent of the strength of the applied external electric field. Therefore, we may assume that electrons are emitted from the U-band levels in high built-in nonuniform electric fields formed in

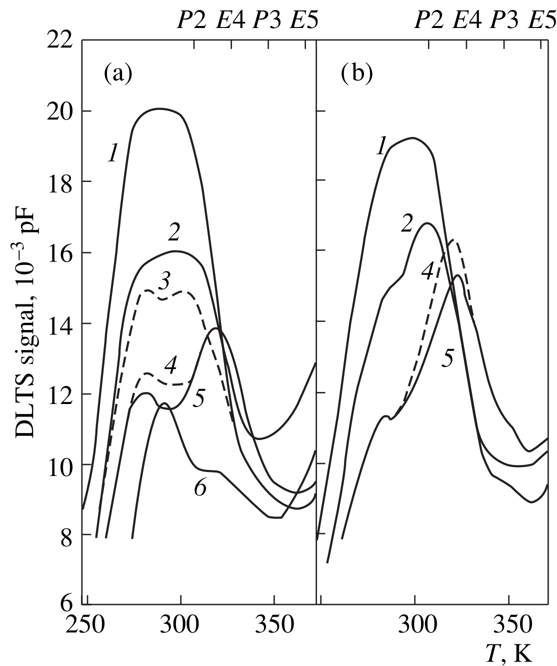

Fig. 2. Spectra of the U band in n-GaAs (*1*) after irradiation with 65-MeV protons at a dose of 6.3×10^{13} cm^{-2}, (*2*) after subsequent isochronous annealing for 5 min with (a) $U = 0$ V and (b) U = 15 V at annealing temperatures of (*2*) 250, (*3*) 275, (*4*) 325, (*5*) 375, and (*6*) 500°C. The time window $t_1/t_2 = 2 \times 10^{-3}/10^{-2}$ s/s.

the vicinity of the interface between a defect cluster and the semiconductor matrix. In this case, the rate of electron emission from the traps located in the SCR changes radically owing presumably to the Pool–Frenkel effect, which can result in an appreciable broadening of the DLTS peak to the low-temperature region [8].

Experiments show that, in the samples irradiated with neutrons, the U peak becomes partially resolved into two peaks as a result of subsequent annealing [5, 9]; at the same time, in proton-irradiated n-GaAs, such a resolution is attained without annealing if the mode of incomplete filling of the traps is used (Fig. 1b, curves *2*', *3*'). This circumstance suggests that the U band is formed by two types of defects, which have possibly already been identified in irradiated n-GaAs. Notably, the shape of these peaks and their temperature position are appreciably distorted as a result of the fact that electron emission from these traps to the conduction band occurs in the region of built-in nonuniform electric fields generated by defect clusters.

A decrease in the defect density in a cluster as a result of partial isochronous annealing leads to a decrease in the value of φ_c and, consequently, to a decrease in the strength of the built-in electric field. Therefore, as the temperature of isochronous annealing increases and approaches that corresponding to the cluster decomposition, the shape and the temperature position of each of the peaks, which presumably form the U band, tend towards “true” values that are characteristic of isolated defects. We can identify these peaks by analyzing them at the highest attainable annealing temperatures and by determining the parameters of the defects that are responsible for the U peak.

In Figs. 2a and 2b, we show the DLTS spectra in the region of the U band for the samples irradiated with 65-MeV protons and then annealed isochronously without applying a reverse-bias voltage (Fig. 2a) and with a reverse voltage with a magnitude of U = 15 V applied to the structure (Fig. 2b). In the upper part of Figs. 2a and 2b, we indicate the positions of the DLTS peaks for the well-known $E4$, $E5$, $P2$, and $P3$ centers in n-GaAs irradiated with 1-MeV electrons [10]. It follows from Fig. 2 that, as the annealing temperature increases, the U peak changes its shape, shifts to higher temperatures, and becomes partially resolved into two subpeaks, whose relative contribution to the U-band formation depends heavily on the annealing conditions. This circumstance makes it possible to resolve these peaks and estimate their parameters by varying the isochronous-annealing conditions. An analysis of these subpeaks, designated henceforth as $P2'$ and $P3'$ and obtained after annealing the irradiated samples at temperatures of 500°C at $U = 0$ (the $P2'$ peak) and 325°C at $U = 15$ V (the $P3'$ peak), made it possible to estimate the corresponding parameters at $E_{na} = 0.48$ eV and $\sigma_{na} = 2.2 \times 10^{-15}$ cm^2 for the $P2'$ peak and $E_{na} = 0.68$ eV and $\sigma_{na} = 1.4 \times 10^{-15}$ cm^2 for the $P3'$ peak. As the annealing temperature increases, these estimates approach the parameters of the well-known centers $P2$ ($E_c - 0.5$ eV and 1.4×10^{-15} cm^2) and $P3$ ($E_c - 0.72$ eV and 1.4×10^{-13} cm^2), which were observed in n-GaAs irradiated with gamma-ray photons and 1-MeV electrons [10].

We used the previously obtained expression for the DLTS spectra of samples which contain radiation-defect clusters [8] to describe analytically the U-band shape as a combination of two well-known peaks $P2$ and $P3$; i.e.,

$$R(T) \approx \frac{\bar{N}_T C(W_1^2 - W_0^2)}{2N_d W_1^2 \sigma^2} \int_{r_0}^{3\sigma} r \exp(-r^2/2\sigma) \times [\exp(-\alpha(r)t_1) - \exp(-\alpha(r)t_2)]dr. \quad (1)$$

Here, t_1 and t_2 are the sampling times for the capacitance relaxation, which define the rate window; T is the temperature of the sample; C is the capacitance of the Schottky barrier in the absence of a filling pulse; $\bar{N}_T$ is the macroscopic concentration of the traps that contribute to the U band; α is the rate of electron emission from the traps to the conduction band; r_0 is the radius of the spherical surface of a cluster at which the Fermi

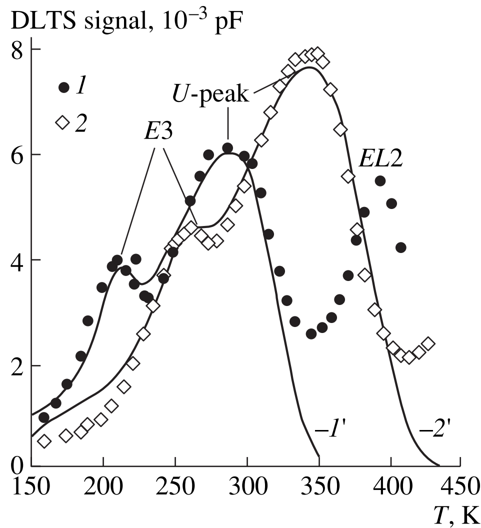

Fig. 3. Experimental (circles *1* and diamonds *2*) and calculated (the solid lines *1*', *2*') DLTS spectra of *n*-GaAs (N_d = 5.7×10^{15} cm^{-3}) irradiated with fast neutrons at a dose of 6.3×10^{13} cm^{-2} for the time windows $t_1/t_2 = 2 \times 10^{-3}/10^{-2}$ s/s and (*2*, *2*') $4 \times 10^{-5}/2 \times 10^{-4}$ s/s, with the variance parameter being equal to σ = 250 Å.

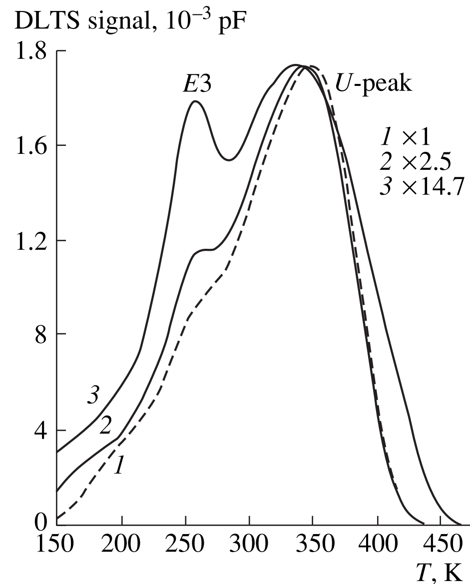

Fig. 4. Calculated DLTS spectra for *n*-GaAs which had dopant concentrations equal to (*1*) 10^{15}, (*2*) 5.5×10^{15}, and (*3*) 10^{17} cm^{-3} and was irradiated with fast neutrons at a dose of 6.3×10^{13} cm^{-2}. The time window $t_1/t_2 = 4 \times 10^{-5}$ s/2×10^{-4} s; the variance parameter σ = 250 Å.

level *F* intersects the deep trap level; and σ is the variance of the normal distribution of the *P*2 and *P*3 centers in the SCR of a cluster. The quantities W_0, W_1, and *C* are related by well-known formulas to the free-carrier concentration N_d in the semiconductor matrix, the voltage *U* applied to the diode, and the contact potential difference across the Schottky barrier. When estimating parameters of a cluster, we used the characteristics reported by Coates and Mitchell [11]. We assumed that defects in the SCR were distributed according to the normal law with a variance σ, whose value was estimated using regression analysis of experimental DLTS spectra with allowance made for the well-known "electrical" sizes of a cluster in the percolation model [11].

The spectrum calculated according to expression (1) (see solid line *1*' in Fig. 3) is in satisfactory agreement with the shape of the experimental *U* band (filled circles in Fig. 3) for *n*-GaAs irradiated with fast neutrons. According to expression (1), the peaks are bound to shift to higher temperatures as the rate window increases; notably, this shift is bound to be accompanied with changes in the shape and height of the peaks. The experimental (*2*) and calculated (*2*') spectra shown in Fig. 3 were obtained using the time window t_1/t_2 = $4 \times 10^{-5}/2 \times 10^{-4}$ s/s; as can be seen, the results of calculations satisfactorily agree with experimental data, which indicates that expression (1) is correct. The results of calculations (Fig. 4) are also consistent with experimental evidence that an increase in the *U*-band half-width is mainly due to an increase in the contribution of the low-temperature wing of this band to the spectrum as the dopant concentration in the material becomes higher [12].

3. CONCLUSIONS

It is well known that the peaks related to the *E*4 and *E*5 traps are dominant in the temperature range of 250–350 K in the DLTS spectra of *n*-GaAs samples irradiated at room temperature with 1- to 2-MeV electrons or gamma-ray photons and obscure the peaks related to the *P*2 and *P*3 traps. The peaks corresponding to the *P*2 and *P*3 traps appear in the spectra only after annealing of irradiated samples at about 200°C or as a result of high-temperature irradiation, in which case the *E*4 and *E*5 defects disappear [10]. It is noteworthy that the contribution of the *P* traps to the spectrum amounts to less than 5% of the total amount of observed radiation defects; however, this contribution increases to 10% if the crystal is irradiated with 5-MeV protons [13]. Therefore, we may expect that the contribution of *P*-type defects to total defect formation is larger in GaAs samples irradiated with high-energy (65-MeV) protons or fast neutrons. The *E*4 and *E*5 defects are annealed out after heat treatment of such samples at a temperature near 200°C; as a result, the shape and intensity of the *U* band change somewhat (Fig. 2). In addition, according to the data shown in Fig. 2, the contribution of the *P*-type defects to formation of the *U* band amounts to about 70%. Presumably, *P*-type traps are more complex defects than *E* traps; the latter are typically related to defects in the As sublattice [10].

Possibly, P traps are complexes of several point defects, since these traps are annealed out at high temperatures (in the range of 450–600°C) [10, 13]. In n-GaAs samples irradiated with ions or fast neutrons, these defects are mainly formed in corresponding clusters. In GaAs the Fermi level in such clusters is pinned at the limiting (steady-state) position at about E_v + 0.6 eV, which causes the space-charge region to be formed at the interface between the defect cluster and the crystal. Notably, emission of electrons from P-type traps to the conduction band occurs in nonuniform electric fields in these regions; this circumstance makes it possible to use the Pool–Frenkel effect to describe the shape of the observed U band and its transformation caused by changes in the conditions of both the DLTS measurements and isochronous annealing of irradiated samples.

REFERENCES

1. G. M. Martin, A. Mitonneau, and A. Mircea, Electron. Lett. **13**, 191 (1977).
2. A. Goltzene, B. Meyer, and C. Schwab, Appl. Phys. Lett. **54**, 907 (1989).
3. S. Makram-Ebeid and P. Boher, Mater. Sci. **10/12**, 1075 (1986).
4. V. N. Brudnyĭ, N. G. Kolin, V. A. Novikov, *et al.*, Fiz. Tekh. Poluprovodn. (St. Petersburg) **31**, 811 (1997) [Semiconductors **31**, 686 (1997)].
5. R. Magno, M. Spencer, J. G. Giessner, and E. R. Weber, in *Abstracts of 13th International Conference on Defects in Semiconductors* (Coronado, Cal., 1984), p. 981.
6. V. N. Brudnyi, S. N. Grinyaev, and V. E. Stepanov, Physica B (Amsterdam) **212**, 429 (1995).
7. D. Stievenard, J. C. Bourgoin, and M. J. Lannoo, J. Appl. Phys. **55**, 1447 (1984).
8. V. A. Novikov and V. V. Peshev, Fiz. Tekh. Poluprovodn. (St. Petersburg) **32**, 411 (1998) [Semiconductors **32**, 366 (1998)].
9. V. N. Brudnyĭ, N. G. Kolin, and A. I. Potapov, Fiz. Tekh. Poluprovodn. (St. Petersburg) **27**, 260 (1993) [Semiconductors **27**, 145 (1993)].
10. D. Pons and J. C. Bourgoin, J. Phys. C: Solid State Phys. **18**, 3839 (1985).
11. R. Coates and E. W. J. Mitchell, Adv. Phys. **24**, 593 (1975).
12. C. E. Barnes, T. E. Zipperian, and L. R. Dawson, J. Electron. Mater. **14**, 95 (1985).
13. V. N. Brudnyĭ, N. G. Kolin, and A. I. Potapov, Izv. Vyssh. Uchebn. Zaved., Fiz. **35** (10), 57 (1992).

Translated by A. Spitsyn

Semiconductors, Vol. 37, No. 2, 2003, pp. 145–147. Translated from Fizika i Tekhnika Poluprovodnikov, Vol. 37, No. 2, 2003, pp. 156–158.
Original Russian Text Copyright © 2003 by Vaksman, Nitsuk, Purtov, Shapkin.

ELECTRONIC AND OPTICAL PROPERTIES OF SEMICONDUCTORS

Inversion of Conductivity Type in ZnSe Single Crystals Obtained by the Method of Free Growth

Yu. F. Vaksman*^, Yu. A. Nitsuk*, Yu. N. Purtov*, and P. V. Shapkin**

* *Mechnikov National University, ul. Petra Velikogo 2, Odessa, 65026 Ukraine*

^*e-mail: vaksman_yu@farlep.net*

** *Lebedev Physical Institute, Russian Academy of Sciences, Leninskiĭ pr. 53, Moscow, 117924 Russia*

Submitted April 25, 2002; accepted for publication June 17, 2002

Abstract—ZnSe:In and (ZnSe:In):Zn single crystals obtained by the method of free growth were studied. Inversion of the conductivity type was attained by annealing crystals in an atmosphere of saturated selenium vapors. Hole conductivity was attained for the first time in (ZnSe:In):Zn crystals with an initially high electron conductivity (3–5 Ω^{-1} cm^{-1}). The origin of donor and acceptor centers responsible for the conductivity of crystals was ascertained. © *2003 MAIK "Nauka/Interperiodica".*

1. INTRODUCTION

Zinc selenide is one of the most promising materials for the fabrication of injection electroluminescent structures and lasers which emit in the blue region of the spectrum. In this context, the problem of obtaining bulk crystals with a high electron conductivity and attaining conductivity-type inversion in a confined *n*-ZnSe layer becomes extremely important.

Undoped ZnSe crystals have a high resistivity ($\rho \sim 10^{10}$ Ω cm). A decrease in the resistivity of crystals is typically attained by annealing them in a melt of high-purity zinc or aluminum. The resistivity of the ZnSe:Zn samples we studied was typically no higher than 40 Ω cm. Doping with aluminum results in a decrease in resistivity to 0.1 Ω cm. At the same time, an increase in the intensity of self-activated long-wavelength luminescence is observed in ZnSe:Al, which reduces the quantum yield of blue emission. It was shown previously by Vaksman *et al*. [1] that crystals obtained by the free-growth method and subsequently subjected to annealing in a zinc melt have a low resistivity (ρ = 0.2–0.3 Ω cm); in addition, the efficiency of the edge emission in these crystals is higher than that of long-wavelength self-activated emission. We believe that such crystals hold considerable promise as a material for light-emitting structures.

In this context, we report in this paper the results of studying the electrical conductivity of ZnSe, ZnSe:In, and (ZnSe:In):Zn crystals annealed in saturated selenium vapors. We show for the first time that it is possible to inverse the conductivity type in zinc selenide crystals with a high electron conductivity. The aim of this study is to clarify the types of dominant intrinsic and impurity defects that induce conductivity-type inversion in the crystals under investigation.

2. EXPERIMENTAL

The ZnSe single crystals under investigation were obtained by the method of free growth on oriented single-crystal ZnSe substrates. Vapor-phase doping of the crystals with indium was effected in the course of the crystal growth. The growth of the crystals was described in detail elsewhere [2]. The indium concentration in the crystals under investigation was determined using the atom-emission method and varied from 10^{16} to 10^{19} cm^{-3}.

The ZnSe crystals were annealed in selenium vapors in evacuated quartz cells for 0.5–20 h at a temperature of 1120 K. Samples annealed in vacuum or in zinc vapors in similar conditions were used as references.

Electric contacts to *n*-ZnSe crystals were formed using fusion of indium. Contacts to *p*-ZnSe samples were obtained by the cathodic sputtering deposition of platinum. We verified that the contacts were nonrectifying by measuring the current–voltage characteristics. The conductivity type was determined from the thermopower sign. The resistivity was measured using the van der Pauw method.

3. ELECTRICAL CONDUCTIVITY OF *n*-ZnSe CRYSTALS

We studied temperature dependences of the dark electrical conductivity in ZnSe and ZnSe:In crystals. We ascertained that the electrical conductivity of undoped *n*-ZnSe crystals was controlled by donors with an activation energy of E_a = 0.66 eV. Interstitial zinc atoms correspond to the donors with this activation energy [3]. The *n*-ZnSe:In crystals were characterized by two values of donor-activation energy: E_a = 0.03 and 0.39 eV. The former value corresponds to In_{Zn}^{+} donor

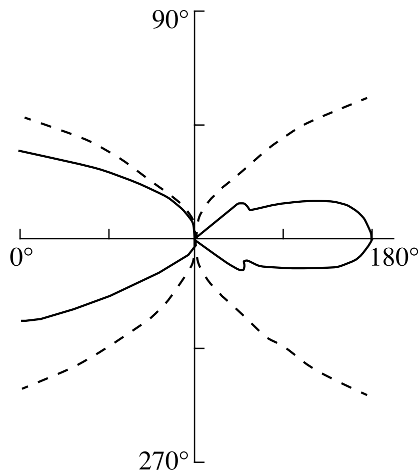

Fig. 1. Indicatrixes of scattering of light in an undoped ZnSe crystal (dotted line) and in a ZnSe crystal doped heavily with indium (the solid line).

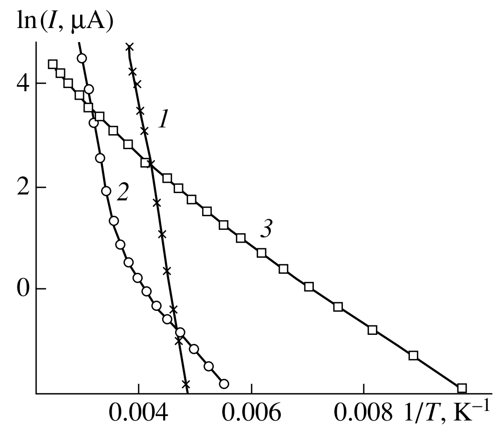

Fig. 2. Temperature dependences of dark current in (*1*) ZnSe:Se, (*2*) (ZnSe:In):Se, and (*3*) [(ZnSe:In):Zn]:Se crystals.

centers, which were identified previously. The donors with an activation energy of 0.39 eV were not detected in undoped crystals. We believe that these donors are related to In_I^{3+} interstitial atoms. The In_I^{3+} centers were detected in ZnSe:In crystals for the first time. Evidently, the formation of these centers becomes possible owing to doping of the crystals in the course of their growth.

A fraction of indium atoms leaves the zinc lattice sites for interstices when the ZnSe:In crystals are annealed in a zinc melt and the indium solubility in the crystals is lowered. This inference is corroborated by an analysis of the absorption spectra of ZnSe:In crystals before and after their annealing in a zinc melt [1]. Escape of indium atoms to interstices is accompanied by the formation of associative macrodefects. In order to estimate the size of the macrodefects, we measured the optical indicatrixes of light scattered in the crystal without absorption. A semiconductor laser emitting at a wavelength of 660 nm was used as the light source. In Fig. 1, we show the indicatrixes of scattering for an undoped ZnSe crystal and a ZnSe crystal doped heavily with indium. It can be seen that the indicatrix of scattering for the heavily doped crystal has a clearly pronounced asymmetry in the forward direction (i.e., in the direction of optical-beam propagation) and features two poorly pronounced maxima at the base of the right-hand side of the diagram. This fact suggests that, in this case, we have Mie scattering by particles whose size is larger than λ. It is also noteworthy that the scattering defects are located in a highly conducting medium with a large dielectric constant (ε = 8.1). This circumstance brings about an increase in the role of the reflected component of optical radiation (the left-hand part of the diagram).

As noted previously [1], the formation of indium-related macrodefects reduces the electron mobility in (ZnSe:In):Zn crystals. In addition, the (ZnSe:In):Zn crystals are grayish, which reduces their optical transmission. The electrical conductivity of ZnSe:In crystals annealed in a zinc melt has a single activation energy, $E_a = 0.02$ eV, which corresponds to In_{Zn}^{+} shallow-level donors.

4. CHARACTERISTICS OF *p*-TYPE CRYSTALS

It was ascertained that conductivity-type inversion occurred in ZnSe, ZnSe:In, and (ZnSe:In):Zn crystals as a result of annealing in selenium vapors. Annealing for 5 h was found to be optimal. The characteristics of the samples annealed in selenium vapors are listed in the table. It should be noted that control annealings of the samples in vacuum or in zinc vapors did not result in inversion of the conductivity type. In particular,

Electrical characteristics of ZnSe crystals with *p*-type conductivity

The crystal type	ρ, Ω cm	μ, cm^2 V^{-1} s^{-1} [3]	*p*, cm^{-3}	E_a, eV
ZnSe:Se	3×10^6	25	5×10^{10}	0.43
(ZnSe:In):Se	1×10^6	25	1×10^{10}	0.12, 0.43
[(ZnSe:In):Zn]:Se	4×10^5	25	3×11^{11}	0.08, 0.12

Note: *p* and μ are the hole concentration and mobility, respectively.

annealing (ZnSe:In):Zn crystals for 5 h in vacuum at 900°C leads to an increase in the resistivity of the crystals from 0.3 to 8 Ω cm. Similar annealing in zinc vapors results in a decrease in the resistivity from 0.3 to 0.2 Ω cm.

In order to determine the origin of the centers responsible for hole conductivity in the crystals under investigation, we studied the temperature dependence of the dark current $I(T)$ (Fig. 2). The hole conductivity in ZnSe:Se is characterized by an activation energy of 0.43 eV (Fig. 2, curve *1*). This value, according to Serdyuk *et al.* [4], corresponds to the activation energy of the $(V_{Zn}V_{Se})^-$ center, which incorporates a doubly charged zinc vacancy. The same defects are observed in (ZnSe:In):Se. However, in a low-temperature region, the hole conductivity of (ZnSe:In):Se crystals has an activation energy of 0.12 eV (Fig. 2, curve *2*). According to Krasnov *et al.* [5], the activation energy E_a = 0.12 eV corresponds to neutral $(V_{Zn}V_{Se})^*$ associative defects. It was ascertained that these defects are also present in [(ZnSe:In):Zn]:Se crystals. At the same time, the *p*-type conductivity of these crystals at low temperatures is controlled by acceptors with an activation energy $E_a = 0.08$ eV (Fig. 2, curve *3*). We observed such shallow acceptor levels in *p*-ZnSe crystals for the first time. Taking into account the amphoteric properties of indium, we may assume that these acceptors are impurity atoms that are localized in the selenium sublattice. This assumption is corroborated by the following facts.

(i) The concentration of zinc vacancies increases and the concentration of selenium vacancies decreases as a result of annealing in selenium vapors. In these conditions, substitution (filling) of selenium vacancies can occur according to the scheme $V_{Se} + \mathrm{In} \longrightarrow \mathrm{In}_{Se}$. This substitution proceeds simultaneously throughout the entire volume of the crystal, since selenium impurity was introduced in the crystals during their growth.

(ii) The solubility of indium in the crystals under consideration increases as a result of annealing the samples in selenium vapors. This inference is corroborated by an increase in the transmittance of (ZnSe:In):Zn crystals after their annealing in selenium vapors.

In order to check the uniformity of the physical properties of [(ZnSe:In):Zn]:Se crystals, we performed a small-angle (5°) lapping of one of the crystal faces. This made it possible to measure the photoluminescence spectra at various distances from the sample surface. We found that these spectra were identical; i.e., they remained unchanged as the distance from the surface was varied. We also measured the resistivity of crystals in the course of consecutive lapping of one of the faces to a certain depth. These results also indicate that crystals are electrically homogeneous. Thus, we may state that the presence of excess indium in interstices of (ZnSe:In):Zn is the main cause of formation of shallow-level In_{Se} acceptor centers during heat treatment of the crystals in selenium vapors. These centers (along with zinc vacancies) give rise to hole conductivity in [(ZnSe:In):Zn]:Se crystals.

The absence of shallow acceptor levels with an activation energy of 0.08 eV in the band gap of (ZnSe:In):Se crystals indicates that the source of efficient indium diffusion to the selenium sublattice is related to indium macrodefects, rather than point interstitial In_I^{3+} centers.

5. CONCLUSIONS

The following conclusions can be drawn on the basis of the above results:

(I) Inversion of the conductivity type occurs in the crystals under investigation as a result of annealing in selenium vapors.

(II) Hole conductivity of ZnSe and ZnSe:In crystals is controlled by zinc vacancies, which are incorporated into $(V_{Zn}V_{Se})^*$ and $(V_{Zn}V_{Se})^-$ associative defects.

(III) The low-temperature conductivity of [(ZnSe:In):Zn]:Se crystals is controlled by shallow-level In_{Se} acceptor centers, which are uniformly distributed over the volume of crystals. Formation of these centers is related to the presence of indium-containing macrodefects in (ZnSe:In):Zn crystals; these macrodefects are located in interstices of the crystal lattice.

REFERENCES

1. Yu. F. Vaksman, Yu. A. Nitsuk, Yu. N. Purtov, and P. V. Shapkin, Fiz. Tekh. Poluprovodn. (St. Petersburg) **35**, 920 (2001) [Semiconductors **35**, 883 (2001)].
2. Yu. V. Korostelin, V. I. Kozlovsky, A. S. Nasibov, and P. V. Shapkin, J. Cryst. Growth **197**, 449 (1999).
3. D. D. Nedeoglo and A. V. Simashkevich, *Electrical and Luminescent Properties of Zinc Selenide* (Shtiintsa, Kishinev, 1980).
4. V. V. Serdyuk, N. N. Korneva, and Yu. F. Vaksman, Phys. Status Solidi A **91**, 173 (1985).
5. A. N. Krasnov, Yu. F. Vaksman, and Yu. N. Purtov, Pis'ma Zh. Tekh. Fiz. **18** (12), 1 (1992) [Sov. Tech. Phys. Lett. **18**, 763 (1992)].

Translated by A. Spitsyn

Semiconductors, Vol. 37, No. 2, 2003, pp. 148–155. Translated from Fizika i Tekhnika Poluprovodnikov, Vol. 37, No. 2, 2003, pp. 159–165.
Original Russian Text Copyright © 2003 by Glinchuk, Prokhorovich.

ELECTRONIC AND OPTICAL PROPERTIES OF SEMICONDUCTORS

Specific Features of Determination of the Concentrations of Shallow-Level Impurities in Semiconductors from Analysis of Edge-Luminescence Spectra

K. D. Glinchuk* and A. V. Prokhorovich

Institute of Semiconductor Physics, National Academy of Sciences of Ukraine, Kiev, 03028 Ukraine

**e-mail: ria@isp.kiev.ua*

Submitted June 4, 2002; accepted for publication June 18, 2002

Abstract—Analytical expressions for the normalized intensities of bands in the spectra of low-temperature (T = 1.8–4.2 K) luminescence, related to the recombination of free electrons at shallow-level acceptors, to the recombination of free holes at shallow-level donors and to the electronic transitions between the components of donor–acceptor pairs and of bound excitons are reported. Different possibilities of using these expressions for determination of the changes in the concentrations of shallow-level acceptors and donors, caused by external factors F, are analyzed. A comparison of the theoretical dependences of the normalized intensities of low-temperature impurity-, donor–acceptor-, and exciton-luminescence bands on F with the relevant dependences used in experiments is performed. © *2003 MAIK "Nauka/Interperiodica".*

1. INTRODUCTION

It is known that a number of intense bands are observed in the low-temperature edge-luminescence spectra (the energy of emitted photons $h\nu$) of semiconductors (Fig. 1). These bands (see, for example, [1]) are due to (1) the radiative recombination of free electrons at shallow-level neutral acceptors A^0 (intensity I_{eA^0}), of free holes at shallow-level neutral donors D^0 (intensity I_{hD^0}), and of free electrons and holes (intensity I_{eh}); (2) the radiative transitions of electrons from donors D^0 to acceptors A^0 (intensity $I_{D^0A^0}$); and (3) the radiative annihilation of both free excitons (intensity I_X) and excitons bound at neutral acceptors A^0X, at ionized donors D^+X, and at neutral donors D^0X (intensities I_{A^0X}, I_{D^+X}, and I_{D^0X}, respectively).

Analysis of the ratios of the intensities of the above-listed edge bands in the luminescence spectra of semiconductors is widely used to determine the concentrations of shallow-level acceptors N_A and donors N_D in the latter and the changes in these concentrations caused by different external factors F (see, for example, [2] and relevant references therein, as well as [3, 4]). However, in order to use this method for the determination of N_A and N_D and their changes, one should carry out a detailed analysis of its validity. Previously [2], such an analysis was performed for semiconductors containing isolated acceptors and donors (to which transitions of only free electrons and holes are possible) (Fig. 1). Evidently, this method is valid for elemental semiconductors, such as Si and Ge, where concentrations of shallow-level acceptors and donors are generally low. In the III–V and II–VI semiconductors, the concentrations of shallow-level acceptors and donors are quite high; therefore, a great number of acceptors and donors form donor–acceptor (DA) pairs with a concentration of N_{DA}.

In this study, we generalized the results obtained in [2] for the case of semiconductors containing rather high concentrations of shallow-level acceptors and donors. Due to high concentrations of shallow-level impurities, intense DA transitions are possible in such semiconductors (Fig. 1). We present relations for the normalized intensities of bands in low-temperature edge-luminescence spectra. These relations make it possible to determine the changes in the concentrations of shallow-level acceptors and donors when external factors are varied.

2. BASIC ASSUMPTIONS

(1) We consider semiconductors containing shallow-level acceptors A and shallow-level donors D. On the one hand, transitions of free electrons and holes to acceptors and donors are possible. On the other hand,

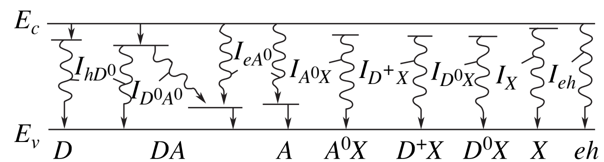

Fig. 1. Radiative transitions in bound (A^0X, D^+X, and D^0X) and free (X) excitons: to isolated donors D and acceptors A; between the components of DA pairs; and between the components of free-electron–free-hole pairs (eh).

1063-7826/03/3702-0148$24.00 © 2003 MAIK "Nauka/Interperiodica"

the transitions of electrons may occur from donors to acceptors; i.e., between the components of DA pairs (Fig. 1). Free excitons X may be bound at one of the components of DA pairs to form exciton–impurity complexes.[1] In addition, the semiconductor under consideration may contain defects of other types, which, to some extent (in comparison with the acceptors and donors), affect the recombination rate of excess electrons and holes (in particular, the concentrations of photoelectrons and photoholes [5]).

(2) Let the generation of excess electrons and holes occur uniformly throughout the semiconductor bulk. We assume that the semiconductor is at a low temperature (T = 1.8–4.2 K). In this temperature range, neither thermal ionization of acceptors and donors nor thermal decay of excitons occurs; and the semiconductor's conductivity, due to the impurity deionization, is governed by excess electrons and holes.

(3) It is known that not only radiative, but also nonradiative electronic transitions (of the same type as Auger transitions) may occur between the components of DA pairs and between the components of free and bound excitons [5–10]. In what follows, we assume that the role of the Auger recombination of DA pairs and bound excitons is insignificant. By this we mean that (i) the distance between the components of DA pairs is relatively large [5, 6]; (ii) the concentrations of excess charge carriers δn and δp and the concentration of DA pairs N_{DA} are not very high [5, 6]; and (iii) excitons are bound at shallow-level acceptors and donors in direct-gap semiconductors, for example, GaAs [6, 8]. In this case, the transitions $e \longrightarrow A^0$, $h \longrightarrow D^0$, and $D^0 \longrightarrow A^0$ between the components of DA pairs and the annihilation of bound excitons result mainly in the emission of photons (Fig. 2).[2]

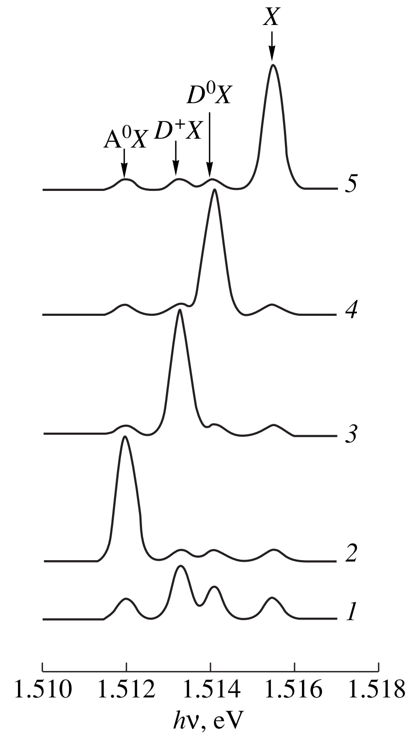

Fig. 2. Calculated exciton-luminescence spectra of GaAs at T = 4.2 K. The ratios of the intensities $I_{A^0X} : I_{D^+X} : I_{D^0X} : I_X$ are assumed to be equal to (*1*) 2 : 5 : 3 : 2; (*2*) 12 : 1 : 1 : 1; (*3*) 1 : 12 : 1 : 1; (*4*) 1 : 1 : 12 : 1; and (*5*) 1 : 1 : 1 : 12. It follows from here (see (9)) that (*1*) $n_X \sim \delta n \delta p$, N_{A^0}, N_{D^+}, N_{D^0}; (*2*) $n_X \sim \delta n \delta p / N_{A^0}$; (*3*) $n_X \sim \delta n \delta p / N_{D^+}$; (*4*) $n_X \sim \delta n \delta p / N_{D^0}$; and (*5*) $n_X \sim \delta n \delta p$.

3. RELATIONS FOR DETERMINING CONCENTRATIONS OF SHALLOW-LEVEL ACCEPTORS AND DONORS IN DIFFERENT CHARGE STATES

It is evident that, at low temperatures (see Section 2), changes in the concentrations of neutral acceptors and donors (N_{A^0} and N_{D^0}, respectively) per unit time are governed by the balance equations

$$\frac{dN_{A^0}}{dt} = c_{pA}^{-}(N_A - N_{A^0})\delta p - c_{nA}^{0} N_{A^0}\delta n - c_n^* N_{D^0} N_{A^0} = 0, \quad (1)$$

$$\frac{dN_{D^0}}{dt} = c_{nD}^{+}(N_D - N_{D^0})\delta n - c_{pD}^{0} N_{D^0}\delta p - c_n^* N_{D^0} N_{A^0} = 0. \quad (2)$$

Here, $N_A - N_{A^0} = N_{A^-}$ and $N_D - N_{D^0} = N_{D^+}$ are the concentrations of ionized acceptors and donors, respectively; δp and δn are the concentrations of excess holes and electrons, respectively; c_{pA}^{-} and c_{pD}^{0} are the coefficients of hole trapping by ionized acceptors and neutral donors, respectively; c_{nA}^{0} and c_{nD}^{+} are the coefficients of electron trapping by neutral acceptors and ionized donors, respectively; and c_n^* is the DA-recombination coefficient. The value of c_n^* heavily depends on the distance between the donor and acceptor in a DA pair; i.e., it is significantly different for DA pairs with dissimilar radii [5, 6]. Therefore, we regard c_n^* as the average value of the DA-recombination coefficient.

Relations (1) and (2) imply that the annihilation of exciton–impurity complexes A^0X, D^+X, and D^0X (Auger processes in such complexes are disregarded) is accompanied by the appearance of isolated acceptors A^0 and donors D^+ and D^0 [11, 12]. In this case, the anni-

[1] We assume that the Bohr radius of bound excitons A^0X, D^+X, and D^0X is significantly smaller than the distance between the components of the DA pair.

[2] In direct-gap semiconductors (in particular, in CdS) the quantum yield of luminescence caused by the annihilation of excitons bound at shallow-level acceptors and donors is close to unity [6, 8].

hilation of bound excitons does not affect N_{A^0}, N_{D^+}, and N_{D^0}; i.e., these quantities are governed only by transitions of electrons and holes to neutral and ionized acceptors and donors. Expressions (1) and (2) are valid if the photogeneration rate of electron–hole pairs (*eh*) is nonzero.

A simple transformation of Eqs. (1) and (2) allows us to obtain quadratic equations in the unknowns N_{A^0}, N_{D^+}, and N_{D^0}. The solutions for these equations will make it possible to determine the steady-state concentrations of neutral acceptors and ionized and neutral donors at different relations between the quantities

$$c_{nD}^{+}N_D\delta n = b \quad \text{and} \quad c_{pA}^{-}N_A\delta p = d,$$
$$c_n^*(b+d) = a^* \quad \text{and} \tag{2a}$$
$$(c_{nA}^0\delta n + c_{pA}^-\delta p)(c_{nD}^+\delta n + c_{pD}^0\delta p) = a.$$

4. INTENSITIES OF BANDS IN THE EDGE-LUMINESCENCE SPECTRUM

Undoubtedly, under the above-mentioned conditions (see item 2 in Section 2), the intensities of the edge-luminescence bands (Fig. 1) are governed by the relations [12]

$$I_{eA^0} = c_{nA}^0 N_{A^0}\delta n, \quad I_{hD^0} = c_{pD}^0 N_{D^0}\delta p,$$
$$I_{D^0A^0} = c_n^* N_{D^0}N_{A^0}, \tag{3}$$

$$I_{eh} = c\delta n\delta p, \quad I_X = \alpha_X n_X, \tag{4}$$

$$I_{A^0X} = \alpha_{A^0X}n_{A^0X} = b_{A^0X}N_{A^0}n_X, \tag{5}$$

$$I_{D^+X} = \alpha_{D^+X}n_{D^+X} = b_{D^+X}N_{D^+}n_X, \tag{6}$$

$$I_{D^0X} = \alpha_{D^0X}n_{D^0X} = b_{D^0X}N_{D^0}n_X. \tag{7}$$

Here,

$$n_X = \frac{b_X\delta n\delta p}{\alpha_X + b_{A^0X}N_{A^0} + b_{D^+X}N_{D^+} + b_{D^0X}N_{D^0}}; \tag{8}$$

n_X, n_{A^0X}, n_{D^+X}, and n_{D^0X} are the concentrations of free excitons and excitons bound at neutral acceptors, ionized donors, and neutral donors, respectively; c is the rate of direct radiative recombination of free electrons and holes; α_X, α_{A^0X}, α_{D^+X}, and α_{D^0X} are the probabilities of radiative annihilation of free excitons and excitons bound at neutral acceptors, ionized donors, and neutral donors, respectively; and b_X, b_{A^0X}, b_{D^+X}, and b_{D^0X} are the probabilities of binding of an electron–hole pair with the formation of a free exciton and binding free excitons at neutral acceptors, ionized donors, and neutral donors, respectively.

The relations for the intensities (5)–(7) and for n_X (8) imply that there are only a small number of acceptors and donors at which excitons are bound; i.e., $n_{A^0X} \ll N_{A^0}$, $n_{D^+X} \ll N_{D^+}$, and $n_{D^0X} \ll N_{D^0}$. This is one of the main conditions for the applicability of the method under consideration [2].

Evidently, when the values of N_{A^0}, N_{D^+}, and N_{D^0} are known (see Eqs. (1) and (2)), relations (3)–(7) allow us to determine the normalized intensities of the edge-luminescence bands which are directly related to the concentrations N_A or N_D.

As follows from (4)–(7), the ratios of the intensities of the exciton-luminescence bands are governed by the expression

$$I_{A^0X} : I_{D^+X} : I_{D^0X} : I_X$$
$$= b_{A^0X}N_{A^0} : b_{D^+X}N_{D^+} : b_{D^0X}N_{D^0} : \alpha_X. \tag{9}$$

It can be seen from (8) and (9) that the shape of the exciton-luminescence spectrum allows us to estimate the relationship between the recombination characteristics of free excitons on the right-hand side of expression (9). Thus, we can estimate the relative role of different channels of annihilation of free excitons and, in particular, determine the dominant mechanism of their recombination (see Fig. 2).

5. THEORETICAL RELATIONS FOR THE NORMALIZED INTENSITIES OF BANDS IN THE EDGE-LUMINESCENCE SPECTRUM

In what follows, we consider the most convenient (i.e., independent of the generation rate of electron–hole pairs) relations for the normalized intensities of the impurity-, DA-, and exciton-luminescence bands, which follow from expressions (3)–(7). These relations allow us to directly determine (without measuring δn and δp simultaneously) the changes in the concentrations of shallow-level acceptors and donors when the external factor F is varied. The changes in the concentrations are derived from an analysis of the dependence of the edge-luminescence intensity on illumination. Evidently, the normalized intensities are convenient if the relevant spectral bands have similar illumination-dependent characteristics.

We will perform a theoretical consideration of the convenient normalized intensities of the edge-luminescence bands for the limiting cases of high and low concentrations δn and δp. We will show that the normalized intensities of the impurity-, DA-, and exciton-luminescence bands may have the convenient form only when

the quantities $b = c^+_{nD} N_D \delta n$ and $d = c^-_{pA} N_A \delta p$ obey the relations

$$b \gg d, \quad b \simeq d, \quad \text{and} \quad b \ll d.$$

This convenient form may also be valid when rather plausible relations

$$c^+_{nD} \delta n \gg c^0_{pD} \delta p, \quad c^-_{pA} \delta p \gg c^0_{nA} \delta n$$

are satisfied. Notably, the ratio $\delta p/\delta n$ is independent of the external factor F and the generation rate of electron–hole pairs L [2]. The observed dependence of the intensities of the edge-luminescence bands on illumination (see Section 7) are indicative of the validity of both of the above relations (we assume that they are valid when L and F vary) and the relation $\delta p/\delta n \neq f(L)$. At the same time, the validity of the relation $\delta p/\delta n \neq f(F)$ can be verified only when δp and δn are high (see Section 7). However, it is not inconceivable that, in a semiconductor containing DA pairs, $\delta p/\delta n = f(F)$ at low δp and δn, while, at high δp and δn, the ratio of these quantities is independent of F [5]. Therefore, in what follows, when considering the convenient normalized intensities of edge-luminescence bands (which imply that the relation $\delta p/\delta n \neq f(F)$ is satisfied), we will restrict our analysis to high generation rates L (i.e., to high δp and δn).

For simplicity, we will not specify the form of the dependence of the concentration of free excitons on their recombination characteristics when determining the convenient normalized intensities of edge-luminescence bands. Undoubtedly, such specification is possible only if one of the mechanisms of free-exciton recombination plays a dominant role in governing the value of n_X. In particular, if we have

$$\alpha_X \gg b_{A^0X} N_{A^0} + b_{D^+X} N_{D^+} + b_{D^0X} N_{D^0},$$

then $n_X \propto \delta n \delta p$; if we have

$$b_{A^0X} N_{A^0} \gg \alpha_X + b_{D^+X} N_{D^+} + b_{D^0X} N_{D^0},$$

then $n_X \propto \delta n \delta p / N_{A^0}$; and if we have

$$b_{D^0X} N_{D^0} \gg \alpha_X + b_{A^0X} N_{A^0} + b_{D^+X} N_{D^+},$$

then $n_X \propto \delta n \delta p / N_{D^0}$ (see relation (8)). As was noted above (see Section 4), we can assess the roles of different channels of free-exciton annihilation in governing n_X (i.e., the shape of the dependence of the concentration of free excitons on their recombination characteristics) from an analysis of the exciton-luminescence spectra (Fig. 2). Evidently, the above-mentioned specification of the shape of the dependence of n_X on $\delta n \delta p$, N_{A^0}, N_{D^+}, and N_{D^0} can significantly increase the number of normalized intensities of the edge-luminescence bands, which are convenient for determination of the changes in N_A and N_D when the external factor F is varied. The convenient normalized intensities can be easily derived from the expressions presented below for the intensities of edge-luminescence bands and for the concentrations of acceptors and donors in different charge states.

5.1. Low Concentrations of Excess Charge Carriers δn and δp

When the concentrations δp and δn are low, the following inequality is satisfied: $c^*_n (b + d) \gg a$ (see (2a)). In this case, it is quite plausible that the DA band is dominant in the impurity-luminescence spectrum; i.e., $I_{D^0A^0} \gg I_{eA^0}, I_{hD^0}$ (see below).

5.1.1. When $b = c^+_{nD} N_D \delta n \gg d = c^-_{pA} N_A \delta p$

In the conditions under consideration, it follows from Eqs. (1) and (2) that

$$N_{A^0} = \frac{c^-_{pA} \delta p}{c^*_n \varphi_{D^0} N_D} N_A \ll N_A,$$
$$N_{D^+} = \frac{c^-_{pA} N_A + c^0_{pD} N_D}{c^+_{nD} \delta n + c^0_{pD} \delta p} \delta p, \quad N_{D^0} \simeq \varphi_{D^0} N_D. \tag{10}$$

Here, if $c_{pA} N_A \gg c^0_{pD} N_D$, then $c^+_{nD} \delta n \gg c^0_{pD} \delta p$;

$$c^-_{pA} N_A \delta p / (c^+_{nD} \delta n + c^0_{pD} \delta p) \ll N_D.$$

The quantity $\varphi_{D^0} = c^+_{nD} \delta n / (c^+_{nD} \delta n + c^0_{pD} \delta p)$ is the probability of an electron being trapped by a donor when the DA-transition rate is low ($c^*_n N_{A^0} \ll c^+_{nD} \delta n + c^0_{pD} \delta p$, see Eq. (2)).

When the above relation between b and d is satisfied, it follows from the inequality $c^*_n b \gg a$ (see (2a)) and expressions (3) and (10) that

$$c^*_n \varphi_{D^0} N_D \gg c^-_{pA} \delta p + c^0_{nA} \delta n, \quad I_{D^0A^0} = c^-_{pA} N_A \delta p,$$

$$I_{D^0A^0} / I_{eA^0} = c^*_n N_{D^0} / c^0_{nA} \delta n = c^*_n \varphi_{D^0} N_D / c^0_{nA} \delta n \gg 1,$$

$$I_{D^0A^0} / I_{hD^0} = c^*_n N_{A^0} / c^0_{pD} \delta p = c^-_{pA} N_A / c^0_{pD} \varphi_{D^0} N_D.$$

Apparently, $I_{D^0A^0} \gg I_{hD^0}$, because we should expect that $c^-_{pA} N_A \gg c^0_{pD} N_D$ due to a significant difference between the c^-_{pA} and c^0_{pD} coefficients ($c^-_{pA} \gg c^0_{pD}$) [2]. It is very likely that this inequality is satisfied even when $N_A < N_D$.

If the quite plausible inequality $c^+_{nD} \delta n \gg c^0_{pD} \delta p$ is satisfied (i.e., $\varphi_{D^0} \simeq 1$), then we have $N_{A^0} \propto N_A \delta p / N_D$,

$N_{D^+} \propto f(N_A, N_D)\delta p/\delta n$, and $N_{D^0} \simeq N_D$. In this case, as follows from expressions (3) and (5)–(7),

$$I_{eA^0} \propto \frac{N_A}{N_D}\delta p \delta n, \quad I_{hD^0} \propto N_D \delta p, \quad I_{D^0A^0} \propto N_A \delta p, \tag{11}$$

$$I_{A^0X} \propto \frac{N_A}{N_D} n_X \delta p,$$
$$I_{D^+X} \propto \frac{c_{pA}^- N_A + c_{pD}^0 N_D}{c_{nD}^+ \delta n} n_X \delta p, \quad I_{D^0X} \propto N_D n_X. \tag{12}$$

Thus, in order to determine the changes in N_A and N_D when the external factor F is varied, we can use the following relations for the normalized intensities of the impurity-, DA-, and exciton-luminescence bands:

$$\frac{I_{D^0A^0}}{I_{hD^0}}, \frac{I_{eA^0}}{I_{eh}} \propto \frac{N_A}{N_D}, \tag{13}$$

$$\frac{I_{D^0X}}{I_X} \propto N_D. \tag{14}$$

Here, the use of convenient normalized intensities of the impurity- and DA-luminescence bands make it possible to determine variation in the relation between N_A and N_D as F changes. The convenient normalized intensities of the exciton-luminescence bands allow us to determine N_D and N_A as functions of the external factor F.

5.1.2. Case of $b = c_{nD}^+ N_D \delta n \simeq d = c_{pA}^- N_A \delta p (|b - d| \ll b, d)$

In this case, it follows from Eqs. (1) and (2) that

$$N_{A^0} = \left(\beta \frac{c_{pA}^- \delta p}{c_n^* N_A}\right)^{1/2} N_A \ll N_A, \quad N_{D^+} \simeq N_D,$$
$$N_{D^0} = \left(\beta^{-1} \frac{c_{nD}^+ \delta n}{c_n^* N_D}\right)^{1/2} N_D \ll N_D. \tag{15}$$

Here,

$$\beta = (c_{nD}^+ \delta n + c_{pD}^0 \delta p)/(c_{pA}^- \delta p + c_{nA}^0 \delta n).$$

Then, it can be easily shown from the inequality $c_n^* (b + d) \gg a$ (see (2a)) and expressions (3), (6), and (15) that

$$I_{D^0A^0} = c_{nD}^+ N_D \delta n = c_{pA}^- N_A \delta p \gg I_{eA^0}, I_{hD^0};$$
$$I_{D^+X} \propto N_D n_X,$$
$$I_{eA^0}/I_{hD^0} \propto \beta \delta n/\delta p, \quad I_{A^0X}/I_{D^0X} \propto \beta.$$

If the relation $b \simeq d$ is not violated when the generation rate L and the external factor F vary, i.e., if $\delta p/\delta n \neq f(L)$ [then $\beta \neq f(L)$] and $N_D(F)\delta n(F) \propto N_A(F)\delta p(F)$ (strictly speaking, the validity of the latter relation is unlikely), for any β, we can use only the following convenient relation for the normalized luminescence-band intensities (this relation makes it possible to determine the dependence of N_D on F):

$$\frac{I_{D^+X}}{I_X} \propto N_D. \tag{16}$$

If $\beta \propto \delta n/\delta p$ (evidently, $\delta n/\delta p \propto N_A/N_D$; see above), i.e., $c_{nD}^+ \delta n \gg c_{pD}^0 \delta p$ and $c_{pA}^- \delta p \gg c_{nA}^0 \delta n$, we can use the following relations to determine the changes in N_A/N_D as F is varied:

$$\frac{I_{eA^0}}{I_{hD^0}} \propto \left(\frac{N_A}{N_D}\right)^2, \tag{17}$$

$$\frac{I_{A^0X}}{I_{D^0X}} \propto \frac{N_A}{N_D}. \tag{18}$$

5.1.3. When $d = c_{pA}^- N_A \delta p \gg b = c_{nD}^+ N_D \delta n$

In this case, it follows from Eqs. (1) and (2) that

$$N_{A^0} \simeq \varphi_{A^0} N_A, \quad N_{D^+} \simeq N_D,$$
$$N_{D^0} = \frac{c_{nD}^+ \delta n}{c_n^* \varphi_{A^0} N_A} N_D \ll N_D. \tag{19}$$

Here,

$$\varphi_{A^0} = \frac{c_{pA}^- \delta p}{c_{pA}^- \delta p + c_{nA}^0 \delta n}$$

is the probability of a hole being trapped by an acceptor when the DA-transition rate is low ($c_n^* N_{D^0} \ll c_{pA}^- \delta p + c_{nA}^0 \delta n$, see Eq. (1)).

As follows from the inequality $c_n^* d \gg a$ (see (2a)) and expressions (3), (6), and (19), when d and b obey the relation under consideration, we have

$$c_n^* \varphi_{A^0} N_A \gg c_{nD}^+ \delta n + c_{pD}^0 \delta p,$$

$$I_{D^0A^0} = c_{nD}^+ N_D \delta n, \quad I_{D^+X} = b_{D^+X} N_D n_X,$$

$$I_{D^0A^0}/I_{hD^0} = c_n^* N_{A^0}/c_{pD}^0 \delta p = c_{nA}^* \varphi_{A^0} N_A / c_{pD}^0 \delta p \gg 1,$$

$$I_{D^0A^0}/I_{eA^0} = c_n^* N_{D^0}/c_{nA}^0 \delta n = c_{nD}^+ N_D / c_{nA}^0 \varphi_{A^0} N_A.$$

Apparently, $I_{D^0A^0} \gg I_{eA^0}$ because one should expect that $c_{nD}^{+} N_D \gg c_{nA}^{0} N_A$ due to the significant difference between the c_{nD}^{+} and c_{nA}^{0} coefficients ($c_{nD}^{+} \gg c_{nA}^{0}$) [2]. It is quite likely that this inequality is satisfied even when $N_D < N_A$.

If the quite plausible inequality $c_{pA}^{-} \delta p \gg c_{nA}^{0} \delta n$ is satisfied (i.e., $\varphi_{A^0} \simeq 1$), we then have $N_{A^0} \simeq N_A$ and $N_{D^0} \propto N_D \delta n / N_A$. In this case, it follows from expressions (3) and (5)–(7) that

$$I_{eA^0} \propto N_A \delta n, \quad I_{hD^0} \propto \frac{N_D}{N_A} \delta n \delta p, \quad I_{D^0A^0} \propto N_D \delta n, \tag{20}$$

$$I_{A^0X} \propto N_A n_X, \quad I_{D^+X} \propto N_D n_X, \quad I_{D^0X} \propto \frac{N_D}{N_A} n_X \delta n. \tag{21}$$

Here, in order to determine the changes in N_A and N_D when F is varied, in addition to relation (16), the following relations for the normalized intensities of the impurity-, DA-, and exciton-luminescence bands can be used:

$$\frac{I_{D^0A^0}}{I_{eA^0}} \propto \frac{I_{hD^0}}{I_{eh}} \propto \frac{N_D}{N_A}, \tag{22}$$

$$\frac{I_{A^0X}}{I_X} \propto N_A, \tag{23}$$

$$\frac{I_{A^0X}}{I_{D^+X}} \propto \frac{N_A}{N_D}. \tag{24}$$

In the conditions under consideration, the use of the intensity I_{A^0X} normalized to I_X makes it possible to directly determine the change in N_A as a function of F. The intensities of the other luminescence bands allow us to determine both the relations between N_D and N_A and the dependence of N_D on F.

5.2. High Concentrations of Excess Charge Carriers δn and δp

When the concentrations δp and δn are high, the following inequality is satisfied: $a \gg c_n^*(b + d)$ (see (2a)); i.e., the bands related to the transitions of free charge carriers are dominant in the impurity-luminescence spectrum ($I_{eA^0}, I_{hD^0} \gg I_{D^0A^0}$). In this case, the concentrations N_{A^0}, N_{D^+}, and N_{D^0} are independent of the relations between the quantities $c_{nD}^{+} N_D \delta n$ and $c_{pA}^{-} N_A \delta p$ and the DA-transition rate. As follows from Eqs. (1) and (2), the concentrations N_{A^0}, N_{D^+}, and N_{D^0} are defined by the expressions

$$N_{A^0} = \frac{c_{pA}^{-} \delta p}{c_{pA}^{-} \delta p + c_{nA}^{0} \delta n} N_A, \quad N_{D^+} = \frac{c_{pD}^{0} \delta p}{c_{nD}^{+} \delta n + c_{pD}^{0} \delta p} N_D,$$
$$N_{D^0} = \frac{c_{nD}^{+} \delta n}{c_{nD}^{+} \delta n + c_{pD}^{0} \delta p} N_D. \tag{25}$$

If

$$c_{pA}^{-} \delta p \gg c_{nA}^{0} \delta n \quad \text{and} \quad c_{nD}^{+} \delta n \gg c_{pD}^{0} \delta p,$$

we have

$$N_{A^0} \simeq N_A, \quad N_{D^+} \propto N_D \delta p / \delta n, \quad N_{D^0} \propto N_D.$$

Then, as follows from expressions (3) and (5)–(7),

$$I_{eA^0} \propto N_A \delta n, \quad I_{hD^0} \propto N_D \delta p, \quad I_{D^0A^0} = c_n^* N_D N_A, \tag{26}$$

$$I_{A^0X} \propto N_A n_X, \quad I_{D^+X} \propto N_D n_X \delta p / \delta n, \quad I_{D^0X} \propto N_D n_X. \tag{27}$$

Evidently, in this case, in order to determine the changes in N_A and N_D in relation to the external factor F, we can use relations (14), (18), and (23).

If the ratio $\delta p / \delta n$ is independent of the generation rate of electron–hole pairs and of external factors, we have $N_{A^0} \propto N_A$ and $N_{D^+} \propto N_{D^0} \propto N_D$. Then, it follows from (3) and (5)–(7) that I_{eA^0}, I_{hD^0}, $I_{D^0A^0}$, and I_{A^0X} are governed by relations (26) and (27) and by the relation

$$I_{D^+X} \propto I_{D^0X} \propto N_D n_X, \quad I_X \propto n_X. \tag{28}$$

Here, as follows from (8), $n_X \propto \delta n \delta p / f(N_A, N_D)$.

Undoubtedly, in this case, relations (14), (16), (18), (23), (24), and the relation

$$\frac{I_{eA^0}}{I_{hD^0}} \propto \frac{N_A}{N_D} \tag{29}$$

describe convenient normalized luminescence intensities that make it possible to determine the changes in N_A, N_D, and N_A/N_D in relation to F. Expressions (25) are also valid (evidently, at any a, i.e., at any δp and δn) for isolated acceptors and donors (for isolated impurities, $c_n^* = 0$; see Fig. 1) [2]. Therefore, in the case of semiconductors containing isolated acceptors and donors, in order to determine the dependences of N_A and N_D on F, we can also use (when relevant criteria are satisfied) relations (14), (16), (18), (23), (24), and (29).

6. COMPARISON WITH THE EXPERIMENTAL DATA

In studies [3, 4], where changes in the intensities of low-temperature ($T = 4.2$ K) edge-luminescence spectra of semiconductors were analyzed in relation to the external factor F, it was assumed that the semiconductors under investigation contained DA pairs. We compare the above theoretical relations for the determination of changes in N_A and N_D caused by variation in F with the relations used in [3, 4]. The authors of these studies, in order to determine changes in the concentrations of shallow-level acceptors (C and Zn atoms) under varying conditions of epitaxial growth of n- and p-GaAs films, analyzed the dependence of the intensity of the DA-luminescence band (related to neutral C^0 or Zn^0 atoms) normalized to I_{D^0X}, $I_{D^0A^0}/I_{D^0X}$, on F. Luminescence peaks were observed at $h\nu_m = 1.490$ and 1.5133 eV for the $D^0 \longrightarrow A^0$ (i.e., $D^0 \longrightarrow C^0$ or $D^0 \longrightarrow Zn^0$) and $D^0X \longrightarrow D^0 + h\nu$ transitions, respectively [1]. It was assumed [1] that, under the experimental conditions, the relation $I_{D^0A^0}/I_{D^0X} \propto N_A$ is satisfied. However, such a relation cannot be satisfied at all (see Subsections 5.1 and 5.2). Another relation is possible, specifically, $I_{D^0A^0}/I_{D^0X} \propto N_A/n_X$ (see relations (20) and (21), (26) and (27)). In this case, $I_{D^0A^0}/I_{D^0X} \propto N_A$ if $n_X \neq f(F)$; i.e., the free-exciton concentration is independent of the external factor F.

7. VERIFICATION OF THE VALIDITY OF DETERMINING CHANGES IN N_A AND N_D IN RELATION TO F FROM AN ANALYSIS OF THE EDGE-LUMINESCENCE SPECTRA

It follows from the above that the correct determination of changes in N_A and N_D from an analysis of the normalized intensities of edge-luminescence bands under varying F is possible in the following cases:

(a) $n_{A^0X} \ll N_{A^0}$, $n_{D^+X} \ll N_{D^+}$, and $n_{D^0X} \ll N_{D^0}$;

(b) When the generation rate of electron–hole pairs L and the external factor F are varied, certain relations remain between the quantities a and $c_n^*(b+d)$ (see (2a)):

$$a \ll c_n^*(b+d) \text{ or } a \gg c_n^*(b+d),$$

and between the quantities b and d: either $b \gg d$, $b \simeq d$, or $b \ll d$. In addition, the quite plausible relations $c_{nD}^+\delta n \gg c_{pD}^0\delta p$ and $c_{pA}^-\delta p \gg c_{nA}^0\delta n$ are satisfied;

(c) The ratio $\delta p/\delta n$ is independent of the generation rate L at high concentrations δn and δp;

(d) The role of the Auger recombination of bound excitons A^0X, D^+X, and D^0X and of DA pairs is insignificant; and

(e) The ratio $\delta p/\delta n$ is independent of the external factor F at high concentrations δn and δp.

It is quite easy to verify that the first four criteria have been met. Evidently both the independence of the normalized intensities of the edge-luminescence bands from L and the form of the dependence of the edge-luminescence intensity on illumination indicate that these criteria are satisfied. In particular, at $b \cup d$ and $\delta n \propto \delta p$ we have

$$I_{eA^0} \propto (\delta n)^{3/2}, \quad I_{hD^0} \propto (\delta p)^{3/2},$$

$$I_{A^0X} \propto (\delta n)^{1/2} n_X, \quad I_{D^0X} \propto (\delta p)^{1/2} n_X$$

(see relations (3) and (15)). It is much more difficult to experimentally verify that criterion (e) has been met (if we restrict the analysis to studying the luminescence characteristics of semiconductors). Indeed, this verification is possible only when we measure the luminescence spectra of semiconductors with quite high concentrations of excess charge carriers δp and δn, i.e., at $a \gg c_n^*(b+d)$ (see (2a)). In this case, we can verify that the criterion $\delta p/\delta n \neq f(F)$ has been satisfied using the relation $I_{D^+X}/I_{D^0X} \propto N_{D^+}/N_{D^0} \propto \delta p/\delta n$ (see relation (27) and study [2]). However, the luminescence bands related to bound excitons D^+X and D^0X are not always observed simultaneously in semiconductors. Therefore, if we cannot directly verify that the ratio $\delta p/\delta n$ is independent of F, we should not use the normalized intensities of edge-luminescence bands, which depend on $\delta p/\delta n$, to determine changes in N_A and N_D when F varies.

8. CONCLUSIONS

It is quite convenient to use the normalized intensities of impurity-, DA-, and exciton-luminescence bands to determine changes in the concentrations of shallow-level acceptors N_A and shallow-level donors N_D, as well as in the relations between them, under the effect of external factors F. In order to obtain reliable data on the dependences of N_A and N_D on F from an analysis of the intensities of the above-mentioned luminescence bands, one should strictly follow the criteria of the applicability of the luminescence method to determine the changes in the concentrations of shallow-level acceptors and donors in semiconductors.

REFERENCES

1. V. I. Gavrilenko, A. M. Grekhov, D. V. Korbutyak, and V. G. Litovchenko, *Optical Properties of Semiconductors* (Naukova Dumka, Kiev, 1987).
2. K. D. Glinchuk and A. V. Prokhorovich, Fiz. Tekh. Poluprovodn. (St. Petersburg) **36**, 519 (2002) [Semiconductors **36**, 487 (2002)].
3. B. J. Scromme, S. S. Bose, and B. Lee, J. Appl. Phys. **58**, 4685 (1985).

4. K. S. Zhuravlev, A. K. Kalagin, N. T. Meshegov, *et al.*, Fiz. Tekh. Poluprovodn. (St. Petersburg) **30**, 1704 (1996) [Semiconductors **30**, 891 (1996)].
5. V. E. Lashkarev, A. V. Lyubchenko, and M. K. Sheĭnkman, *Nonequilibrium Processes in Photoconductors* (Naukova Dumka, Kiev, 1981).
6. A. A. Bergh and P. J. Dean, *Light Emitting Diodes* (Clarendon, Oxford, 1976; Mir, Moscow, 1979).
7. B. L. Gel'mont, V. A. Kharchenko, and I. N. Yassievich, Fiz. Tverd. Tela (Leningrad) **29**, 2351 (1987) [Sov. Phys. Solid State **29**, 1355 (1987)].
8. B. L. Gel'mont, N. N. Zinov'ev, D. I. Kovalev, *et al.*, Zh. Éksp. Teor. Fiz. **94** (3), 322 (1988) [Sov. Phys. JETP **67**, 613 (1988)].
9. V. N. Abakumov, V. I. Perel', and I. N. Yassievich, *Nonradiative Recombination in Semiconductors* (Peterb. Inst. Yad. Fiz., St. Petersburg, 1997).
10. A. V. Sachenko, A. P. Gorban, and V. P. Kostylyov, Semicond. Phys. Quantum Electron. Optoelectron. **3**, 5 (2000).
11. T. Taguchi, J. Shiraruji, and Y. Inuishi, Phys. Status Solidi B **68**, 727 (1975).
12. T. Schmidt, K. Lischka, and W. Zulehner, Phys. Rev. B **45**, 8989 (1992).

Translated by Yu. Sin'kov

Semiconductors, Vol. 37, No. 2, 2003, pp. 156–159. Translated from Fizika i Tekhnika Poluprovodnikov, Vol. 37, No. 2, 2003, pp. 166–168.
Original Russian Text Copyright © 2003 by Gorskyi.

ELECTRONIC AND OPTICAL PROPERTIES OF SEMICONDUCTORS

Classification of Frequencies of the Shubnikov–de Haas Oscillations in Layered Charge-Ordered Crystals under Magnetic Breakdown

P. V. Gorskyi

Chernovtsy National University, Chernovtsy, 58000 Ukraine

Submitted December 18, 2001; accepted for publication June 20, 2002

Abstract—The existence of magnetic breakdown frequencies of Shubnikov–de Haas oscillations in layered charge-ordered crystals has been proved. Classification of the magnetic breakdown frequencies has been performed. © *2003 MAIK "Nauka/Interperiodica".*

At present, the processing of experimental data on the de Haas–van Alphen (DHVA) and Shubnikov–de Haas (SDH) oscillations is mainly carried out on the basis of the Lifshits and Kosevich (LK) theory [1], which unambiguously relates the oscillation frequencies of the DHVA and SDH effects to the extreme cross sections of the Fermi surface (FS) by the planes perpendicular to the direction of a magnetic field. However, first of all, the LK theory is only correct in a quasi-classical approximation that is valid if the cyclotron energy is small in comparison with the Fermi energy. Secondly, even with the validity of a quasi-classical approximation, the Fermi surface can be determined from extreme cross sections if they have only an almost circular or ellipsoidal shape, i. e., in the approximation of nearly free electrons [2], which is correct for most normal metals. However, there are a number of semiconductor structures, in particular, semiconductor superlattices [3], for which this approximation is not appropriate. In this case, as was shown in [4], the oscillation frequencies of the DHVA effect could be expressed in terms of the Fermi energy and the Fourier transform of the energy of interlayer electron motion. At the same time, only some of these frequencies can be identified with Fermi surface sections, even with not necessarily extremal ones. Even for a narrow conduction miniband, when the first harmonic of the Fourier transform is sufficient for determining the energy of electron interlayer motion, the LK theory is only correct when a narrow conduction miniband is divided into a number of Landau subbands. This is correct not only for the DHVA but also for the SDH effects if it is possible to ignore the influence of a magnetic field on carrier scattering. However, if the SDH effect is clearly pronounced, as is shown in [5], it is necessary to consider the influence of magnetic quantization not only on the energy spectrum of the charge carriers but also on carrier scattering. If the relaxation time is inversely proportional to the density of states in a magnetic field, which is, in particular, correct for charge carrier scattering by acoustic phonons, in the case of a narrow conduction miniband, the SDH oscillation frequencies are completely consistent with the LK theory, although their relative contribution, in this case, does not correspond to a quasi-classical approximation; i. e., the SDH oscillation spectrum is simpler than the DHVA oscillation spectrum. However, this is, generally speaking, not correct if the corrugation of the FS is more complex; i. e., the tight binding approximation is inadequate for a description of the interlayer motion of electrons. Nevertheless, in charge-ordered layered crystals, to which some semiconductor superlattices, dichalcogenides of transition metals, intercalated graphite compounds [6, 7], and other crystals belong, a classification of the SDH oscillation frequencies can be used which is fairly simple and convenient for the processing and interpretation of the experimental data. This is the subject of this study.

It was shown [8] that charge ordering can occur in highly anisotropic (quasi-two-dimensional) layered structures. This ordering consists in the simple alternation of layers more or less occupied by electrons and is caused by the effective attraction between electrons due to competition of the electron–phonon interaction and Coulomb repulsion. In this case, the electron energy in a quantizing magnetic field H, perpendicular to the layers, can be expressed as

$$\varepsilon_{\pm}(n, k_z) = \mu^* H(2n+1) \pm \sqrt{W_0^2\delta^2 + \Delta^2\cos^2 ak_z} \quad (1)$$

if the reference point of energy is placed at the midgap between minibands. In formula (1), $\mu^* = \mu_B \frac{m_0}{m^*}$; μ_B is the Bohr magneton; m_0 is the free electron mass; n is the number of the Landau level; m^* is the effective electron mass in the plane of layer; W_0 is the effective constant of attractive interaction and is directly proportional to the electron concentration in the approximation of a self-consistent field; δ is the ordering parameter, which

describes nonequivalence of the layer occupation by electrons and is equal to the ratio between the electron density difference in neighboring layers and average electron density (at zero temperature $\Delta = 0$, $H = 0$, $\delta \longrightarrow 1$; in the state of unorder, $\delta = 0$); Δ is the miniband half-width in the unordered state; k_z is the quasi-momentum component in the direction perpendicular to the layers; and a is the distance between translationally equivalent layers.

Assuming that the electron relaxation time is inversely proportional to the density of states in a magnetic field [9], the oscillating component of conductivity σ_{zz} for scattering by acoustic phonons in the approximation $h\nu \ll kT \ll \mu^*H$ (ν is the highest phonon frequency) can be expressed, according to [5], as

$$\sigma_{os} = \sigma_{LK} + \sigma_{MB}, \tag{2}$$

where σ_{LK} is the component of conductivity, the oscillation frequencies of which are unambiguously related to extreme sections of the FS by the planes perpendicular to the magnetic field; and σ_{MB} is the so-called "magnetic breakdown" component of conductivity, which we will analyze in detail. This component, as a function of energy, can be written as

$$\begin{gathered}\zeta \le -\Delta_\delta \quad \sigma_{MB} = 0,\\ \text{for} \quad -\Delta_\delta \le \zeta \le -W_0\delta\end{gathered} \tag{3}$$

$$\begin{aligned}\sigma_{MB} &= \frac{32\pi\tau_0 e^2 m^* a\Delta}{h^4 kT|\mu^*H|}\\ &\times \sum_{l=1}^{\infty}(-1)^l f_l^{\sigma}\left(\frac{\pi l}{\mu^*H}\right)(W_0^4\delta^4 - W_0^2\delta^2\Delta^2)\\ &\times\left[\cos\left(\frac{\pi l\zeta}{\mu^*H}\right)\left[\mathrm{Si}\left(\frac{\pi l\zeta}{\mu^*H}\right) + \mathrm{Si}\left(\frac{\pi l\Delta_\delta}{\mu^*H}\right)\right]\right.\\ &\left.+\sin\left(\frac{\pi l\zeta}{\mu^*H}\right)\left[\mathrm{Ci}\left(\frac{\pi l\Delta_\delta}{\mu^*H}\right) - \mathrm{Ci}\left(\frac{\pi l\zeta}{\mu^*H}\right)\right]\right],\end{aligned} \tag{4}$$

$$\text{for} \quad -W_0\delta \le \zeta \le W_0\delta$$

$$\begin{aligned}\sigma_{MB} &= \frac{32\pi\tau_0 e^2 m^* a\Delta}{h^4 kT|\mu^*H|}\\ &\times \sum_{l=1}^{\infty}(-1)^l f_l^{\sigma}\left(\frac{\pi l}{\mu^*H}\right)(W_0^4\delta^4 - W_0^2\delta^2\Delta^2)\\ &\times\left[\cos\left(\frac{\pi l\zeta}{\mu^*H}\right)\left[\mathrm{Si}\left(\frac{\pi l W_0\delta}{\mu^*H}\right) - \mathrm{Si}\left(\frac{\pi l\Delta_\delta}{\mu^*H}\right)\right]\right.\\ &\left.-\sin\left(\frac{\pi l\zeta}{\mu^*H}\right)\left[\mathrm{Ci}\left(\frac{\pi l\Delta_\delta}{\mu^*H}\right) - \mathrm{Ci}\left(\frac{\pi l W_0\delta}{\mu^*H}\right)\right]\right].\end{aligned} \tag{5}$$

For $W_0\delta \le z \le \Delta_\delta$, σ_{MB} can be obtained by the summation of expression (5) and the term $\sigma_{MB}^{(1)}$, which is equal to

$$\begin{aligned}\sigma_{MB}^{(1)} &= \frac{32\pi\tau_0 e^2 m^* a\Delta}{h^4 kT|\mu^*H|}\\ &\times \sum_{l=1}^{\infty}(-1)^l f_l^{\sigma}\left(\frac{\pi l}{\mu^*H}\right)(W_0^2\delta^2\Delta^2 - W_0^4\delta^4)\\ &\times\left[\cos\left(\frac{\pi l\zeta}{\mu^*H}\right)\left[\mathrm{Si}\left(\frac{\pi l W_0\delta}{\mu^*H}\right) - \mathrm{Si}\left(\frac{\pi l\zeta}{\mu^*H}\right)\right]\right.\\ &\left.+\sin\left(\frac{\pi l\zeta}{\mu^*H}\right)\left[\mathrm{Ci}\left(\frac{\pi l\zeta}{\mu^*H}\right) - \mathrm{Ci}\left(\frac{\pi l W_0\delta}{\mu^*H}\right)\right]\right].\end{aligned} \tag{6}$$

For $\zeta > \Delta_\delta$, $\sigma_{MB}(H)$ can be obtained by summation of expression (5) and the term $\sigma_{MB}^{(2)}$, which is equal to

$$\begin{aligned}\sigma_{os}^{(2)} &= \frac{32\pi\tau_0 e^2 m^* a\Delta}{h^4 kT|\mu^*H|}\\ &\times \sum_{l=1}^{\infty}(-1)^l f_l^{\sigma}\left(\frac{\pi l}{\mu^*H}\right)(W_0^2\delta^2\Delta^2 - W_0^4\delta^4)\\ &\times\left[\cos\left(\frac{\pi l\zeta}{\mu^*H}\right)\left[\mathrm{Si}\left(\frac{\pi l W_0\delta}{\mu^*H}\right) - \mathrm{Si}\left(\frac{\pi l\Delta_\delta}{\mu^*H}\right)\right]\right.\\ &\left.+\sin\left(\frac{\pi l\zeta}{\mu^*H}\right)\left[\mathrm{Ci}\left(\frac{\pi l\Delta_\delta}{\mu^*H}\right) - \mathrm{Ci}\left(\frac{\pi l W_0\delta}{\mu^*H}\right)\right]\right].\end{aligned} \tag{7}$$

$$f_l^{\delta} = (\pi^2 lkT/\mu^*H)/\sinh(\pi^2 lkT/\mu^*H). \tag{8}$$

The following designations are used in formulas (4)–(8): ζ is the electron chemical potential reckoned from the middle of the gap between minibands; $\Delta_\delta = \sqrt{W_0^2\delta^2 + \Delta^2}$; τ_0 is a constant of a crystal and has the dimension of time and characterizes the scattering intensity; T is temperature; Si(…) and Ci(..) are the integral sine and cosine; and sinh is the hyperbolic sine; and the other designations, with the exception of standard ones, are explained above. It should be noted that formulas (3)–(8) are correct both for the charge carrier scattering by acoustic phonons and other mechanisms of scattering for which the relaxation time of longitudinal momentum is inversely proportional to the density of states. In these cases, only the factors before the summation over l should be changed.

It follows from formulas (4)–(7) that for $\Delta_\delta/\mu^*H \ll 1$ and $W_0\delta/\mu^*H \ll 1$, when integral sines and cosines can be represented by polynomials [10], the basic fre-

quency of the magnetic-breakdown oscillations as a function of $1/H$ can be defined by the formula

$$\omega_1 = \pi\zeta/\mu^*; \quad (9)$$

for $\delta \neq 0$, i. e., in the case of ordering, ω_1 can in no way be identified with any section of the FS by the plane perpendicular to the magnetic field.

However, in the intermediate range of magnetic fields, if the integral sine and cosine can be presented by asymptotic expansions which contain sines and cosines of appropriate arguments, the oscillation pattern is more complex. In particular, it follows from (4) that, for $-\Delta_\delta \leq \zeta \leq -W_0\delta$, the basic frequencies of the magnetic breakdown oscillations are given by

$$\omega_2 = 2\pi\zeta/\mu^*, \quad (10)$$

$$\omega_3 = \pi|\zeta - \Delta_\delta|/\mu^* \quad (11)$$

and they cannot be identified with any sections of the FS by the planes perpendicular to the magnetic field in the range of $-\Delta_\delta \leq \zeta \leq -W_0\delta$. However, the frequency

$$\omega_4 = \pi(\zeta + \Delta_\delta)/\mu^* \quad (12)$$

is identified with stationary sections of the FS by the planes $k_z = 0$ and $k_z = \pm\pi/a$. In this region, the FS consists of three separated parts.

In the range $-W_0\delta \leq \zeta \leq W_0\delta$, when the FS becomes connected, new oscillation frequencies occur in addition to the frequencies which are determined by formulas (11) and (12), where ω_3 is the magnetic-breakdown and ω_4 is quasi-classical frequencies. These new frequencies are defined by the expressions

$$\omega_5 = \pi|\zeta - W_0\delta|/\mu^*, \quad (13)$$

$$\omega_0 = \pi(\zeta + W_0\delta)/\mu^*. \quad (14)$$

In this case, ω_5 cannot be identified with any stationary cross sections of the FS by the planes perpendicular to the magnetic field. The frequency ω_6 is related to the stationary cross sections of the "necks" which occur as a result of the FS transformation from closed to open. However, for $\zeta > W_0\delta - \Delta_\delta/2$, the frequency ω_5 can no longer be classified as a pure magnetic-breakdown frequency, because it is identified with nonstationary sections of the FS by four planes which can be described by the equations

$$k_z = \pm\arccos\left((4\zeta^2 - 4\zeta W_0\delta)^{\frac{1}{2}}/\Delta\right)/a, \quad (15)$$

$$k_z = \pm\left[\pi - \arccos\left((4\zeta^2 - 4\zeta W_0\delta)^{\frac{1}{2}}/\Delta\right)/a\right]. \quad (16)$$

Analysis of Eqs. (15) and (16) shows, however, that they are meaningful only if $\delta < \Delta/(\sqrt{3}\,W_0)$. In charge-ordered layered crystals, we have $\Delta < W_0$. As a result, under the conditions of charge ordering ($\delta \approx 1$), the frequency ω_6 corresponds to magnetic breakdown for $-W_0\delta \leq \zeta \leq W_0\delta$. This inference is especially true for materials with a high critical transition temperature.

For $W_0\delta \leq \zeta \leq \Delta_\delta$, the occupation of a higher miniband sets in, and a new portion of the FS, which is completely enclosed by the first one, appears. Due to this fact, new oscillation frequencies do not appear; only frequencies ω_1 in strong magnetic fields and ω_2 and ω_3 in intermediate magnetic fields are of magnetic-breakdown nature. However, if $\zeta > (\Delta_\delta + W_0\delta)/2$, then the frequency ω_3 is related to the nonstationary sections of the FS by the planes perpendicular to the magnetic field; these planes are described by the equations

$$k_z = \pm\arcsin\left((4\zeta\Delta_\delta - 4\zeta^2)^{\frac{1}{2}}/\Delta\right)/a, \quad (17)$$

$$k_z = \pm\left[\pi - \arcsin\left((4\zeta\Delta_\delta - 4\zeta^2)^{\frac{1}{2}}/\Delta\right)/a\right]. \quad (18)$$

For $\zeta > \Delta_\delta$, only oscillations with the frequencies ω_3, ω_4, ω_5, and ω_6 occur in intermediate magnetic fields. These frequencies are solely related to the stationary sections of the FS by the planes $k_z = 0$, $k_z = \pm\pi/a$, and $k_z = \pm\pi/2a$. In addition, in strong magnetic fields, magnetic-breakdown oscillations with a frequency ω_1 occur.

It should be noted that the conditions $W_0\delta/\mu^*H < 1$ and $\Delta_\delta/\mu^*H < 1$, at which oscillations with a frequency ω_1 occur, are actually the conditions for magnetic breakdown between minibands, because $2W_0\delta$ is the gap between them and $2\mu^*H$ is the energy gap between the neighboring Landau subbands. Oscillations with other magnetic breakdown frequencies can be related to the electron reflection from the Brillouin zone boundaries. The amplitudes of these oscillations are not large in intermediate magnetic fields when $W_0\delta/\mu^*H$ and Δ_δ/μ^*H, but at the same time, they are not too small in comparison with unity. This is important because a sharp increase in conductivity occurs not only at the crossing of the Fermi level with the Landau level but also under the conditions of singularity in the density of states, i.e., at the crossing of the Landau level with the miniband boundaries. However, the amplitudes of all magnetic-breakdown oscillations vanish for $\delta = 0$.

REFERENCES

1. I. M. Lifshits and A. M. Kosevich, Izv. Akad. Nauk SSSR, Ser. Fiz. **19**, 395 (1955).
2. N. B. Brandt and S. M. Chudinov, *Electrons and Phonons in Metals* (Mosk. Gos. Univ., Moscow, 1990).

3. A. I. Chaikovskij, M. G. Shmelev, and H. C. Quang, J. Phys. C: Solid State Phys. **10**, 3315 (1977).
4. P. V. Gorskiĭ, Fiz. Tekh. Poluprovodn. (Leningrad) **17**, 936 (1983) [Sov. Phys. Semicond. **17**, 588 (1983)].
5. P. V. Gorskiĭ, Fiz. Nizk. Temp. **12**, 584 (1986).
6. J. M. Harper and T. H. Geballe, Phys. Lett. A **54** (1), 27 (1975).
7. C. Zeller, G. M. T. Foley, E. R. Falardeau, and F. L. Vogel, Mater. Sci. Eng. **3** (1), 255 (1977).
8. É. A. Pashitskiĭ and A. S. Shpigel', Fiz. Nizk. Temp. **4**, 976 (1978).
9. V. F. Gantmakher and I. B. Levinson, *Scattering of Charge Carriers in Metals and Semiconductors* (Nauka, Moscow, 1984).
10. E. Jahnke, F. Emde, and F. Losch, *Tables of Higher Functions*, 6th ed. (McGraw-Hill, New York, 1960; Nauka, Moscow, 1968), p. 65.

Translated by I. Kucherenko

Semiconductors, Vol. 37, No. 2, 2003, pp. 160–164. Translated from Fizika i Tekhnika Poluprovodnikov, Vol. 37, No. 2, 2003, pp. 169–172.
Original Russian Text Copyright © 2003 by Averkiev, Monakhov, Sablina, Koenraad.

ELECTRONIC AND OPTICAL PROPERTIES OF SEMICONDUCTORS

On the Experimental Data Processing of Magnetoresistance Oscillations in Two-Dimensional Electron Gas

N. S. Averkiev*, A. M. Monakhov*^, N. I. Sablina*, and P. M. Koenraad**

** Ioffe Physicotechnical Institute, Russian Academy of Sciences, Politekhnicheskaya ul. 26, St. Petersburg, 194021 Russia*

^e-mail: amon@les.ioffe.rssi.ru

*** Eindhoven University of Technology, The Netherlands*

Submitted May 18, 2002; accepted for publication June 25, 2002

Abstract—A new method for processing data on the Shubnikov–de Haas effect in quasi-two-dimensional systems is suggested. © *2003 MAIK “Nauka/Interperiodica”.*

1. INTRODUCTION

It is known that the kinetic coefficients of a degenerate electron gas oscillate in a quantizing magnetic field if the Fermi quasi-levels intersect the Landau levels. Such parameters as the effective mass, relaxation time, and the concentration of charge carriers are usually determined from the measurements of the oscillation of conduction (the Shubnikov–de Haas effect). However, it should be noted that only the Fermi energy can be obtained directly from the period of oscillations in a reverse magnetic field. For obtaining other parameters, one should invoke theoretical considerations describing this effect and the procedure for processing experimental data. This procedure is not trivial since the least-squares method is hardly applicable to the oscillating functions, and Fourier analysis requires special analysis of nonoscillating parts and the consideration of limitation in the range of measured fields [1, 2].

Analysis of experimental data becomes more complicated if the conductivity is caused by charge carriers from two or more subbands of dimensional quantization (henceforth, for simplicity, we restrict ourselves to the case of two occupied subbands). A theory describing the Shubnikov–de Haas effect with account of intersubband scattering is given in [3].

In this paper, we describe a method for processing experimental data using the formulas given in [3]. We believe that this method is simpler and yields better results compared to conventional Fourier analysis.

2. THE PROCEDURE FOR CALCULATIONS

As shown in [3], if two subbands of dimensional quantization are filled, the components ρ_{xx} of a resistivity tensor are described by the following expressions:

$$\rho_{xx} = \rho_{xx}^{TD} + \rho_{xx}^{TI},$$

$$\rho_{xx}^{TD} = (\rho_{xx}^{HF} + \rho_{xx}^{LF})\frac{\lambda(T)}{\sinh\lambda(T)}, \tag{1}$$

$$\rho_{xx}^{TI} = \rho_{xx}^{0} + \rho_{xx}^{nd}.$$

Here,

$$\lambda(T) = \frac{2\pi^2 T}{\hbar\omega_c}, \quad \omega_c = \frac{eH}{mc},$$

and

$$\rho_{xx}^{HF} = A_{HF}2\cos\left(2\pi\frac{\mu_1}{\hbar\omega_c} + \pi\right)\exp\left(-\frac{\pi}{\omega_c\tau_1}\right),$$

$$\rho_{xx}^{LF} = A_{LF}2\cos\left(2\pi\frac{\mu_2}{\hbar\omega_c} + \pi\right)\exp\left(-\frac{\pi}{\omega_c\tau_2}\right), \tag{2}$$

$$\rho_{xx}^{nd} = A_{nd}2\cos\left[2\pi\frac{\mu_1 - \mu_2}{\hbar\omega_c}\right]\exp\left[-\frac{\pi}{\omega_c\tau_1} - \frac{\pi}{\omega_c\tau_2}\right].$$

The quantities ρ_{xx}^0, A_{HF}, A_{LF}, and A_{nd} are nonoscillating functions of ω_c. These functions and the notation used in the expressions (2) are given in the *Appendix*.

We should note that the variations in resistivity ρ with magnetic field, at least for two-dimensional systems, are more suitable for processing than the corresponding variations in conductivity σ (although the analytical expressions for σ are simpler), since the dependence of classical magnetoresistance on a magnetic field for ρ in two-dimensional systems is much weaker than for σ. Thus, in the case of a single filled subband of dimensional quantization for a degenerate Fermi gas, the quantity ρ_{xx}^0 in a classical limit is independent of the field, while its counterpart σ_{xx}^0 depends

1063-7826/03/3702-0160$24.00 © 2003 MAIK “Nauka/Interperiodica”

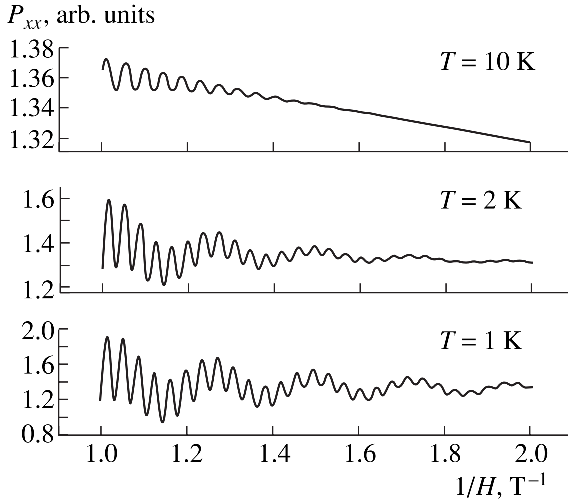

Fig. 1. Initial dependences of ρ_{xx} on the reciprocal magnetic field: the top, middle, and bottom curves are for the temperatures of 10, 2, and 1 K, respectively. For the sake of convenience, $\rho_{xx}(H)$ is divided by ρ_{xx} $(H = 0)$.

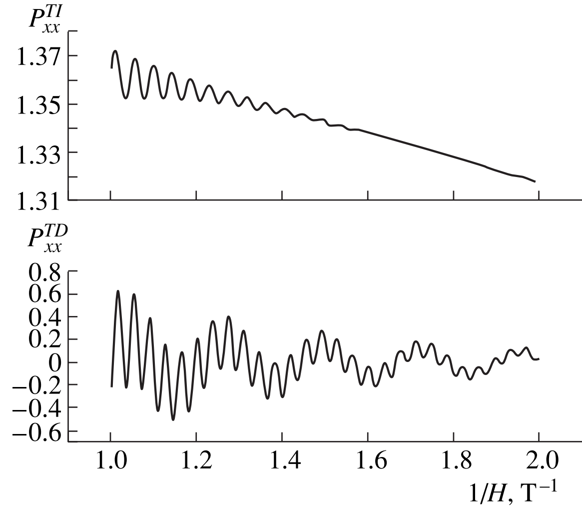

Fig. 2. Temperature-dependent and temperature-independent parts of ρ_{xx} (the bottom and the top curves, respectively) obtained by the subtraction of any pair of curves in Fig. 1.

on the magnetic field so strongly that it becomes almost impossible to distinguish the oscillating σ_{xx}^{nd} component against the background of this strong dependence.

Expression (1) contains a temperature dependent (TD) and a temperature independent (TI) part. The latter contains smoothly varying classical magnetoresistance ρ_{xx}^{0} and a temperature-independent oscillating function ρ_{xx}^{nd} of the second order with respect to the parameter $\exp(-\pi/\omega_c\tau_i)$. The TD part contains a term corresponding to high-frequency (HF) oscillations responsible for the occupation of the lower subband of dimensional quantization, and a term corresponding to low-frequency (LF) oscillations responsible for the occupation of the upper subband.

For illustration, will employ formulas (1) and (2) to calculate the dependence of ρ_{xx} on the reciprocal field using values of parameters close to those observed in experiment [4]. We consider the case where the occupancy of the second subband is relatively small ($\simeq$10%). Figure 1 shows these dependences at several temperatures and the following values of parameters of a medium: concentration in the first subband $N_1 = 1 \times 10^{12}$ cm^{-2}; in the second subband, $N_2 = 0.4 \times 10^{11}$ cm^{-2}; the relaxation time in the first subband $\tau_1 = 0.8 \times 10^{-12}$ s; in the second subband, $\tau_2 = 4 \times 10^{-12}$ s; and the time of intersubband scattering $\tau_{12} = 6 \times 10^{-12}$ s.

First, we separate the TD and TI parts from ρ_{xx}. As follows from expression (1), to do this it is sufficient to have the two experimental dependences $\rho_{xx}(T_1)$ and $\rho_{xx}(T_2)$ measured at different temperatures. Subtracting one dependence from the other, we obtain

$$\rho_{xx}(T_1) - \rho_{xx}(T_2) = \rho_{TD}\left(\frac{\lambda}{\sinh\lambda}(T_1) - \frac{\lambda}{\sinh\lambda}(T_2)\right).$$

Multiplying the result by $\left(\frac{\lambda}{\sinh\lambda}(T_1) - \frac{\lambda}{\sinh\lambda}(T_2)\right)$, we exclude the temperature dependence and obtain ρ_{xx}^{TD}, which contains all the information about the system. Similarly we can separate the TI part. The result of such subtraction is shown in Fig. 2.

Thus, if we have a set of experimental curves $\rho_{xx}(T)$ obtained at different temperatures for the same sample, the above subtraction procedure should yield the same result for all pairs. This, in our opinion, is a good method for the preliminary rejection of invalid experimental data (or for theoretical verification in any specific experimental situation).

The following procedure for experimental data processing is to some extent similar to Fourier analysis but, in our opinion, is more convenient and simpler.

Let us consider, for example, ρ_{xx}^{TD}. This quantity is a sum of two oscillating functions which decrease in a reciprocal field. These functions can be separated by considering the fact that the function $\cos\left(2\pi\frac{\mu_1}{\hbar\omega_c} + \pi\right)$ goes through zero halfway between the maximum and the minimum of high-frequency oscillations. At these points, the function becomes equal to ρ_{xx}^{LF}. Thus, by dividing the distance between the maximum and the

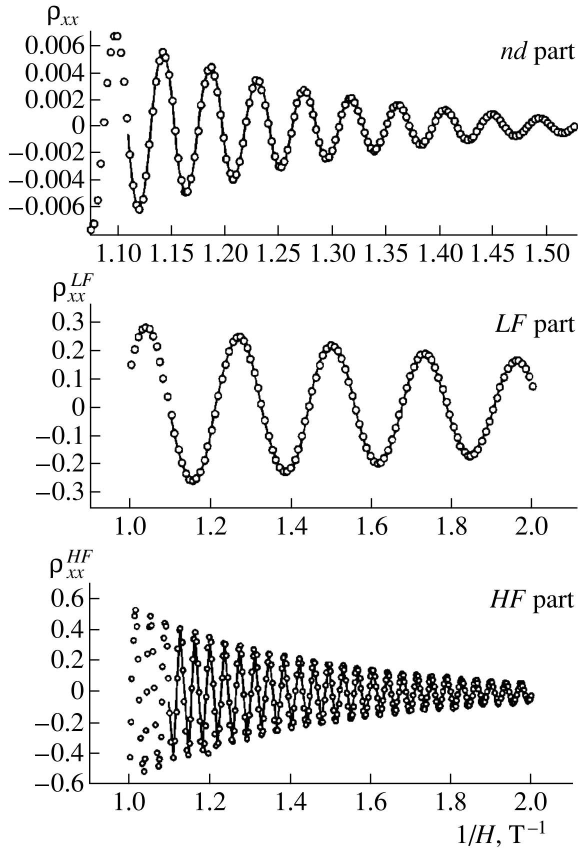

Fig. 3. Terms ρ_{xx}^{HF}, ρ_{xx}^{LF}, and ρ_{xx}^{nd} separated out from the curves shown in Fig. 2. The results of straightforward calculation using formulas (1) and (2) are shown by the circles.

minimum in two and finding the value of ρ_{xx}^{TD} at this point, we separate the low-frequency part ρ_{xx}^{LF} from ρ_{xx}^{TD}. The high-frequency part can be obtained by subtracting ρ_{xx}^{LF} from ρ_{xx}^{TD} (this, of course, requires the interpolation of ρ_{xx}^{LF}). The separation of σ_{xx}^{nd} from σ_{TI}^{0} (classical magnetoresistance) can be performed in a similar way.

It should be noted that, generally speaking, the maxima for ρ_{xx}^{TD} do not coincide with the maxima for $\cos\left(2\pi\frac{\mu_j}{\hbar\omega_c}+\pi\right)$. The quantity ρ_{xx}^{TD} has the form

$$f_1(\omega)\cos(\Omega_1\omega)+f_2(\omega)\cos(\Omega_2\omega); \tag{3}$$

therefore, the condition for the extremum of expression (3) is

$$\begin{aligned}&-\Omega_1 f_1\sin(\Omega_1\omega)+f_1'\cos(\Omega_1\omega)\\&+f_2'\cos(\Omega_2\omega)-\Omega_2 f_2\sin(\Omega_2\omega)=0.\end{aligned} \tag{4}$$

The condition for the applicability of the above simple procedure is

$$\frac{f_2\Omega_2}{f_1\Omega_1}\ll 1,\quad \frac{f_1'}{f_1\Omega_1}\ll 1,\quad \frac{f_2'}{f_1\Omega_1}\ll 1. \tag{5}$$

These conditions, as a rule, are satisfied for actual values of parameters, but, if required, the values corresponding to maxima could be refined, for example, by using a standard iterative procedure,

$$\begin{aligned}&-\Omega_1 f_1(\omega_i)\sin(\Omega_1\omega_{i+1})+f_1'\cos(\Omega_1\omega_i)\\&+f_2'(\omega_i)\cos(\Omega_2\omega_i)-\Omega_2 f_2\sin(\Omega_2\omega_i)=0,\end{aligned}$$

which relates the roots at preceding (ω_i) and succeeding (ω_{i+1}) iterations.

After the procedure for the elimination of high-frequency oscillations is completed, all curves, except for ρ_{xx}^{0}, should be centered with respect to zero and have no beats. This serves as additional verification of the theory. The result of this procedure is shown in Fig. 3. Such separation is quite competitive in precision with Fourier analysis if conditions (5) are satisfied. This can be justified by comparing the division procedure and the straightforward calculation of the data shown by circles in Fig. 3 by formula (2).

In principle, the curves obtained allow one to calculate all the parameters characterizing the system: E_F, Δ, τ_1, τ_2, and τ_{12}. For the HF parts, again it is sufficient to consider the values corresponding only to maxima (minima) in the curve; then, the fitting function for A_{HF} turns out to be simpler and more convenient for using the least-squares method than the initial oscillating function (E_F can be easily determined from the period of oscillations).

As for ρ_{xx}^{LF}, the number of oscillations for the relatively underpopulated second subband may be small. In this case, the entire function should be fitted.

3. CONCLUSIONS

Thus, we suggested a procedure for determining the kinetic coefficients in quasi-two-dimensional structures from Shubnikov–de Haas oscillations. It should be emphasized that, in order to determine the concentration of charge carriers in the lower subband of dimensional quantization, complicated processing is not required. Such processing is useful only if one wants to know the relaxation times in the first and second subbands or the time of intersubband transitions. The suggested procedure is also applicable when the charge carrier concentration in the second subband is low and its contribution to the total conductivity in the absence of a magnetic field can hardly be observed.

In addition, this procedure is useful for the verification of both the experimental data and the adequacy of

the theoretical model used for data processing for the experimental situation.

Notably, the limitation imposed on the applicability of (1) by the fact that this expression is derived in the approximation of a short-range potential is unimportant since the transition to a long-range potential requires only the substitution of times τ_1 and τ_2 in the preexponential factors of expression (1) by the corresponding transport times.

APPENDIX

Here, we present explicit forms of the quantities involved in formulas (1) and (2) for the case of occupation of two subbands of dimensional quantization [3]. In the case under consideration, the system is characterized by the following quantities: the Fermi level in the first subband of dimensional quantization μ_1 reckoned from the bottom of the first subband; the Fermi level in the second subband μ_2 reckoned from the bottom of the second subband (these quantities can be easily expressed in terms of the surface densities of charge carriers in each subband); the relaxation times of charge carriers in the first and second subbands τ_1 and τ_2, respectively; and the time of intersubband transitions τ_{12}. We introduce additional designations:

$$\tau_{11} = \frac{\tau_1\tau_{12}}{\tau_{12}-\tau_1},$$

$$\tau_{22} = \frac{\tau_2\tau_{12}}{\tau_{12}-\tau_2}.$$

The results of calculating σ_{ik} are given in [3]. Transition from the σ_{ik} matrix to the reciprocal matrix $\rho_{ik} = [\sigma_{ik}]^{-1}$ requires taking into account the condition for the applicability of the theory $\exp\left(-\frac{\pi}{\omega_c\tau_i}\right) \ll 1$; therefore, it is necessary to expand the quantity $\rho_{xx} = \frac{\sigma_{xx}}{\sigma_{xx}^2+\sigma_{xy}^2}$ in a power series of these parameters and to consider only the zeroth- and the first-order terms for ρ_{xx}^{TD}, and the second-order terms for ρ_{xx}^{TI}. As a result, we obtain

$$\rho_{xx} = \frac{\sigma_{xx}^0}{(\sigma_{xx}^0)^2+(\sigma_{xy}^0)^2}(1 + A_1\delta_1 + A_2\delta_2 + A_{12}\delta_{12}),$$

which yields

$$\rho_{xx}^0 = \frac{\sigma_{xx}^0}{(\sigma_{xx}^0)^2+(\sigma_{xy}^0)^2},$$

$$A_{HF} = \frac{\sigma_{xx}^0}{(\sigma_{xx}^0)^2+(\sigma_{xy}^0)^2}A_1,$$

$$A_{LF} = \frac{\sigma_{xx}^0}{(\sigma_{xx}^0)^2+(\sigma_{xy}^0)^2}A_2,$$

$$A_{nd} = \frac{\sigma_{xx}^0}{(\sigma_{xx}^0)^2+(\sigma_{xy}^0)^2}A_{12}.$$

The quantities A_i are expressed in terms of conductivity components in the following way:

$$A_1 = \frac{\sigma_{xx}^{(1)}}{\sigma_{xx}^0} - 2\frac{\sigma_{xx}^0\sigma_{xx}^{(1)}+\sigma_{xy}^0\sigma_{xy}^{(1)}}{(\sigma_{xx}^0)^2+(\sigma_{xy}^0)^2},$$

$$A_2 = \frac{\sigma_{xx}^{(2)}}{\sigma_{xx}^0} - 2\frac{\sigma_{xx}^0\sigma_{xx}^{(2)}+\sigma_{xy}^0\sigma_{xy}^{(2)}}{(\sigma_{xx}^0)^2+(\sigma_{xy}^0)^2}, \quad (6)$$

$$A_{12} = \frac{\sigma_{xx}^{(nd)}}{\sigma_{xx}^0} - 2\frac{\sigma_{xx}^0\sigma_{xx}^{(nd)}+\sigma_{xy}^0\sigma_{xy}^{(nd)}}{(\sigma_{xx}^0)^2+(\sigma_{xy}^0)^2}.$$

The quantities appearing in (6), according to [3], are given by

$$\sigma_{xx}^0 = \frac{4\pi e^2}{\hbar^2}\left(\frac{\mu_1\tau_1}{1+(\omega_c\tau_1)^2} + \frac{\mu_2\tau_2}{1+(\omega_c\tau_2)^2}\right),$$

$$\sigma_{xy}^0 = \frac{4\pi e^2}{\hbar^2}\left(-\frac{\mu_1\tau_1^2\omega_c}{1+(\omega_c\tau_1)^2} - \frac{\mu_2\tau_2}{1+(\omega_c\tau_2)^2}\right),$$

$$\sigma_{xx}^{(1)} = \frac{4\pi e^2}{\hbar^2}\left[\frac{\mu_1\tau_1}{1+(\omega_c\tau_1)^2}\left(\frac{2(\omega_c\tau_1)^2}{1+(\omega_c\tau_1)^2} + \frac{\tau_1}{\tau_{12}}\frac{1-(\omega_c\tau_1)^2}{1+(\omega_c\tau_1)^2}\right) - \frac{\mu_2\tau_2^2}{\tau_{12}}\frac{(1-(\omega_c\tau_2)^2)}{(1+(\omega_c\tau_2)^2)^2}\right];$$

$\sigma_{xx}^{(2)}$ can be easily obtained from $\sigma_{xx}^{(1)}$ by the substitution $\tau_1 \longrightarrow \tau_2$; i.e.,

$$\sigma_{xx}^{(nd)} = \frac{4\pi e^2}{\hbar^2}\left[\frac{\mu_1\tau_1^2}{\tau_{12}(1+(\omega_c\tau_1)^2)^2}\times\left((\omega_c\tau_1)^2 - 1 + \frac{\tau_1}{\tau_{11}}\frac{1-3(\omega_c\tau_1)^2}{1+(\omega_c\tau_1)^2}\right) + \frac{\mu_2\tau_2^2}{\tau_{12}(1+(\omega_c\tau_2)^2)^2}\left((\omega_c\tau_2)^2 - 1 + \frac{\tau_2}{\tau_{22}}\frac{1-3(\omega_c\tau_2)^2}{1+(\omega_c\tau_2)^2}\right)\right],$$

$$\sigma_{xy}^{(1)} = \frac{4\pi e^2}{\hbar^2}\left[-\frac{\mu_1\tau_1^2\omega_c}{1+(\omega_c\tau_1)^2}\left(\frac{2\tau_1}{\tau_{12}(1+(\omega_c\tau_2)^2)^2}\right.\right.$$

$$\left.\left.-\frac{1+3(\omega_c\tau_1)^2}{(\omega_c\tau_1)^2(1+(\omega_c\tau_1)^2)^2}\right)+\frac{2\mu_2\tau_2^3\omega_c}{\tau_{12}(1+(\omega_c\tau_2)^2)^2}\right],$$

$$\sigma_{xy}^{(2)} = \frac{4\pi e^2}{\hbar^2}\left[-\frac{\mu_2\tau_2^2\omega_c}{1+(\omega_c\tau_1)^2}\left(\frac{2\tau_2}{\tau_{12}(1+(\omega_c\tau_2)^2)}\right.\right.$$

$$\left.\left.-\frac{1+3(\omega_c\tau_2)^2}{(\omega_c\tau_2)^2(1+(\omega_c\tau_2)^2)}\right)+\frac{2\mu_1\tau_1^3\omega_c}{\tau_{12}(1+(\omega_c\tau_1)^2)^2}\right],$$

$$\sigma_{xy}^{(nd)} = \frac{4\pi e^2}{\hbar^2}\left[\frac{2\mu_1\tau_1^3\omega_c}{\tau_{12}(1+(\omega_c\tau_1)^2)^2}\left(1+\frac{\tau_1}{\tau_{12}}\frac{(\omega_c\tau_1)^2-3}{(1+(\omega_c\tau_1)^2)}\right)\right.$$

$$\left.+\frac{2\mu_2\tau_2^3\omega_c}{\tau_{12}(1+(\omega_c\tau_2)^2)^2}\left(1+\frac{\tau_1}{\tau_{12}}\frac{\omega_c\tau_2-3}{1+(\omega_c\tau_2)^2}\right)\right].$$

ACKNOWLEDGMENTS

We thank L. Golub and S. Tarasenko for their helpful participation in discussions. This study was supported in part by the Russian Foundation for Basic Research; INTAS; the Presidium of the Russian Academy of Sciences program “Low-Dimensional Quantum Nanostructures”; and by the Ministry of Industry, Science, and Technology of the Russian Federation.

REFERENCES

1. D. R. Leadley, R. Fletcher, R. J. Nicholas, *et al.*, Phys. Rev. B **46**, 12439 (1992).
2. X. C. Zhang, A. Pfeuffer-Jeschke, K. Ortner, *et al.*, Phys. Rev. B **63**, 245305 (2001).
3. N. S. Averkiev, L. E. Golub, S. A. Tarasenko, and M. Willander, J. Phys.: Condens. Matter **12**, 2517 (2001).
4. T. H. Sander, S. N. Holmes, and J. J. Harris, Phys. Rev. B **58**, 13856 (1998).

Translated by A. Zalesskiĭ

Semiconductors, Vol. 37, No. 2, 2003, pp. 165–167. Translated from Fizika i Tekhnika Poluprovodnikov, Vol. 37, No. 2, 2003, pp. 173–175.
Original Russian Text Copyright © 2003 by Niftiev, Alidzhanov, Tagiev, Muradov.

Electrical Properties of $FeIn_2Se_4$ Single Crystals

N. N. Niftiev, M. A. Alidzhanov, O. B. Tagiev, and M. B. Muradov

Azerbaijanian State Pedagogical University, Baku, 370000 Azerbaijan

Submitted June 5, 2002; accepted for publication June 27, 2002

Abstract—The temperature dependence of electrical conductivity and current–voltage characteristics of $FeIn_2Se_4$ single crystals were studied. It is shown that the current in the nonlinear range of the current–voltage characteristic is caused by the field effect. The activation energy of charge carriers, the concentration of traps, and the shape of a potential well in the region of a trap are determined. © *2003 MAIK "Nauka/Interperiodica".*

In recent years, great interest has been expressed in the semiconductors of the $A^{II}B_2^{III}X_4^{VI}$ type (where A stands for Fe, Mn, Ni, and Co; B, for Ga and In; and X, for S, Se, and Te) containing elements with unfilled *d* shells [1–6]. These compounds are promising as materials for lasers, light modulators, photodetectors, and other functional devices controlled by a magnetic field.

Electrical properties of $FeIn_2Se_4$ single crystals are poorly understood. In this paper, we report the results of studying the temperature dependence of electrical conductivity $\sigma(T)$ and current–voltage characteristics in $FeIn_2Se_4$ single crystals.

Single crystals of $FeIn_2Se_4$ in the form of plane-parallel platelets were grown by the Bridgman–Stockbarger method.

X-ray analysis showed that $FeIn_2Se_4$ crystallized in a hexagonal lattice with the following parameters: a = 4.18 Å, c = 19.47 Å, c/a = 4.65 [3]. The current–voltage characteristics were measured in the samples with In contacts fired-in on the opposite surfaces of plates. The distance between contacts varied within 20–150 µm.

The current–voltage characteristics of the In–$FeIn_2Se_4$–In structures at various temperatures are shown in Fig. 1. The curves consist of two portions: an ohmic portion ($J \propto U$) and a portion of nonlinear increase in current ($J \propto U^n$, $n > 1$).

Figure 2 shows that the ohmic portion can be approximated by the relation $\sigma \propto \exp(10^3/T)$ and consists of three straight lines with different slopes. The slope in the high-temperature region decreases more considerably with decreasing temperature than in the low-temperature region. The values of the activation energy for impurity levels in $FeIn_2Se_4$ single crystals, calculated from the slopes for the above three temperature portions, are E_1 = 0.13 eV, E_2 = 0.28 eV, and E_3 = 0.45 eV.

Figure 3a shows the electric-field dependencies of electrical conductivity (as plots of $\log\sigma$ vs. $\sqrt{F}$) measured at various temperatures in the region of a sharp increase in current. The exponential law for the increase in the electrical conductivity with field was first advanced by Frenkel [7] in the form

$$\sigma = \sigma_0 \exp(\beta\sqrt{F}), \quad (1)$$

where β is the Frenkel coefficient,

$$\beta = \frac{\sqrt{e^3}}{kT\sqrt{\pi\varepsilon\varepsilon_0}}, \quad (2)$$

e is the electron charge, ε is the dielectric constant of free space, k is the Boltzmann constant, and T is the absolute temperature. From the slopes of the straight lines in Fig. 3a, the values of β determined for various temperatures fall within (2–3) × 10^{-2} $(cm/V)^{1/2}$. The

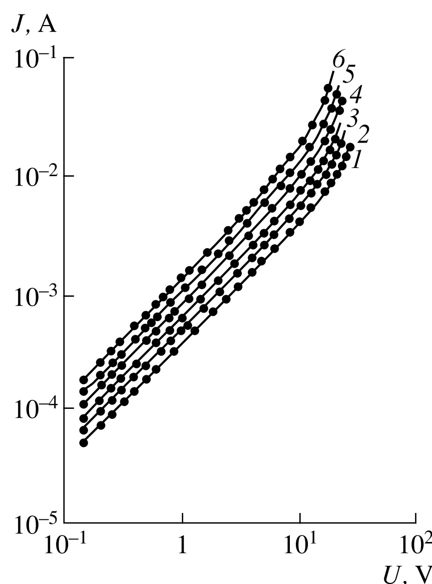

Fig. 1. Dark current–voltage characteristics of the In–$FeIn_2Se_4$–In structures at the temperatures T = (*1*) 300, (*2*) 310, (*3*) 323, (*4*) 339, (*5*) 348, and (*6*) 363 K.

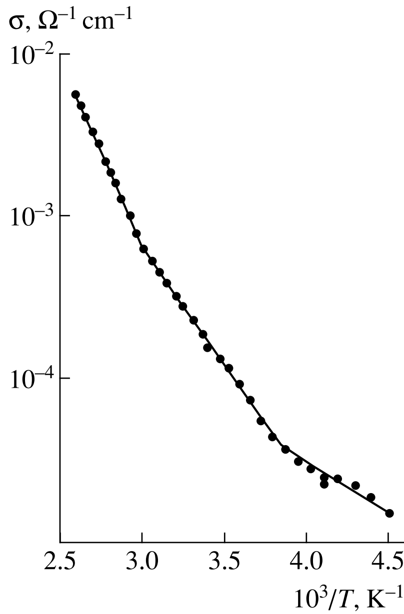

Fig. 2. Temperature dependence of electrical conductivity for the $FeIn_2Se_4$ single crystal.

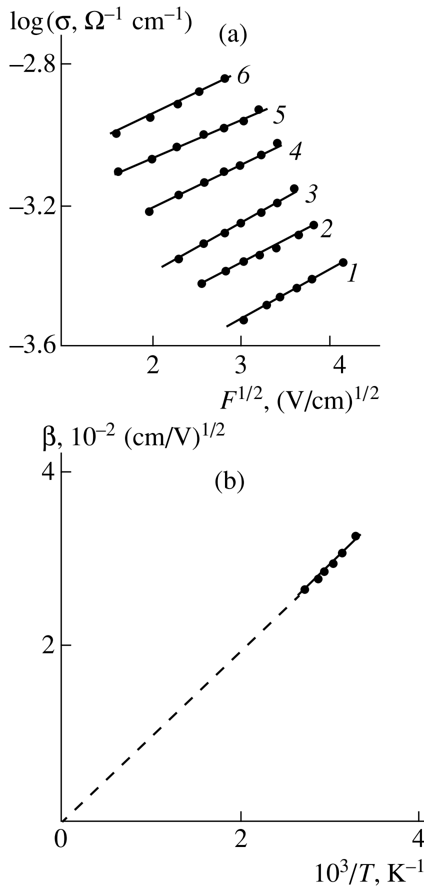

Fig. 3. (a) Electrical conductivity of $FeIn_2Se_4$ single crystals as a function of the field F at T = (*1*) 300, (*2*) 310, (*3*) 323, (*4*) 339, (*5*) 348, and (*6*) 363 K. (b) Temperature dependence of the Frenkel coefficient β.

temperature dependence of β (see Fig. 3b) was obtained from the dependence $\sigma(F^{1/2})$ at different temperatures. As can be seen, β increases with decreasing temperature and the dependence $\beta \propto 10^3/T$ is well obeyed. Such temperature variation in β is in agreement with the Frenkel theory, and the extrapolated straight line $\beta \propto 10^3/T$, in accordance with formula (2), passes through the origin of coordinates. It is shown by Hill [8] that the smallest electric field magnitude, which corresponds to the nonlinear relationship $\sigma = f(F)$, contains information about the concentration of defects responsible for thermal-field ionization and electrical conductivity in $FeIn_2Se_4$ crystals. Using the expression

$$N_t = \left(\frac{2e}{kT\beta}\sqrt{F_c}\right)^3, \quad (3)$$

we can estimate the concentration of ionized centers N_t in $FeIn_2Se_4$ provided we know the values of the lowest electric field F_c at which a nonlinear $\sigma(F)$ dependence sets in. We found that $N_t = 1.1 \times 10^{15}$ cm^{-3}. Of great importance is knowing the shape of a potential well. The function $\varphi(x)$ is the potential energy that depends on the distance to an impurity center or trap (x is the distance along the direction of an applied field). The energy changes under the action of an electric field [8]. It can be shown [8, 9] that

$$\varphi(x) = -\frac{kT\beta}{2}\sqrt{F} = eFx, \quad (4)$$

$$x = \frac{kT\beta}{2e}\frac{1}{\sqrt{F}}. \quad (5)$$

Using the experimental data and relations (4) and (5), we determined the shape of a potential well in $FeIn_2Se_4$, as shown in Fig. 4.

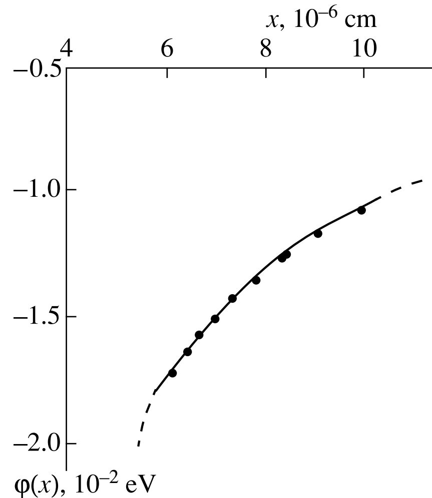

Fig. 4. The shape of a potential well associated with an electron trap in $FeIn_2Se_4$.

If the form of the potential energy for the interaction with a center is known, one can obtain information about the structure of trap centers. As was pointed out in [9], an electron escapes from the center if the condition $\varepsilon_e > E_0 - \Delta U_0$ is satisfied. The electron must conserve energy until it passes the saddle point and not loose energy as a result of thermal collisions.

This situation takes place if the mean free path of an electron exceeds the effective dimensions of a potential well. The mean free path of charge carriers is determined by the following formula [9]:

$$\lambda = \frac{1}{e}f(F_e) = \frac{kT\beta}{2e}\frac{1}{\sqrt{F}}. \quad (6)$$

The mean free path of an electron in $FeIn_2Se_4$ crystals, calculated from experimental data according to formula (6), is equal to approximately 9.8×10^{-6} cm.

Thus, the measurements of the current–voltage characteristics and the $\sigma(T)$ dependence show that the current in the linear portion of the characteristics is caused by the field effect. The values of the activation energy of charge carriers, the concentration of traps, and the shape of a potential well were determined.

REFERENCES

1. T. Kanomata, H. Ido, and T. Kaneko, J. Phys. Soc. Jpn. **34**, 554 (1973).
2. B. K. Babaeva, in *Ternary Semiconductors and Their Applications* (Shtiintsa, Kishinev, 1976).
3. B. K. Babaeva and P. G. Rustamov, in *Studies in Inorganic and Physical Chemistry* (Nauka, Baku, 1977).
4. R. N. Bekimbetov, Yu. V. Rud', and M. A. Tairov, Fiz. Tekh. Poluprovodn. (Leningrad) **21**, 1051 (1987) [Sov. Phys. Semicond. **21**, 642 (1987)].
5. R. N. Bekimbetov, N. N. Konstantinova, Yu. V. Rud', and M. A. Tairov, Neorg. Mater. **24**, 1969 (1988).
6. N. N. Niftiev, A. G. Rustamov, and O. B. Tagiev, Fiz. Tekh. Poluprovodn. (St. Petersburg) **28**, 752 (1994) [Semiconductors **28**, 442 (1994)].
7. Ya. I. Frenkel', Zh. Éksp. Teor. Fiz. **8**, 1292 (1938).
8. R. H. Hill, Philos. Mag. **23**, 59 (1971).
9. N. G. Volkov and V. K. Lyapidevskiĭ, Fiz. Tverd. Tela (Leningrad) **14**, 1337 (1972) [Sov. Phys. Solid State **14**, 1149 (1972)].

Translated by A. Zalesskiĭ

Semiconductors, Vol. 37, No. 2, 2003, pp. 168–171. Translated from Fizika i Tekhnika Poluprovodnikov, Vol. 37, No. 2, 2003, pp. 176–179.
Original Russian Text Copyright © 2003 by Gorleĭ, Grushka.

An Impurity Band in $Hg_3In_2Te_6$ Crystals Doped with Silicon

P. N. Gorleĭ and O. G. Grushka

Chernovtsy National University, Chernovtsy, 58012 Ukraine

Submitted April 23, 2002; accepted for publication June 27, 2002

Abstract—The influence of silicon impurity on the energy-band spectrum in the $Hg_3In_2Te_6$ semiconductor compound, which incorporated a high concentration of stoichiometric vacancies, was studied on the basis of the results of electrical and optical measurements. It is shown that silicon impurity forms an impurity band of donor states whose density can be approximated by a Gaussian distribution with a peak at E_c – 0.29 eV. The emergence of the impurity band is accompanied with the formation of a quasi-continuous spectrum of localized states in the band gap (E_g = 0.74 eV); the density of these states is shown to increase as the doping level increases. All states merge into a continuous band if the impurity concentration $N_{Si} > 4.5 \times 10^{17}$ cm^{-3}. Experimental data are explained on the basis of the effect of impurity self-compensation, in which case donor impurity states arise simultaneously with acceptor states of defects. *© 2003 MAIK "Nauka/Interperiodica".*

Crystals of the $Hg_3In_2Te_6$ compound belong to semiconductors with a sphalerite structure, in the unit cells of which there are more sites than atoms. A sixth fraction of cationic sites, which are unoccupied by atoms, gives rise to a high concentration of stoichiometric vacancies (~10^{21} cm^{-3}). These defects radically reduce the sensitivity of $Hg_3In_2Te_6$ electrical properties to the introduction of a fairly high concentration (~10^{19} cm^{-3}) of extraneous impurities; notably, this concentration is still lower than that of intrinsic structural defects [1, 2]. Other important properties of this material are also related to the special features of its structure; these properties include a high resistance of $Hg_3In_2Te_6$ to ionizing radiation, inertness of the surface to adsorption of atoms from atmospheric air, high quantum efficiency of photoconductivity in a wide range of photon energies (0.74–3.0 eV), and so on. As a result, this material has found a wide range of applications [3].

It is of interest to study the influence of doping on the energy-band spectrum and the concentration of levels in the band gap of $Hg_3In_2Te_6$; such studies can provide insight into the origin of self-compensation of impurities in $Hg_3In_2Te_6$ and into the role of stoichiometric vacancies in this phenomenon.

An $Hg_3In_2Te_6$ ingot was doped with silicon impurity in the course of Bridgman–Stockbarger growth. The concentration of introduced Si impurity was 10^{19} cm^{-3}. The distribution of impurity over the $Hg_3In_2Te_6$ ingot length was studied by analyzing the optical-absorption spectra of samples cut from different parts of the ingot. The spectral dependences of the absorption coefficient were determined from the reflection $R(h\nu)$ and transmission $T(h\nu)$ spectra measured at 300 K in the photon-energy range of 0.05 eV < $h\nu$ < 0.74 eV. The form of variation in the absorption coefficient along the ingot length in the entire spectral range suggested that, in the course of planar crystallization, silicon impurity was distributed nonuniformly throughout the crystal with the distribution coefficient $k < 1$. It was found that the concentration of impurity atoms N_{Si} in the starting part of the ingot (from which samples 1–3 were prepared; see table) is much lower than the average concentration of introduced Si impurity; in contrast, the impurity is accumulated in the end part of the ingot, which results

Characteristics of studied samples

Sample no.	N_{Si}, cm^{-3}	E, meV	n_i, cm^{-3}	$\lvert R\sigma \rvert$, cm^2 V^{-1} s^{-1}
			T = 300 K	
0	0	14	10^{12}–10^{13}	250–350
1	1.6×10^{17}	23	1.65×10^{13}	307
2	2.7×10^{17}	25	1.72×10^{13}	272
3	4.5×10^{17}	34	2.05×10^{13}	205
4	–	36	7.44×10^{12}	308

1063-7826/03/3702-0168$24.00 © 2003 MAIK "Nauka/Interperiodica"

in an appreciable decrease in transmission to a degree of complete opacity of the material in this part of the ingot. A steep slope of the concentration profile along the ingot length is typically [4] observed for deep-level impurities with small values of k ($k \ll 1$).

The spectral dependence of the absorption coefficient in the region of the fundamental-absorption edge is described by Urbach's relation $\alpha \propto \exp[-(E_g - h\nu)/E]$. As the impurity concentration increases, the steepness of the absorption edge decreases and the characteristic energy E determined from the slope of the linear portion of the dependence $\ln\alpha = f(h\nu)$ (see the inset in Fig. 1) increases (see table).

Extrapolated linear portions of spectral dependences of the absorption coefficient in the region where the Urbach rule is obeyed converge to a common point at $h\nu = E_g = 0.74$ eV for samples with different impurity concentrations. This observation indicates that the value of E_g is not affected by doping. Both the absorption coefficient and the characteristic energy E correlate with the doping level. Diffuseness of the absorption edge and its exponential dependence on $h\nu$ for sample 0 (see the inset in Fig. 1) are induced by the tails of the density of states at the edges of allowed bands in the starting (nominally undoped) $Hg_3In_2Te_6$ crystals. The tails in the density of states are presumably [5] caused by crystal field fluctuations, which are introduced by intrinsic defects (in the case under consideration, these are stoichiometric vacancies). Doping brings about an increase in the characteristic energy E, which is indicative of additional broadening of the tails in the density of states and the appearance of localized states in the band gap; these states form a quasi-continuous set and merge with the bands of free charge carriers. Notably, the density of these states increases as the concentration of Si impurity increases.

A selective absorption band peaked at $h\nu = E_0 = 0.45$ eV (Fig. 1) is observed in the spectral range of 2–25 μm against a background of continuous structureless absorption, which increases with the doping level; this band is distinct in the spectra of samples 1–3 with a low impurity concentration N_{Si} and disappears when N_{Si} exceeds a certain value. If we assume that the impurity band features a Gaussian distribution of the density of states, the absorption coefficient can be expressed as [6]

$$\alpha(h\nu) = \alpha_0 \exp[-(h\nu - E_0)^2/\gamma^2]. \quad (1)$$

The quantity γ defines the half-width of the impurity band and is given by

$$\gamma = \frac{e^2}{\varepsilon\varepsilon_0}\left(\frac{Nr_0}{4\pi}\right)^{1/2}, \quad (2)$$

where

$$r_0 = \left(\frac{\varepsilon\varepsilon_0 k_B T}{2e^2 n_i}\right)^{1/2}$$

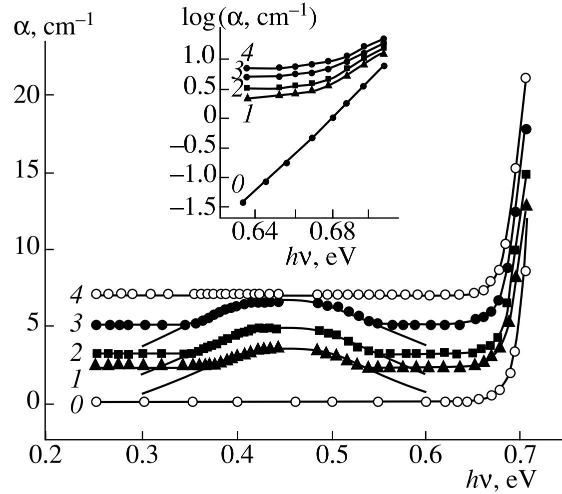

Fig. 1. Absorption spectra of $Hg_3In_2Te_6$ samples either (*0*) undoped or (*1–4*) doped with silicon; the parameters of the samples are listed in the table. The numbers at the curves coincide with numbers of the samples in the table. The same spectra in the region of exponential increase in the absorption coefficient are shown in the inset.

is the Debye screening length, N is the impurity concentration, k_B is the Boltzmann constant, and n_i is the concentration of intrinsic charge carriers at 300 K.

Formula (1) can be used to describe satisfactorily the shape of the impurity absorption band in samples 1–3 for the values of N_{Si} listed in the table. These values were determined from the best fit of calculated curves to experimental data. The dependences calculated using formula (1) are shown in Fig. 1 by the solid lines.

According to Shklovskii and Efros [5], formula (2) defines the rms potential of randomly distributed screened impurities, which governs the spread of impurity levels in energy positions and broadening of the impurity band.

The observed selective-absorption band is most likely related to optical transitions from the valence band to the levels of the donor centers, which are ionized at room temperature. Taking this circumstance into account, we may assume that the peak in the density of states responsible for the appearance of the selective-absorption band is located below the conduction-band bottom and is spaced from the latter at $E_{d0} = E_g - E_0 = 0.29$ eV.

Electrical measurements showed that the Si-doped $Hg_3In_2Te_6$ samples under investigation retain intrinsic electrical conductivity at $T \gtrsim 300$ K; the electron type of this conductivity is caused by the ratio between the electron and hole mobilities $b = \mu_n/\mu_p > 1$. Samples 1–4 do not differ from undoped samples in the concentration of intrinsic charge carriers ($n_i \approx 10^{13}$ cm^{-3}); however, the former samples have a somewhat lower Hall mobility $|R\sigma|$ (see table) for the same value of n_i.

Temperature dependences of electrical conductivity $\sigma(T)$, the Hall coefficient $R(T)$, and thermoelectric

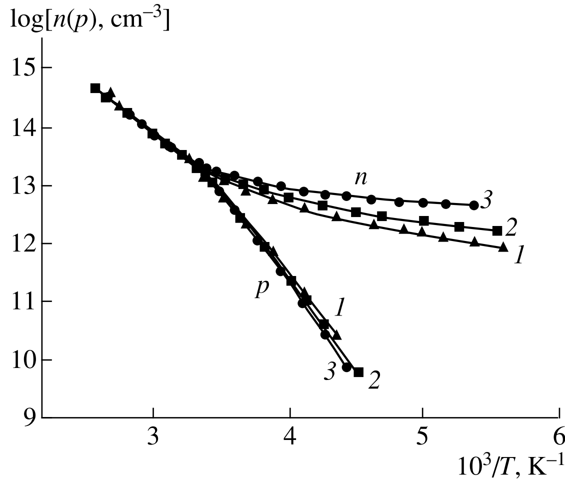

Fig. 2. Temperature dependences of charge-carrier concentrations n and p for samples *1–3*. Numbers at the curves coincide with numbers of the samples in the table.

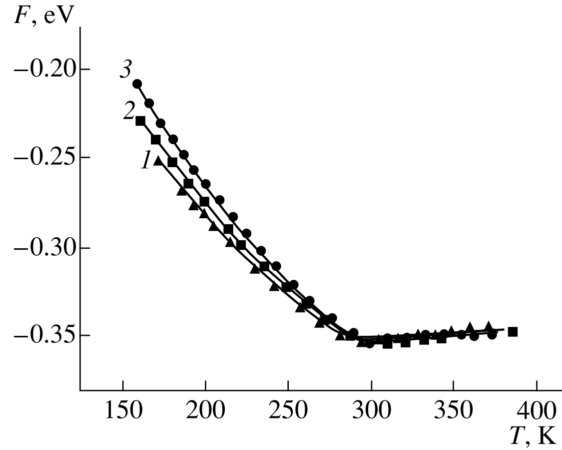

Fig. 3. Temperature dependences of the Fermi level position for samples *1–3*. Numbers at the curves coincide with numbers of the samples in the table.

power $\alpha_{th}(T)$ were analyzed using the well-known relations [7] for the case of mixed conductivity; i.e.,

$$\sigma = e\mu_p(nb + p), \quad (3)$$

$$R = \frac{A(p - nb^2)}{e(p + nb)^2}, \quad (4)$$

$$n = N_c \exp(-F/k_B T), \quad p = N_v \exp[-(E_g - F)/k_B T],$$

$$\alpha_{th} = \frac{\alpha_{th}^{(p)} - \alpha_{th}^{(n)} b}{1 + b},$$

$$\alpha_{th}^{(n)} = -\frac{k_B}{e}\left(r + 2 + \frac{F}{k_B T}\right), \quad (5)$$

$$\alpha_{th}^{(p)} = \frac{k_B}{e}\left(r + 2 + \frac{E_g - F}{k_B T}\right),$$

where N_c and N_v are the effective densities of states in the conduction and valence bands, respectively; F is the Fermi level position; A is the Hall factor; and r is a quantity that depends on the mechanism of scattering of the charge carriers. If the latter are scattered by acoustic lattice vibrations, we have $r = 0$.

The quantities n_i, F, b, μ_p, N_c, and N_v were determined for the region of intrinsic conductivity using the equality $n = p = n_i$ in the case of $r = 0$.

Equations (3)–(5) were solved simultaneously for the region of transition from the intrinsic to extrinsic types of conductivity, in which case $n \neq p$; in calculations, we used the values of N_c and N_v determined at T = 300 K and took into account the temperature dependences of these quantities. The calculated temperature dependences $\log n(p) = f(10^3/T)$ and $F(T)$ are shown in Figs. 2 and 3. As can be seen from Fig. 2, a correlation between electron (n) and impurity (N_{Si}) concentrations in the samples is observed in the region of low temperatures. However, the values of N_{Si} exceed those of $n \approx (10^{12}–10^{13})$ cm^{-3} by more than five orders of magnitude. This observation is indicative of a large degree of compensation $K = N_a/N_d \approx 0.999$ [$N_{a(d)}$ is the concentration of acceptor (donor) impurity].

The spectra of absorption, which increases in the entire transparency range of 2–25 μm as the doping level increases, indicate that the $Hg_3In_2Te_6$ band gap is filled with both donor and acceptor states as a result of doping with silicon. A number of electronic transitions in a wide range of photon energies (0.05–0.62 eV) are induced by the localized states, which are distributed quasi-continuously throughout the band gap. The areas under the peaks against the background of structureless absorption are approximately the same for samples 1–3 (Fig. 1), although the impurity concentrations differ; this effect is a result of pronounced (although incomplete) compensation of donors that form the impurity band. Disappearance of the corresponding peak for sample 4 occurs owing to the fact that this peak merges completely with the increasing background absorption. Transformation of the absorption spectra shown in Fig. 1 is caused by the simultaneous formation of compensating defects with inclusions of doping impurity and a transition to complete compensation of the formed states. Probably, the formation of pairs consisting of doping impurity and defects occurs with the involvement of stoichiometric vacancies, which ensures a decrease in energy and relaxation of the crystal structure.

It is worth noting that we failed to perform calculations for sample 4 at T < 300 K using formulas (3)–(5) owing to an anomalous temperature dependence of the thermoelectric power α_{th}, which has a sharp maximum |–2150| μV/K in the region of 230 K; on both sides of this maximum, α_{th} decreases to |–500| μV/K at $T \approx 180$ K

and to |–700| μV/K at 270 K. We are still unable to interpret such behavior of $\alpha_{th}(T)$.

In order to determine the energy position of the impurity band from electrical measurements, we used a differential method for an analysis of curves $n(T)$; this method was suggested by Hoffmann [8]. As can be seen from Fig. 3, the Fermi level shifts monotonically into the depth of the band gap as the temperature increases. Electrons are released when the Fermi level intersects an impurity level.

According to Hoffmann [8], the derivative $-k_BTdn/dF$ has a maximum when F coincides approximately with the donor level E_d. Therefore, the abscissa point corresponding to the maximum of the dependence of $-k_BTdn/dF$ on F defines the energy position $E_c - E_d$.

In Fig. 4, we show the results of differential analysis of the dependences $\log n(10^3/T)$ (Fig. 2) in the temperature range of 170–300 K. If the temperature variations $\Delta T = T_i - T_j$ were small, we determined the dependence of $-k_BTdn/dF$ on $F(T)$ in terms of the function $Z(x)$ [8], where

$$Z = -\frac{k_B}{2}(T_i + T_j)\frac{n(T_i) - n(T_j)}{F(T_i) - F(T_j)},$$

$$x = [F(T_i) + F(T_j)]/2.$$

In contrast to the dependences $\log n(10^3/T)$ (Fig. 2), which do not exhibit any special features in the range of 170–300 K, the curves $-k_BTdn/dF$ plotted versus $F(T)$ (Fig. 4) have a single peak; the latter corresponds to the energy level $E_c - E_d \approx 0.28$ eV, since the Fermi energy at which the peak is observed is $F \approx E_d$.

The small height of this peak and the appreciable shift of this peak to lower energies when compared with the position of the optical maximum result from a large degree of compensation [8]. However, a somewhat decreased value of E_d compared to the optical value $E_{d0} = 0.29$ eV can be caused by electrical conductivity via the percolation level, which is located below the conduction-band bottom owing to the fact that the allowed-band edges are diffuse and by approximations used in determining E_d from electrical measurements, i.e., by assuming that the values of N_c, N_v, A, and r are fixed.

The studies we performed showed that silicon impurity affects the energy-band spectrum of $Hg_3In_2Te_6$ by introducing localized states of acceptor and donor types, which are distributed quasi-continuously throughout the entire band gap; notably, an impurity band with a peak in the density of states at $E_c - 0.29$ eV is formed against the aforementioned states if $N_{Si} \lesssim 4.5 \times 10^{17}$ cm^{-3}. If $N_{Si} > 4.5 \times 10^{17}$ cm^{-3}, the complete compensation of oppositely charged centers occurs; as a result, a continuous structureless band of localized states is formed in the band gap.

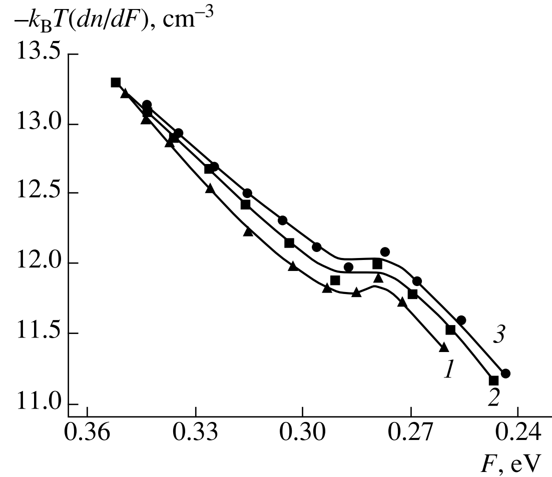

Fig. 4. Dependences of the function $-k_BTdn/dF$ on the Fermi level position F for samples *1–3*. The numbers at the curves coincide with numbers of the samples in the table.

REFERENCES

1. O. G. Grushka, Z. M. Grushka, V. M. Frasunyak, and V. S. Gerasimenko, Fiz. Tekh. Poluprovodn. (St. Petersburg) **33**, 1416 (1999) [Semiconductors **33**, 1272 (1999)].
2. O. G. Grushka, P. M. Gorleĭ, A. V. Bestsennyĭ, and Z. M. Grushka, Fiz. Tekh. Poluprovodn. (St. Petersburg) **34**, 1197 (2000) [Semiconductors **34**, 1147 (2000)].
3. G. G. Grushka, A. P. Bakhtinov, and Z. M. Grushka, J. Adv. Mater. **4** (1), 36 (1997).
4. *Physics and Materials Technology of Semiconductors with Deep Levels*, Ed. by V. I. Fistul' (Metallurgiya, Moscow, 1987).
5. B. I. Shklovskiĭ and A. L. Éfros, *Electronic Properties of Doped Semiconductors* (Nauka, Moscow, 1979; Springer, New York, 1984).
6. V. P. Gribkovskiĭ, *The Theory of Absorption and Emission of Light in Semiconductors* (Nauka i Tekhnika, Minsk, 1976).
7. P. S. Kireev, *Physics of Semiconductors* (Vysshaya Shkola, Moscow, 1975).
8. H. J. Hoffmann, Appl. Phys. **19**, 307 (1979).

Translated by A. Spitsyn

Semiconductors, Vol. 37, No. 2, 2003, pp. 172–177. Translated from Fizika i Tekhnika Poluprovodnikov, Vol. 37, No. 2, 2003, pp. 180–186.
Original Russian Text Copyright © 2003 by Drapak, Manasson, Netyaga, Kovalyuk.

SEMICONDUCTOR STRUCTURES, INTERFACES, AND SURFACES

Electrical Properties of the p^+-Bi_2Te_3–p-GaSe Isotype Heterostructure

S. I. Drapak*^, V. A. Manasson, V. V. Netyaga*, and Z. D. Kovalyuk***

** Frantsevich Institute of Problems in Materials Science (Chernovtsy Branch), National Academy of Sciences of Ukraine, ul. I. Vilde 5, Chernovtsy, 58000 Ukraine*

^e-mail: chimsp@unicom.cv.ua

*** Antena Development, Waveband Corporation, Torrance, Ca. 90501, USA*

Submitted April 16, 2002; accepted for publication May 29, 2002

Abstract—Electrical properties of a p^+-Bi_2Te_3–p-GaSe isotype heterostructure fabricated for the first time are reported. A qualitative model is suggested which explains the emergence of negative differential conductivity for a forward-biased structure and for a reverse-biased structure, which is also illuminated. *© 2003 MAIK "Nauka/Interperiodica".*

1. INTRODUCTION

Gallium monoselenide GaSe belongs to a widespread class of layered III–VI compounds. It is used as a base material for the development of various photosensitive structures. Based on GaSe, solar cells [1], high-efficiency photodiodes [2], and sensors of polarized radiation [3] have been developed. The sensitivity of native oxide of this semiconductor in the ultraviolet spectral region means GaSe can be considered as a promising material for the development of sensors of ultraviolet radiation [4]. Native anisotropy of chemical bonds inside the layers and between them exists both for this material and other layered semiconductors (InSe, GaS, Bi_2Te_3, etc.). It is believed that, due to this, the substrates from these materials, which are obtained by cleavage in air, are perfect not only geometrically but also in that they are inert to atomic adsorption from the atmosphere [5–7]. Because of this circumstance, data on the influence of the interface for heterojunctions or the GaSe surface for Schottky barriers are virtually absent in the literature. As an exception to this circumstance, there are several studies in which the native oxide layer was intentionally formed at the GaSe surface, for example [8], or the contact of GaSe with such semiconductors as Ge or Si was investigated [9]. In the latter case, deviations of electrical characteristics from ideal ones were explained by the influence of the Ge or Si surface. Analysis of experimental current–voltage (*I*–*V*) characteristics of GaSe-based structures is also hampered by a high series resistance, which depends nonlinearly on the voltage. Because of this circumstance, instead of dark *I*–*V* characteristics, their photoelectrical modification is often reported in the literature (see, for example, [10]). Note that the large series resistance of GaSe-based structures is one of the factors which hinders wide practical use of this semiconductor. However, reduction of the series resistance to the conventional values for commercial Si or GaP diodes can lead to nontrivial results. In this case, the electrical characteristics of the structure will be determined mainly by the interface properties rather than the barrier properties. This is especially noticeable for structures with a low potential-barrier height.

In this study, a p^+-Bi_2Te_3–p-GaSe isotype heterostructure fabricated for the first time is investigated. The series resistance to a direct current for the structure was ~20–40 Ω, whereas the potential-barrier height, which was experimentally determined from capacitance–voltage (*C*–*V*) characteristics, was 0.1 eV.

2. EXPERIMENTAL

To reduce the series resistance, Dy-doped GaSe single-crystals with a majority carrier density $p \approx 10^{16}$ cm^{-3} at 300 K were used to fabricate the heterojunctions. As a contacting material, we used weakly degenerate Bi_2Te_3 with a hole density $p = 1.6 \times 10^{19}$ cm^{-3} at the same temperature. This was grown using the Bridgman–Stockbarger technique with no deviation from stoichiometry. The carrier density for both semiconductors was determined from Hall measurements. The semiconductor surfaces were prepared by cleavage in air. They were not subjected to any additional treatment (mechanical, chemical, or thermal). Heterojunctions were fabricated by fitting onto an optical contact [11]. The thickness of GaSe substrates was 1–1.5 mm, and the thickness of bismuth chalcogenide was 0.1–0.2 mm. The area of the samples investigated was $s \approx 0.3$ cm^2. Current-carrying contacts both from the GaSe side and from the Bi_2Te_3 side were deposited by In alloying at 150–180°C and retained nonrectifying properties over the entire range of current densities investigated. Het-

erostructures thus formed possess clearly pronounced rectifying properties in a wide temperature range. For a voltage of 1.5–2 V, the forward current exceeds the reverse one by no less than a factor of 5×10^3. The forward portion of the *I–V* characteristic corresponds to the positive voltage applied to GaSe.

To determine the mechanisms of current flow across the heterostructure, the forward and reverse *I–V* characteristics were measured in the voltage range from –11 to +11 V at various fixed temperatures from 230 to 333 K. Three methods of measurements were used.

(i) Measurement by varying the voltage applied to the structure with a certain step (a static *I–V* characteristic). The rate of varying the voltage (both increasing and decreasing) was varied in the range of 10–200 mV/s. Variation in the rate caused no variations in the shape of the *I–V* characteristic. The measurements were carried out using an H.F.-FRA-1255&1286 amplitude–frequency analyzer. The measuring complex was controlled using a CorrWare-v.2.2 program.

(ii) Measurement by specifying certain values of bias voltage (by points). The values of the voltage and the current were fixed during the third second after applying a bias to the structure.

(iii) The ac measurement at a frequency of 50 Hz.

A typical static *I–V* characteristic of the p^+-Bi_2Te_3–p-GaSe structure at $T = 290$ K is shown in Fig. 1 (curves *1*, *2*). Dependence *1* corresponds to varying the bias voltage applied to the structure from –11 to +11 V, and dependence *2* corresponds to the reverse variation of the voltage. As can be seen from Fig. 1, the *I–V* characteristic includes a portion with a negative differential conductivity (NDC). In the case of measuring the *I–V* characteristic by points, the shape of the characteristic remains qualitatively the same (Fig. 1, curve *3*). However, starting from bias voltages $V \gtrsim 4.5$ V, a certain delay in the current density from dependences *1* and *2* was observed. Measurements of the ac *I–V* characteristic (dynamic *I–V* characteristic) showed no evidence of an NDC portion. Only the variation in the position of the forward portion from position *4* to position *5* (see Fig. 1) with a relaxation time of 4–6 s was displayed by an oscillograph. This observation indicates that the processes governing the emergence of NDC in the p^+-Bi_2Te_3–p-GaSe structure are slow. In this case, the forward portion of the *I–V* characteristic was in state *3* for 4–6 s, whereas it was in state *4* for a time interval that was an order of magnitude shorter. Upon illumination of the heterojunction by light with a power of 100 mW/cm^2, the emergence of an NDC portion was also observed in the reverse portion of the *I–V* characteristic (see inset in Fig. 1).

The investigations carried out demonstrated that the electrical properties of isotype Bi_2Te_3–GaSe heterostructures are independent of whether the structures were fabricated within 5–6 min after cleavage of

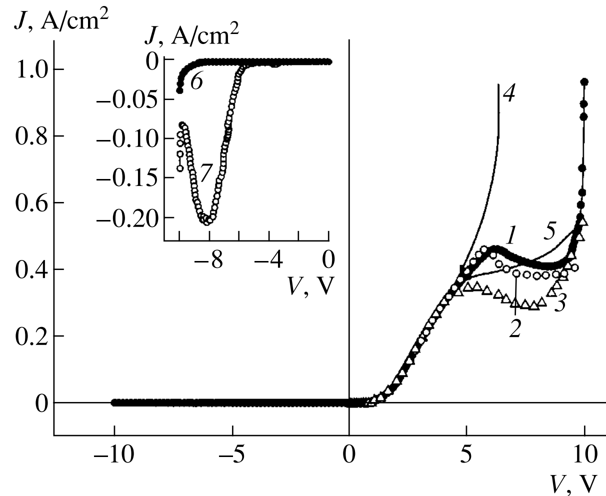

Fig. 1. Typical static (*1*, *2*), dynamic (*4*, *5*), and measured by points (*3*) current–voltage characteristics of the p^+-Bi_2Te_3–p-GaSe isotype heterostructure at $T = 290$ K. Reverse portions of the static current–voltage characteristic of the structure in dark (*6*) and under illumination (*7*) are shown in the inset. The majority carrier density for GaSe was $p = 9.5 \times 10^{15}$ cm^{-3} at room temperature.

contacting semiconductors or within 30 min. However, a dependence of electrical properties on the impurity concentration in GaSe was found. Thus, for the GaSe substrate with a majority carrier density $p = 2.7 \times 10^{16}$ cm^{-3}, a shift of the onset of the NDC portion to lower bias voltages $V \approx 3.5$ V was observed. Alternatively, with decreasing carrier density in GaSe, the NDC portion shifted to higher voltages. For example, for $p = 6 \times 10^{15}$ cm^{-3}, the onset of NDC was fixed at $V \approx 8.5$–9 V. Another special feature of the heterostructure under investigation is that the diffusion potential, which was determined from the *C–V* characteristic (0.1 eV), diverges considerably with the current-cutoff voltage of the *I–V* characteristic for relatively high voltages (≈1.2 eV). The current-cutoff voltage is used to estimate the potential-barrier height [12]. The *C–V* characteristics were measured according to the procedure [13] using an H.F.-FRA-1255&1286 analyzer under the control of a ZPlot-v.1.5 program.

3. DISCUSSION

First of all, it should be noted that the investigation of the temperature dependence of resistivity for GaSe and Bi_2Te_3 gives no grounds to relate the NDC portion of the p^+-Bi_2Te_3–p-GaSe heterostructure to the effect of temperature on the conduction of one (or both) of the contacting semiconductors. Making allowance for the degeneracy of hole gas in Bi_2Te_3, the emergence of NDC also cannot be explained by using a tunnel diode model. Even under equilibrium conditions, the valence band of p-GaSe is located facing the levels allowed for Bi_2Te_3.

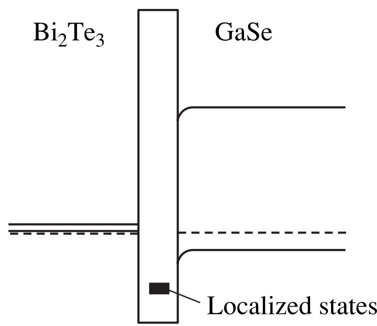

Fig. 2. Energy-band diagram of a p^+-Bi_2Te_3–p-GaSe heterostructure under equilibrium conditions.

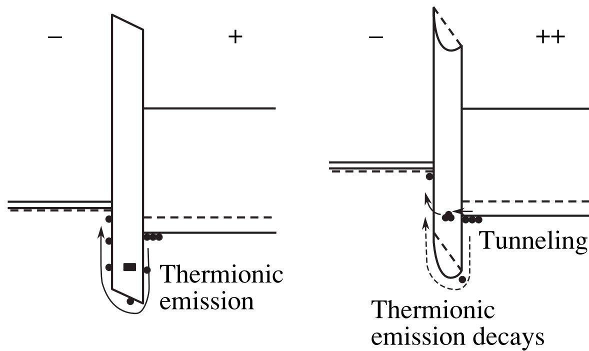

Fig. 3. Energy-band diagram of a forward-biased p^+-Bi_2Te_3–p-GaSe heterostructure.

It is known that slow processes can be caused either by a system of charged particles, which possess ensemble properties [14], or by the recharging of surface states located in the oxide layer [15–17]. The former assumption seems to be rather improbable. Even making allowance for the injecting role of nonrectifying contacts in a system consisting of a rear nonrectifying contact In and p^+-Bi_2Te_3–p-GaSe, plasma formation for the forward bias is possible only in Bi_2Te_3. However, the resistivity of Bi_2O_3 is substantially lower compared with that of GaSe. Because of this circumstance, the variation in the voltage applied to bismuth chalcogenide will cause no noticeable variation in the voltage across the heterostructure. The injection of minority carriers through p^+-Bi_2Te_3 into GaSe is also impossible due to the high potential barrier for electrons, which is caused by the conduction-band offset ΔE_c for contacting semiconductors.

In spite of the fact that the GaSe surface is considered inert to atomic adsorption from the atmosphere [5–7], it is our opinion that the latter assumption is more realistic. The experimentally observed hysteresis (Fig. 1, dependences *1*, *2*), which is characteristic of certain types of insulator films [15], is also indicative of the presence of an oxide layer at the interface between contacting semiconductors. Indeed, it is known that an ultrathin oxide layer exists at the interface in GaSe-based structures [18–20]. On the one hand, the data [18, 19] refer to heterostructures fabricated at temperatures which considerably exceed room temperature (T = 400–450°C), where the growth of native oxide is rather intense [21]. On the other hand, Bakumenko *et al.* [20] reported on the influence of keeping GaSe substrates in air on the work function of this material. According to [20], even within several minutes (the characteristic time is 5–6 min), the GaSe surface is covered with a Ga_2O_3 layer ~0.6–0.8 nm thick. Then, oxide growth is substantially decelerated. Within 96 h, its thickness increases by a factor of no more than 1.5. It seems likely that this circumstance explains the identity of electrical characteristics of heterojunctions which were fabricated within 5–6 and 30 min after cleavage of contacting semiconductors.

An energy-band diagram of the p^+-Bi_2Te_3–p-GaSe heterostructure under equilibrium conditions is shown in Fig. 2. Allowance is made for a thin insulator layer (the bandgap E_g for Ga_2O_3 is 4.6 eV [22]) and deep-level traps localized in this layer. When constructing the energy diagram, E_g for GaSe and E_g' for Bi_2Te_3 were set at 2.0 [23] and 0.17 eV [24], respectively. The surface bending of bands, which is equal to φ_0 = 0.1 eV for GaSe, as mentioned above, was determined from the C–V characteristic. The position of the Fermi level for GaSe was determined from the formula [25]

$$\Delta\mu = E_F - E_V = kT\ln(N_V/p), \quad (1)$$

where E_F and E_V is the energy position of the Fermi level and the valence-band top for the base semiconductor, respectively; k is the Boltzmann constant; T is the absolute temperature; p is the equilibrium majority-carrier density; $N_V = 2(2\pi m_p kT/h^2)^{3/2}$ is the effective density of states for the valence band; and m_p is the effective hole mass. Setting $m_p = 1.34m_0$ for GaSe [24], we calculate $\Delta\mu$ = 0.215 eV at 300 K. The Fermi level position for Bi_2Te_3 $\Delta\mu'$ was estimated from the formula [26]

$$p = 4\pi(2m_p kT/h^2)^{3/2}F_{1/2}[(E_V' - E_F')/kT],$$

where E_F' and E_V' are the energy positions of the Fermi level and the valence band top for Bi_2Te_3, respectively; and $F_{1/2}$ is the Fermi integral. As a result, $\Delta\mu' = E_F' - E_V'$ equals $\Delta\mu' \approx (3–5) \times 10^{-2}$ eV at room temperature.

As can be seen from Fig. 2, the bands are flat in GaSe even at moderate forward biases $V \gtrsim (2–3)kT$ (Fig. 3). Thus, the structure under investigation is similar to a classical metal–insulator–metal system with the only difference in that the majority carriers are holes rather than electrons in the case under consideration. According to [15–17], charge transport in such a system is controlled by the thermionic emission and is described by the expression

$$I = I_S\exp(eV/kT - 1), \quad (3)$$

where $I_S = A^*T^2\exp(-W_m/kT)$ is the saturation current, $A^* = 4\pi m_p k^2 e/h^3$ is the effective Richardson constant, and W_m is the anode work function. In the case under consideration, the W_m quantity in the formula for I_S should be replaced by the work function for the semiconductor into which the majority carriers are injected for the forward bias. This semiconductor is Bi_2Te_3, and $W_m = \chi + E_g' + \Delta\mu'$, where χ is the electron affinity of the semiconductor. Charge transport in a metal–semiconductor–metal system can also proceed via tunneling. However, we do not consider this case, since tunneling implies that the current is independent of temperature (or I_S depends on T very weakly), which contradicts the experimental data.

Thus, for a forward bias across the p^+-Bi_2Te_3–p-GaSe heterostructure, a major part of the voltage drops across the insulator layer. This is caused by a low potential-barrier height for GaSe (0.1 eV) and, consequently, low resistance of the space charge region (SCR). Upon reaching a certain forward bias, the valence band of GaSe descends to the level of localized states in an insulator (slow levels) (Fig. 3). In this case, a fraction of the holes from GaSe tunnels to these states. The charge, which introduces holes into the insulator, causes both the barrier height (solid lines with arrows instead of dotted lines in Fig. 3) and, in its turn, the thermionic current to increase. The states localized in the insulator can also contribute to carrier transport through the insulator, for example, via multistep tunneling. However, these processes are slow and ineffective compared with thermionic emission. Even the emergence of certain positive charge feedback is possible: the larger the number of holes tunneling into localized states in the insulator, the higher the barrier. Because of this circumstance, it is energetically favorable for an even larger number of holes to tunnel into the insulator, and so on. The further increase in the current with increasing forward bias is caused by the fact that the valence band of GaSe descends below the localized slow states and the capture of charge carriers by traps becomes impossible.

For a reverse bias, the SCR located in GaSe has a higher resistivity than that of the insulator. Because of this circumstance, the major part of the voltage applied to the p^+-Bi_2Te_3–p-GaSe structure drops across the SCR (Fig. 4). For the region of low reverse biases, the dependence $I = f(V)$ is sublinear, which is characteristic of currents controlled by generation–recombination processes in the SCR. For voltages $|V| \gtrsim 0.4$–0.5 V, a slow increase in the current changes to a steeper superlinear rise, which is most probably associated with carrier tunneling through the barrier in GaSe. Such an assumption is quite plausible if we take into account that the potential barrier in GaSe takes a parabolic shape under the action of image forces. For a barrier

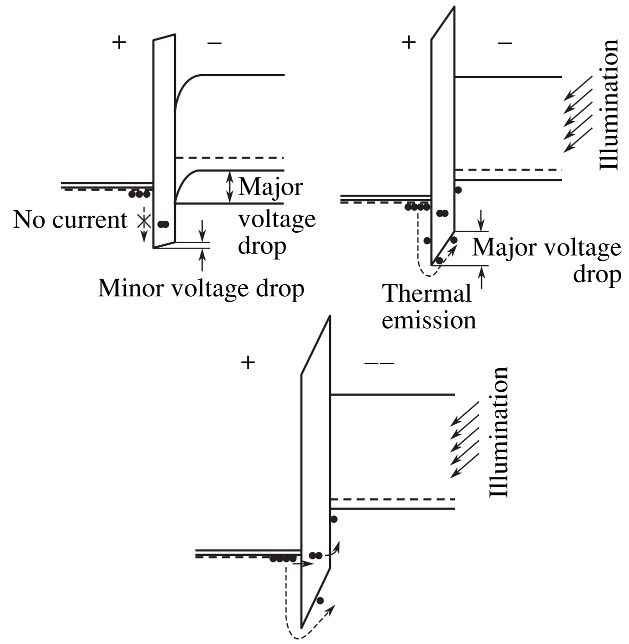

Fig. 4. Energy-band diagram of a reverse-biased p^+-Bi_2Te_3–p-GaSe heterostructure.

with a parabolic shape, the tunnel current is described by the expression [16]

$$I = A\frac{e^3\sqrt{2m_n}V(\varphi_0 - eV)^{1/2}N_a}{2\pi^2\hbar^2\varphi_0^{1/2}(2\varepsilon\varepsilon_0\varphi_0)^{1/2}} \times \exp\left(-\frac{4}{3}\frac{\sqrt{m_n\varepsilon\varepsilon_0}}{\hbar N_a^{1/2}}\frac{\varphi_0^{3/2}}{\sqrt{(\varphi_0 - eV)}}\right), \quad (4)$$

where ε and ε_0 are the dielectric constants for the semiconductor and free space, respectively. According to expression (4), the I–V characteristic for carrier tunneling through the barrier should be a straight line in coordinates

$$\ln\left[\frac{I}{V(\varphi_0 - eV)^{1/2}}\right] = f\left[\frac{1}{(\varphi_0 - eV)^{1/2}}\right],$$

which is in fact observed experimentally (Fig. 5, dependence *1*).

The situation changes for a heterostructure exposed to light. Illumination affects the barrier located in GaSe and leads to flattening of the bands in GaSe. The situation becomes similar to a forward-biased heterostructure, with the only difference in that the holes now move in the reverse direction (from Bi_2Te_3 into GaSe). The larger part of the voltage applied to the structure now drops across the insulator, and the overbarrier current of the thermionic emission becomes the dominant mechanism of charge transport through the insulator (Fig. 4). The NDC occurs when the valence band of Bi_2Te_3 approaches the slow states localized in the insu-

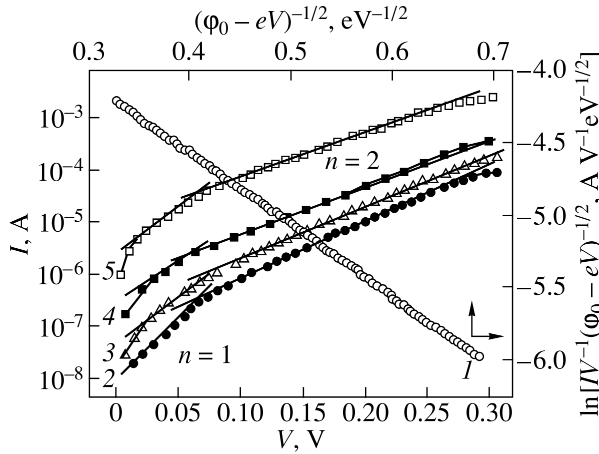

Fig. 5. Comparison of expression (4) with the experimental voltage dependence of the reverse current for a p^+-Bi_2Te_3–p-GaSb heterostructure at room temperature (curve *1*), and forward portions of current–voltage characteristics at temperatures T = (*2*) 238, (*3*) 263, (*4*) 293, and (*5*) 323 K.

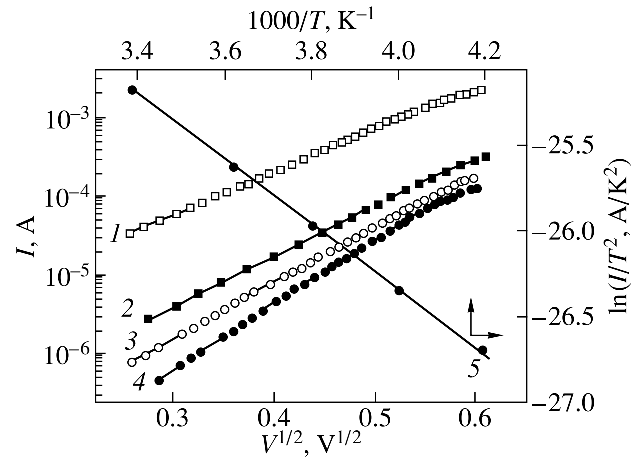

Fig. 6. Forward portions of current–voltage characteristics for a p^+-Bi_2Te_3–p-GaSe heterostructure as an $\ln I$ vs. $V^{1/2}$ plot at temperatures T = (*1*) 323, (*2*) 295, (*3*) 263, and (*4*) 238 K, and the temperature dependence of the $\ln(I/T^2)$ quantity (curve *5*).

lator. The current reaches saturation and then starts to decrease with increasing applied potential owing to positive feedback (Fig. 4). An increase in the current with further increase in the reverse bias is associated both with the descent of the Bi_2Te_3 valence band below slow states and with tunnel breakdown of the heterostructure.

It should also be noted that the charge transport above the barrier formed by the insulator in the metal–insulator–metal system implies that the insulator conductivity is equal to zero and predetermines the value of the ideality coefficient for the I–V characteristic $n = 1$:

$$I \propto \exp\left(\frac{eV}{nkT}\right).$$

As the applied voltage increased, the coefficient took the value $n = 2$ over the entire temperature range under investigation (Fig. 5, dependences *2*–*5*). At the same time, the I–V characteristic of the structure for voltages $V \gtrsim 3kT$ is described by the expression $I \propto \exp V^{1/2}$ (Fig. 6, dependences *1*–*4*). This is typical of both Schottky emission [16],

$$I = A^*T^2\exp\left[-\frac{\varphi_B - \sqrt{eV/4\pi\varepsilon_i d}}{kT}\right], \tag{5}$$

and Frenkel-type ionization [16],

$$I \propto V\exp\left[-\frac{\varphi_B^* - \sqrt{eV/\pi\varepsilon_i d}}{kT}\right], \tag{6}$$

where d is the insulator thickness, ε_i is the dielectric constant of the insulator, and φ_B^* denotes the trap depth rather than the barrier height. The linearity of the $1/T$ dependence of $\ln(1/T^2)$ (Fig. 6, dependence *5*) suggests that Schottky emission is favorable. This is also confirmed by the fact that the barrier height for the semiconductor–insulator–semiconductor contact, which was determined from the relationship [16]

$$\ln I = \ln(A^*T^2) - 0.43e\varphi_B/kT, \tag{7}$$

equals $\varphi_B \approx 1.2$ eV at $T = 295$ K. This is in good agreement with the current cutoff voltage and explains the difference between this quantity and the contact potential difference determined from the C–V characteristic. However, the thickness of the insulator layer, which was found from the relationship [15]

$$\tan\beta = \frac{0.43}{kT}\sqrt{\frac{e^3}{4\pi d\varepsilon_i}} \tag{8}$$

(β is the slope of the I–V characteristic in the coordinates $\ln I = f(V^{1/2})$), equals ≈2 nm, which somewhat exceeds the value expected (0.6–0.8 nm, according to [20]). Such a discrepancy can be explained by a number of reasons. First, when analyzing the experimental results, we made allowance for the presence of native oxide at the GaSe surface only. However, a similar oxide layer can also be formed at the Bi_2Te_3 surface. Allowance should also be made for the air gap between two contacting semiconductors. In this case, formally dividing the quantity obtained from relationship (8) by three, we obtain good agreement with the results reported by Bakumenko *et al.* [20]. Second, recent investigations of native GaSe oxide [4] indicate that it can also consist of GaO and Ga_2O rather than Ga_2O_3 only. The dielectric constants for these oxides differ from this quantity for Ga_2O_3. Allowance made for this circumstance can affect the results obtained from formula (8). Third, charge transport through the insulator can also be controlled by currents limited by the space charge rather than by the Schottky emission only. This

is confirmed by the dependence of the current on the forward voltage, which is close to quadratic.

4. CONCLUSIONS

Thus, the suggested model explains well the reasons for the emergence of negative differential conductivity (NDC) in a forward-biased p^+-Bi_2Te_3–p-GaSe isotype heterostructure and in a reverse-biased structure, which were also illuminated. In addition, it is possible to make the following conclusions.

(i) With the use of Dy-doped GaSe substrates, structures with series resistance typical of industrial Si diodes can be fabricated.

(ii) For the interpretation of experimental results and the development GaSe-based semiconductor devices, allowance should be made for the influence of the interface.

(iii) The electrical properties of the forward-biased heterojunction and of the reverse-biased heterojunction under illumination are determined by the interface properties and imply the existence of an ultrathin oxide layer at the surface of contacting semiconductors.

(iv) Rectification in the system under investigation is attained due to a barrier at the semiconductor–insulator interface. This explains the distinction between the contact potential difference for GaSe and the cutoff voltage of the current–voltage characteristic.

(v) The principle mechanism determining charge transport in a forward-biased p^+-Bi_2Te_3–p-GaSe heterostructure is the Schottky emission, which does not exclude the simultaneous possibility of the flow of currents limited by the space charge.

(vi) The electrical properties of the structure under investigation without illumination are determined by the properties of the potential barrier located in GaSe.

(vii) The emergence of NDC in the p^+-Bi_2Te_3–p-GaP structure is associated with the localization of deep traps in the insulator layer.

ACKNOWLEDGMENTS

We thank V.I. Litvinov for his interest and helpful participation in discussions.

REFERENCES

1. S. I. Drapak, V. N. Katerinchuk, Z. D. Kovalyuk, and V. A. Manasson, Fiz. Élektron. **41**, 92 (1990).
2. S. I. Drapak and Z. D. Kovalyuk, Pis'ma Zh. Tekh. Fiz. **27** (18), 1 (2001) [Tech. Phys. Lett. **27**, 755 (2001)].
3. V. A. Manasson, Z. D. Kovalyuk, S. I. Drapak, and V. N. Katerinchuk, Electron. Lett. **26**, 664 (1990).
4. V. P. Savchun and V. B. Kutsai, Thin Solid Films **361–362**, 361 (2000).
5. R. H. Williams and A. J. McAvej, J. Vac. Sci. Technol. **2**, 867 (1972).
6. F. Mayer, E. E. de Kluizerenaar, and D. den Engelsen, IOSA **63**, 529 (1979).
7. L. B. Anan'ina, V. L. Bakumenko, and V. F. Chishko, Fiz. Tekh. Poluprovodn. (Leningrad) **10**, 2373 (1976) [Sov. Phys. Semicond. **10**, 1405 (1976)].
8. S. I. Drapak, V. N. Katerinchuk, Z. D. Kovalyuk, and V. A. Manasson, Phys. Status Solidi A **115**, K35 (1989).
9. R. R. Daniels, G. Margaritondo, C. Quaresima, *et al.*, J. Vac. Sci. Technol. **3**, 979 (1985).
10. V. N. Katerinchuk and M. Z. Kovalyuk, Pis'ma Zh. Tekh. Fiz. **25** (2), 29 (1999) [Tech. Phys. Lett. **25**, 54 (1999)].
11. V. L. Bakumenko and V. F. Chishko, Fiz. Tekh. Poluprovodn. (Leningrad) **11**, 2000 (1977) [Sov. Phys. Semicond. **11**, 1171 (1977)].
12. E. H. Rhoderick, *Metal–Semiconductor Contacts* (Clarendon Press, Oxford, 1978; Radio i Svyaz', Moscow, 1982).
13. Yu. A. Gol'dberg, O. V. Ivanova, T. V. L'vova, and B. V. Tsarenkov, Fiz. Tekh. Poluprovodn. (Leningrad) **18**, 1472 (1984) [Sov. Phys. Semicond. **18**, 919 (1984)].
14. É. I. Adirovich, P. M. Karageorgiĭ-Alkalaev, and A. Yu. Leĭderman, *Double-Injection Currents in Semiconductors* (Sovetskoe Radio, Moscow, 1978).
15. P. T. Oreshkin, *Physics of Semiconductors and Insulators* (Vysshaya Shkola, Moscow, 1977).
16. S. Sze, *Physics of Semiconductor Devices* (Wiley, New York, 1981; Mir, Moscow, 1984), Vol. 1.
17. V. V. Pasynkov and L. K. Chirkin, *Semiconductor Devices* (Vysshaya Shkola, Moscow, 1987).
18. C. Tatsuyama, S. Ichimura, and H. Iwakuro, Jpn. J. Appl. Phys. **21**, L25 (1982).
19. M. V. Kurik, Z. D. Kovalyuk, and V. N. Katerinchuk, Fiz. Tekh. Poluprovodn. (Leningrad) **17**, 1883 (1983) [Sov. Phys. Semicond. **17**, 1204 (1983)].
20. V. L. Bakumenko, Z. D. Kovalyuk, E. A. Tishin, and V. F. Chishko, Fiz. Élektron. **19**, 123 (1979).
21. S. I. Drapak, V. N. Katerinchuk, Z. D. Kovalyuk, and V. A. Manasson, *Photoelectric Properties of the In_2O_2–Ga_2O_3–GaSe Heterostructure with Tunneling-Thin Insulator Layer* (Inst. Probl. Materialoved., Kiev, 1989).
22. T. Hariu, S. Sasaki, H. Adachi, and H. Shibata, Jpn. J. Appl. Phys. **16**, 841 (1977).
23. H. Landolt and R. Börnstein, *Numerical Data and Functional Relatioships in Science and Technology*, New Ser. Group III: *Crystal and Solid State Physics*, Ed. by O. Madelung (Springer, Berlin, 1983), Vol. 17.
24. *Physicochemical Properties of Semiconductors*, Ed. by A. V. Novoselova, V. B. Lazarev, Z. S. Medvedeva, N. P. Luzhina, and A. A. Levin (Nauka, Moscow, 1979).
25. V. L. Bonch-Bruevich and S. G. Kalashnikov, *Physics of Semiconductors* (Nauka, Moscow, 1965).
26. R. A. Smith, *Semiconductors* (Cambridge Univ. Press, Cambridge, 1959; Inostrannaya Literatura, Moscow, 1962).

Translated by N. Korovin

Semiconductors, Vol. 37, No. 2, 2003, pp. 178–182. Translated from Fizika i Tekhnika Poluprovodnikov, Vol. 37, No. 2, 2003, pp. 187–191.
Original Russian Text Copyright © 2003 by Vaĭpolin, Nikolaev, V. Rud', Yu. Rud', Terukov, Fernelius.

Fabrication and Properties of Photosensitive Structures Based on $ZnIn_2S_4$ Single Crystals

A. A. Vaĭpolin*, Yu. A. Nikolaev*, V. Yu. Rud'^, Yu. V. Rud'*, E. I. Terukov*, and N. Fernelius*****

** Ioffe Physicotechnical Institute, Russian Academy of Sciences, St. Petersburg, 194021 Russia*
*** St. Petersburg State Polytechnical University, St. Petersburg, 195251 Russia*
^e-mail: rudvas@spbstu.ru
**** Air Force Wright Lab., Wright Patterson AFB, OH, USA*

Submitted June 10, 2002; accepted for publication June 17, 2002

Abstract—Photosensitive structures based on single crystals of the $ZnIn_2S_4$ ternary compound were fabricated and studied for the first time. The optoelectronic properties of this compound and corresponding structures were analyzed using the results of measurements of the optical-absorption spectra of $ZnIn_2S_4$ crystals, steady-state current–voltage characteristics, and photosensitivity of the structures at $T = 300$ K. It is concluded that surface-barrier structures and heterojunctions based on $ZnIn_2S_4$ can be used as wide-band photodetectors of natural optical radiation. © *2003 MAIK "Nauka/Interperiodica".*

Effects to make the atomic composition of diamond-like materials more complex is one of the main lines of development in modern semiconductor science and technology; as a result of research in this field, the range of semiconducting materials is widening and new physical phenomena are being discovered [1, 2]. Numerous $A^{II}B_2^{III}C_4^{IV}$ ternary compounds belong to promising multicomponent semiconductors; even early studies of these compounds have shown that some of them can be applied to optoelectronics [3–6]. The conventional methods for growing these materials make it possible to obtain only crystals with *n*-type electrical conductivity [3]. Therefore, in order to realize the potential of $A^{II}B_2^{III}C_4^{IV}$ compounds in optoelectronics, it is topical, at present, to develop the foundations for the formation of efficient energy barriers in corresponding structures. In this paper, we report data related to the fabrication and investigation of photosensitive structures based on homogeneous $ZnIn_2S_4$ (ZIS) crystals.

1. Photosensitive structures were fabricated using ZIS single crystals grown by gas-transport reactions. This method made it possible to obtain plane-parallel plates with dimensions of $\approx 15 \times 15 \times 0.1$ mm^3; in transmitted white light, these plates had a uniform light-orange color. X-ray diffraction analysis of ZIS single crystals has shown that the method employed makes it possible to obtain crystals which belong to the $R3m$ point group with a (D_{3d}^5) symmetry and have unit-cell parameters $a_H = 3.8697 \pm 0.0006$ Å and $c_H = 37.0145 \pm 0.0057$ Å ($a_R = 12.539$ Å, $\alpha_R = 17°45'$) at $T = 300$ K. These parameters are consistent with relevant published data [3, 7]. The level of the structural quality of the crystals obtained made it possible to radically improve the accuracy in determining the parameters a_H and c_H in comparison with published data [7]. Undoped ZIS crystals have "dark" resistivity $\rho \cong 10^8$–10^9 Ω cm at $T = 300$ K.

2. Studies of contact phenomena in ZIS crystals with a fairly high resistivity have made it possible to observe the phenomenon of rectification in surface-barrier structures formed by the vacuum deposition of semitransparent layers of pure In onto the freshly cleaved surface of ZIS plates with average dimensions of $10 \times 10 \times 0.1$ mm^3. In Fig. 1, we show a typical steady-state current–voltage (I–V) characteristic of one of the In/ZIS structures at $T = 300$ K. A negative external-bias voltage applied to the barrier contact corresponded to the conducting state for all obtained structures. The forward portion of I–V characteristics in the structures subjected to bias voltages $U > 5$ V are typically described by the relation

$$I = \frac{U - U_0}{R_0},$$

where the cutoff voltage $U_0 \approx 5$ V and the residual resistance $R_0 \cong 10^7$–10^8 Ω at $T = 300$ K. The reverse current of these structures without illumination is described by the power law $I_r \propto U_r^{0.4}$, which can be related to an imperfect periphery of the structures. When the structures are exposed to the integrated light of an incandescent lamp (≈100 W), the forward and reverse currents increase by a factor of $\approx 10^3$, whereas the shape of the I–V characteristics does not change much.

The photovoltaic effect was observed for the first time in In/ZIS surface-barrier structures; this effect was typically dominant when the structures were illuminated from the barrier-contact side. The photovoltage sign was independent of both the incident-photon energy and the location of an optical probe at the surface of the structures. The photovoltage was invariably positive at the substrate crystal, which is consistent with the rectification direction in the In/ZIS structures under consideration. When the barrier side of the structures was exposed to the radiation of a GaN light-emitting diode (≈10 mW), the photovoltage in the best structures was as high as 20 mV and was much higher than in the case of illumination with an incandescent lamp of higher power. As can be seen from the table, the highest voltage photosensitivity for the structures under consideration is $S_u^m \cong 10$ V/W under illumination from the barrier-contact side. Typical spectral dependences of the relative quantum efficiency of photoconversion η for several In/ZIS structures are shown in Fig. 2; the parameters of one of the best structures are listed in the table. If these structures are illuminated from the contact-barrier side (Fig. 2, curves *1*, *3*, *4*), photosensitivity is observed in a wide spectral range, from 0.8 to 3.8 eV. If the structures are illuminated from the side of the crystalline substrate ($d = 0.1$–0.3 mm; see Fig. 2, curve *2*), a sharp falloff is observed at short wavelengths ($\hbar\omega >$ 2.5 eV) in the η spectrum and is related to a rapid increase in the absorption of radiation in the crystalline substrate; the location of this falloff on the photon-energy scale is governed by the substrate thickness d. As d increases, the short-wavelength falloff of η shifts to longer wavelengths owing to an increase in the distance between the layer with photogenerated charge carriers and the active region of the surface-barrier structure. The long-wavelength portion of spectral dependences (see Fig. 2, curves *1*–*4*) is virtually independent of the side from which the structure is illuminated; this observation indicates that radiation is absorbed in the bulk of the structure. The spectral dependences are linearized in the coordinates $(\eta\hbar\omega)^{1/2}$ (Fig. 3); notably, two cutoff photon energies ($\varphi_1 \cong 0.8$–1.1 eV and $\varphi_2 \cong 1.5$–1.8 eV) are observed, as a rule, when the dependences $(\eta\hbar\omega)^{1/2}(\hbar\omega)$ are extropolated to the abscissa. Observation of the Fowler law in the photosensitivity spectra of the surface-barrier In/ZIS structures under consideration is related to photoemission of charge carriers from the metal into the semiconductor; therefore, the cutoff energies φ_1 and φ_2 can be identified with potential-barrier heights. Apparently, the fact that the values of φ_1 and φ_2 vary from structure to structure within the aforementioned ranges may be caused by the possible influence of the In/ZIS surface state and conditions of the structures' fabrication on the parameters of the resulting barriers. At the same time, the presence of two barriers differing in height may suggest that special features of emission of photogenerated charge carriers are caused by the complex energy spectrum of the crystals under consideration. As the photon energy increases, the emission is controlled, at first, by the lower level in the band gap of ZIS crystals and then by the upper level.

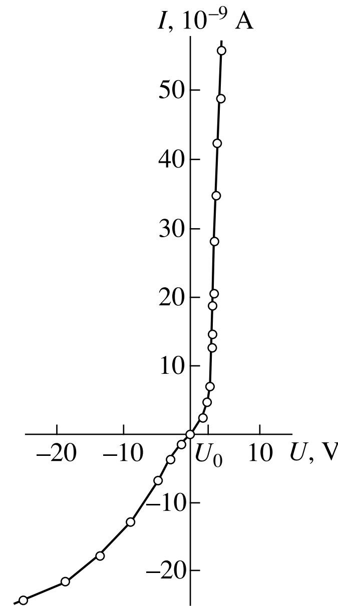

Fig. 1. The steady-state current–voltage characteristic of an In/ZIS surface-barrier structure at $T = 300$ K. Positive polarity of external bias applied to the ZIS crystal corresponds to the conducting state of the structure.

The spectral dependences of the optical-absorption coefficient α for ZIS crystals used for fabricating photosensitive structures are shown in Fig. 2 (curves *5*, *6*). It can be seen that an exponential increase in α sets in at $\hbar\omega > 2.5$ eV, which is consistent with the energy position of the short-wavelength falloff in the spectra of In/ZIS structures (Fig. 2, curves *2*–*4*). This observation makes it possible to unambiguously relate the falloff of η at $\hbar\omega > 2.5$ eV to an increase in the optical absorption of ZIS crystals as a consequence of the onset of interband absorption.

The ZIS crystals are found to be similar to pseudo-direct-gap $A^{II}B^{IV}C_2^V$ compounds by the value of S

Photoelectric parameters of structures based on $ZnIn_2S_4$ crystals ($T = 300$ K)

Type of the structure	$\hbar\omega^m$, eV	S, eV^{-1}	δ, eV	S_u^m, V/W
In/ZIS	3.05–3.28	11	0.85	10
n-InSe/ZIS	2.3	20	0.50	1
p-GaSe/ZIS	2.4	10	0.43	50

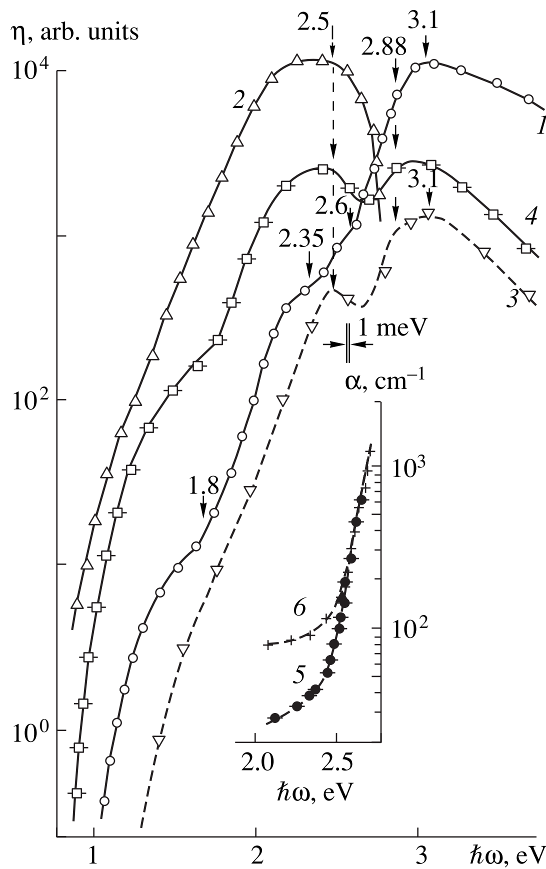

Fig. 2. Spectral dependences of (curves *1–4*) the quantum efficiency of photoconversion η in surface-barrier In/ZIS structures and (the inset, curves *5*, *6*) the optical-absorption coefficient α in ZIS crystals at T = 300 K. The structures were illuminated from (curves *1*, *3*, *4*) the barrier side and (curve *2*) the ZIS crystal side. Curves *1* and *2* correspond to sample 5; curve *3*, to sample 7; curve *4*, to sample 8; and curves *5* and *6*, to sample 10. The plate thickness d = (*1–4*) 0.15, (*5*) 0.155, and (*6*) 0.045 mm. Curves *1–4* are shifted along the vertical axis.

[8, 9]. Extrapolation of the portion of the sharp increase in the spectrum of α for ZIS crystals makes it possible to estimate the energy of band-to-band transitions at $E' \cong$ 2.6 eV. The similarity of ZIS crystals to $A^{II}B^{IV}C_2^V$ compounds also manifested itself in the spectral dependences of η. This similarity consists in the fact that a decrease in photosensitivity is observed in the spectra of η in the vicinity of $\hbar\omega \cong 2.5$ eV both for In/ZIS structures illuminated from the barrier-contact side and for a Cu/$ZnSiP_2$ structure [10]; this decrease in photosensitivity can be related to the increasing role of charge-carrier surface recombination at $\hbar\omega > 2.5$ eV (Fig. 2, curves *3*, *4*). In some of the structures, an increase in photosensitivity (with inflection in the region of E' and a subsequent exponential increase in η) is observed (Fig. 2, curve *1*) instead of the short-wavelength falloff of η; apparently, this anomalous behavior is indicative of an increase in the energy-barrier strength, which, in turn, ensures that surface recombination is suppressed.

An exponential increase in the photosensitivity of the structures at $\hbar\omega > 2.7$ eV and an inflection at $\hbar\omega \cong$ 2.88 eV (Fig. 2, curves *1*, *2*, *4*) can be related to the onset of band-to-band transitions in ZIS. It is worth noting that the photon energy $\hbar\omega = 2.88$ eV corresponding to the inflection in the η spectra coincides with the ZIS band gap E_1 determined from optical-absorption spectra [3]. An increase in the photosensitivity of In/ZIS structures at $\hbar\omega > 2.88$ eV with the subsequent formation of an absolute maximum at E_2 = 3.1 eV may be indicative of a complex energy-band structure of ZIS, which has not been adequately studied [11–13].

It should be specially emphasized that the ratio between photosensitivity at $\hbar\omega \cong 3.1$ eV and photosensitivity at $\hbar\omega \cong 2.5$ eV for the investigated In/ZIS structures varies from 2 to 0.8, which can be caused by changes in the concentrations and types of structural defects. This circumstance suggests that the photosensitivity spectra of In/ZIS structures can be used to analyze the growth conditions of ZIS crystals.

3. In addition to surface-barrier ZIS-based structures, we also explored the possibility of obtaining a heterojunction in ZIS crystals. We used the method of depositing semiconductors onto an optical contact [14]. This is related to the high structural quality of (0001) planes, which can be easily obtained by splitting the ZIS plates. We used InSe ($n = 2 \times 10^{17}$ cm^{-3}) and GaSe ($p = 3 \times 10^{16}$ cm^{-3}) crystals as the second components for the heterojunction. These crystals can be easily split owing to their layered structure; they then form mirror planes with a natural cleavage. Using a simple superposition of ZIS plates onto *n*-InSe and *p*-GaSe wafers, we obtained heterojunction structures which can be illuminated both from the wide-gap ZIS side and from the side of the InSe and GaSe wafers.

Steady-state *I–V* characteristics indicate that the *n*-InSe/ZIS and *p*-GaSe heterojunctions reproducibly exhibit a moderate rectification ratio (the ratio between the forward and reverse currents at U = 20 V equals about 2 to 4 for different heterojunctions); notably, the conducting state in these heterojunctions corresponds to a negative external bias voltage applied to InSe in *n*-InSe/ZIS structures and to a positive bias voltage applied to GaSe in *p*-GaSe/ZiS structures. The photosensitivity of these heterojunctions prevails when they are illuminated from the ZIS side, whereas the sign of the photovoltage is independent of the side from which the structure is illuminated and is coincident with the direction of rectification. The residual resistance of both heterojunctions is close to that measured in surface-barrier structures.

The spectral dependences of the relative quantum efficiency of photoconversion in typical heterojunctions are shown in Fig. 4. Some parameters of typical heterojunctions are listed in the table.

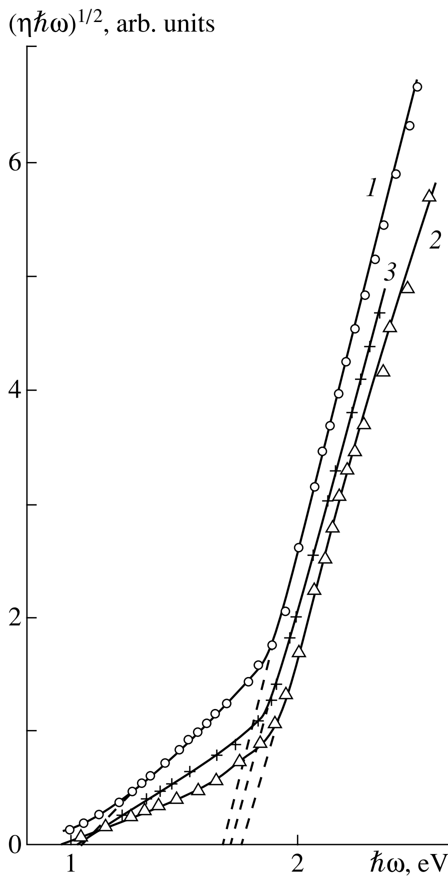

Fig. 3. Dependences of $(\eta\hbar\omega)^{1/2}$ on the photon energy $\hbar\omega$ for In/ZIS structures at T = 300 K. Structures were illuminated from the barrier side. Curve *1* corresponds to sample 5; curve *2*, to sample 9; and curve *3*, to sample 17.

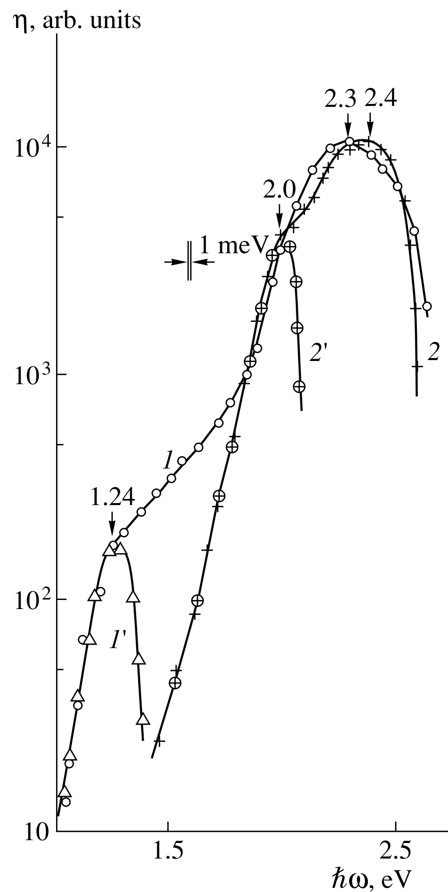

Fig. 4. Spectral dependences of relative quantum efficiency of photoconversion η in the (*1*, *1*') *n*-InSe/ZIS and (*2*, *2*') *p*-GaSe/ZIS heterojunctions at T = 300 K. The structures were illuminated from the (curves *1*, *2*) ZIS side, (curve *1*') InSe side, and (curve *2*') GaSe side.

The main special features of spectra of η for newly fabricated heterojunctions are the following. The photosensitivity of each of the heterojunctions is observed in the spectral range which is limited on the long-wavelength side by interband absorption in the narrow-gap portion of the heterojunction. The long-wavelength exponential falloff of η was used to determine the characteristic slope $S = \delta(\ln\eta)/\delta(\hbar\omega)$. Inflections in photosensitivity spectra recorded with the heterojunction being illuminated from the ZIS side (Fig. 4, curves *1*, *2*) and the short-wavelength falloff of η in the situation where the heterojunction is illuminated from the side of III–VI wafers (Fig. 4, curves *1*', *2*') correspond to interband absorption in the InSe and GaSe crystals, respectively [7]. The spectral range of photosensitivity for heterojunctions narrows as the band gap of the III–VI crystal widens; however, the positions of photosensitivity maxima $\hbar\omega^m$ in these heterojunctions are closely spaced, since these positions are controlled by absorption in the same ZIS crystal. At the same time, certain differences in the spectral position of the short-wavelength cutoff are caused by variations in the thickness of the ZIS plates used in the heterojunction. We draw attention to the observation that the width of the photosensitivity band at its half-height δ is virtually the same for heterojunctions with different III–VI components (see table). This circumstance is caused by the fact that the highest photosensitivity is observed in the region of a steep increase in absorption in ZIS in both heterojunctions (Fig. 2, curves *5*, *6*). It is also noteworthy that the contribution of optical absorption in the InSe narrow-gap component of the InSe/ZIS heterojunction to the photosensitivity (Fig. 4, curve *1*) is smaller than that in GaSe of the GaSe/ZIS heterojunction (Fig. 4, curve *2*). These distinctions are caused by the higher doping level of InSe compared to that of GaSe; as a result, the active region in the GaSe/ZIS heterojunction is largely shifted to ZIS, in contrast to what occurs in the GaSe/ZIS heterojunction.

Thus, single crystals of the $ZnIn_2S_4$ ternary compound can be employed in the development of photosensitive structures designed to operate in the spectral

range of 1–3.5 eV. The results of studying the photosensitivity spectra of corresponding surface-barrier structures and heterojunctions can be used in monitoring the quality of ZIS single crystals.

REFERENCES

1. N. A. Goryunova, *Compound Diamond-like Semiconductors* (Sovetskoe Radio, Moscow, 1968).
2. V. D. Prochukhan and Yu. V. Rud', Fiz. Tekh. Poluprovodn. (Leningrad) **12**, 209 (1978) [Sov. Phys. Semicond. **12**, 121 (1978)].
3. A. N. Georgobiani, S. I. Radautsan, and N. M. Tiginyanu, Fiz. Tekh. Poluprovodn. (Leningrad) **19**, 193 (1985) [Sov. Phys. Semicond. **19**, 121 (1985)].
4. A. A. Lebedev, P. N. Metlinskiĭ, Yu. V. Rud', and V. G. Tyrzyu, Fiz. Tekh. Poluprovodn. (Leningrad) **11**, 1038 (1977) [Sov. Phys. Semicond. **11**, 615 (1977)].
5. A. V. Lunev, P. N. Metlinskiĭ, Yu. V. Rud', *et al.*, Zh. Prikl. Spektrosk. **43**, 312 (1985).
6. R. N. Bekimbetov, Yu. V. Rud', and M. A. Tairov, Fiz. Tekh. Poluprovodn. (Leningrad) **21**, 1051 (1987) [Sov. Phys. Semicond. **21**, 642 (1987)].
7. *Physicochemical Properties of Semiconductors: A Reference Book* (Nauka, Moscow, 1978).
8. Yu. A. Valov, A. A. Lebedev, K. Ovezov, *et al.*, Pis'ma Zh. Tekh. Fiz. **2** (22), 1042 (1976) [Sov. Tech. Phys. Lett. **2**, 410 (1976)].
9. A. Shileika, Surf. Sci. **37**, 730 (1973).
10. A. A. Lebedev, K. Ovezov, V. D. Prochukhan, and Yu. V. Rud', Pis'ma Zh. Tekh. Fiz. **1** (4), 195 (1975) [Sov. Tech. Phys. Lett. **1**, 93 (1975)].
11. V. L. Panyutin, B. É. Ponedel'nikov, A. É. Rozenson, and V. I. Chizhikov, Fiz. Tekh. Poluprovodn. (Leningrad) **14**, 1000 (1981) [Sov. Phys. Semicond. **14**, 594 (1981)].
12. V. I. Chizhikov, V. L. Panyutin, B. E. Ponedelnikov, and A. F. Rosenson, J. Phys. (Paris) **42**, 1003 (1981).
13. V. I. Chizhikov, Doctoral Dissertation (Kuban State Univ., Krasnodar, 2001).
14. I. V. Bodnar, V. Yu. Rud', and Yu. V. Rud', Cryst. Res. Technol. **31**, 261 (1996).

Translated by A. Spitsyn

Semiconductors, Vol. 37, No. 2, 2003, pp. 183–186. Translated from Fizika i Tekhnika Poluprovodnikov, Vol. 37, No. 2, 2003, pp. 192–195.
Original Russian Text Copyright © 2003 by Slobodchikov, Salikhov, Samorukov.

SEMICONDUCTOR STRUCTURES, INTERFACES, AND SURFACES

Charge Transport in Fe–*p*-InP Diode Structures

S. V. Slobodchikov, Kh. M. Salikhov, and B. E. Samorukov

Ioffe Physicotechnical Institute, Russian Academy of Sciences, Politekhnicheskaya ul. 26, St. Petersburg, 194021 Russia

Submitted June 19, 2002; accepted for publication June 27, 2002

Abstract—The mechanism of charge transport in Fe–*p*-InP diode structures and its dependences on illumination and magnetic field were investigated. It is shown that a double injection in a drift approximation into a high-resistivity π-layer is the main mechanism of charge transport. Phenomena of the suppression of a forward current with light (negative photoresponse) and a sharp increase in the differential resistance in a magnetic field are observed and discussed. © *2003 MAIK "Nauka/Interperiodica".*

It is known that doping of *n*-InP with Fe is the main method for obtaining semi-insulating crystals which are widely used in fabricating transistor structures, lasers, photodiodes, and photodetectors. Numerous investigations of the electrical and photoelectric characteristics of bulk InP:Fe crystals were carried out, and semi-insulating layers obtained by Fe implantation were investigated [1].

Due to investigations of Au–*n*-InP:Fe diode structures, the process of enhancement of the photocurrent, which is associated with the formation of a static domain, is revealed [2]. However, in the course of investigations of diode structures formed by a metal and InP, the structure with an Fe barrier contact was not investigated. In this paper, certain results of the investigation of the electrical and photoelectric characteristics of the Fe–*p*-InP structure are reported.

The samples were fabricated using Fe deposition by thermal evaporation. For the fabrication of the structures, Czochralski-grown bulk *p*-InP crystals with a hole concentration $p_0 = 3 \times 10^{16}$ cm^{-3} were used. It turned out that the Fe deposition on the *n*-InP crystals did not give rise to a barrier contact. Armco iron with a purity no lower than 99.9 % (attained by purification by melting in an electromagnetic field) was used as the starting Fe material. The substrate temperature was ≈200–230°C. Deposition was carried out in vacuum at no lower than $(3–5) \times 10^{-6}$ Torr. The Fe layer thickness was ≈0.1 μm. Nonrectifying contacts were formed by deposition of the Ag/Zn alloy.

The current–voltage (*I*–*V*) characteristics and the influence of illumination and a magnetic field on them were investigated.

Figure 1 shows the *I*–*V* characteristics (forward portion) which were recorded for a typical sample of the Fe–*p*-InP diode structure at $T = 300$ and 100 K. A characteristic feature of the curves, which are plotted on a log–log scale, is the existence of two parts. For low bias voltages (curve *1*, $T = 300$ K), an almost ohmic dependence with a certain spread from sample to sample is observed. For higher bias voltages, a power-law dependence with the exponent $n = 3.3–3.4$ is observed, i.e.,

$$I = a_1 V + a_2 V^n. \quad (1)$$

A decrease in temperature changes the character of the dependence. For the first portion, $I \propto V^{2.1}$, whereas for the second portion, $I \propto V^{5–5.5}$. Such a dependence may indicate that the mechanism of double injection in the drift approximation is predominate [3, 4]. According to the theory, the ohmic portion in the $I = f(V)$ curve should be succeeded by the following portion in the semiconductor mode (for the *p*-active region):

$$J \approx q\tau\mu_n\mu_p(p_0 - n_0)\frac{V^2}{d^3}. \quad (2)$$

The insulator mode is characterized by the current

$$J \approx q\tau\mu_n\mu_p\frac{V^3}{d^5}. \quad (3)$$

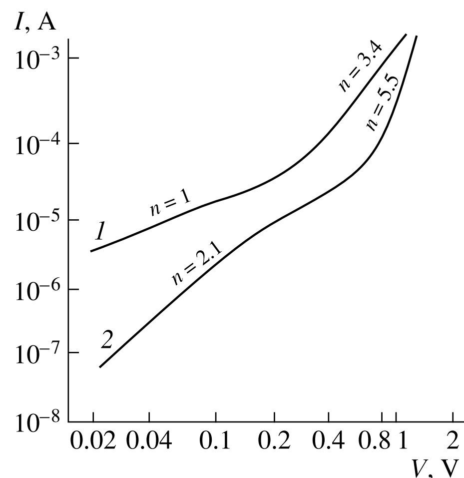

Fig. 1. Current–voltage characteristics (forward portions) of the Fe–*p*-InP structure at temperatures T = (*1*) 300 and (*2*) 100 K.

1063-7826/03/3702-0183$24.00 © 2003 MAIK "Nauka/Interperiodica"

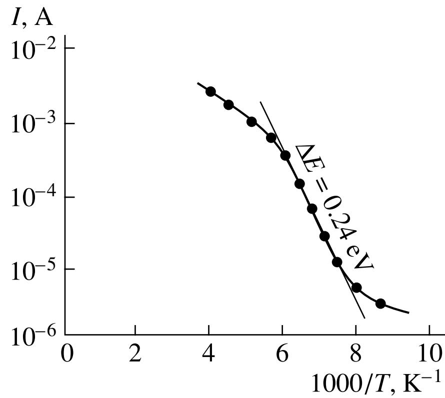

Fig. 2. Temperature dependence of the forward current for the Fe–*p*-InP structure.

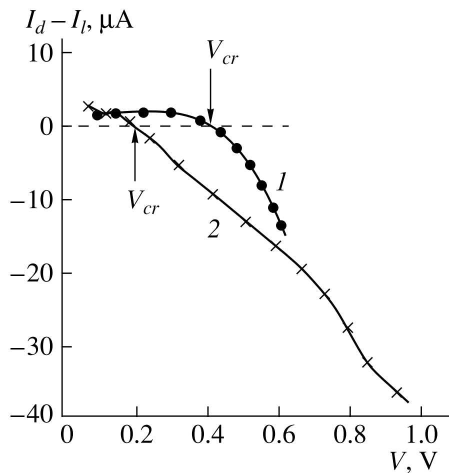

Fig. 3. Suppression of the forward current ($I_d - I_l$) as a function of the bias. Temperature T = (*1*) 300 and (*2*) 100 K.

In expressions (2) and (3), p_0 and n_0 are the equilibrium carrier concentrations, q is the elementary charge, d is the thickness of the active (high-resistivity) region, and the other symbols take their conventional meanings. Consequently, the above-mentioned active region, which was formed in the course of Fe deposition, should exist in the Fe–*p*-InP diode structure—the so-called π-layer. The formation of this layer can be a consequence of certain factors. It seems likely that Fe ions diffuse into the bulk upon heating and act as a compensating impurity. Further, the ability of Zn atoms to interact with the defects in the InP lattice with the formation of active centers, including compensating ones, could play a noticeable role [5]. It is possible that certain types of the Fe–Zn complex are formed in this case.

It should be noted that large n values, which exceed 2 and 3 in expressions (2) and (3), respectively, are associated with the increasing role of the diffusion component from injecting contacts [4, 6]. In the case under consideration, this phenomenon occurs at the Fe–π-layer interface and at the π-layer–*p*-InP interface. As the applied voltage increases, the boundaries of diffusion regions shift closer to each other, thus decreasing the effective thickness of the drift region $d_{ef} = d - d_{dif1} - d_{dif2}$. This affects the analytical form of dependences (2) and (3), in which d_{ef} should now be substituted for d, whereas the exponents increase to $n > 2$ and to $n > 3$. In this case, in the semiconductor mode, $I \propto V^{2/[1 - m(L_a/d)]}$, where m is about 2 or 3, and the ambipolar diffusion length [3] is given by

$$L_a = \left[\frac{2kT\mu_n\tau}{q}(b+1)\right]^{1/2}. \quad (4)$$

For further estimations of the charge transport mechanism and characteristics of the π-layer, the temperature dependence of the forward current for a fixed bias $V = 0.8$ V in the range of 100–300 K was measured. This corresponded to the second portion of the I–V characteristic with the values $n > 3$. The temperature dependence of current is shown in Fig. 2, and the activation energy $\Delta E = 0.24$ eV is determined from the exponential-law portion. From a comparison of dependences (2) and (3), temperature variation of the equilibrium concentration p_0 in the semiconductor mode should be expected. We may assume that the variation in mobilities μ_n and μ_p in the temperature range investigated is slight. As for variation in τ, it is also moderate (by a factor of 2–3). This was demonstrated by measurements of the photocurrent dependence for the reverse bias, which is determined mainly by the lifetime τ_p. Thus, the activation energy of 0.24 eV determines the position of a deep compensated-impurity level. In this case, as it is known,

$$p \approx 2\left(\frac{2\pi m_p kT}{h^2}\right)^{3/2}\exp\left(-\frac{\Delta E}{kT}\right). \quad (5)$$

Thus, at $T = 130$ K and $m_p = 0.4m_0$, we have $p_0 \approx 10^8$ cm^{-3}. From formula (4), the estimation of L_a/d yields ≈0.14–0.20. This ratio of the ambipolar diffusion length to the π-layer thickness is moderate. This is indicative of a large contribution of diffusion components of the current to the overall charge-transport mechanism. From the ohmic portion at $T = 130$ K, we find the resistance $R \approx 1.6 \times 10^5$ Ω. In this case, $d \approx 0.5$ μm and, consequently, $L_a \approx 0.07$–0.10 μm; i.e., the lifetime τ is assumed to be in the range of 10^{-9}–10^{-10} s. An increase in n with decreasing temperature corresponds to theoretical conclusions, implying an increased contribution of the diffusion component to the total current.

The effect of suppression of the direct current by white or monochromatic light should be attributed to the special features of the mechanism of charge transport in the Fe–*p*-InP diode structure. Curves which illustrate the difference between the forward dark current without illumination by white light I_d and with illumination I_l depending on the bias are shown in Fig. 3.

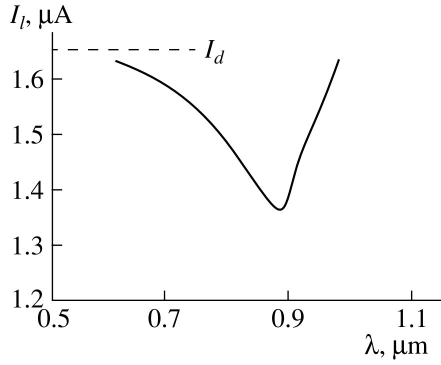

Fig. 4. Spectral dependence of suppression of the direct current.

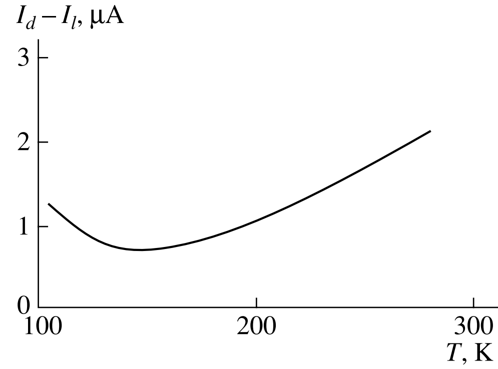

Fig. 5. Temperature dependence of suppression of the direct current.

The curves were recorded at T = 100 and 300 K. The negative photosensitivity encompasses a wide bias range at room temperature. The sign of I_d–I_l changes to positive for $V_{cr} \approx 0.4$ V, whereas $V_{cr} \approx 0.2$ V at $T = 100$ K. The dependence of the effect of suppression on the spectrum of light is given in Fig. 4. This curve reproduces the spectral curve of conventional photosensitivity, and the magnitude of half-decay $1/2I_l$ yields a value of 1.35 eV, i.e., E_G for InP. With respect to these specific features, we may assume that the effect of suppression of the direct current of the structure is associated with the compensation of the intrinsic photocurrent with the opposite sign. This current is generated by the Schottky barrier at the interface formed by Fe and the π layer of InP. The larger the generation of minority carriers, i.e., electrons into the π region, and the larger the rate of recombination with dark holes, the stronger the effect of suppression. This explains the spectral curve of suppression (Fig. 4). The open-circuit voltage of the photodiode Schottky structure can be represented as [7]

$$qV_{oc} = nkT\left[\ln\frac{J_{sc}}{A^*T^2} + \frac{\varphi_B}{kT} + C\chi^{1/2}\delta\right], \quad (6)$$

where n is the nonideality coefficient; J_{sc} is the density of the short-circuit current; A^* is the effective Richardson constant; φ_B is the Schottky barrier height; C is a constant; and χ and δ are the barrier height and the thickness of the possible transition (oxide) layer, respectively.

The calculated value A^* for p-InP with $m_p = 0.4m_0$ is equal to ≈50 A/cm^2 K^2. We believed that there are no additional transition layers between Fe and the π layer. In this context, assuming that $n \approx 1$ and ignoring the third term in formula (6), let us estimate φ_B. For measured values $V_{oc} \approx 1.4 \times 10^{-6}$ V and $J_{sc} \approx 5 \times 10^{-9}$ A, we obtain $\varphi_B \approx 0.36$ eV for monochromatic light $\lambda = 0.90$ μm and $T = 300$ K. This value is close to V_{cr} (Fig. 3). In its essence, this is a method for estimating the Schottky barrier height from the effect of suppression of the forward current by light. For $V > V_{cr}$, the Schottky barrier flattens.

With a further increase in the bias (under constant illumination), the double injection of dark carriers changes to the double injection of photogenerated carriers. The analytically positive photosensitivity is given by $\Delta I_{ph} = I_l - I_d \propto V^2$ and is to a large extent determined only by the generation and recombination in the π layer.

The temperature dependence of suppression of the current is shown in Fig. 5. The effect is most clearly pronounced at $T \approx 140$ K and noticeably weakens near room temperature. This dependence is mainly caused by a temperature-related shift of the Fermi level or the quasi-Fermi level for nonequilibrium electrons and holes. In this context, the dependence is caused by variations in the activity of main recombination centers in the processes of trapping and recombination of charge carriers.

Note that the existence of the mechanism of double injection into the high-resistivity compensated layer is an attribute of the structures with the suppression of the current by light. This follows from our results, as well as from the data for a p-Si–n^+-ZnO–n-ZnO–Pd structure [8].

A specific feature of a diode structure is the use of ferromagnetic Fe as the barrier metal. In this context, it was of interest to examine the influence of a magnetic field on the charge transport of dark and photogenerated carriers. No variations in the forward or reverse currents in fields of 1–20 kOe were found for either the magnetic field parallel to the plane of the S ($H \parallel S$) structure or for the ($H \perp S$) orientation. However, the variations in the photovoltage and photocurrent for the $H \parallel S$ configuration exhibited characteristic features (Fig. 6). The photocurrent for the short-circuit mode decreases with increasing magnetic field, with a minimum at $H_{cr} \approx 1.4 \times 10^4$ Oe. In contrast, the photovoltage increases and $\Delta V^H_{ph} = V^H_{ph} - V^0_{ph}$ is highest at approximately the same V_{cr}.

It is known that for low photovoltages

$$V_{ph} \approx I_{ph}R_d, \quad (7)$$

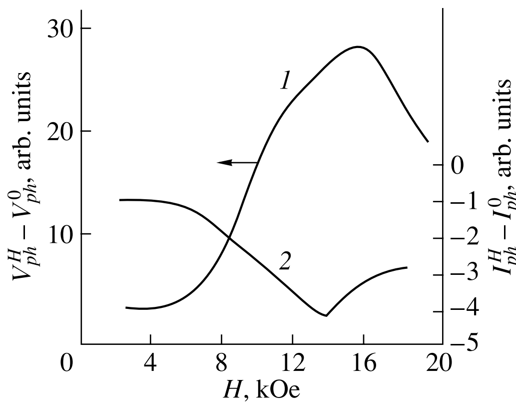

Fig. 6. Magnetic field dependence of (*1*) photovoltage and (*2*) photocurrent for the Fe–*p*-InP structures.

where R_d is the differential resistance for zero bias. Thus, an increase in V_{ph} is caused by an extremely sharp rise in the differential resistance. Therefore, R_d, which was recalculated for $\lambda_{max} = 0.76$ μm at an identical width of the monochromator slit, increases from 40 Ω ($H = 2.8 \times 10^3$ Oe) to 250 Ω (H_{cr}), i.e., by more than a factor of 6. For the structure investigated, the differential resistance should be determined by the generation–recombination component of the current, so that

$$R_d \propto \frac{\tau_0}{n_i}. \quad (8)$$

From this it follows that variation in the lifetime τ_0, i.e., the variation in the mechanism and rate of recombination for nonequilibrium charge carriers, governs variation in R_d. In this context, we may conclude that the magnetic field exerts a certain effect on recombination. A sharp variation in the magnetoresistance of Si-based Schottky diodes was revealed [9]. This phenomenon was explained by the intersection of levels, which include magnetic sublevels of the triplet state of a recombination center. This phenomenon affects the recombination rate.

Under our experimental conditions, this effect seems insignificant. Because of this circumstance, variation in the recombination rate should be explained by a nonuniform distribution of recombination centers at the heterostructure surface. More detailed elucidation of the mechanism of a change in R_d in a magnetic field calls for further investigation with the use of more sophisticated experimental procedures.

ACKNOWLEDGMENTS

We thank M.M. Mezdrogina and V.M. Botnaryuk for their help in fabricating the diode structures.

REFERENCES

1. J. Cheng, S. R. Forrest, B. Tell, *et al.*, J. Appl. Phys. **58**, 1780 (1985).
2. G. G. Kovalevskaya, S. V. Slobodchikov, and G. M. Filaretova, Fiz. Tekh. Poluprovodn. (Leningrad) **17**, 1991 (1983) [Sov. Phys. Semicond. **17**, 1271 (1983)].
3. M. A. Lampert and P. Mark, *Current Injection in Solids* (Academic, New York, 1970; Mir, Moscow, 1973), Chap. 2.
4. É. I. Adirovich, P. M. Karageorgiĭ-Alkalaev, and A. Yu. Leĭderman, *Double-Injection Currents in Semiconductors* (Sovetskoe Radio, Moscow, 1978), Chap. 2.
5. E. V. K. Rao, M. Diamei, and P. Kranz, J. Appl. Phys. **61**, 4812 (1987).
6. R. Baron, J. Appl. Phys. **39**, 1435 (1968).
7. G. P. Srivastava, P. K. Bhatnagar, and S. R. Dhariwal, Solid-State Electron. **22**, 581 (1979).
8. S. V. Slobodchikov, Kh. M. Salikhov, E. M. Russu, and Yu. G. Malinin, Fiz. Tekh. Poluprovodn. (St. Petersburg) **35**, 479 (2001) [Semiconductors **35**, 464 (2001)].
9. D. J. Miller and J. J. Lobb, Appl. Phys. Lett. **65**, 1391 (1994).

Translated by N. Korovin

Semiconductors, Vol. 37, No. 2, 2003, pp. 187–193. Translated from Fizika i Tekhnika Poluprovodnikov, Vol. 37, No. 2, 2003, pp. 196–202.
Original Russian Text Copyright © 2003 by Drapak, Orletskii, Kovalyuk, Netyaga.

SEMICONDUCTOR STRUCTURES, INTERFACES, AND SURFACES

Barrier Formation in a Heterostructure Formed of Native Oxide and *p*-InSe. Electrical and Photoelectrical Properties

S. I. Drapak*, V. B. Orletskii, Z. D. Kovalyuk, and V. V. Netyaga

Frantsevich Institute of Problems in Materials Science (Chernovtsy Branch), National Academy of Sciences of Ukraine, ul. I. Vilde 5, Chernovtsy, 58001 Ukraine

**e-mail: chimsp@unicom.cv.ua*

Submitted February 13, 2002; accepted for publication July 2, 2002

Abstract—On the basis of a complex investigation of the electrical and photoelectrical properties and the noise characteristics of heterostructures formed of *p*-InSe and native oxide, the dynamics of barrier formation is followed as a function of the temperature and time modes of oxidation. It is found that barrier formation occurs in structures oxidized for $\lesssim$30 min at $T = 400°C$. With an increase in the oxidation time to 60 min, the barrier is generally formed. The oxide film is a bilayer with different chemical compositions at the surface and at the interface. The largest signal-to-noise ratios are obtained in the case of 1.5-h oxidation of the base material ($T = 400°C$) mainly because of a low dark current. Low dark currents are attained in such structures due to the development of a rather homogeneous high-resistance interlayer. When *p*-InSe is oxidized for longer than 100 min, the oxide becomes homogeneous. However, the type of conduction in the base semiconductor changes in this case, which leads to a decrease in the barrier height and to an increase in the dark current. Due to this, the photoelectrical parameters degrade. *© 2003 MAIK "Nauka/Interperiodica".*

1. INTRODUCTION

Indium monoselenide (InSe) belongs to a widespread class of layered III–V compounds. Substrates with atomically smooth surfaces and a small number of dangling bonds which call for no special treatment can be prepared from this compound by cleavage in air. This fact is stimulating the development and investigation of photosensitive InSe-based diode structures of various types (Schottky barriers, metal–insulator–semiconductor structures, semiconductor–insulator–semiconductor structures, and heterojunctions). The lattice mismatch of contacting materials is not as substantial for structures based on layered semiconductors compared with conventional semiconductors [1]. Due to this circumstance, the results of investigations of new heterojunctions including both semiconductors, e.g., $AgIn_5S_8$ [2], and unconventional materials in the device industry, e.g., protein [3], systematically appear in the literature.

It is known that one of the methods for the fabrication of heterostructures is the thermal treatment of the starting material. A number of studies are devoted to the investigation of InSe oxidation and the properties of thus-fabricated heterostructures [4–16]. All of these reports can be arbitrarily divided into three groups. Studies of the first group (with an exclusively materials science orientation) are devoted to the investigation of the chemical composition of the native oxide, which is formed at the InSe surface under various temperature–time modes of oxidation [4, 5, 7, 8, 12–14, 16]. In these studies, X-ray measurements, Raman spectroscopy, and other measuring methods were used.

The studies of the second group (with a more applied character) are devoted to the investigation of the electrical properties of the oxide–*p*-InSe heterostructure [6, 9, 11, 15]. The third group includes investigations of the photoelectrical properties of the above structure [9–11, 15]. The contents of these studies were restricted to the spectra of the relative quantum efficiency of photoconversion, which were used to either confirm or disprove certain conclusions made in the studies of the first or second group. Despite a large number of reports on this subject, the data on the oxide composition are rather contradictory. In addition, investigation of the electrical properties of oxide–*p*-InSe heterostructures is based mainly on analysis of the forward portions of the photoelectrical modifications of current–voltage (*I*–*V*) characteristics, i.e., the dependences of the short-circuit current I_{sc} on the open-circuit voltage V_{oc}. In isolation from other investigative techniques, this circumstance may lead to an incomplete understanding of the processes that occur in such structures.

We report results of a complex investigation of the changes in the electrical and photoelectrical properties of a heterostructure consisting of *p*-InSe and native oxide depending on the duration of the thermal treatment of the base semiconductor. The purpose of this

1063-7826/03/3702-0187$24.00 © 2003 MAIK "Nauka/Interperiodica"

Electrical and photoelectrical properties of the structure formed by p-InSe and native oxide

Oxidation time t, min	15	30	60	90	120
V_{oc}, V upon illumination with power density $P \approx 100$ mW/cm^2	0.5	0.32–0.35	0.22	0.18	0.1
Diffusion potential φ_0 determined from the dependence $C = f(V)$, eV	Measurements are hampered	Measurements are hampered	0.7	0.7	0.25
Dependence of $C = f(V)$ on frequency	Virtually absent	Virtually absent	No	No	Yes
Excess of the forward current over the reverse current at $\|V\| = 1$–1.5 V	By a factor of 1.5–2	By a factor of ~2	10	100	10
The forward direction in the structure corresponds to "+" applied to the material	InSe	InSe	InSe	InSe	Oxide

study was to optimize the main photoelectrical parameters for further practical application.

2. EXPERIMENTAL

Cadmium-doped p-InSe was grown using the technique of nonstoichiometric growth of InSe [17]. The single crystals were electrically homogeneous with a free-carrier density of $p \approx 10^{14}$ cm^{-3} and a Hall mobility of ~50 cm^2 V^{-1} s^{-1} at $T = 300$ K. The 0.5-mm-thick substrates were cleaved from an ingot along the (001) plane and oxidized at $T = 400$°C for 15, 30, 60, 90, and 120 min. According to [13], heterostructures oxidized in the temperature range $T = 350$–450°C have the highest photosensitivity. In addition, the highest-quality In_2O_3 : Sn (ITO) films, which are used in industry, are formed at $T = 400$–420°C [18]. At the same time, according to [19], heating p-InSe in air to $T > 520$°C changes the type of conduction of this semiconductor. In this case, if the oxide film consists mainly of In_2O_3, the structures formed of n-oxide and n-InSe are nonrectifying. After thermal treatment, the samples were cooled to room temperature, cut off along the perimeter, and cleaved again from the side opposite to that with the oxide. Silver was used to form ohmic contacts.

We measured the forward and reverse I–V characteristics, their temperature dependences, the photoelectric modification of the forward portion of the I–V characteristic at room temperature, the capacitance–voltage (C–V) characteristics, the frequency dependence of the impedance in the frequency range of 10^3–2×10^7 Hz, and the spectrum of the relative quantum efficiency upon illumination of the structures from the oxide side at room temperature. In order to analyze the barrier formation in more detail, the level and character of the noise and the signal-to-noise ratios (V_s/V_n) were investigated. The photoelectrical properties were measured using a K-54.410 serial system.

3. RESULTS AND DISCUSSION

The structures obtained using the above-described temperature and time modes exhibit rectifying properties (see table).

Upon illumination of the studied structures formed of p-InSe and native oxide, the photovoltaic effect occurs, which is stronger when the oxide side is illuminated. As can be seen from the results listed in the table, the open-circuit voltage V_{oc}, under identical illumination conditions, decreases with an increase in the oxidation time. The highest values of V_{oc} are attained for the p-InSe substrates oxidized for 15 and 30 min (the dark I–V characteristics of the structures obtained using these oxidation modes are almost identical). In this case, the dark I–V characteristics of such structures (Fig. 1, dependences *1*, *2*) are linear in the coordinates $\log J = f(\log V)$ with a slight deviation ($J \propto V^{1.1-1.2}$) of the forward portion from linearity. It should be noted that the forward characteristic of such structures measured by the photoelectric technique (Fig. 1, curves *5*, *6*), i.e., the forward portion of the dependence $J_{sc} = f(V_{oc})$ (J_{sc} is the short-circuit current density), is in fact similar to the forward I–V characteristics reported in [11]. This forward portion can be described by the expression $J_{sc} \propto \exp(eV_{oc}/nkT)$, where n at $T = 288$ K varied from sample to sample in the range of 1.6–1.8 and 1.8–2.2 for the structures oxidized for 15 and 30 min, respectively. However, a steady increase in V_{oc} with an increase in the illumination time was observed during the measurements, which is characteristic of the photoconductivity of films with various times of trap charging, which have not yet formed [20]. Because of this, in order to obtain dependences *5* and *6* (Fig. 1), we measured the values of J_{sc} and V_{oc} after a specified time interval after exposing the samples to light. Most likely, the high values of V_{oc} for such structures may be attributed to the emergence and summation of barrier-layer photovoltages generated by barriers connected in series in the films that have not yet formed. The emergence of barriers is due to the existence of crystalline grains,

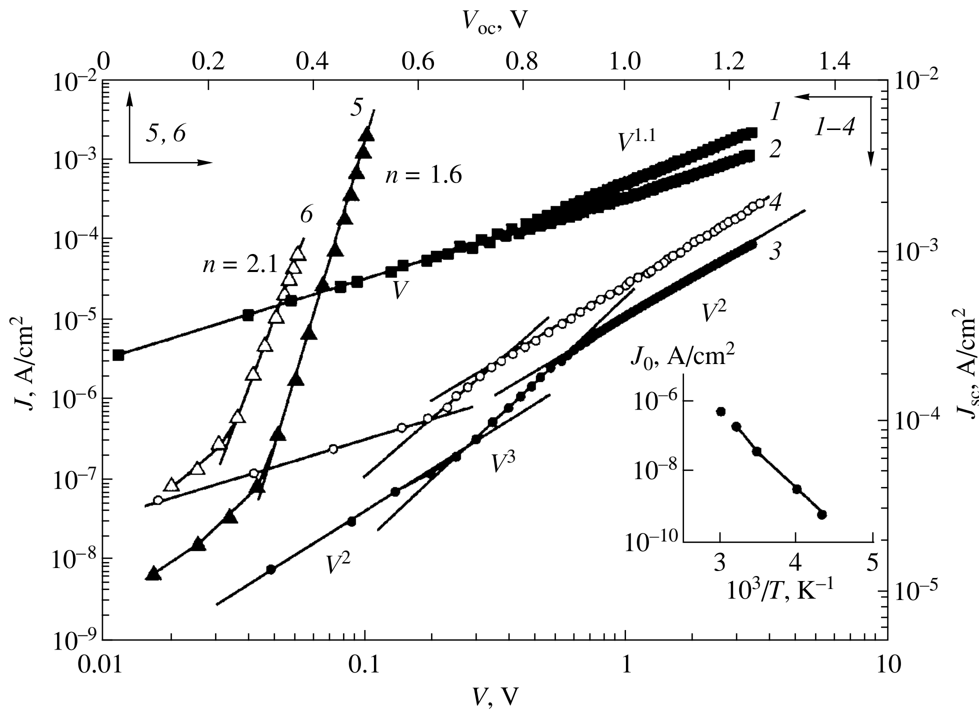

Fig. 1. (*1*, *3*, *4*) Forward and (*2*) reverse portions of the current–voltage characteristics of the structure consisting of *p*-InSe and the native oxide and the photoelectrical modification of the forward portions $\log J_{sc} = f(V_{oc})$ (curves *5*, *6*) at $T = 288$ K. The oxidation time t = (*5*) 15, (*1*, *2*, *6*) 30, (*3*) 60, and (*4*) 120 min. The temperature dependence of the forward-current density J_0 at a constant voltage of 0.1 V for the structure obtained by oxidation of the substrate for 60 min is in the inset.

block boundaries, etc., in such films, as is observed in polycrystalline films of PbS, CdTe, Ge, etc. [20]. The measurements of the *C–V* characteristics of the structures obtained by oxidation for 15 and 30 min, which were aimed at determining the contact potential difference φ_0, were hindered for the following reasons. There was a significant spread of the capacitance, depending on the applied reverse bias, and no distinct fall-off of the $C^2(V)$ dependences was observed. In this case, within the spread of values, we can regard the capacitance of such structures as frequency-independent. One of the major causes of such behavior of the *C–V* characteristics is the absence of a formed barrier, which is confirmed by the character and level of noise (Fig. 2, dependence *1*). According to [21–23], a low noise signal V_n under forward and reverse biases is characteristic of the structures with weakly developed fluctuations of the potential profile. Such fluctuations exert almost no effect on the carrier distribution over the sample bulk. The intrinsic noise of such layers is governed by generation–recombination noise, which is caused by fluctuations in the generation, recombination, and attachment of carriers in the bulk and at the surface of crystallites. The photoelectric modification of the forward portions of the *I–V* characteristics of such structures represents a complex process of summation of the photovoltages developed by barriers connected in series in the oxide films that have not been completely formed. A decrease in V_{oc} in the case of oxidation for 30 min is, most likely, related to the coarsening of grains, to a decrease in their number in the oxide, and, as a consequence, to a decrease in the number of barriers between crystallites. The spectral dependence of the relative quantum effi-

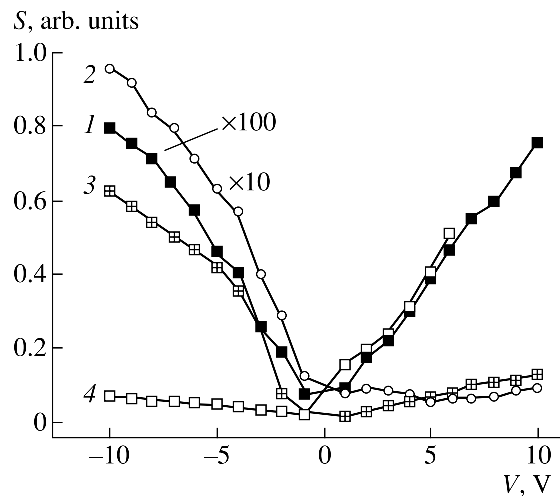

Fig. 2. The noise spectral density S as a function of the bias for the structures obtained by oxidation for t = (*1*) 30, (*2*) 60, (*3*) 90, and (*4*) 120 min. The “+” terminal of the external current source is applied to InSe. The measurements were carried out at frequencies as high as 1200 Hz; Δf = 160 Hz.

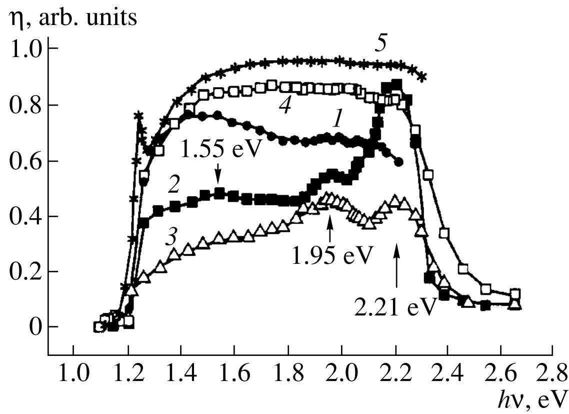

Fig. 3. Spectral dependence of the relative quantum efficiency of photoconversion $\eta(h\nu)$ for the structures consisting of *p*-InSe and the native oxide obtained by oxidation of the base semiconductor for t = (*1*) 15 and 30, (*2*) 60, (*3*) 90, and (*4*) 120 min, and for *p*-InSe that was not subjected to any thermal treatment (dependence *5*).

ciency of photoconversion $\eta(h\nu)$(PS) was obtained for such structures as the ratio of the short-circuit current to the number of incident photons (Fig. 3, dependence *1*). This dependence differs from a similar dependence for InSe that was not subjected to thermal treatment (Fig. 3, dependence *5*) by the absence of an exciton peak and by the noticeable falloff of the sensitivity in the short-wavelength region. This fact is indicative of the deterioration of the base-semiconductor surface due to the onset of formation of the oxide layer and to an increase in the surface-recombination rate at the face surface of the cell. Furthermore, the emergence of a weak peak at $h\nu \approx 1.95$ eV (this value is close to the bandgap of γ-In_2Se_3 (E_g = 2.0 eV)) is noted [24].

During further oxidation of *p*-InSe, the situation changes radically. As can be seen from the table, the forward current begins to substantially exceed the reverse current at $|V|$ = 1–1.5 V. The *C*–*V* characteristics of such structures are independent of frequency and are linear in the coordinates $C^{-2} = f(V)$, which is indicative of the formation of a heterostructure with an abrupt junction. In this case, the contact potential difference φ_0, which is determined from the *C*–*V* characteristic, equals 0.7 eV for the samples oxidized for 60 and 90 min. Barrier formation in the oxide–*p*-InSe structure is also confirmed by the noise characteristics (Fig. 2, dependences *2*, *3*). In this case, additional sources of current noise appear [21–23]. Notably, the forward portions of the *I*–*V* characteristics of the structures obtained by oxidation for 60 and 90 min are almost identical (Fig. 1, dependence *3*). These portions consist of three parts: (i) $J \propto V^2$, (ii) $J \propto V^3$, and (iii) $J \propto V^2$. Such dependence of the current on the applied voltage is characteristic of space-charge-limited currents; this implies the presence of a high-resistance interlayer at the interface. The possibility that a layer with other electrical characteristics exists at the interface in the native oxide is quite reasonable: the film formed at the InSe surface in the initial stage of oxidation blocks the access of air to the crystal bulk. Data on layers with different chemical compositions of the film are absent in [4, 5, 7, 8, 12–14, 16]. This suggests that the methods used in these studies make it possible to determine the chemical composition of the oxide mainly at the surface. The absence of kinks in the dependence $C^{-2} = f(V)$ indicates that the structure consisting of native oxide and *p*-InSe can be regarded as a semiconductor–insulator–semiconductor structure when the oxidation times are equal to 60 and 90 min. According to the Lambert theory for insulators with a single trap level [25], the voltage at which the $J \propto V^3$ part of the *I*–*V* characteristic transforms into the $J \propto V^2$ part is determined by the expression

$$V_e = eN_t d^2/2\varepsilon_0\varepsilon, \quad (1)$$

where e is the elementary charge, N_t is the trap density, d is the thickness of the high-resistance layer, ε_0 is the permittivity of free space, and ε is the relative permittivity of the high-resistance layer. The evaluation of the d quantity, performed by measuring the capacitance at a zero bias, yields a value of ~2 μm. Unfortunately, as was noted above, data on the transition layer are absent in the literature and we can only make assumptions about the nature of this layer. According to [13], the oxide film obtained at 400°C $\lesssim T \lesssim$ 500°C consists of In_2O_3 with inclusions of $In_2(SeO_4)_3$ and In_2Se_3 [16]. Because of this circumstance, it is reasonable to suggest that the phases formed with a lack of oxygen, i.e., preferentially In_2Se_3, are dominant in the bulk of the oxide film. Let us assume the layer permittivity to be equal to $\varepsilon = 9.53$ (the permittivity of In_2Se_3 [24]) and determine the value of V_e from dependence *3* (Fig. 1) (V_e = 0.75 V). Thus, we can evaluate the trap density in the high-resistance layer from formula (1): $N_t = 2.5 \times 10^{14}$ cm^{-3} for the structures oxidized for 60 min. The dependence of the current density on the voltage within the $J \propto V^2$ part is determined by the Mott formula [20]:

$$J = \frac{9}{8}\mu\varepsilon\varepsilon_0\frac{V^2 N_v}{d^3 N_t}\exp\left(-\frac{E_s}{kT}\right), \quad (2)$$

where μ is the hole mobility in the high-resistance layer, N_v is the effective density of states in the valence band, and E_s is the energy position of the trap level reckoned from the bottom of the valence band of the high-resistance layer. Because of this, the current should depend exponentially on the quantity E_s/kT at a constant bias, which has been observed experimentally (see inset in Fig. 1). The value of $E_s \approx 0.25$ eV, which was determined from the slope of this dependence, is in good agreement with the activation energy of the acceptor level in the band gap of InSe [26]. This may indicate that InSe is present in the transition layer. Let us assume that the increase in the oxidation time to

90 min does not affect the composition of the transition layer. Having evaluated the thickness of this layer (which decreased by a factor of ~1.5), we can conclude from the capacitance measurements at a zero bias and the voltage $V_e = 0.4$ V that the trap density decreases by a factor of almost 1.5 (for this oxidation mode, $N_t = 1.8 \times 10^{14}$ cm^{-3}). Thus, the structure of the transition layer becomes more homogeneous and, as a consequence, the rectifying properties of the heterostructure are improved (see table). The inhomogeneity of both the face and transition layers in the structures obtained by oxidation of the base semiconductor for 60 min is also clearly seen from the spectral dependence of the relative quantum efficiency of photoconversion (Fig. 3, dependence *2*). The peaks at 1.55 and 1.95 eV may be attributed to the formation of β and γ polymorphs of In_2Se_3 [24] in the transition layer. Apparently, the appearance of the most intense peak with a sharp short-wavelength edge should be attributed to the formation of indium selenate $In_2(SeO_4)_3$ ($E_g = 2.15$ eV [8]). Most likely, this compound is the dominant component of the upper layer of the oxide. With an increase in the oxidation time to 90 min, the inhomogeneity of the native oxide decreases. This manifests itself in that the peak related to β-In_2Se_3 vanishes, and the peaks with energies of 1.95 and 2.21 eV have similar amplitudes (Fig. 3, dependence *3*).

The forward portion of the *I–V* characteristic of the structures obtained by oxidation for 120 min also consists of three parts (Fig. 4, dependence *4*). The middle and last parts are qualitatively similar to the relevant parts of the forward characteristic of the structures obtained by oxidation for 60 (curve *3*) and 90 min. At low forward voltages, the dependence $J \propto V$, which is usually attributed to leakage currents [27], manifests itself in curve *4* (Fig. 1) instead of the quadratic dependence in the case of curve *3*. This change in the behavior of the forward portions of the *I–V* characteristics may be caused by micropores appearing at the oxide surface due to the effect of temperature during the 120-min oxidation. Characteristic features of such structures, in comparison with the structures oxidized for 60 and 90 min (see table), are both a change in the conditions in which the forward current flows and a decrease in the diffusion potential φ_0 by a factor of almost 3. Furthermore, we found that the dependence of the capacitance on voltage $C = f(V)$ becomes frequency-dependent, which is characteristic of the overwhelming majority of structures fabricated on the basis of layered semiconductors. This frequency dependence is due to the effect of the high series resistance. These circumstances are indicative of a change in the conduction type of the base material, whereas the chemical composition of the layer remains relatively constant. This is also confirmed by the values of the noise level measured at forward and reverse biases (Fig. 2, dependence *4*). Taking into account that the oxidation of InSe is a temperature–time process, the change in the conduction type of the substrate agrees with the data reported in [19, 26]. In this case, for the substrate oxidized for 120 min, the φ_0 quantity was determined according to the procedure described in [28]. In this procedure, the cutoff voltages $V_0(\omega)$ related to the dependences $C^{-2}(V)$ are approximated to zero frequency at various frequencies ω. In this case, an equivalent scheme of the heterostructure is usually presented as shown in Fig. 4a. In this scheme, R_d is the series resistance of the sample, C_d is the capacitance of the diode under investigation, and R_d is the diode resistance. In the course of the experiment, the fixed value of the capacitance C_m expressed through the parameters of the equivalent scheme is determined by the equation

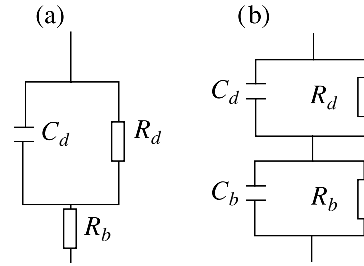

Fig. 4. The equivalent schemes of the oxide–*p*-InSe structures formed by oxidation of substrates (a) for 120 min; and (b) for 60 and 90 min, with allowance made for the thin high-resistance interlayer.

$$C_m = \frac{C_d}{(1 + R_b/R_d) + \omega^2 R_b^2 C_d^2}. \tag{3}$$

The violation of the condition $R_b^2 \omega^2 C_d^2 \ll 1$ leads to the frequency dependence of the capacitance–voltage dependence. According to [29], in the case of diode structures fabricated by oxidation of the substrate for 60 and 90 min, we should use a more detailed equivalent scheme which makes allowance for the base capacitance C_b (Fig. 4b). In this case, we have

$$C_m = \frac{B}{(1 + R_b/R_d)^2 + \omega^2 R_b^2 (C_d + C_b)^2}, \tag{4}$$

where the numerator B equals

$$B = (R_b/R_d + 1)C_d + (R_b/R_d)C_b$$
$$+ (R_b/R_d)(C_d + C_b) + \omega^2 R_b^2 C_b C_d (C_d + C_b).$$

Assuming $R_b \approx R_d$ and taking into account that $(R_b \omega C_d)^2 \gg 1$, we derive $C_m \approx C_d C_b/(C_d + C_b)$. Since $C_d \gg C_b$, $C_m \approx C_b$, i.e., for $R_b \approx R_d$, C_m is equal to the capacitance of two capacitances connected in series. The magnitude of this quantity tends toward the base capacitance C_b. In this case, the capacitance is frequency-independent. It is worth noting that the equivalent scheme shown in Fig. 4b is used for the investigation of the dielectric dispersion in two-layer semicon-

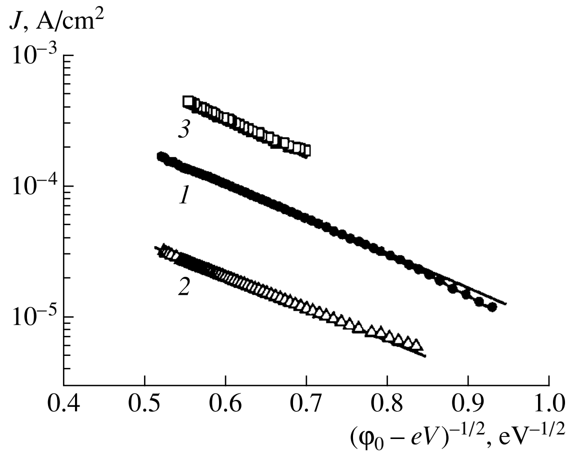

Fig. 5. Comparison of the voltage dependences of the reverse-current density with expression (5) for the structures fabricated by oxidation of InSe for (*1*) 60, (*2*) 90, and (*3*) 120 min. $T = 288$ K.

ductors or insulators [20]. We should also note that the application of both equivalent schemes to the structure under investigation implies that the upper oxide layer (oxidation for 60 or 90 min) should have a considerably higher conduction in comparison with the high-resistance interlayer and the base conductor. For the latter case (oxidation for 120 min), the results indicate that a quite homogeneous oxide layer is formed.

It should be noted that for all oxidation times, the noise-density spectrum corresponds to the run of the dependence f^{γ} (Hooge's law). This spectrum has two clearly pronounced portions in the case of reverse-biased structures (here $f = \omega/2\pi$). In the first portion (0–4 V), the exponent γ steadily increases in the range of 0.45–3 with an increase in the annealing time from 30 to 90 min. In the second portion (4–10 V), $\gamma \approx 0.2$–1, which differs from similar values for *p*-InSe-based photoresistors only by the magnitude [30]. It should also be noted that the signal-to-noise ratio V_s/V_n increases with the oxidation time and attains the largest value for structures fabricated by oxidation for 90 min.

The spectrum $\eta(h\nu)$ of structures obtained by oxidation of the base semiconductor for 120 min (Fig. 3, dependence *4*) has the shape of a band with no pronounced peaks. A slight decrease in sensitivity in the short-wavelength region is observed. Furthermore, a short-wavelength edge is somewhat extended in comparison with the two previous oxidation modes. These facts may indicate both defect formation at the face side of the structure due to prolonged thermal treatment and relative chemical constancy of the oxide layer.

The variation in the reverse portions of the *I–V* characteristics with the oxidation time also illustrates well the dynamics of the development of the native oxide. For InSe substrates oxidized for 15 and 30 min, the dependence of the current density on the reverse voltage is linear, as was mentioned above (Fig. 1, dependence *2*). Such behavior is characteristic of leakage currents [27] and is caused by the formation of a large number of crystalline grains and blocks at the surface of the base semiconductor.

For *p*-InSe samples oxidized for 60 min, the dependence of the current density on the reverse voltage in the range of $0 < |V| < 0.7$–0.8 is governed by space-charge-limited currents. This is indicative of the formation of an insulator interlayer between the upper oxide layer and the base semiconductor. At higher reverse biases, the current density J is described by the expression typical for the tunnel current [31]:

$$J = a_1 \exp[-b_1/(\varphi_0 - eV)^{1/2}]. \quad (5)$$

Here, b_1 is a parameter independent of V; a_1 is a parameter which makes allowance for the degree of population of the energy levels from which tunneling occurs. The graphical representation of formula (5) concerning the *I–V* characteristic of the sample oxidized for 60 min is shown in Fig. 5, dependence *1*.

For the structures fabricated by oxidation for 90 min, the reverse portion of the *I–V* characteristic has a more complex shape and consists of three portions. (i) In the range of $0 < |V| < 0.25$–0.3 V, space-charge-limited currents play an important role. (ii) For 0.25–0.3 < V < 0.7–0.8 V, the *I–V* characteristic is described by the expression $J \propto (\varphi_0 - eV)^{1/2}$, which is characteristic of generation–recombination processes in the space-charge region [32]. (iii) For $|V| > 0.7$–0.8 V, the reverse portion of the *I–V* characteristic is described by expression (5) (Fig. 5, dependence *2*). In this case, a decrease in the effect of space-charge-limited currents and the emergence of generation–recombination currents indicates that the density of states decreases in the transition layer; i.e., the layer becomes more homogeneous. Because of this circumstance, the reverse-current density decreases by an order of magnitude in comparison with the case of oxidation for 60 min.

For the structures fabricated by oxidation of the substrate for 120 min, the effect of space-charge-limited currents becomes even less substantial. These currents are observed in the range of reverse biases $0 < |V| <$ 0.15–0.2 V. Taking into account the significant decrease in the diffusion potential and the appearance of frequency dispersion of the capacitance, this circumstance indicates that the high-resistance transition layer virtually vanishes. In the range of 0.15–0.2 < $|V|$ < 1.8–2.0 V, the *I–V* characteristic is linear (leakage currents), which may be indicative of violation of oxide-layer integrity, i.e., the appearance of small defects, cracks, etc. Due to this, an increase in the reverse-current density by a factor of ~15 in comparison with the case of oxidation for 90 min is observed. Finally, only for $|V| > 1.8$–2.0 V, the *I–V* characteristic of different samples is described by expression (5).

4. CONCLUSIONS

The dynamics of barrier development was studied on the basis of an analysis of the changes in the current–voltage, capacitance–voltage, photoelectric, and noise characteristics of structures consisting of *p*-InSe and native oxide with oxidation time at $T = 400°C$. It is found that structures with optimal electrical and photoelectrical parameters are obtained by oxidation of the base semiconductor for 90 min. The *C–V* characteristic of such structures is independent of the measurement frequency, which is due to the fact that the native oxide is bilayered, whereas the contact potential difference φ_0 is equal to 0.7 eV. The character and the level of the noise in such structures differ from those predicted by Hooge's law, as in the case of the photoresistive effect in InSe. For shorter oxidation times, the film is not formed, as indicated by low noise both at forward and reverse biases. For oxidation times longer than 100 min, the potential barrier decreases to 0.27 eV, which cannot be explained by changes in the chemical composition of the oxide layer. Changes in the polarity of the current, noise characteristics, and the constancy of the short-wavelength photoresponse limit are indicative of a change in the type of conduction of the base material. Notably, frequency dispersion of capacitance arises, which indicates that a high-resistance interlayer at the interface vanishes. The possibility of fabricating structures consisting of *p*-InSe and native oxide is also demonstrated; this is largely due to the fact that the main component of the oxide is indium selenate $In_2(SeO_4)_3$ rather than In_2O_3.

REFERENCES

1. A. Koma, J. Cryst. Growth **201–202**, 236 (1999).
2. I. V. Bodnar', V. F. Gremenok, V. Yu. Rud', and Yu. V. Rud', Fiz. Tekh. Poluprovodn. (St. Petersburg) **33**, 805 (1999) [Semiconductors **33**, 740 (1999)].
3. V. Yu. Rud', Yu. V. Rud', and V. Kh. Shpunt, Pis'ma Zh. Tekh. Fiz. **25**, 76 (1999) [Tech. Phys. Lett. **25**, 328 (1999)].
4. H. Iwakuro, C. Tatsuyama, and S. Ichimura, Jpn. J. Appl. Phys. **21**, 94 (1982).
5. I. Miyake, T. Tanpo, and C. Tatsuyama, Jpn. J. Appl. Phys. **23**, 172 (1984).
6. V. N. Katerinchuk and M. Z. Kovalyuk, Pis'ma Zh. Tekh. Fiz. **18**, 70 (1992) [Sov. Tech. Phys. Lett. **18**, 394 (1992)].
7. V. N. Katerinchuk, M. Z. Kovalyuk, and A. D. Ogorodnik, Neorg. Mater. **32**, 827 (1996).
8. O. A. Balitskii, R. V. Lutsiv, V. P. Savchun, and J. M. Stakhira, Mater. Sci. Eng. B **56**, 5 (1998).
9. V. P. Savchun and J. M. Stakhira, Phys. Status Solidi A **156**, 113 (1996).
10. V. N. Katerinchuk and M. Z. Kovalyuk, Pis'ma Zh. Tekh. Fiz. **23**, 1 (1997) [Tech. Phys. Lett. **23**, 377 (1997)].
11. V. N. Katerinchuk, Z. D. Kovalyuk, and A. V. Zaslonkin, Pis'ma Zh. Tekh. Fiz. **25**, 34 (1999) [Tech. Phys. Lett. **25**, 520 (1999)].
12. J. M. Stakhira, V. P. Savchun, and V. B. Kytsay, Mol. Phys. Rep. **23**, 184 (1999).
13. V. P. Savchun and V. B. Kytsay, Thin Solid Films **361–362**, 123 (2000).
14. O. A. Balitskii, N. N. Berchenko, V. P. Savchun, and J. M. Stakhira, Mater. Chem. Phys. **65**, 130 (2000).
15. V. N. Katerinchuk, Z. D. Kovalyuk, T. V. Betsa, *et al.*, Pis'ma Zh. Tekh. Fiz. **27**, 62 (2001) [Tech. Phys. Lett. **27**, 424 (2001)].
16. O. A. Balitskii, V. P. Savchun, and V. O. Yukhymchuk, Semicond. Sci. Technol. **17**, L1 (2002).
17. A. Chevy, A. Kuhn, and M.-S. Martin, J. Cryst. Growth **38**, 118 (1977).
18. T. Nakao, T. Nakada, Y. Nakayama, *et al.*, Thin Solid Films **370**, 155 (2000).
19. A. Segura, J. P. Guesdon, J. M. Besson, and A. J. Chevy, J. Appl. Phys. **54**, 876 (1983).
20. P. T. Oreshkin, *Physics of Semiconductors and Insulators* (Vysshaya Shkola, Moscow, 1977).
21. N. B. Lukyanchikova, A. A. Konoval, and M. K. Sheinkman, Solid-State Electron. **18**, 65 (1975).
22. N. B. Lukyanchikova, Litov. Fiz. Sb. **20**, 25 (1980).
23. N. B. Lukyanchikova, Élektron. Prom. **6**, 28 (1983).
24. C. Julien, M. Eddrief, M. Balkanski, *et al.*, Phys. Status Solidi A **88**, 687 (1985).
25. M. A. Lambert, Phys. Rev. **103**, 1648 (1956).
26. C. M. Martínez-Tomaz, V. Múñoz, M. V. Andrés, *et al.*, Z. Phys. B: Condens. Matter **91**, 25 (1993).
27. V. L. Bakumenko and V. F. Chishko, Fiz. Tekh. Poluprovodn. (Leningrad) **11**, 2000 (1977) [Sov. Phys. Semicond. **11**, 1171 (1977)].
28. Yu. A. Gol'dberg, O. V. Ivanova, T. V. L'vova, and B. V. Tsarenkov, Fiz. Tekh. Poluprovodn. (Leningrad) **18**, 1472 (1984) [Sov. Phys. Semicond. **18**, 919 (1984)].
29. A. A. Lebedev, A. A. Lebedev, and D. V. Davydov, Fiz. Tekh. Poluprovodn. (St. Petersburg) **34**, 113 (2000) [Semiconductors **34**, 115 (2000)].
30. Z. D. Kovalyuk, V. B. Orletskii, I. M. Budzulyak, and V. V. Netyaga, J. Phys. Stud. **5**, 43 (2001).
31. B. L. Sharma and R. K. Purohit, *Semiconductor Heterojunctions* (Pergamon Press, Oxford, 1974; Sovetskoe Radio, Moscow, 1979).
32. V. I. Strikha, *Contact Phenomena in Semiconductors* (Vysshaya Shkola, Kiev, 1982).

Translated by N. Korovin

Semiconductors, Vol. 37, No. 2, 2003, pp. 194–199. Translated from Fizika i Tekhnika Poluprovodnikov, Vol. 37, No. 2, 2003, pp. 203–208.
Original Russian Text Copyright © 2003 by Yu. Drozdov, Baĭdus', Zvonkov, M. Drozdov, Khrykin, Shashkin.

LOW-DIMENSIONAL SYSTEMS

Segregation of Indium in InGaAs/GaAs Quantum Wells Grown by Vapor-Phase Epitaxy

Yu. N. Drozdov*^, N. V. Baĭdus', B. N. Zvonkov**, M. N. Drozdov, O. I. Khrykin*, and V. I. Shashkin***

** Institute for Physics of Microstructures, Russian Academy of Sciences, Nizhni Novgorod, 603950 Russia*

^e-mail: drozdyu@ipm.sci-nnov.ru

*** Physicotechnical Research Institute at Nizhni Novgorod State University, Nizhni Novgorod, 603950 Russia*

Submitted December 18, 2001; accepted for publication April 15, 2002

Abstract—Distribution of indium atoms in structures which contained double InGaAs/GaAs quantum wells and were grown by vapor-phase epitaxy from metal–organic compounds was studied. Experimental indium-concentration profiles were obtained using Auger electron spectroscopy. A model of growth with allowance made for indium segregation and a model for the Auger profiling were used in the calculations of profiles. Fitting calculated profiles to experimental ones made it possible to estimate the activation energies for In–Ga exchange in the context of a kinetic model for segregation. These energies are found to be somewhat higher than those that are well known for molecular-beam epitaxy, which is related to stabilization of the growth surface by hydrogen atoms in a vapor-phase reactor. © *2003 MAIK "Nauka/Interperiodica".*

1. INTRODUCTION

When epitaxial layers of solid solutions are grown, segregation (separation) of one of the solution components by the growth surface gives rise to distortion of the concentration profile, which most profoundly affects thin layers of the quantum-well (QWs) type. Segregation of indium during the growth of InGaAs layers on GaAs(100) substrates was repeatedly observed in the course of molecular-beam epitaxy (MBE), in which case low growth rates and high reproducibility of results made it possible to evaluate the parameters of the process [1–6]. Three principle models are used. The first (simplest) model of exponential increase or decrease in concentration corresponds to a constant coefficient of the concentration distribution between the solid phase and the surface [1–4]. The second (kinetic) model describes segregation as a combination of two thermally activated processes of exchange of In–Ga atoms between the surface and the upper layer of the solid phase [6]. In the third (thermodynamic) model, it is assumed that the probability of exchange of the atoms is very high during monolayer growth; as a result, an equilibrium distribution of concentration is established (see [7] for the case of Ge segregation).

In the case of vapor-phase epitaxy from metal–organic compounds (MOVPE), the presence of hydrogen as the carrier gas in the reactor enhances surface stability [8] and (in combination with other factors) can suppress segregation. Nevertheless, recent observations [9–13] can be interpreted as manifestations of indium segregation; however, a comprehensive qualitative explanation of the results and especially a quantitative description of this phenomenon are still lacking.

Difficulties encountered in experimental studies of segregation are associated with the necessity of analyzing the concentration profiles of elements in the layer with a high resolution. In this study, the indium concentration profile in MOVPE structures with two InGaAs QWs was investigated using high-resolution Auger electron spectrometry combined with layer-by-layer etching with argon ions. The spread function of the Auger spectrometer was determined using test samples and was used in calculations of the concentration profiles of elements. We simulated the growth (with allowance made for segregation) and subsequent process of layer-by-layer analysis. Comparison between the experimental and calculated profiles made it possible to determine accurately the growth parameters and assess the applicability of the models developed initially for MBE to the MOVPE process.

2. EXPERIMENTAL

Epitaxial structures were grown in a horizontal MOVPE reactor in hydrogen flow under atmospheric pressure. We used trimethylgallium, trimethylindium, and arsine as sources of gallium, indium, and arsenic, respectively.

Structures A, B, C, and D each contained two InGaAs QWs separated by a GaAs layer and coated with a similar GaAs layer. The thickness of each layer was about 10 nm. We attempted to remove excess indium in structure C by etching off the upper monolayer of each of the QWs; to this end, we introduced

1063-7826/03/3702-0194$24.00 © 2003 MAIK "Nauka/Interperiodica"

Parameters of growth processes and computation models

Structure	T_g, °C	Additives	Parameters of models											
			a model involving exchange between the layer and the surface											exponential model
			layer 1			layer 2		layer 3			layer 4		σ, nm	
			t, s	F_{In}, ML/s	F_{Ga}, ML/s	t, s	F_{Ga}, ML/s	t, s	F_{In}, ML/s	F_{Ga}, ML/s	t, s	F_{Ga}, ML/s		L_s, nm
A	650	–	8	0.44	2.5	20	1.5	8	0.43	2.2	20	2.2	1.0	3.0
B	500	–	24	0.165	0.62	60	0.43	24	0.185	0.64	60	0.54	0.8	1.5
C	650	CCl_4	8	0.46	2.5	20*	1.55	8	0.5	2.35	20*	1.95	1.2	2.0
D	650	Bi	8	0.27	1.85	20	1.8	8	0.36	1.9	20	2.45	1.0	3.0

* Growth of the layer sets in after removal of a single previous monolayer. Designations: T_g is the growth temperature; t is the duration of the layer growth (specified in the model as in the growth process); F are the indium and gallium fluxes expressed in monolayers per seconds (ML/s); σ is the measure of the surface roughness; and L_s is the segregation length. In the model with exchange, we used the parameters E_1 = 1.95 eV and E_2 = 2.25 eV.

CCl_4 into the reactor at the end of the InGaAs-layer growth. The role of CCl_4 as an etchant for InGaAs was previously outlined [14]. When growing QWs in structure D, we additionally introduced bismuth impurity into the reactor; this impurity has been used in MBE to suppress In segregation [4]. We employed laser sputtering of a Bi target similarly to [15]. Data on growth temperatures and durations of different growth stages are listed in the table.

The In concentration profiles were measured using an ÉSO-3 Auger spectrometer in the high-resolution mode with simultaneous layer-by-layer etching with 500-eV Ar^+ ions [16]. We detected In (406 eV) and Ga (1069 eV) lines. The Ga concentration profile was used to take into account a drift of sensitivity during measurements of In distribution; this drift was related to the long duration of measurements (up to two hours).

In addition, we used a DRON-4 diffractometer with a Ge(400) monochromator to record the θ/2θ X-ray diffraction spectra in the vicinity of the GaAs(400) peak using Cu$K_{\alpha 1}$ radiation.

3. METHODS FOR DATA PROCESSING

3.1. A Model of the Layer-by-Layer Analysis

We calculated the Auger profile for a given "true" distribution using the method suggested by Hoffmann [17]. We took into account the three following parameters of the process, namely, the depth of the atomic-mixing zone (w), the information-significant escape depth for Auger electrons (λ), and the surface roughness characterized by a Gaussian distribution with the variance σ. The quantity w was assumed to be equal to the projected range of 500-eV Ar^+ ions with allowance made for the angle of beam incidence (60°) (w = 1.0 nm). The escape depth for Auger electrons, with allowance made for their energy and the collection geometry, was estimated as λ = 0.6 nm. The etching-induced surface roughness in the analyzed zone (the diameter of this zone was 5 μm) was estimated from the steepest experimental slope with the two other parameters of the Auger profiling being fixed. As a result of fitting, we obtained σ = 0.5 nm. In the course of simulation, this quantity was varied, since it included the specific surface roughness of samples.

We calculated the X-ray diffraction spectrum on the basis of a dynamic theory using a recurrent formula which described an addition to the structure of a homogeneous layer. The gradient layers were partitioned into sublayers with x_{In} = const; the number of partitions was sufficiently large so that the discretization did not affect results. We specified the scale coefficients of the profile on the axes of depth and concentration as adjustable parameters. We found that it was sufficient to specify two scale multipliers in the course of fitting the calculated spectrum to the experimental spectrum within the accuracy of measurement. In fact, X-ray diffraction was used to obtain a more accurate normalization of profiles reconstructed using the Auger experiments [18].

3.2. Models of Growth with Segregation

We used two models of segregation in the analysis of experimental data; one of these models is exponential, while the other is kinetic. A thermodynamically equilibrium limit is attained only at low growth rates and high temperatures; because of this circumstance, we did not use the thermodynamic model.

In both models, it is assumed that we have layer growth and the thickness of an InGaAs(100) monolayer (d_{ML}) is equal to the halved lattice constant. At each step of the growth stage, we specify the duration of the process and fluxes of indium (F_{In}) and gallium (F_{Ga}) at the growth surface in fractions of a monolayer per second. It is assumed that arsenic atoms are always available in sufficient amount. The time required to grow a monolayer is defined as $t_{ML} = 1/(F_{In} + F_{Ga})$.

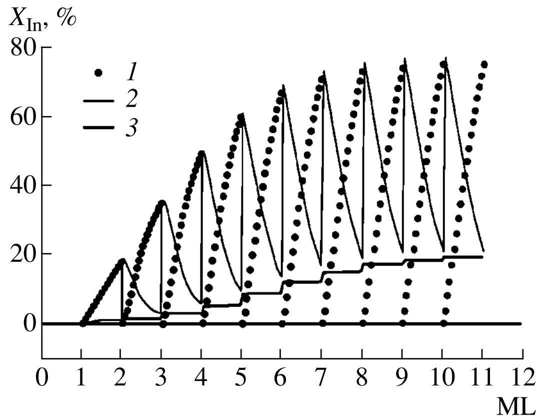

Fig. 1. Representative results of calculations of In content (*1*) at the surface and (*2*) in the upper layer according to the exchange model taking into account variation in this content during the growth of monolayers. Curve *3* represents variations in the In concentration in the second (from the surface) layer of the solid phase.

The model of exponential growth (decay) [1] yields the following expression for the atomic fraction of indium in the *j*th monolayer (ML):

$$X_{In}(j) = X_{lim} - (X_{lim} - X_0)S^j.$$

Here,

$$X_{lim} = \frac{F_{In}}{F_{In}} + F_{Ga}$$

is the atomic fraction at the end of the previous growth stage, and the parameter S is related to the segregation length as

$$S = \exp(-d_{ML}/L_s).$$

This model corresponds to a constant coefficient of concentration distribution between the solid phase and surface, which is correct only for low impurity concentrations. In addition, the model in question does not describe the segregation mechanism; therefore, we have a specific segregation length for each growth temperature. Nevertheless, the general shape of the atomic-fraction profile is described correctly in the first approximation, and the involvement of only a single parameter makes this model attractive for implementation [1–4, 10].

The second (kinetic) model describes the segregation as a combination of two thermally activated processes of exchange of In–Ga atoms between the surface and the solid-phase upper layer [6]. The parameters of the model include the activation energy for exchange between indium atoms in the upper layer and gallium atoms at the surface (E_1), the corresponding energy for exchange between indium atoms at the surface and gallium atoms in the upper layer (E_2), and the frequency factor (ν). If $E_1 < E_2$, we have segregation (ejection) of indium atoms by the growth surface. The growth of a monolayer is described by the following equation [6]:

$$\frac{dX_{In}^{(s)}9t}{dt} = F_{In} + P_1 X_{In}^{(b)}(t)X_{Ga}^{(s)}(t) - P_2 X_{In}^{(s)}(t)X_{Ga}^{(b)}(t). \quad (1)$$

Here, t is time; $X_{In}^{(b)}$ and $X_{In}^{(s)}$ are the atomic fractions of indium in the upper layer and at the surface, respectively; $X_{Ga}^{(b)}$ and $X_{Ga}^{(s)}$ are the corresponding atomic fractions for gallium; $P_1 = \nu\exp(-E_1/kT)$ is the probability (frequency) of exchange between indium in the upper layer and gallium at the surface; P_2 is the probability of the inverse process; k is the Boltzmann constant; and T is the growth temperature. We have $X_{In}^{(b)}(t) + X_{Ga}^{(b)}(t) = 1$ in the solid phase; however, the total content of indium and gallium (in fractions of monolayers) at the surface varies from zero at the beginning of monolayer growth to $X_{In}^{(s)} + X_{Ga}^{(s)} = 1$ at the end of growth. The filled surface layer solidifies and becomes the solid-phase upper layer; thereafter, the process recurs. Diffusion in the bulk and reevaporation from the surface were disregarded since the probability of these processes is lower than that of the exchange between the surface and the upper layer.

In Fig. 1, we show an example of the calculated atomic fraction of indium at the surface (curve *1*) and in the upper layer (*2*); in calculations, we used the exchange model taking into account variations in atomic fractions during growth of monolayers. We specified the fluxes $F_{In} = 0.2$ ML/s and $F_{Ga} = 0.8$ ML/s. The parameters $E_1 = 1.8$ eV, $E_2 = 2.0$ eV, and $\nu = 10^{13}$ s^{-1} were taken from [7]. The growth duration and temperature were 10 s and 500°C, respectively. It can be seen that the curves do not level off (steady-state values are not attained); i.e., the conditions are such that thermodynamic equilibrium is far from being established.

4. RESULTS OF ANALYSIS BASED ON SEGREGATION MODELS

In Fig. 2, circles represent experimental atomic-fraction profiles for indium in the structures grown at 650°C (*A*), at 500°C (*B*), at 650°C with CCl_4 being introduced at the end of growth of each QW (*C*), and at 650°C with the addition of bismuth (*D*). A qualitative analysis of profile *A* clearly indicates that we have indium segregation; i.e., indium is present at the surface of the upper GaAs layer. A decrease in the growth temperature to 500°C (structure *B*) results in the disappearance of In at the surface; i.e., segregation is largely suppressed. Almost the same result is obtained when the upper layer of each of the QWs is etched off (structure *C*). The introduction of bismuth into structure *D* virtually did not affect segregation.

Numerical simulation of growth and layer-by-layer analysis made it possible to select the parameters that ensured good agreement between the calculated and experimental profiles. The growth durations and component fluxes used in the growth model are listed in the table. These parameters correspond to rectangular profiles shown in Fig. 2. In order to fit the calculated profiles to experimental ones, we had to use increased exchange-activation energies ($E_1 = 1.95$ eV, $E_2 = 2.25$ eV) compared to the available published values for MBE (1.8 and 2.0 eV, respectively). If $E_1 = 1.8$ eV, segregation in the course of low-temperature growth (structure *B*) will be even more pronounced than for structure *A*; therefore, the value of E_1 was increased to 1.95 eV, in which case the calculated profile coincides with the experimental profile within measurement accuracy. Similarly, an increase in E_2 made it possible to explain a large amount of indium at the surface of structure *A*. Such an increase in the barrier heights for the outflow of atoms to the surface in the course of MOVPE can be related to stabilization of unsaturated arsenic bonds with hydrogen in the solid-phase upper layer [8].

Etching of the surface of structure *C* with CCl_4 was simulated by removing the solid-phase upper monolayer after the growth of each of the two InGaAs layers. Figure 3 illustrates the process in more detail. Curves *1* and *4* outline the specified rectangular profile and the resulting calculated profile with allowance made for the spread function of the spectrometer; these profiles are the same as those shown in Fig. 2 for structure *C*. Curve *2* in Fig. 3 represents the atomic fraction of indium $X_{In}^{(s)}$ at the surface with allowance made for the etching off of a single monolayer at the points indicated by arrows. The atomic fraction of indium at the end of growth of each monolayer was used as the value of $X_{In}^{(s)}$. Curve *3* illustrates what this atomic fraction would be without etching. A shift of profile *3* is related to a decrease in the total thickness of the structure by two monolayers when the depth *z* is reckoned from the surface. The appreciable difference between profiles *2* and *3* is caused by the fact that, in the exchange model under consideration, the excess indium accumulated as a result of segregation is concentrated in the upper monolayer of the solid phase; it is this monolayer that is etched off. Etching with CCl_4 in the course of MOVPE can be compared with the evaporation of indium from the surface as a result of high-temperature heat treatment in the course of MBE [5].

In the model of layer-by-layer analysis, we specified the depth of the ion-mixing layer $w = 1.0$ nm and the information-significant depth $\lambda = 0.6$ nm. The surface-roughness variance σ was varied, since this parameter is specific for different samples (see table). It can be seen from Fig. 2 that the calculated profiles (lines) coincide closely with the experimental profiles (circles), which validates the models we used.

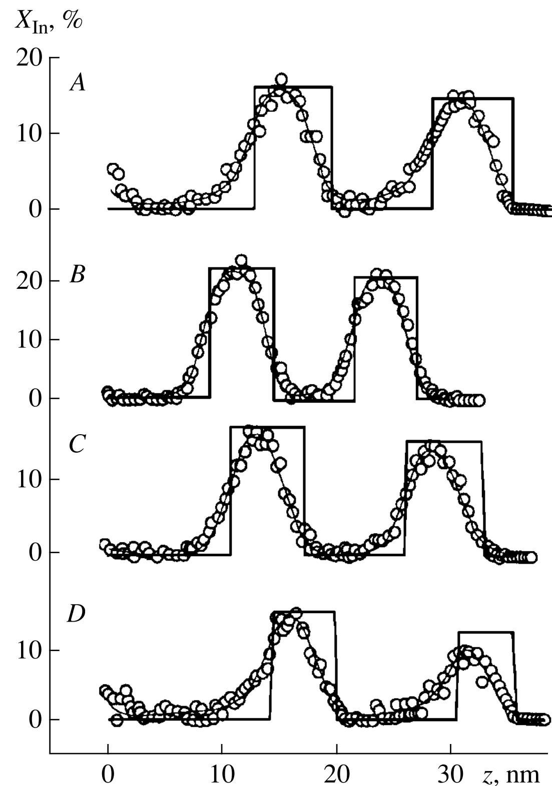

Fig. 2. Experimental (circles) and calculated (lines) profiles of In concentration in structures *A*, *B*, *C*, and *D* with two InGaAs quantum wells. The rectangular profiles illustrate the specified growth model disregarding the effect of segregation and the spread function of the Auger spectrometer. The coordinate *z* is reckoned from the structure surface.

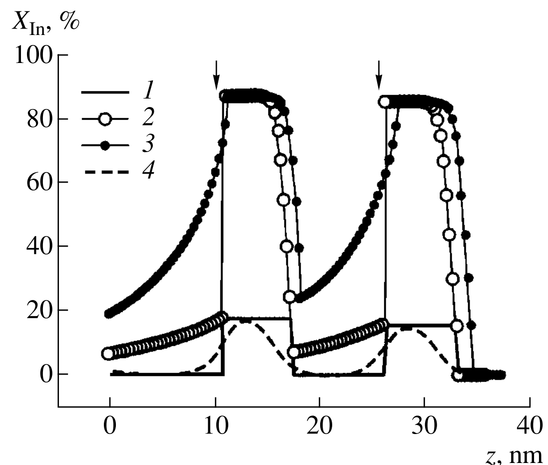

Fig. 3. Calculated In concentration profiles according to the model of the growth process for structure *C* with account taken of etching off of a monolayer at the end of growth of each of the InGaAs layers. The instants of time corresponding to etching are indicated by arrows. Curve *1* corresponds to the specified growth model; circles *2* represent the In concentration at the surface of a growing layer with allowance made for etching; filled circles *3* represent the same dependence with etching being disregarded (for the sake of comparison); and the dotted line *4* represents the calculated In concentration profile with the spread function of the Auger spectrometer taken into account.

The use of an exponential model of segregation also leads to satisfactory agreement between the calculated and experimental profiles for the values of segregation length L_s listed in the table and for $\sigma = 0.5$ nm. It can be seen that both a decrease in the growth temperature and etching off of excess indium partly suppress segregation (the segregation length decreases). The effect of bismuth impurity is insignificant. However, it is impossible to account for a large outflow of indium to the surface of structures *A* and *D* using this simplified model.

5. DISCUSSION

The question arises as to what extent the model, according to which excess indium is located in the upper solid-phase layer, is realistic. In our opinion, the data reported by Garcia *et al*. [19] validate the model. It was observed [19] that the substrate was bent during deposition of the InGaAs layer. The extent of bending first increased during deposition of the layer, then remained constant during interruption (although the As flux was not interrupted), and surprisingly increased again during subsequent overgrowth with pure GaAs. We may suggest the following interpretation of experimental data in the context of the growth model that involves the exchange of atoms between the layer and the surface. In the course of InGaAs layer growth, excess indium content is observed in the upper solid-phase layer; however, this layer differs from bulk InGaAs in its mechanical characteristics since the bonds at its surface are not saturated. As a result, this layer does not contribute to the elastic deformation of the substrate. During an interruption interval, the layer does not grow even though arsenic is still supplied; this absence of growth is caused by the fact that indium appears at the surface, while Ga is not supplied. In the course of subsequent overgrowth with a GaAs layer, exchange occurs; i.e., we have, in fact, a growing InGaAs layer with decreasing indium content, which leads to an increase in the extent of substrate bending. Direct *in situ* measurements of concentrations at the surface and in the bulk [7] corroborate this model of growth in an MBE reactor.

When applying the MBE model of layer growth to MOVPE structures, we should make certain that growth actually proceeds in the layer-by-layer way. As experimental verification, we can use the data of atomic-force microscopy applied to structures that were similar to those under consideration and were grown on substrates with vicinal surfaces (i.e., misoriented by about 0.2° in reference to the main crystallographic directions). Steps that had a 0.3-nm height and were separated by wide terraces were observed at the surface [20]. The validity of the model under consideration is also confirmed by the insignificant roughness of the surface.

The question arises as to whether the suggested interpretation of experimental profiles is unambiguous. Apparently, this interpretation is still ambiguous since we disregarded the kinetics of chemical reactions and the gas-dynamic characteristics of the MOVPE reactor. We can also cite a certain contradiction in the data: in our calculations, the Ga flux for the fourth layer has to be set larger than that for the second layer (see table), although in actual processes the Ga flux was maintained constant for all four layers of the structure. However, the fluxes in the model and in the actual process have a somewhat different meaning: experimentally, we are dealing with trimethylgallium introduced into the reactor, whereas gallium is supplied to the growth surface in the model. In this context, the origin of the aforementioned contradiction remains unclear.

Nevertheless, the results of our study show that the model with segregation can be used to interpret experimental profiles and should be considered as a plausible one for describing the MOVPE process. Differences between the segregation processes in MOVPE and the high-vacuum MBE processes consist in the following: in the former processes, potential barriers for the appearance of cations at the surface are higher and the effect of bismuth as a surfactant differs from that in the latter processes. These differences can be attributed to a higher concentration of hydrogen at the surface in the MOVPE process, in which case hydrogen is used as the carrier gas.

6. CONCLUSIONS

We used a gas-phase reactor with atmospheric pressure to grow a number of structures with double InGaAs QWs; the resulting indium concentration profile was measured using layer-by-layer Auger electron analysis. The growth and analysis processes were simulated using a single computational algorithm; calculated profiles were then fitted to experimental profiles, which made it possible to determine more accurately the parameters of the growth model that involves segregation. The models we used are satisfactorily consistent with experimental data. We revealed the following special features:

(i) A model with thermally activated exchange between a layer and the surface makes it possible to describe the indium profiles in structures grown at various temperatures;

(ii) Activation energies for processes of exchange between indium and gallium atoms were found to be higher than those reported for the high-vacuum (MBE) processes. We suggest that this observation is due to stabilization of the growth surface with hydrogen, which is present in the reactor as the carrier gas;

(iii) Introduction of bismuth into the reactor did not affect the segregation parameters, in contrast to what takes place in the MBE processes, which can also be related to the surface state; the latter differs from that under high-vacuum conditions;

(iv) Introduction of CCl_4 at the end of InGaAs layer growth appreciably reduced the effect of segregation on

the indium profile in the structure, which was attributed to the etching off of the upper layer where excess indium was located.

ACKNOWLEDGMENTS

This study was supported by the Russian Foundation for Basic Research (project nos. 00-02-16141 and 01-02-16441), by the Special Federal Scientific and Technological Programs “The Physics of Solid-State Nanostructures” and “Surface Atomic Structures”, and by NATO (project no. SfP-973799, “Semiconductors”).

REFERENCES

1. K. Muraki, S. Fukatsu, and Y. Shiraki, Appl. Phys. Lett. **61**, 557 (1992).
2. H. Toyoshima, T. Niwa, J. Yamazaki, and A. Okmato, Appl. Phys. Lett. **63**, 821 (1993).
3. P. Yashar, M. R. Pillai, J. Mirecki-Millunchik, and S. A. Barnett, J. Appl. Phys. **83**, 2010 (1998).
4. M. R. Pillai, S.-S. Kim, S. T. Ho, and S. A. Barnett, J. Vac. Sci. Technol. B **18**, 1232 (2000).
5. K.-J. Chao, N. Liu, and C.-K. Shih, Appl. Phys. Lett. **75**, 1703 (1999).
6. O. Dehaese, X. Wallart, and F. Mollot, Appl. Phys. Lett. **66**, 52 (1995).
7. Y.-J. Zheng, A. M. Lam, and J. R. Engstrom, Appl. Phys. Lett. **75**, 817 (1999).
8. M. Sato and Y. Horikoshi, J. Appl. Phys. **69**, 7697 (1991).
9. F. Bugge, U. Zeimer, M. Sato, *et al.*, J. Cryst. Growth **183**, 511 (1998).
10. A. A. Marmalyuk, O. I. Govorkov, A. V. Petrovsky, *et al.*, in *Proceedings of 9th International Symposium on Nanostructures: Physics and Technology* (St. Petersburg, Russia, 2001), p. 63.
11. S. Yu. Karpov and Yu. N. Makarov, in *Proceedings of 9th International Symposium on Nanostructures: Physics and Technology* (St. Petersburg, Russia, 2001), p. 47.
12. T. S. Yeoh, R. B. Swint, A. E. Huber, *et al.*, Appl. Phys. Lett. **79**, 221 (2001).
13. J. A. Gupta, S. P. Watkins, A. D. Crozier, *et al.*, Phys. Rev. B **61**, 2073 (2000).
14. T. S. Babushkina, L. M. Batukova, B. N. Zvonkov, and V. N. Portnov, Izv. Ross. Akad. Nauk, Ser. Neorg. Mater. **28** (2), 299 (1992).
15. A. A. Biryukov, B. N. Zvonkov, E. A. Uskova, *et al.*, in *Proceedings of Meeting on Nanophotonics* (Nizhni Novgorod, 2001), p. 98.
16. M. N. Drozdov, V. M. Danil’tsev, Yu. N. Drozdov, *et al.*, Pis’ma Zh. Tekh. Fiz. **22** (18), 61 (1996) [Tech. Phys. Lett. **22**, 761 (1996)].
17. S. Hoffman, Rep. Prog. Phys. **61**, 827 (1998).
18. Yu. N. Drozdov, M. N. Drozdov, V. M. Danil’tsev, *et al.*, in *Proceedings of Meeting on Nanophotonics* (Nizhni Novgorod, 2000), p. 246.
19. J. M. García, J. P. Silveira, and F. Briones, Appl. Phys. Lett. **77**, 409 (2000).
20. Yu. N. Drozdov, N. V. Vostokov, D. M. Gaponova, *et al.*, in *Abstracts of 5th Russian Conference on Physics of Semiconductors* (Nizhni Novgorod, 2001), Vol. 2, p. 324.

Translated by A. Spitsyn

Semiconductors, Vol. 37, No. 2, 2003, pp. 200–206. Translated from Fizika i Tekhnika Poluprovodnikov, Vol. 37, No. 2, 2003, pp. 209–215.
Original Russian Text Copyright © 2003 by Radantsev, Ivankiv, Yafyasov.

LOW-DIMENSIONAL SYSTEMS

Rashba Effect in Inversion and Accumulation InAs layers

V. F. Radantsev*, I. M. Ivankiv, and A. M. Yafyasov**^**
** Gorkii Ural State University, ul. Lenina 51, Yekaterinburg, 620083 Russia*
e-mail: victor.radantsev@usu.ru;
*** St. Petersburg State University, Universitetskaya nab. 7/9, St. Petersburg, 198504 Russia*
^e-mail: yafyasov@desse.phys.spbu.ru
Submitted April 11, 2002; accepted for publication June 3, 2002

Abstract—Self-consistent calculations of the Rashba splitting both in inversion and accumulation InAs layers were carried out using a method based on reducing 6 × 6 and 8 × 8 Kane matrix equations to a Schrödinger-type equation. Disregarding the Γ_7-band contribution yielded a splitting magnitude overestimated by 50%. The essentially nonlinear dependence of splitting on the two-dimensional (2D) wavevector k restricts the applicability of the Rashba parameter α (coefficient at the k-linear term in the spectrum), including its value at the Fermi level, because of a strong dependence of the latter on the approximations applied to the two-dimensional spectrum. The relative differences $\Delta n/n$ of the spin-split subband populations, calculated for the inversion layer, were found to be 2–3 times lower than those measured by Matsuyama *et al.* (see text). The experimental study of accumulation InAs layers showed that the corresponding value $\Delta n/n$ does not exceed the calculated one, ~0.02. The approach employed to describe the 2D spectrum (including spin–orbit splitting) was also shown to be adequate when applied to the case of quasi-classical quantization in a classically self-consistent surface potential. © *2003 MAIK “Nauka/Interperiodica”.*

The Rashba effect (spin–orbit splitting of the two- and one-dimensional spectra in asymmetric quantum wells (QWs) [1–3]), which forms the basis of the concept for a promising spintronics device, i.e., a spin field-effect transistor [4], is attracting considerable attention from experimenters [5] and theorists [6]. Most of the studies in this line of inquiry are concerned with heterostructures based on InGaAs with asymmetric QWs. However, in recent years, emphasis has been placed on metal–insulator–semiconductor (MIS) structures and materials with a narrower Kane gap [7, 8]. The Rashba splitting in these systems should be most pronounced due to small effective masses, a heavier spin–orbit coupling, and extremely asymmetric potential wells of inversion and accumulation layers. The Rashba parameters α obtained in [7] for inversion InAs layers not only exceed those in heterostructures, but also exhibit a significantly heavier dependence on an applied external electric field, which is a critical factor from the viewpoint of field-effect transistor development.

In contrast to heterostructures, where the confining potential is often poorly known, the Rashba effect can be calculated reliably enough for MIS structures. The theoretical estimates of α obtained in [7] agree well with the experimental data of the same study. However, the validity of the approximations used in [7] causes serious doubts. This is true for the model of a triangular potential well, which is absolutely inadequate for the case of surface QWs in narrow-gap semiconductors even with respect to the number of populated two-dimensional (2D) subbands, not to mention the Rashba effect, which is very sensitive to the shape of the potential. The same is also valid for a two-band approximation ignoring the spin-split-off valence band in the initial volume Hamiltonian, which can have a significant effect on the potential and 2D spectrum parameters, since the spin–orbit splitting $\Delta = \Gamma_8 - \Gamma_7$ of the InAs valence band is close to the Kane gap $E_g = \Gamma_6 - \Gamma_8$. The wavevector-linear approximation applied in [7] to the spin–orbit splitting of the 2D spectrum is also inconsistent with the Hamiltonian of the system with the splitting saturated as the 2D wave vector k increases [9–11].

In this paper, we report results of the self-consistent calculation of the 2D spectrum in inversion and accumulation InAs layers using a realistic three-band Kane model with successive consideration of the effects of nonparabolicity and interband mixing by the electrostatic surface potential. We also discuss experimental data on accumulation layers in InAs-based MIS structures. The spectrum and experimentally studied parameters of 2D subbands are theoretically described within the approach [10] based on the reduction of the initial matrix equation to a Schrödinger-type equation. However, [10] is based on a two-band Hamiltonian that does not yield the dependence of the Rashba splitting on the parameter Δ, whereas the effect itself is directly caused by spin–orbit coupling. The two-band model corresponding to the limiting case of $\Delta \longrightarrow \infty$ is valid for narrow-gap semiconductors like HgCdTe with $\Delta \gg E_g$. However, as indicated above, its validity seems to be doubtful in the case of 2D InAs-based systems, especially when describing spinor-type effects.

Without a magnetic field, taking the Γ_7 band into consideration readily fits with the scenario of [10] and the problem can be reduced to the following Schrödinger-type equation:

$$\frac{d^2\varphi^\pm}{dz^2} + (K^\pm(E, V(z), k))^2\varphi^\pm = 0, \quad (1)$$

$$(K^\pm)^2 = \frac{3E_+E_-}{2P^2}C_{\rm KG} - k^2 - \frac{1}{2E_+}\frac{d^2V}{dz^2}C_{r1} - \frac{3}{4}\left(\frac{1}{E_+}\frac{dV}{dz}\right)^2 C_{r2} \pm \frac{k}{2E_+}\frac{dV}{dz}C_{\rm so}, \quad (2)$$

where P is the Kane matrix element of the momentum operator,

$$E_+ = E - V(z) + E_g, \quad E_- = E - V(z)$$

(the energies are measured from the band Γ_6 bottom), and the factors

$$C_{\rm KG} = 1 - \frac{E_\Delta}{3E_\Delta + 2},$$

$$C_{r1} = 1 - \frac{E_\Delta}{(E_\Delta + 1)(3E_\Delta + 2)},$$

$$C_{r2} = 1 - \frac{1}{3}\frac{E_\Delta(4 + 19E_\Delta + 18E_\Delta^2)}{(3E_\Delta + 2)^2(E_\Delta + 1)^2},$$

$$C_{\rm so} = 1 - \frac{E_\Delta(3E_\Delta + 1)}{(E_\Delta + 1)(3E_\Delta + 2)},$$

defined only by the ratio

$$E_\Delta = \frac{E_+}{\Delta},$$

describe the Γ_7 band contribution. In contrast to the direct numerical integration of initial matrix equations, this approach allows easy extraction of the terms responsible for the nonparabolicity effects (the first two terms, an analogue of the Klein–Gordon–Fock equation in the corresponding relativistic problem) and the spinor-type effects, i.e., the resonance interband mixing (the third and fourth terms) and the spin–orbit splitting described by the last term linear in k and the electric field. From the standpoint of the problem under consideration, an important advantage is the possibility of a direct comparison of commonly used methods based on an approximate description of spin–orbit splitting.

In these methods, a phenomenological term with the Rashba parameter, which is linear with respect to the 2D quasimomentum, is introduced into the dispersion relations of the electron spectrum of the size quantization subbands calculated ignoring the spin effects.

At $\Delta \longrightarrow \infty$, the factors C_i in relation (2) describing the effects of the interaction with the Γ_7 band are equal to unity and, to the accuracy of notation, we obtain the equations of [10]. However, these factors, except for the spin–orbit term, do not drastically change in another extreme case, $\Delta \longrightarrow 0$. The factors C_{r1} and C_{r2} at $\Delta = 0$ are also equal to unity (at an arbitrary E_Δ, they differ from unity by no more than 15%). As for the Klein–Gordon term, the factor $C_{\rm KG}$, which depends on Δ, is equal to 3/2 in the limit of $\Delta \longrightarrow 0$, which corresponds to mass renormalization at the conduction band bottom at $\Delta \longrightarrow 0$ in comparison with the case $\Delta \longrightarrow \infty$. Thus, the consideration of the Γ_7-band contribution should not cause significant variations in the 2D subband parameters calculated ignoring spin–orbit splitting, which is confirmed by numerical calculations (see below).

Only the spin–orbit term shows significant changes in comparison with the two-band model. This term is Δ-linear at small Δ/E_g; in the limit $\Delta \longrightarrow 0$, the splitting according to the Rashba mechanism disappears. If we introduce the volume effective mass at the conduction band bottom,

$$m_b = \frac{3\hbar^2 E_g(E_g + \Delta)}{2P^2(3E_g + 2\Delta)},$$

it becomes evident that the spin–orbit term in the resulting effective potential

$$V_{\rm so} = \frac{\hbar^2}{2m_b}\frac{k}{2E_+}\frac{dV}{dz}C_{\rm so} = \frac{\hbar^2}{2m_b}\frac{\Delta(2E_+ + \Delta)}{E_+(E_+ + \Delta)(3E_+ + 2\Delta)}k\frac{dV}{dz} \quad (3)$$

is similar in structure to that derived in [11, 12] (and coincides with it in the limit of large E_g) as a correction to the one-band approximation,

$$V_{\rm so} = \alpha k = \alpha_m k\frac{dV}{dz},$$

with the coefficient

$$\alpha_m = \frac{\hbar^2}{2m_b}\frac{1}{E_g}\frac{\Delta(2E_g + \Delta)}{(E_g + \Delta)(3E_g + 2\Delta)} = \frac{P^2}{3E_g^2}\frac{\Delta(\Delta + 2E_g)}{(\Delta + E_g)^2} \quad (4)$$

depending on the parameters of the band structure.

In the self-consistent solution to Eq. (1) and the Poisson equation, we used the model of a box with a fictitious rear wall spaced by a distance L greatly exceeding the Debye screening length (the Thomas–Fermi length in accumulation layers) L_D, as well as the model with zero boundary conditions for the wave function at the front (the interface with an insulator) and rear walls. The box sizes were determined from the condition that the solution be independent of L (as a rule, this is met to a high accuracy even at $L \approx 5L_D$). The results calculated for the inversion InAs channel with $N_A - N_D = 1.8 \times 10^{17}$ cm^{-3} (the parameters of the material studied in [7]) and the accumulation InAs layer with $N_D - N_A = 1.8 \times 10^{17}$ cm^{-3} (the parameters of the

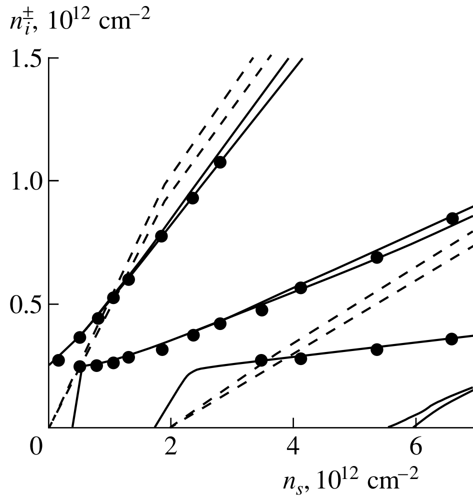

Fig. 1. Spin subband population versus the total surface electron density for accumulation (solid lines) and inversion (dashed lines) InAs layers, calculated using the three-band Kane model and experimentally determined (circles).

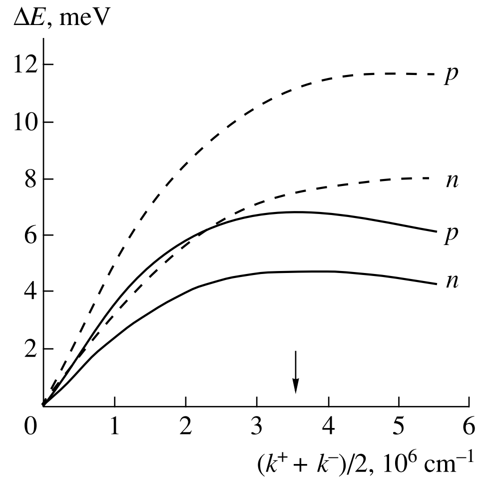

Fig. 2. Energy splitting calculated versus the wave vector using the three- (solid lines) and two-band (dashed lines) models for the main subband of accumulation (n) and inversion (p) InAs layers at $n_0 = 2 \times 10^{12}$ cm^{-2}. The arrow corresponds to $k = k_F$.

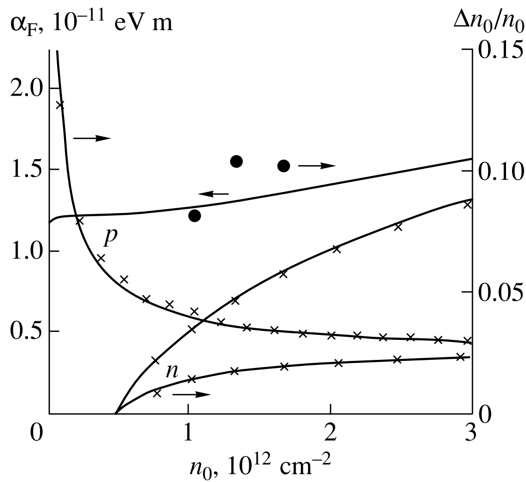

Fig. 3. Concentration dependences of $\Delta n_i/n_i$ and the Rashba parameter (in approximation (6)) calculated using the three-band model for the main subband of accumulation (n) and inversion (p) InAs layers. Dots and crosses correspond to the experimental values $\Delta n_i/n_i$ from [7] and the quasi-classical calculation, respectively.

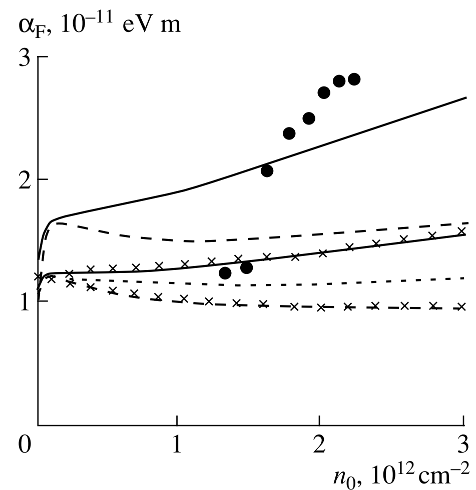

Fig. 4. Concentration dependences of the Rashba parameter for the main subband calculated in the two- (two upper curves) and three-band approximations for the inversion InAs layer, using approximations (6) (solid lines) and (5) (dashed lines), as well as the parabolic approximation (dotted lines). Dots and crosses correspond to the data of [7] and the quasi-classical calculation, respectively.

sample we studied, see below) are shown in Figs. 1–4. The dispersion relations calculated ignoring the spin–orbit term within both two- and three-band models in all of the 2D subbands and in the entire actual interval of band bendings and energies are well described by a Kane-type dispersion relation (a parabolic approximation is unsatisfactory even at relatively small band bendings),

$$E_i^{\pm} = \sqrt{(s_i \hbar k)^2 + (m_i s_i^2)^2} - m_i s_i^2 \pm \alpha_i k, \tag{5}$$

where the parameters approximating the spectrum, i.e., the subband "rest masses" m_i and the Kane velocities s_i, are uniquely determined from the calculated Fermi energies E_F, quasi-momenta k_F, and cyclotron masses in the ith subband; and α_i is the Rashba parameter α in the ith subband. In view of further discussion, we wrote this expression taking into account the Rashba splitting (usually ignored at this stage) in the form conventionally used when analyzing experimental data.

According to what was stated above, when ignoring the Rashba term in ratio (2) (or when averaging over

two spin portions of the spectrum), the results calculated using the three- and two-band Kane models are almost identical. In particular, in the case of the distribution of carriers over 2D subbands (see Fig. 1), which is usually studied experimentally, the differences between the concentrations averaged over two portions of the spectrum for both models are virtually imperceptible on the plot scale. The features of the accumulation layer (including those related to the spin effects) in the concentration region near the subband population onset are caused by a degenerate continuum of bulk electrons and call for special discussion, which is beyond the scope of this study.

However, the spin–orbit splitting data calculated using the two- and three-band Kane approximations significantly differ. Disregarding interaction with the Γ_7 band results in the overestimation of the splitting at the Fermi level by more than one-and-a-half times (see Fig. 2). As is readily seen from Eqs. (1) and (2), the Rashba splitting $\Delta E = E^+ - E^-$ is nonlinear in k because of the nonparabolicity of the system (the first term in Eq. (2) involves squared energy).

However, when analyzing the Rashba splitting parameter, it is conventionally assumed that ΔE can be described by a term that is linear with respect to k and the electric field in Eq. (2). The results of numerical calculation indicate that a split spectrum cannot be described even qualitatively using a parabolic approximation or approximation (5). The data presented hereinafter are related to the main subband $i = 0$. However, the results for excited subbands are very close to the corresponding data calculated for $i = 0$ at identical subband concentrations n_i. A much better fit is attained when using the approximation (more consistent with the Kane Hamiltonian, see [9])

$$E^{\pm} = \sqrt{(s_i\hbar k)^2 + (m_i s_i^2)^2 \pm 2m_i s_i^2 \alpha_i k} - m_i s_i^2 \quad (6)$$

with the saturated splitting $\Delta^{\max} = 2\alpha_i m_i s_i/\hbar$. However, the calculated dependences $\Delta E(k)$ do not simply level off at large k (as Eq. (6) shows). The splitting ΔE decreases after reaching a maximum at k close to k_F and disappears in the limiting case $k \longrightarrow \infty$.

Thus, to correctly describe the spectrum, the phenomenological parameter α_i in relations (5) and (to a significantly smaller extent) (6) should be treated as depending on the wave vector. As for its value α_F at the Fermi level, which is, as a rule, used as a measure of the spin–orbit splitting, one important point to remember is the ambiguity related to the strong dependence of α_F on the analytical approximations used, which are frequently inadequate. A characteristic of the Rashba effect that is much more convenient (especially when comparing the magnitudes of an effect in various materials and structures), independent from the models used, and, most importantly, directly measured is the "polarization degree"

$$\frac{\Delta n_i}{n_i} = \frac{n_i^- - n_i^+}{n_i^- + n_i^+},$$

where $n_i^{\pm}$ is the population of spin subbands. We emphasize that this parameter also immediately defines the phase difference "collected" within the length L of the spin transistor channel,

$$\theta = L\Delta k_F \approx (\Delta n_i/n_i)\sqrt{n_i/2}.$$

The values of $\Delta n_i/n_i$ calculated within the three-band approximation, as well as the values of α_F calculated from $\Delta n_i/n_i$ using approximation (6), are shown in Fig. 3. As the number of the populated 2D subbands (see Fig. 1), the value of $\Delta n_i/n_i$ and the run of its dependence on concentration are very sensitive to the substrate type and doping level. Although the absolute value of the splitting ΔE via the Rashba mechanism increases with n_i, the relative splitting $\Delta E/E_F$ and the polarization degree in the inversion layer (p-type substrate) decreases especially in the region of small n_i. This is related to an additional (most significant at small n_i) contribution of the electric field caused by the depletion layer charge ($N_{depl} \approx (1.3–1.5) \times 10^{12}$ cm^{-2}) to the splitting. We note that the Rashba parameter at the Fermi level $\alpha_F = \sqrt{\pi}\hbar^2(\sqrt{n_-} - \sqrt{n_+})/m_i$ (calculated in approximation (6)) increases in this case. In contrast, in the accumulation layer, the splitting ΔE and $\Delta n_i/n_i$ are smaller than in an undoped material due to field screening by the degenerate gas of continuum electrons. As the subband concentrations increase, the contribution of these competing factors decreases. In the region of rather high n_i, when the parameters of the space-charge region are mainly controlled by 2D electrons, the differences in ΔE, $\Delta n_i/n_i$, and α_F decrease for the inversion and accumulation layers, approaching the corresponding values for undoped InAs (Fig. 3).

As was mentioned above, the phenomenological parameter α is not a sufficiently good characteristic of the Rashba effect in the Kane-type semiconductors (where this phenomenon was observed experimentally) due to the strong energy dependence and the approximations used to describe the spectrum. This is illustrated by the concentration dependences of α_F shown in Fig.4 and calculated from the values n_i^- and n_i^+ for various Kane approximations and at various analytical approximations of the spectrum $E(k)$. Only in the region of extremely small band bendings, when the effects of nonparabolicity are weak, the parameter α_F does not significantly depend on the type of approximation. As the surface QW deepens, approximations (5) and (6) yield, respectively, smaller and larger values of

α_F in comparison with the simplest parabolic approximation. Within the latter, the Rashba parameter is weekly sensitive to n_i, i.e., to the electric field near the surface. As a result, the dependences of α_F on the electric field applied to the MIS structure (the most important parameter from the viewpoint of the implementation of a field-effect transistor), calculated on the basis of approximations (5) and (6), significantly differ. Approximation (5), which is linear in k, predicts a decrease in α_F as n_i increases at $n_i < 2 \times 10^{12}$ cm^{-2}, whereas approximation (6) (closest to the numerical calculation results) yields an increase in the Rashba parameter with the field. As in the case of the parameters ΔE and $\Delta n_i/n_i$, the two-band approximation yields an overestimate of α_F by more than 1.5 times; however, this approximation retains almost unchanged dependences of $\alpha_F(n_i)$.

The results of calculations are compared in Fig. 4 to the experimental data [7] obtained by measuring the subband populations in approximation (5) with the dispersion parameters of a nonsplit spectrum, which were calculated by the authors of [7] using the two-band model for the approximation of a triangular potential well. In spite of the fact that the experimental values of α_F conform quite well to the data we calculated at the lowest (in the range studied in [7]) concentrations, the calculated concentration dependence $\alpha_F(n_i)$ is weaker than that of [7] by an order of magnitude. Such pronounced disagreement cannot be caused solely by the inadequate approximations used in [7] when calculating $\alpha_F(n_i)$. The degrees of polarization $\Delta n_i/n_i$ are also two–three times higher than the calculated data (Fig. 3), at least in the case of the subband concentrations, at which such data may be extracted from the oscillatory curves of Fig. 1 in [7].

Although there are several mechanisms which can cause the spin–orbit splitting to increase, the causes of such significant disagreement remain unclear. The renormalization due to the correlation–exchange corrections [13] cannot play a significant role because of the small parameters of the electron–electron interaction in narrow-gap materials. The calculations based on the results of [13] yield an increase in the splitting magnitude no larger than 5–15%. We note that the substitution of the zero boundary conditions used above for the spinor components corresponding to the Γ_6 band with the zero-flux conditions for a complete spinor [14] yields, in general, a slightly larger magnitude of splitting; however, in this case the increase also does not exceed 20–30%.

In the case of heterostructures with asymmetrical QWs, there exists an additional and rather significant (probably dominant in the structures with narrow wells) mechanism related to the contribution of states at the interface to the Rashba splitting; i.e., the difference in the boundary conditions for various spin components of the wave function. However, in the case of MIS structures, there are a number of factors, in our opinion, suggesting that the role of this mechanism cannot be dominant. The potential barrier (higher than 2.5–3 eV) at the interface with an insulator is much higher than in semiconductor heterostructures, and the boundary conditions are close to zero. Thus, the difference in the boundary conditions for two spin polarizations should also be slight. The significant width of the QW in MIS structures based on narrow-gap materials and the large contribution of the field effect inside the well (in contrast to the heterostructures whose bands inside the well are almost flat) represent other factors counting in favor of the aforementioned assumption. The latter conforms to the results calculated in [11], showing that the influence of the interface in asymmetrical heterostructures is insignificant even at a barrier lower than 1 eV in the case of a flat potential profile inside a well wider than 5–6 nm, which is lower than the values in the system under consideration by almost an order of magnitude.

It is noteworthy that there are experimental arguments in favor of this reasoning. The 2D gas parameters in the accumulation layers we studied (see below) are absolutely insensitive to the material used for the gate insulator. In spite of the fact that we failed to observe Rashba splitting, because of an insufficient number of oscillations, the study [15] of a related system based on narrow-gap II–VI compounds (HgCdTe and HgMnTe) shows the Rashba splitting to be independent of the parameters and even the type of insulator (anodic oxide, SiO_2, Al_2O_3, and Blodgett–Langmuir films). The "Rashba polarization" $\Delta n_i/n_i$ when there are equal subband populations is uniquely defined by the band parameters of the semiconductor and doping.

In this context, we note that consideration of the boundary conditions at the interface with an insulator encounters serious difficulties which, in some respects, are of a fundamental nature. Furthermore, there are no reliable data on the basic energy parameters of actual interfaces in MIS structures. As a rule, amorphous or semiamorphous materials (anodic oxides, SiO_2) or even organic compounds (Blodgett–Langmuir films, liquid crystals) are used as the gate insulator. In these cases, the description of the energy spectrum of the insulator on the basis of the symmetry classification (as a rule, within the Kane approach) of the semiconductor energy bands, hence, the adequacy of the calculation methods (joining of Kane components of wave functions), applied to semiconductor heterostructures seems to be doubtful.

Also noteworthy is the probable contribution of error in determining the experimental populations of the spin subbands to the observed disagreement between theory and experiment. The inversion layers studied in [7] exhibited a single node of beats. However, it is easy to ascertain that the values $n_i^{\pm}$ and spe-

cifically $\Delta n_i/n_i$ extracted from the Fourier spectra are very sensitive to the range of magnetic fields used in a Fourier analysis even with 2–3 beat nodes. The splitting $\Delta n_i/n_i$ for the intervals between beat antinodes can exceed that for intervals ending near the nodes by as much as 50%. This factor can have the most significant effect (and this is confirmed by simulation) on the concentration dependences of α_F due to the beat node displacement over the magnetic field, observed in [7]. It is noteworthy that α_F is in fact independent of concentration in the region $n_i \gtrsim 2 \times 10^{12}$ cm^{-2}, where the oscillation amplitudes in [7] are rather high and a pronounced splitting of the Fourier spectrum is observed.

It is somewhat unexpected that the values $\Delta n_i/n_i$ determined in [7] are virtually the same as in the inversion layers of narrow-gap HgCdTe ($E_g = 0.05$–0.1 meV) [10]. At the same time, the effect in InAs is expected to be at least three times weaker due to significantly wider Kane gaps and a smaller spin–orbit splitting of the valence band (the simplest estimation may be carried out using Eq. (4)). Meanwhile, in the case of HgCdTe, disagreement between theory and experiment (the three- and two-band approximations yield close results, in this case, because of the inequality $\Delta \gg E_g$) is not far beyond the limit of error.

We know of no experimental studies of the Rashba effect for accumulation layers. Therefore, we prepared and studied structures formed of Pb, anodic oxide, and n-InAs with a donor concentration equal to the acceptor concentration in the inversion layers studied in [7]. Since conventional galvanomagnetic methods are inapplicable to such structures because the accumulation layer conductance is shunted by bulk material, magnetic oscillations of the capacitance were studied, which immediately yielded data on the density of states in the magnetic field. According to Fig. 3, the effects calculated in the inversion and accumulation layers slightly differ in the region of subband concentrations $n_i \approx 2 \times 10^{12}$ cm^{-2}. Although pronounced capacitance oscillations corresponding to the population of up to three 2D subbands were observed in the structures under study up to ~30 K, no beats caused by the Rashba splitting were observed for any subband. At the same time, the distribution of carriers over subbands, as well as the cyclotron masses determined from the temperature dependences of oscillation amplitudes, are in good agreement with the calculated data (see Fig. 1). In general, the absence of beats in accumulation layers does not contradict theoretical predictions. According to the data of Fig. 3, in this case, we have $\Delta n_i/n_i \approx 0.02$ and the expected number of oscillations between neighboring beat nodes is $N = 1/(2\Delta n/n) \approx 25$, whereas no more than ten oscillations from a single subband (as in the inversion layers studied in [7]) were experimentally observed.

In conclusion, we will mention another methodical advantage of the approach used for the calculation of the 2D spectrum. As was repeatedly noted beginning from the Ando study [16], the quasi-classical approach is adequate to describe the 2D spectrum in surface layers of narrow-gap semiconductors using the simplest two-band approximation (ignoring the heavy portion of the Γ_8 band). As was shown above, this approach is valid with respect to the parameters unrelated to spin effects. Since we are dealing with a Schrödinger-type equation within the method used in this study, a quasi-classical approach can also be used to evaluate the spinor-type effects, including interband mixing and spin–orbit splitting. The results of such calculations (as an example, some of them are shown in Figs. 3 and 4) also confirm the adequacy of the quasi-classical approximation with respect to these effects. The differences in ΔE, $\Delta n_i/n_i$, and α, which were self-consistently calculated both within the three- and two-band approximations for identical 2D concentrations in the case of quasi-classical quantization of the spectrum in a classically self-consistent surface potential well, do not exceed 1–2%. These differences are much less than typical experimental errors. Meanwhile, the algorithms employed in the quasi-classical calculation are incomparably simpler, and the computing time is shorter by four–five orders of magnitude. The same is valid for the calculation of the differences between the "resonance shift" of the energy levels due to mixing of the 2D layer states and the 3D states of the valence band by the surface potential.

ACKNOWLEDGMENTS

This study was supported by the Ministry of Education (project no. E00-3.4-278), the federal program "Russian Universities", and the US CRDF (project REC-005).

REFERENCES

1. É. I. Rashba, Fiz. Tverd. Tela (Leningrad) **2**, 1224 (1960) [Sov. Phys. Solid State **2**, 1109 (1960)].
2. F. J. Ohkawa and Y. Uemura, J. Phys. Soc. Jpn. **37**, 1325 (1990).
3. Yu. A. Bychkov and E. I. Rashba, J. Phys. C (Amsterdam) **17**, 6039 (1984).
4. S. Datta and B. Das, Appl. Phys. Lett. **56**, 665 (1990).
5. D. Grundler, Phys. Rev. Lett. **84**, 6074 (2000); X. C. Zhang, A. Pfeuffer-Jeschke, K. Ortner, *et al.*, Phys. Rev. B **63**, 245305 (2001); C. H. Rowe, J. Nehls, R. A. Stradling, *et al.*, Phys. Rev. B **63**, 201307 (2001); V. B. Bozhevol'nov, I. M. Ivankiv, V. F. Radantsev, and A. M. Yafyasov, Zh. Éksp. Teor. Fiz. **119**, 154 (2001) [JETP **92**, 135 (2001)]; C. M. Hu, J. Nitta, A. Jensen, *et al.*, Phys. Rev. B **63**, 125333 (2001).
6. P. Pfeffer and W. Zawadzki, Phys. Rev. B **59**, R5312 (1999); R. Winkler, Phys. Rev. B **62**, 4245 (2000);

D. Grundler, Phys. Rev. B **63**, 161307 (2001); M. V. Entin and L. I. Magarill, Phys. Rev. B **64**, 085330 (2001).

7. T. Matsuyama, R. Kürsten, C. Meißner, *et al.*, Phys. Rev. B **61**, 15588 (2000).
8. V. F. Radantsev, A. M. Yafyasov, V. B. Bogevolnov, and I. M. Ivankiv, J. Phys.: Condens. Matter **13**, 851 (2001).
9. V. F. Radantsev, Zh. Éksp. Teor. Fiz. **96**, 1793 (1989) [Sov. Phys. JETP **69**, 1012 (1989)].
10. V. F. Radantsev, T. I. Deryabina, G. I. Kulaev, and E. L. Rumyantsev, Phys. Rev. B **53**, 15756 (1996).
11. E. A. De Andrada, E. Silva, G. C. La Rocca, *et al.*, Phys. Rev. B **55**, 16293 (1997).
12. L. G. Gerchikov and A. V. Subashiev, Fiz. Tekh. Poluprovodn. (St. Petersburg) **26**, 131 (1992) [Sov. Phys. Semicond. **26**, 73 (1992)].
13. G. H. Chen and M. E. Raikh, Phys. Rev. B **60**, 4826 (1999).
14. G. E. Marques and L. J. Sham, Surf. Sci. **113**, 131 (1982).
15. V. F. Radantsev, A. M. Yafyasov, and V. B. Bogevolnov, Semicond. Sci. Technol. **16**, 320 (2001).
16. T. Ando, J. Phys. Soc. Jpn. **54**, 2676 (1985).

Translated by A. Kazantsev

Semiconductors, Vol. 37, No. 2, 2003, pp. 207–209. Translated from Fizika i Tekhnika Poluprovodnikov, Vol. 37, No. 2, 2003, pp. 216–218.
Original Russian Text Copyright © 2003 by Burbaev, Kurbatov, Pogosov, Rzaev, Sibel'din.

LOW-DIMENSIONAL SYSTEMS

Photoluminescence from Germanium Quantum Wells and Quantum Dots in Silicon Grown by MBE at Low Temperature

T. M. Burbaev, V. A. Kurbatov*, A. O. Pogosov, M. M. Rzaev, and N. N. Sibel'din

Lebedev Physical Institute, Russian Academy of Sciences, Leninskiĭ pr. 53, Moscow, 119991 Russia

**e-mail: kurbatov@mail.lebedev.ru*

Submitted May 28, 2002; accepted for publication June 3, 2002

Abstract—The low-temperature ($T = 2$ K) photoluminescence (PL) has been studied in Si/Ge structures grown by MBE at a low (250–350°C) temperature of Ge deposition. The luminescence spectra change dramatically when the average thickness of the Ge layer exceeds six monolayers. In this case, the PL line from the pseudomorphic layer (quantum well) retains its spectral position and increases in intensity at the expense of the luminescence line from islands (quantum dots), which then totally fades. The data obtained indicate a considerable difference between the epitaxial growth modes dominating in low and conventional (500–700°C) temperature ranges. *© 2003 MAIK "Nauka/Interperiodica".*

It is generally assumed that the epitaxy of Ge on Si proceeds via the Stranski–Krastanow mechanism: at the initial stage, a continuous pseudomorphic Ge layer (wetting layer) is formed, which behaves like a quantum well (QW) for holes in an Si matrix; after a critical thickness is reached, layer-by-layer growth gives way to the formation of self-organized nanocrystals [islands and quantum dots (QD)] [1]. This is confirmed by experimental studies of structures grown at epitaxial temperatures of 500–750°C [2–4]. At the same time, it is generally assumed that the formation of islands is suppressed at epitaxial temperatures of 360°C or lower [4] owing to the low diffusion rate of adatoms. This assumption, however, contradicts the results of several studies of islands produced at epitaxial temperatures of 200–300°C [5–7].

We present photoluminescence (PL) data for Si/Ge structures grown at low (250–350°C) temperatures which demonstrate anomalous behavior of photoluminescence from the Ge QW and the QD in Si: as the average thickness of the deposited Ge layer increases within a certain range of thicknesses, the QD emission intensity decreases with a simultaneous enhancement of the QW emission.

Structures with Ge layers 6–9.5 monolayers (ML) thick in Si were grown in Katun machines (at the Lebedev Physical Institute in Moscow and at the Institute of Semiconductor Physics, Siberian Division, Russian Academy of Sciences, Novosibirsk, Russia) and in a Riber Siva 45 machine (at the Institute of Semiconductor Physics, University of Linz, Austria). All the samples comprised 4–5 Ge layers separated with [100] Si layers of 10 nm (Katun, 300°C) or 25.5 nm (Riber, 250 and 350°C) thickness. An exception was the sample with a single Ge layer with an average thickness of 9.5 ML (300°C). In several samples used for studies with atomic-force microscopy (AFM), the upper Ge layer was not covered with Si.

Figure 1 summarizes the data obtained; it shows the energy position of the zero-phonon PL line as a function of the average thickness of the deposited Ge layer. In the same figure, data from [2] for a deposition temperature of 740°C illustrate well-known concepts: with the beginning of island formation, the WL thickness is stabilized (the position of the QW PL line remains virtually unchanged), and the deposited excess Ge gathers

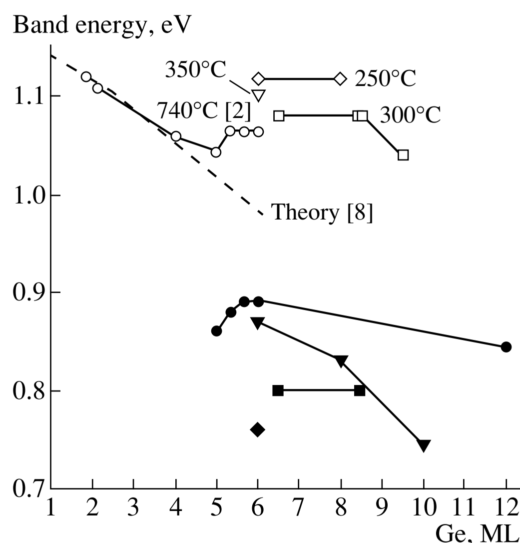

Fig. 1. The energy of zero-phonon PL lines vs. the average thickness of Ge layers deposited at different temperatures. Data: (top) QW and (bottom) QD.

1063-7826/03/3702-0207$24.00 © 2003 MAIK "Nauka/Interperiodica"

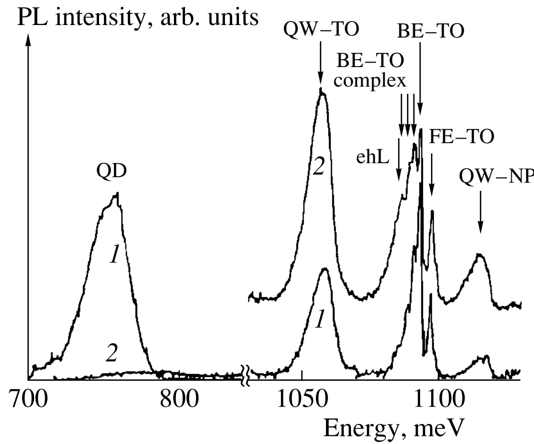

Fig. 2. Low-temperature PL spectra of Si/Ge structures with Ge layers deposited at 250°C, with an average thickness of (*1*) 6ML and (*2*) 8ML. Recorded at $T = 2$ K. In the high-energy portion, spectrum *2* is shifted up in respect to the axis. QW–TO and QW–NP, respectively, are the phonon (Si) and zero-phonon emission lines of the QW. QD is the QD emission line. BE–TO and BE–TO complex, respectively, are the phonon lines from bound excitons and bound exciton complexes in Si; FE–TO is the phonon line from free excitons in Si; ehL is the emission line from electron–hole droplets in Si.

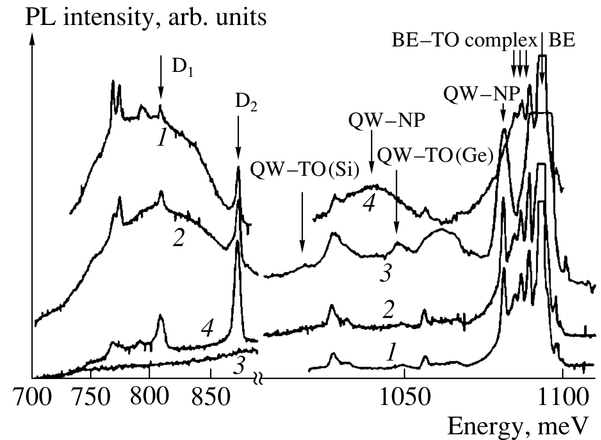

Fig. 3. PL spectra of Si/Ge structures with Ge layers grown at 300°C. Recorded at $T = 2$ K. Average thickness of the Ge layers in the structures: (*1*) 6, (*2*) 8.5, (*3*) 8.5, and (*4*) 9.5 ML. Spectra *2*, *3*, and *4* in the high-energy portion and spectra *1* and *2* in the low-energy portion are shifted up in respect to the axis. D_1 and D_2 are lines of emission from dislocations. Other designations are the same as in Fig. 2.

into islands, which change their shape in the course of growth; they are then penetrated by misfit dislocations and stop luminescing.

On the whole, the data we obtained for the epitaxial temperature of 350°C are in agreement with commonly accepted concepts: at a certain thickness of the deposited layer (in our case, 6 ML), emission is observed from the QW and QD simultaneously; as the thickness of the deposited layer increases, the QW emission disappears, the QD emission line shifts to a lower energy, and the intensity of the latter decreases steeply (which is seen from PL spectra not presented here).

The samples grown at Ge-epitaxy temperatures of 300 and 250°C show the opposite behavior: as the Ge layer thickness increases, the QD emission disappears and the QW emission is still observed and even grows in intensity. For example, for structures grown at an epitaxial temperature of 250°C, emission related to islands (QDs) is observed from a sample with an average Ge thickness of 6 ML; when the average thickness increases to 8 ML, the QD PL disappears and the intensity of the QW emission increases (Fig. 2).

It is noteworthy that, in the energy range related to emission from electron–hole droplets in Si (1086 meV, ehL in Fig. 2), the luminescence observed is excessive with respect to that observed when the structure is excited from the substrate side. This effect is observed, to a lesser or greater extent, in all of the structures studied.

Figure 3 presents the emission spectra of samples *1*–*4*, which were grown on the Katun machine at a Ge-epitaxy temperature of 300°C. As in the preceding case of 250°C, emission at energies of ~ 800 meV, which can be attributed to islands, is observed for structures with thinner Ge layers. In the range of QW emission (1000–1100 meV), samples *1*, *2*, and *3* show virtually identical characteristics of QW emission, despite the admittedly different Ge layer thicknesses (samples *1* and *2*) and the inevitable technological scatter (samples *2* and *3* were grown on different machines). The zero-phonon line has precisely the same energy (1080 meV) for all three samples, and its width does not exceed 1 meV, as indicated by more detailed measurements. This circumstance indicates an extremely high uniformity of the pseudomorphic layer formed under the given conditions. In this context, it is no coincidence that the experimental energy positions of the QW emission lines correspond with those calculated in [8] for an integer number of monolayers: 2 ML at an epitaxial temperature of 250°C and 3 ML at 300°C (Fig. 1). The available data do not allow us to select a single reason for the occurrence of this process. A combination of conditions may be important here: temperature, duration, and configuration of the process, and even the amount and type of uncontrollable impurities introduced during epitaxy. Here, it is worth noting that the phonon replica of the QW line in the PL spectrum related to a Ge phonon was observed earlier only in structures intentionally doped during epitaxy [9].

The cessation of QD luminescence with an increase in the amount of deposited Ge suggests that the area of the solid pseudomorphic layer (QW) grows due to recrystallization of the bases of the islands, which may be induced by their coalescence upon an increase in density. It necessary to note that, when islands have a small size, the bases cover the entire surface of a struc-

ture even when there is a small amount of deposited material: e.g., only 2.5 ML suffices for pyramidal islands with a 10-nm base. The AFM surface image of one of the samples (8.5 ML and 300°C, see spectrum *3* in Fig. 3) shows a continuous profile with a typical period of ~30 nm, which presumably results from complete coverage of the surface with islands and their coalescence, which is also confirmed by the small (~0.5 nm) depth of the profile. It may be assumed that at an epitaxial temperature below 350°C, the deposited layer grows according to the Volmer–Weber mechanism, whereby islands start to appear even at the initial stage of growth, without the formation of a wetting layer. A similar change in growth mechanisms, from Stranski–Krastanow to Volmer–Weber, has been observed, particularly when InAs was deposited on Si at temperatures below 400°C [10].

The entire set of data obtained indicates that the mechanism of Ge growth on Si changes substantially when the MBE temperature is lower than 350°C.

ACKNOWLEDGMENTS

We are grateful to O. P. Pchelyakov for providing several structures grown at the Institute of Semiconductor Physics, Siberian Division, Russian Academy of Sciences; and to F. Scheffler for the opportunity of working in his laboratory.

This study was supported by the Presidium of the Russian Academy of Sciences program "Low-Dimensional Quantum Structures," by the Scientific and Technical Program of the Russian Federation (project nos. 37.039.1.1.0041 and 40.072.1.1.1180), and by the "Scientific School" program (grant no. 00-15-96568).

REFERENCES

1. O. P. Pchelyakov, Yu. B. Bolkhovityanov, A. V. Dvurechenskiĭ, *et al.*, Fiz. Tekh. Poluprovodn. (St. Petersburg) **34**, 1281 (2000) [Semiconductors **34**, 1229 (2000)].
2. G. Abstreiter, P. Schittenhelm, C. Engel, *et al.*, Semicond. Sci. Technol. **11**, 1521 (1996).
3. P. Schittenhelm, C. Engel, F. Findeis, *et al.*, J. Vac. Sci. Technol. B **16** (3), 1575 (1998).
4. O. G. Schmidt, C. Lange, and K. Eberl, Appl. Phys. Lett. **75**, 1905 (1999).
5. A. B. Talochkin, A. V. Efanov, V. A. Markov, and A. I. Nikiforov, Izv. Ross. Akad. Nauk, Ser. Fiz. **63**, 290 (1999).
6. V. A. Markov, H. H. Cheng, Chin-ta Chia, *et al.*, Thin Solid Films **369**, 79 (2000).
7. T. M. Burbaev, T. N. Zavaritskaya, V. A. Kurbatov, *et al.*, Fiz. Tekh. Poluprovodn. (St. Petersburg) **35**, 979 (2001) [Semiconductors **35**, 941 (2001)].
8. J. Brunner, J. F. Nutzel, M. Gail, *et al.*, J. Vac. Sci. Technol. B **11**, 1097 (1993).
9. L. P. Rokhinson, D. C. Tsui, J. L. Benton, and Y.-H. Xie, Appl. Phys. Lett. **75**, 2413 (1999).
10. D. V. Denisov, V. M. Ustinov, G. É. Tsyrlin, and V. A. Egorov, in *Proceedings of Conference on Nanophotonics* (Nizhni Novgorod, 2002), p. 161.

Translated by D. Mashovets

Semiconductors, Vol. 37, No. 2, 2003, pp. 210–214. Translated from Fizika i Tekhnika Poluprovodnikov, Vol. 37, No. 2, 2003, pp. 219–223.
Original Russian Text Copyright © 2003 by Makarov, Ledentsov, Tsatsul'nikov, Cirlin, Egorov, Ustinov, Zakharov, Werner.

LOW-DIMENSIONAL SYSTEMS

Optical Properties of Structures with Ultradense Arrays of Ge QDs in an Si Matrix

A. G. Makarov*^, N. N. Ledentsov*, A. F. Tsatsul'nikov*, G. E. Cirlin*, V. A. Egorov*, V. M. Ustinov*, N. D. Zakharov, and P. Werner****

** Ioffe Physicotechnical Institute, Russian Academy of Sciences, St. Petersburg, 194021 Russia*

^ e-mail: makarov@mail.ioffe.ru

*** Max-Planck Institute of Microstructure Physics, Halle/Saale, Germany*

Submitted June 10, 2002; accepted for publication June 14, 2002

Abstract—The structural and optical properties of ultrathin Ge insertions in an Si matrix were studied. Transmission electron microscopy revealed the spontaneous formation of arrays of disk-shaped quantum dots (QDs) with a small lateral size (3–10 nm) at a nominal Ge insertion thicknesses, from submonolayer to nearly critical, for the transition to 3D growth by the Stranski–Krastanow mechanism. Optical study revealed type-I band alignment in these structures, which results from the strong contribution of the electron–hole Coulomb interaction overpowering the repulsion potential for an electron existing in the Ge conduction band. The small lateral size of QDs lifts the selection rule prohibiting indirect recombination in the inverse *k* space. At the same time, the high surface density of QDs (10^{12}–10^{13} cm^{-2}) and the possibility of their stacking with the use of ultrathin Si spacers allows the obtainment of an ultrahigh volume density of QDs (up to 10^{19} cm^{-3}), which is necessary to achieve stimulated emission in Si. A sample with stacked QDs formed by 0.7-nm-thick Ge insertions exhibited a superlinear increase of the photoluminescence (PL) intensity, accompanied by narrowing of the PL line. The doping of Ge–Si structures with donors allows for a drastic increase in the PL intensity at high temperatures, which prevents depletion of the active region in weakly localized electrons. *© 2003 MAIK "Nauka/Interperiodica".*

1. INTRODUCTION

Ongoing interest in Si/Ge nanostructures is due to considerable progress in the development of new devices based on nanoheterostructures with size quantization [1]. The successful design of transistors, photodetectors and emitters of light, operating on intrasubband transitions in quantum wells (QW), should be noted. At the same time, numerous attempts to derive effective emitters of light, relying on band-to-band transitions in QWs in a given system, have failed. In this case, effective Si/Ge emitters of light, lasers especially, might potentially ensure the most direct integration of silicon technology with optoelectronic data transmission systems, both within a single silicon chip and in telecommunication applications.

As shown earlier, the use of Si/SiGe QWs does not noticeably reduce the time of radiative recombination [2]. Further, owing to specific features of the band structure and the character of strains in coherent Si–Ge QWs, the Ge–Si heterojunction is of type II [3], and the overlap of the electron and hole wave functions is reduced not only in *k*-space, but also in real space. The spatial separation of electrons and holes at the heterojunction results in a characteristic short-wavelength shift of the photoluminescence (PL) line with an increase in excitation density, which is typical of type-II QWs [2, 3].

In recent years, active studies aimed at enhancing PL efficiency were devoted to the application of 3D SiGe and GeSiC/Si QDs obtained in the Stranski–Krastanow (SK) growth mode on the Si surface [4]. However, the large size of SK QDs, combined with a high Ge content, results in even stronger spatial separation of the wave functions of a hole localized in a Ge QD and an electron localized in an Si matrix. The structures also exhibit a strong short-wavelength shift of the luminescence from an SK QD as the pumping intensity rises, which is typical of type-II QDs [5]. The relatively large QD size ($\gtrsim$10 nm) demands that relatively thick ($\gtrsim$10 nm) Si spacers be used. The surface density of SK QDs is about 10^9–10^{10} cm^{-2}, and the maximum volume density of SK QDs is also very low (10^{15}–10^{16} cm^{-3}). Such a low density creates problems for realizing lasing even for direct-gap QDs in an InAs–GaAs system [6]. Further, the band structure in the *k*-space of Si varies only slightly, because the characteristic size of hole localization in real space strongly exceeds the Bohr radius of a hole.

It should be noted that there exists another class of QDs produced by ultrathin [7, 8], e.g., submonolayer, insertions of a narrow-gap material in a wide-gap matrix [9]. The characteristic lateral size of these QDs is much smaller and their density is much higher than those for SK QDs [9]. The possibility of densely stacking these QDs enables ultrahigh modal gain (up to 10^4–10^5 cm^{-1}) in wide-gap direct-gap materials whose exciton has a small Bohr radius [9].

1063-7826/03/3702-0210$24.00 © 2003 MAIK "Nauka/Interperiodica"

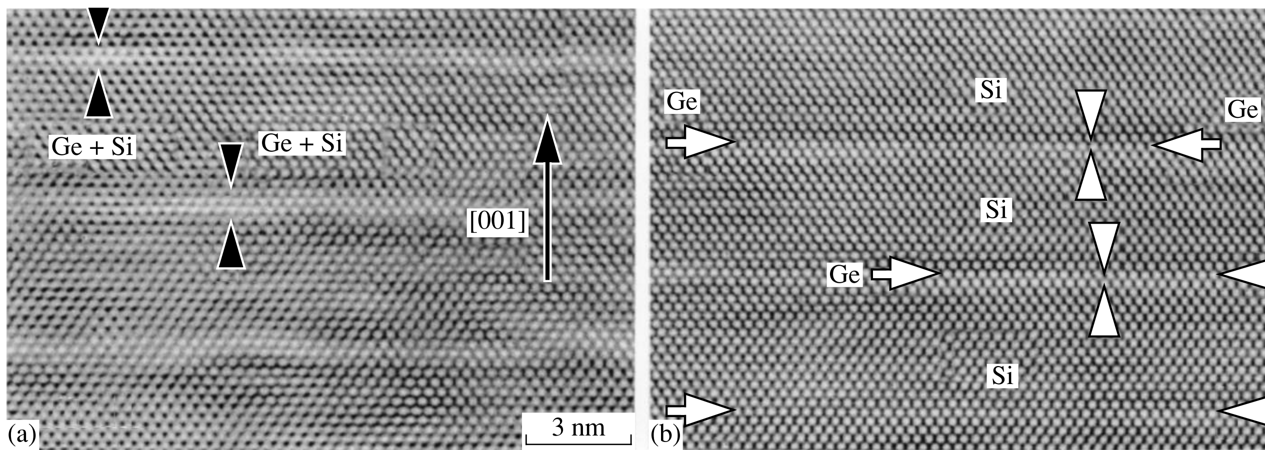

Fig. 1. Cross-sectional TEM images of structures containing (a) submonolayer (0.07 nm) and (b) monolayer (0.136 nm) Ge insertions in a Si matrix.

For the Ge–Si system, fabrication of QDs of this kind, if possible, will resolve all the basic problems of optoelectronic applications. First, a small (3–5 nm) lateral QD size effectively lifts the momentum selection rule for radiative recombination with electrons from the indirect minimum of the conduction band. At the same time, the repulsive potential in the conduction band appears to be weak, which allows the localization of an electron and hole in the same spatial region [10].

As shown earlier in the case of ultrathin type-II layers, the effective localization of an electron on a hole can be achieved even on the basis of type-II heterostructures with a high potential barrier in the conduction band [10]. This is so because the Coulomb attraction of an electron exceeds its repulsive action at a certain small thickness of the barrier. Indeed, a short-wavelength shift of the PL line with a rise in pumping power is absent in the case of ultranarrow Ge insertions in an Si matrix [2]. In addition, the use of ultrasmall QDs simplifies the electron localization in contrast to the QW case, because the barrier strength decreases in the lateral direction.

In this study, we propose the optoelectronic application of ultrasmall QDs grown by depositing Ge layers with a thickness below the critical one, which is necessary for the transition to 3D growth by the SK mechanism. We demonstrate that, under certain deposition conditions, ultradense arrays of QDs are obtained, in which, with account taken of the Coulomb interaction, both a direct gap structure in real space and a maximum delocalization of the hole wave function in *k*-space are realized, which favors radiative recombination. Finally, an ultrahigh density of QDs can be obtained in these structures for achieving sufficiently high gain for lasing. Dense QD arrays can be closely stacked along the growth direction, this being another key advantage for achieving the necessary high gain.

It is also shown that the doping of structures with Sb suppresses depletion of electrons in the active medium and significantly enhances the efficiency of radiative recombination. The possibility of obtaining stimulated emission from Si–Ge structures is discussed.

2. EXPERIMENTAL

The samples under study are periodical Ge insertions in an Si matrix deposited on a 100-nm-thick buffer layer grown by MBE at a substrate temperature of 600°C. Two types of superlattices were grown. The first comprised 20 layers of submonolayer Ge insertions of varied thickness separated with 4- to 5-nm-thick Si spacers; the effective thickness of Ge layers in the structures varied from 0.07 to 0.14 nm. The other type of superlattice, comprising 10 periods, included 0.5- to 0.7-nm Ge layers separated with 11-nm-thick Si spacers. These spacers consisted of 9 nm of undoped Si and 2 nm of Si doped with 5×10^{16} cm^{-3} Sb at their centers. The undoped and doped superlattices were grown at temperatures of 750 an 700°C, respectively. To prevent the segregation of Sb, the spacers were grown at 600°C. The growth rate for Si and Ge was 0.05 and 0.005 nm s^{-1}, respectively. The total vapor pressure in the MBE chamber was not less than 5×10^{-9} Torr. Growth was monitored by recording RHEED patterns. The initial (2×2) reconstruction of the Si surface was preserved during the growth, with only a slight broadening of the principal reflections being observed, irrespective of the growth temperature. Thus, even in upper layers, no appreciable density of 3D islands was formed by the SK mechanism. The TEM study was performed using a JEM 4010 electron microscope with a 400-kV accelerating voltage. The PL was excited with an Ar-ion laser (λ = 514.5 nm) and detected with a cooled Ge photodiode.

3. RESULTS

Figure 1a shows a cross-sectional TEM image of a structure containing submonolayer Ge insertions with

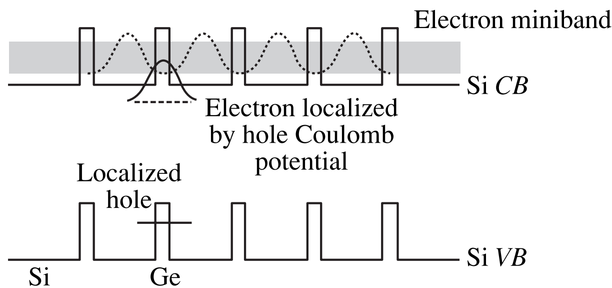

Fig. 2. Schematic band diagram of a multilayer structure with Ge insertions in a Si matrix.

an effective thickness of 0.07 nm, grown at a substrate temperature of 650°C. The thickness of Si spacers between the Ge insertions was 4.4 nm. In order to analyze the distribution of Ge atoms in each layer, a special digital analyzer of HRTEM images is necessary. Analysis shows that the Ge insertions do not constitute a solid layer; instead, a high density of nanodomain formations 3–5 nm in size with a surface density of $\approx 5 \times 10^{11}$ cm^{-2} is observed [11, 12]. Furthermore, local 3D islands with a specific size of about 10 nm are formed. In the case of Ge insertions with a thickness of about one monolayer (ML) or more, the typical lateral size of a nanodomain was 7–10 nm.

Figure 2 schematically shows the band diagram of the structures under study. The Ge insertions form potential wells in the valence band and potential barriers in the conduction band of the Si–Ge system. In multilayer structures, minibands are formed in the Si conduction band, with the wave function of the electron having a minimum near the Ge insertions. When nonequilibrium holes captured by the Ge potential wells appear in the Si matrix, an additional Coulomb potential is formed, which attracts an electron to a hole. Since the Coulomb energy in Si is rather high (14.7 meV) and the barrier in the conduction band is comparatively low (<100 meV [3]), an electron can be effectively localized in the Coulomb potential of a hole in the Ge region, as shown in the general case for ultranarrow type-II QWs.

Figure 3 shows typical PL spectra of a sample with a submonolayer (0.1 nm) Ge insertion in the Si matrix. PL spectral lines related to acoustical and optical phonons of the Si matrix are observed, as are lines of PL from Ge insertions (Ge^{NP}, Ge^{TO}, and Ge^{TO-O}) peaked at 1.121, 1.064, and 1.004 eV, respectively.

An interesting distinction of submonolayer Ge insertions is the long-wavelength shift of the PL lines related to the Ge QD as the excitation density increases. In this situation, at low excitation densities, the zero-phonon PL line lies at an energy close to that expected from the dependence of the PL energy on the thickness of Ge insertions, which was obtained in [13]. An energy shift with pumping was not observed in structures with a Ge insertion thickness slightly exceeding 1 ML, which was also stated earlier [2]. The lack of a shift indicates the absence of spatial separation between electrons and holes and confirms the validity of the type-I QD model. The long-wavelength shift with an increase in the excitation density, which is observed for submonolayer insertions, is evidently due to the formation of multiple-exciton complexes associated with a QD. This once again emphasizes the increasing role of the Coulomb attraction between electrons and holes in the case when the repulsive action of the Ge potential barrier in the Si conduction band becomes weaker.

A characteristic feature of the Ge–Si PL spectra is fast thermal quenching. In our opinion, this feature is associated with thermal emission of weakly localized electrons and their subsequent nonradiative recombination on the surface and in the bulk of the Si substrate.

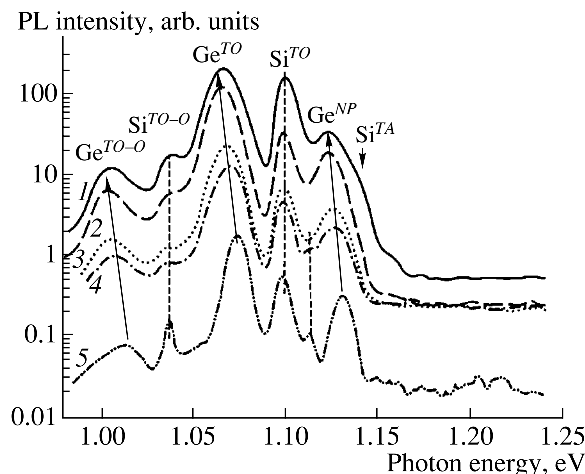

Fig. 3. The dependence of PL spectra on the pumping density for a structure with submonolayer QDs (0.74 ML of Ge) at 15 K. Noteworthy is the long-wavelength shift of the PL lines with increasing excitation density: (*1*) 1000, (*2*) 150, (*3*) 50, (*4*) 25, and (*5*) 15 W cm^{-2}.

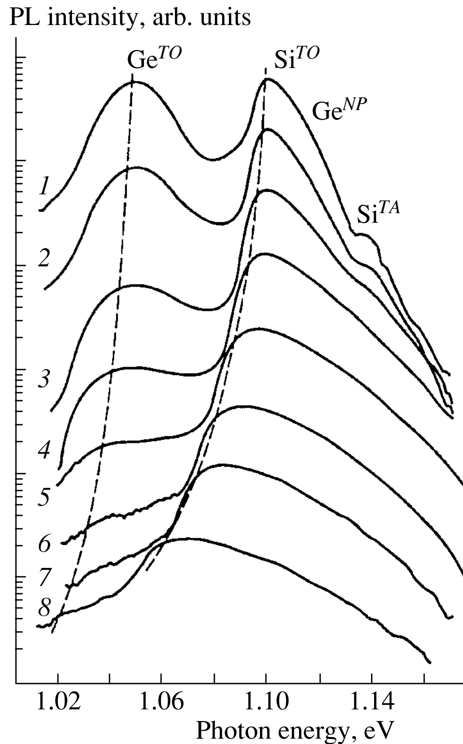

Fig. 4. The dependence of PL spectra of a Si–Ge structure doped with Sb as the donor impurity (3.7 ML of Ge, the excitation density 50 W cm^{-2}) on the observation temperature: (*1*) 18, (*2*) 50, (*3*) 130, (*4*) 170, (*5*) 210, (*6*) 230, (*7*) 250, and (*8*) 300 K.

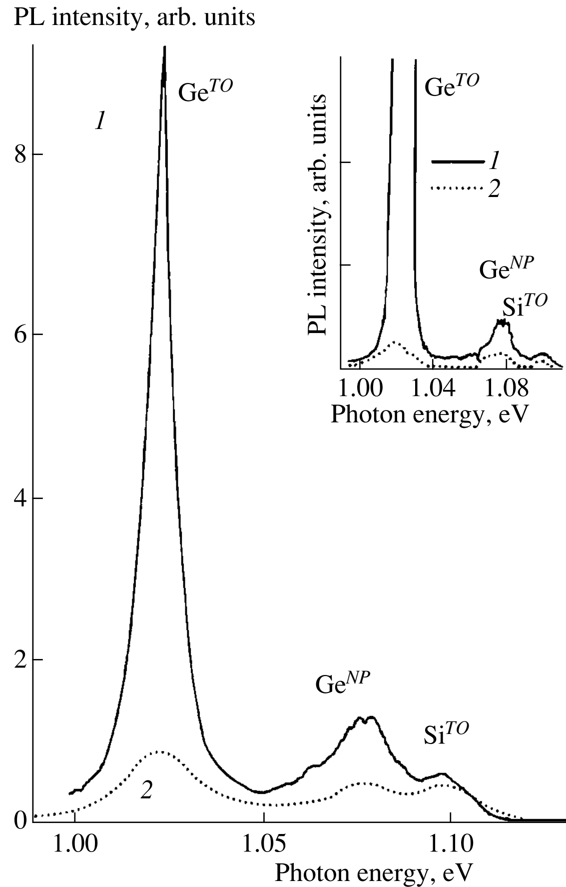

Fig. 5. The dependence of PL spectra of Si–Ge structures doped with Sb as the donor impurity on the observation temperature: (*1*) 30 and (*2*) 60 K. Insert: similar spectra at 15 K (5.1 ML of Ge). The excitation density: (*1*) 432 and (*2*) 186 W cm^{-2}.

Even relatively weak doping of the active region of a structure with a donor impurity (with an average concentration of $\approx 10^{16}$ cm^{-3}), which gives rise to a moderate density of equilibrium electrons, dramatically enhances the PL intensity and enables it to be observed up to room temperature. Figure 4 shows the temperature dependence of PL spectra. The long-wavelength shift of the Ge PL line is evidently weaker than that of the Si line. This fact, observed in all the samples (with submonolayer or monolayer insertions, doped or undoped), and the lack of a short-wavelength shift with increasing excitation density presumably indicate that the electron miniband in Si is thermally filled with electrons as the temperature rises. To counteract this effect, the donor doping level should be raised substantially, to the point of degeneracy.

The high intensity and temperature stability of the PL in doped samples with Ge–Si QDs allowed us to observe a narrowing of the PL line as the observation temperature decreased at high excitation densities, or as the excitation density increased at a fixed temperature (Fig. 5). The narrowing of the PL line is accompanied by a dramatic rise in the integral PL intensity. This effect is observed in the vertical direction and only in the samples with a polished back surface. This may indicate that stimulated emission is obtained in a vertical Si cavity with an active region of dense stacked arrays of Ge QDs.

4. CONCLUSIONS

The structural and luminescent properties of structures with dense arrays of high-density Ge dots have been studied. As shown, these structures are arrays of type-I QDs. The doping of QDs allowed us to obtain high PL intensity at elevated temperatures and superlinear growth of the PL intensity with a rise in the excitation density, which may indicate the occurrence of stimulated emission in Si–Ge heterostructures. Presumably, the use of ultradense arrays of small-size Ge–Si QDs heavily doped with donor impurities will enable lasing in Si–Ge structures at room temperature in the near future.

REFERENCES

1. D. Bimberg, M. Grundmann, and N. N. Ledentsov, *Quantum Dot Heterostructures* (Wiley, New York, 1998).

2. L. C. Lenchyshyn, M. L. W. Thewalt, D. C. Houghton, *et al.*, Phys. Rev. B **47**, 16655 (1993).

3. T. Baier, U. Mantz, K. Thonke, *et al.*, in *Proceedings of 22nd International Conference on the Physics of Semiconductors, Vancouver, 1994*, Ed. by D. J. Lockwood (World Sci., Singapore, 1995), Vol. 2, p. 1568.

4. O. P. Pchelyakov, Yu. B. Bolkhovityanov, A. V. Dvurechenskiĭ, *et al.*, Fiz. Tekh. Poluprovodn. (St. Petersburg) **34**, 1281 (2000) [Semiconductors **34**, 1229 (2000)].

5. M. W. Dashiel, U. Denker, C. Müller, *et al.*, Appl. Phys. Lett. **80**, 1279 (2002).

6. N. N. Ledentsov, M. Grundmann, F. Heinrichsdorff, *et al.*, IEEE J. Sel. Top. Quantum Electron. **6**, 439 (2000).

7. N. N. Ledentsov, I. L. Krestnikov, M. V. Maximov, *et al.*, Appl. Phys. Lett. **69**, 1343 (1996).

8. N. N. Ledentsov, I. L. Krestnikov, M. V. Maximov, *et al.*, Appl. Phys. Lett. **70**, 2766 (1997).

9. I. L. Krestnikov, N. N. Ledentsov, A. Hoffmann, and D. Bimberg, Phys. Status Solidi A **183**, 207 (2001).

10. N. N. Ledentsov, J. Böhrer, M. Beer, *et al.*, Phys. Rev. B **52**, 14058 (1995).

11. N. D. Zakharov, P. Werner, U. Gösele, *et al.*, Mater. Sci. Eng. B **87**, 92 (2001).

12. N. D. Zakharov, G. E. Cirlin, P. Werner, *et al.*, in *Proceedings of 9th International Symposium on Nanostructures: Physics and Technology 2001* (St. Petersburg, 2001), p. 21.

13. L. P. Rokinson, D. C. Tsui, J. L. Benton, and Y.-H. Xie, Appl. Phys. Lett. **75**, 2413 (1999).

Translated by D. Mashovets

Semiconductors, Vol. 37, No. 2, 2003, pp. 215–219. Translated from Fizika i Tekhnika Poluprovodnikov, Vol. 37, No. 2, 2003, pp. 224–229.
Original Russian Text Copyright © 2003 by Aleshkin, Andronov, Dubinov.

LOW-DIMENSIONAL SYSTEMS

Population Inversion between Γ Subbands in Quantum Wells under the Conditions of Γ–*L* Intervalley Transfer

V. Ya. Aleshkin*, A. A. Andronov, and A. A. Dubinov

Institute for Physics of Microstructures, Russian Academy of Sciences, Nizhni Novgorod, 603600 Russia

**e-mail: aleshkin@ipm.sci-nnov.ru*

Submitted June 11, 2002; accepted for publication June 25, 2002

Abstract—Monte Carlo simulations of electron transport in $Al_xGa_{1-x}As/GaAs/In_yGa_{1-y}As$ double-quantum-well heterostructures in high lateral electric fields are carried out. It is shown that, under the conditions of intervalley Γ–*L* electron transfer, there exists a population inversion between the first and the second quantum-confinement subbands in the Γ valley. The population inversion appears in the fields exceeding 4 and 5.5 kV/cm at 77 and 300 K, respectively. The gain in a superlattice composed of such quantum wells is estimated to be on the order of 100 cm^{-1} for radiation with a wavelength of 12.6 μm. © *2003 MAIK "Nauka/Interperiodica".*

1. INTRODUCTION

In cascade lasers [1], population inversion between quantum-confinement subbands is achieved via tunneling injection of the charge carriers in the upper subband; this mechanism of population inversion in quantum wells (QWs) was considered for the first time by Kazarinov and Suris back in 1971 [2]. In the "fountain" laser [3], population inversion between subbands occurs due to light-induced transitions of electrons to the upper quantum-confinement subband. A number of mechanisms leading to the population inversion between the subbands are related to electron heating in a high electric field oriented parallel to the QW layers (see, e.g., [4, 5]). In particular, it was suggested that population inversion may result from the intervalley Γ–*X* transfer in GaAs/AlGaAs heterostructures. However, Monte Carlo simulations indicate that, in this case, population inversion can be attained only in electric fields well above the threshold for the Gunn effect (~8 kV/cm) [6]; this hinders the implementation of such a scheme.

In this paper, we consider another possible method for the attainment of population inversion between subbands; this method relies on the intervalley Γ–*L* transfer of hot electrons in double QWs. The fields required to attain population inversion in the Γ–*L* scheme are much lower than those in the Γ–*X* scheme, which is an advantage of the former. Monte Carlo simulations of electron transport indicate that the population inversion between the first and the second quantum-confinement subbands in the Γ valley takes place in the fields above 4 kV/cm at the liquid-nitrogen temperature and above 5.5 kV/cm at room temperature.

2. A MODEL FOR ELECTRON TRANSPORT IN A PAIR OF TUNNELING-COUPLED QUANTUM WELLS

The structure under consideration consists of two tunneling-coupled QWs for electrons both in the Γ and in the *L* valleys (see Fig. 1a). The wave functions of the Γ-valley electrons in the two lowest quantum-confinement subbands are localized in different QWs and, thus, the electron transfer between subbands Γ_1 and Γ_2 due to scattering by polar optical phonons is suppressed; it is this scattering mechanism that is mainly responsible for the relaxation of the population inversion and brings about the need for high electric fields in the Γ–*X* laser. A significant feature of this structure should be noted: the wave function of the lowest *L* subband (L_1) is localized in the same QW as the wave function of the Γ_2 subband. Because of this circumstance, the overlap between the wave functions of subbands L_1 and Γ_2 is substantially larger than the overlap between the wave functions of the first *L* and Γ subbands (see Fig. 1b). Thus, in high lateral fields, when the filling of the states in subband L_1 sets in, the electrons from these states are scattered mainly to the Γ_2 subband, which leads to population inversion between the second and the first Γ subbands. This advantageous band structure can be realized due to the presence of a $In_{0.25}Ga_{0.75}As$ alloy layer, which forms (with respect to GaAs) a well for the electrons in the Γ valley and a barrier, in the *L* valley.

This alignment of the *L* valleys in the InGaAs alloy with respect to GaAs (which is crucial for the mechanism of population inversion under discussion) follows from recent measurements and calculations of the energy positions of *L* and Γ valleys in InAs [7, 8]. We assumed the energy spacing between Γ and *L* valleys to

1063-7826/03/3702-0215$24.00 © 2003 MAIK "Nauka/Interperiodica"

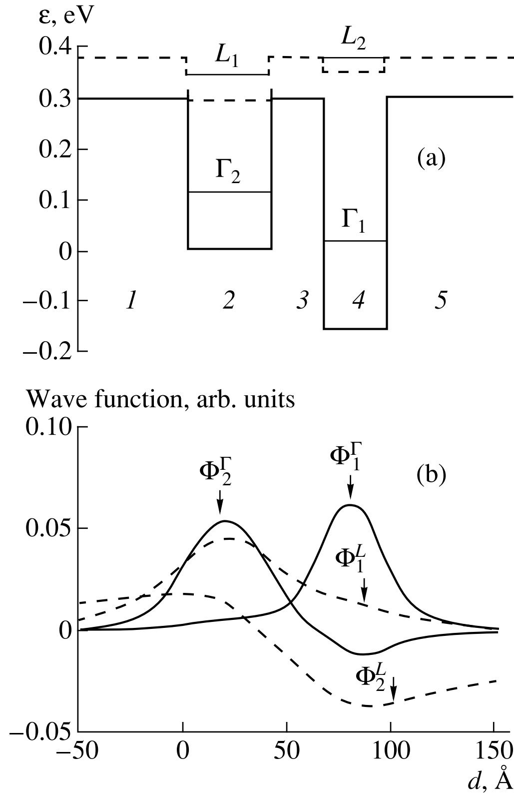

Fig. 1. (a) Energy-band diagram and (b) electron wave functions in a system of two tunneling-coupled quantum wells. Energies are measured from the bottom of the GaAs conduction band. The profiles of the conduction-band bottom in Γ and *L* valleys are drawn by solid and bold-dashed lines, respectively. The heterostructure layers are composed of $Al_{0.4}Ga_{0.6}As$ (regions *1*, *3*, and *5*), GaAs (region *2*), and $In_{0.25}Ga_{0.75}As$ (region *4*). The thicknesses of layers *2*, *3*, and *4* are 39, 25, and 30 Å, respectively.

be 1.1 and 0.29 eV in InAs and GaAs, respectively. The Γ band-edge offset at the $In_yGa_{1-y}As$ heterointerface was assumed to be 0.63*y* eV. To calculate the Γ- and *L*-band offsets at the GaAs/$In_yGa_{1-y}As$ heterojunction, linear interpolation in *y* was used. The energy positions of the Γ and *L* valleys in $Al_xGa_{1-x}As$ alloy were taken from [9].

The spectrum and the wave functions of the Γ-valley electrons in the $Al_xGa_{1-x}As/In_yGa_{1-y}As$ heterostructure with such a pair of tunneling-coupled QWs were calculated by solving the Schrödinger equation in the Kane model approximation. The electron states in the *L* valley were determined using the effective-mass approximation Hamiltonian. The transverse m_t and the longitudinal m_l effective masses of electrons in the *L* valley in all layers were taken to be 0.075 and 0.19 of the free-electron mass, respectively. The axes *x*, *y*, and *z* of the coordinate system were oriented along the crystallographic axes [100], [010], and [001]. We assume that the growth axis of the structure coincides with the *z* axis and, thus, the four *L* valleys are equivalent. Assuming that the motion in the *xy* plane is infinite, we can write the wave function of an electron in the *i*th subband of the valley α (where α = Γ, *L*) as

$$\Psi_i^\alpha = \frac{1}{\sqrt{S}}\Phi_i^\alpha(z)\exp(i\mathbf{kr}), \tag{1}$$

where **r** and **k** are the in-plane radius vector and wave vector of an electron, respectively; and *S* is the area of the structure. For the case of electrons in the *L* valley, we omitted the insignificant phase factor $\exp ig(k_x, k_y)z$, where $g(k_x, k_y)$ is a linear function of k_x and k_y. The calculated wave functions (labeled by Φ_i^α) and quantum-confinement levels are shown in Fig. 1. The dependences of the Γ-valley effective electron masses in AlGaAs and InGaAs alloys on the Al and In content, which are required for this calculation, were taken from [7, 8].

We ignore the effects of nonparabolicity in our treatment of electron transport in the QW plane. Thus, we assume that the energy of an electron in the *i*th subband of the valley α equals $E_i^\alpha + \hbar^2k^2/2m_\alpha$. In this approximation, we ignore the anisotropy of the dispersion relation in the *L* valley and use the two-dimensional density-of-state effective mass for electrons in the *L* subbands:

$$m_L = \sqrt{m_t\left(\frac{2}{3}m_l + \frac{1}{3}m_t\right)}.$$

3. ELECTRON SCATTERING

In high electric fields, the scattering of electrons in the structure under study mainly occurs due to their interaction with optical and intervalley phonons. Thus, we ignored acoustic-phonon scattering, as well as electron–electron and charged-impurity scattering, assuming that the electron density is sufficiently low. In our consideration of electron scattering by polar optical phonons, we assumed that the phonon dispersion relation is the same as in bulk GaAs. In addition, we assumed that the phonon gas is in equilibrium and is characterized by the temperature of the crystal. To calculate the probability of electron transitions due to scattering by polar optical phonons from the *i*th to the *j*th subband in the valley α, we used a conventional approach [10], which yielded the following expression for the probability density of such a transition:

$$\begin{aligned} W_{ij}^{+\alpha}(\mathbf{k}_i, \mathbf{k}_j) &= \frac{2\pi}{\hbar}\left|V_{ij}^\alpha(\mathbf{k}_i, \mathbf{k}_j)\right|^2\left(N_q + \frac{1}{2} \pm \frac{1}{2}\right) \\ &\times \delta\left(E_i^\alpha - E_j^\alpha + \frac{\hbar^2(k_i^2 - k_j^2)}{2m_\alpha} \mp \hbar\omega_0\right). \end{aligned} \tag{2}$$

Here, $\mathbf{k}_i$ is the wave vector of the electron in the *i*th subband; **q** is the wave vector of the optical phonon; the upper and lower signs correspond to phonon emission and absorption, respectively; $\hbar\omega_0$ is the longitudinal

optical phonon energy; and N_q is the number of longitudinal optical phonons with the wave vector $\mathbf{q}$,

$$N_q = \frac{1}{\exp(\hbar\omega_0/k_B T) - 1},$$

where k_B and T stand for the Boltzmann constant and the temperature, respectively. The squared matrix element of the electron–phonon interaction operator can be expressed as [10]

$$\left|V_{ij}^{\alpha}(\mathbf{k}_i\mathbf{k}_j)\right|^2 = \frac{\pi e^2 \hbar\omega_0}{S\bar{\varepsilon}|\mathbf{k}_i - \mathbf{k}_j|}\iint dz dz_1 \Phi_i^{\alpha}(z)\Phi_1^{\alpha*}(z_1) \times \Phi_j^{\alpha}(z)\Phi_j^{\alpha*}(z_1)\exp\{-|z - z_1||\mathbf{k}_i - \mathbf{k}_j|\}, \tag{3}$$

where $\bar{\varepsilon} = (1/\varepsilon_\infty - 1/\varepsilon_0)^{-1}$, with ε_∞ and ε_0 being the high-frequency and low-frequency dielectric constants of GaAs, respectively.

In Figs. 2a and 2b, we plot the electron-energy dependences of the rates of intrasubband and intersubband optical-phonon scattering at liquid-nitrogen temperature (T = 77 K) (labels with superscripts OA and OE indicate the transitions accompanied by phonon absorption and emission, respectively):

$$\nu_{ij}^{\alpha}(\varepsilon) = \sum_{k_j}[W_{ij}^{+\alpha}(\mathbf{k}_i, \mathbf{k}_j) + W_{ij}^{-\alpha}(\mathbf{k}_i, \mathbf{k}_j)],$$
$$\varepsilon = E_i^{\alpha} + \frac{\hbar^2 k_i^2}{2m_\alpha}. \tag{4}$$

Since the dominant scattering process at this temperature is the spontaneous phonon emission, the scattering rate as a function of the electron energy has a threshold. Note that the scattering rate decreases with increasing electron energy, which is caused by an increase in the average wave vector of emitted phonons.

The rates of electron transitions from the ith subband in the valley α to the jth subband in the valley β due to intervalley-phonon scattering were calculated by the formula

$$\nu_{ij}^{\pm\alpha\beta} = \frac{D_{\alpha\beta}^2 m_\beta}{2\rho\hbar^2\Omega}\left(N_q + \frac{1}{2} \pm \frac{1}{2}\right)\int\left|\Phi_i^{\alpha}(z)\right|^2\left|\Phi_j^{\beta}(z)\right|^2 dz. \tag{5}$$

Next, we took into account the electron scattering by intervalley phonons from the ith subband in the valley α to the jth state of the continuum (three-dimensional states) in the valley β,

$$\nu_{ij}^{\pm\alpha\beta} = \frac{D_{\alpha\beta}^2 m_\beta^{3/2}\sqrt{E_i \mp \hbar\Omega - \Delta}}{\sqrt{2}\pi\rho\hbar^3\Omega} \times \left(N_q + \frac{1}{2} \pm \frac{1}{2}\right)\int\left|\Phi_i^{\alpha}(z)\right|^2\left|\Phi_j^{\beta}(z)\right|^2 dz, \tag{6}$$

Fig. 2. The rates of (a) intrasubband and (b) intersubband electron transitions at liquid-nitrogen temperature due to scattering by optical and intervalley phonons as a function of total electron energy. Labels with superscripts OA and IA correspond to the transitions caused by optical and intervalley phonon absorption, respectively; those with superscripts OE and IE, to the transitions caused by optical and intervalley phonon emission.

as well as the reverse transitions from the ith state of the continuum in the valley α to the jth subband in the valley β:

$$\nu_{ij}^{\pm\alpha\beta} = \frac{D_{\alpha\beta}^2 m_\beta}{2\rho\hbar^2\Omega L_z} \times \left(N_q + \frac{1}{2} \pm \frac{1}{2}\right)\int\left|\Phi_i^{\alpha}(z)\right|^2\left|\Phi_j^{\beta}(z)\right|^2 dz. \tag{7}$$

In the above expressions, $D_{\alpha\beta}$ is the intervalley-coupling constant [11], $\hbar\Omega$ is the energy of the intervalley phonon, ρ is the material density, E_i is the total energy of the electron in the ith subband, Δ is the energy spacing between the ith subband and the continuum, m_β is the density-of-states effective mass in the valley β (with the number of equivalent valleys taken into account), and L_z is the period of the structure (we assume that the structure is periodic). In this approximation, the scattering probability is independent of both the electron kinetic energy (except for the case of electron transitions into the states of the continuum) and the scattering angle. The calculated rates of different intrasubband

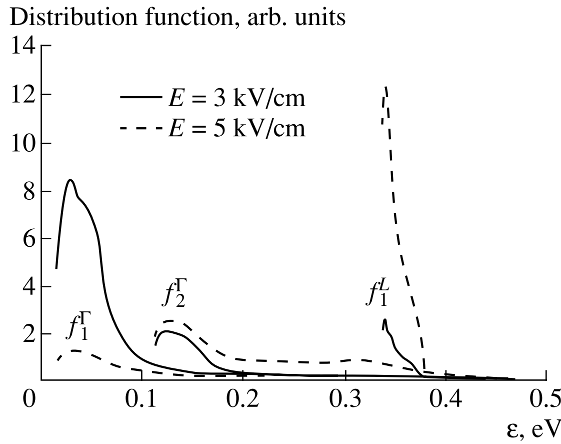

Fig. 3. Dependences of electron distribution functions at $T = 77$ K in the two lowest Γ subbands and the first L subband on the total electron energy for two different values of the electric-field strength; the curves are obtained from Monte Carlo simulations of the electron transport.

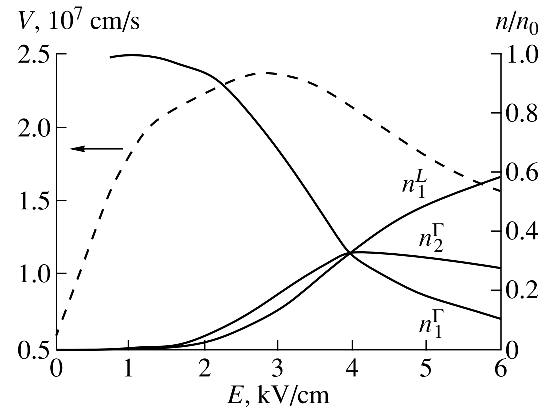

Fig. 4. Electric-field dependences of the relative electron concentrations n/n_0 in the two Γ subbands and the first L subband and of the average drift velocity of electrons V in the structure under consideration at $T = 77$ K; the curves are obtained from Monte Carlo simulations.

and intersubband electron transitions at liquid-nitrogen temperature due to scattering by intervalley phonons are shown in Figs. 2a and 2b, respectively (labels with superscripts IA and IE indicate transitions due to phonon absorption and emission, respectively).

Note that the rates of intersubband transitions in the Γ valley are two orders of magnitude lower than the rates of the intrasubband transitions in the L valley, and the rates of the transitions from L_1 to the Γ_2 subband are six times higher than the corresponding rates of transitions from L_1 to the Γ_1 subband and three times higher than the rates of intersubband transitions in the Γ valley. The rates of the transitions from the Γ valley to the L valley are one and a half orders of magnitude higher than the rates of the reverse transitions and are comparable to the rates of intrasubband transitions in the Γ valley. Thus, due to phonon scattering, electrons heated in a high electric field will accumulate in the L_1 subband, from which they will be transferred mainly to the Γ_2 subband. Owing to the suppression of the transitions between the lowest Γ subbands, the electron flow from Γ_2 to Γ_1 is small, which favors the appearance of population inversion between these subbands.

4. RESULTS OF ELECTRON-TRANSPORT SIMULATIONS

The distribution functions and concentrations of electrons in different subbands, as well as the average drift velocity of electrons, were calculated using the Monte Carlo method. Electron transitions to all Γ and L subbands were taken into account. In addition, transitions to the states of the continuum in the L valley were considered because the difference in energy between the continuous spectrum and the upper L subband is small. Transitions to the continuum states in the Γ valley were disregarded, since they appear in the energy region corresponding to the L valleys.

The calculated distribution functions of electrons over their total energies ε in the two lowest Γ subbands and in the lowest L subband are plotted in Fig. 3 for two different values of the electric field. One can see that the distribution function in the second Γ subband has a small peak near 0.31 eV. This feature can be attributed to intense electron transitions from the lowest L subband due to the intervalley-phonon scattering (Fig. 1). The distribution function in the first Γ subband has no such features, because the rate of the corresponding transition is low (Fig. 2). Indeed, in high fields, a large number of electrons from the L valley undergo a high-probability transition to the second Γ subband with the emission of an intervalley phonon. This leads to a considerable transfer of electrons from the L valley to the second Γ subband. At the same time, the rate of electron transitions from the second to the first Γ subband caused by polar-optical phonon scattering is low.

Thus, in high electric fields, electrons are transferred from the Γ_1 to the L_2 subband, then from L_2 to L_1 and from L_1 to the Γ_2 subband, where they are accumulated; this leads to electron population inversion between the first and the second Γ subbands.

Figure 4 shows electric-field dependences of the relative electron concentrations n/n_0 in the two Γ subbands and in the lowest L subband at liquid-nitrogen temperature. One can see that, in the fields exceeding 4 kV/cm, population inversion between the first and the second quantum-confinement subbands sets in. The electric-field dependence of the average drift velocity V of electrons in the structure under study is also plotted in Fig. 4. One can see that, in the fields above ~3 kV/cm, a decrease in V takes place, which is related to the accumulation of electrons in the L valley.

Now, let us estimate the possible gain in such a structure. An approximate expression for the gain at a frequency ω (corresponding to the transition energy $E_2 - E_1$) is

$$\beta_{12} = \alpha \frac{4\pi|z_{12}|^2(n_2 - n_1)\omega\tau}{\sqrt{\varepsilon_0}L_z}. \quad (8)$$

Here, $\alpha = e^2/\hbar c$ is the fine-structure constant; $|z_{12}|$ is the matrix element of the z operator; τ is the phase-relaxation time, which characterizes the spectral width of the radiative transition between the first and the second subbands; and L_z is the characteristic length of wave localization in the z direction. If the system is periodic along the z axis (i.e., if it consists of a large number of pairs of tunneling-coupled QWs in which the wave is localized), its period can be taken as L_z. Assuming that $\omega\tau \approx 10$, $\varepsilon_0 \approx 13$, $n_2 - n_1 \approx 1.5 \times 10^{11}$ cm^{-2}, $L_z \approx 2 \times 10^{-6}$ cm (a periodic structure is implied), and $z_{12} \approx 7.2 \times 10^{-8}$ cm (which corresponds to the structure considered in this study), from (8) we find that $\beta_{12} \approx 100$ cm^{-1} for the wavelength $\lambda_{12} \approx 12.6$ μm. It should be mentioned that, for this wavelength, the lattice absorptance in GaAs at 77 K is below 0.2 cm^{-1} [12].

For $T = 300$ K, similar calculations yield the threshold field for the population inversion $E = 5.5$ kV/cm in the Γ_1 and Γ_2 subbands and the population inversion at E = 6 kV/cm $(n_1^\Gamma - n_2^\Gamma)/n_0 \approx 10\%$ (here, n_0 is the total electron density).

It also follows from the calculations that, in high electric fields, the electron lifetime in the Γ_2 subband is mainly controlled by the transitions to the upper states (L subbands and the continuum states) due to heating. In the field of 5 kV/cm, the rate of these transitions is higher by a factor by 4 than the rate of the transitions to the Γ_1 subband. This suggests that selective suppression of the mobility in the Γ_2 subband (e.g., by introducing heterointerface roughness in the QW where the wave function of this subband is mainly localized [5]) can lead to a reduction of heating in this subband and to a decrease in the rate of electron transitions to the upper states, thus enhancing electron accumulation in the Γ_2 subband and increasing the population inversion. Alternatively, a structure with a thinner barrier between the coupled QWs could be used in this case, which, for the same level of population inversion, will result in a larger value of the matrix element of the Γ_2–Γ_1 optical transition and, consequently, in a more pronounced laser effect.

5. CONCLUSIONS

We can conclude from the results obtained in this study that the structure under consideration holds great promise for developing a laser based on the intervalley transfer mechanism. A discussion of the detailed configuration of such a laser, the ways of suppressing high-field domains, as well as the competitiveness of the suggested design with respect to quantum-cascade lasers, is beyond the scope of this paper. We only mention that an intervalley-transfer laser may comprise a heterostructure consisting of repeated double QWs separated by AlGaAs barriers and grown on a semi-insulating substrate. In such a structure, the free-carrier absorption (which is always important in cascade lasers) is low for the TM mode. Thus, it is possible that the suggested design may be implemented in a system with low gain of the laser mode, e.g., in a structure with a small number of double-QW periods, which implies low threshold currents of such lasers.

ACKNOWLEDGMENTS

This study was supported in part by the Russian Foundation for Basic Research (project nos. 00-02-16159 and 02-02-16763); the program “Support for Leading Scientific Schools” (project no. 00-15-96618); the Ministry of Industry, Science, and Technology of the Russian Federation; the Russian Academy of Sciences program “Low-dimensional Quantum Structures”; and INTAS (project no. 99-0996).

REFERENCES

1. J. Faist, F. Capasso, D. L. Sivco, *et al.*, Science **264**, 553 (1994); F. Capasso, C. Gmachi, D. L. Sivco, and A. Y. Cho, Phys. World, June 27 (1999).
2. R. F. Kazarinov and R. A. Suris, Fiz. Tekh. Poluprovodn. (Leningrad) **5**, 797 (1971) [Sov. Phys. Semicond. **5**, 707 (1971)].
3. O. Gauthier-Lafaye, F. H. Julien, S. Cabaret, and J.-M. Lourtioz, Appl. Phys. Lett. **74**, 1537 (1999).
4. V. Ya. Aleshkin and A. A. Andronov, Pis’ma Zh. Éksp. Teor. Fiz. **68**, 73 (1998) [JETP Lett. **68**, 78 (1998)].
5. V. Ya. Aleshkin and A. A. Dubinov, Fiz. Tekh. Poluprovodn. (St. Petersburg) **36**, 724 (2002) [Semiconductors **36**, 685 (2002)].
6. V. Ya. Aleshkin, A. A. Andronov, and E. V. Demidov, Izv. Ross. Akad. Nauk, Ser. Fiz. **63**, 231 (2000).
7. G. W. Charach *et al.*, J. Appl. Phys. **86**, 452 (1999).
8. C. B. Geller, W. Wolf, S. Picozzi, *et al.*, Appl. Phys. Lett. **79**, 368 (2001).
9. S. Adachi, J. Appl. Phys. **58**, R1 (1985).
10. V. F. Gantmakher and I. B. Levinson, *Scattering of Charge Carriers in Metals and Semiconductors* (Nauka, Moscow, 1984).
11. R. Michevicius and A. Reklaitis, Semicond. Sci. Technol. **5**, 805 (1990).
12. A. Dargys and J. Kundrotas, *Handbook on Physical Properties of Ge, Si, GaAs, and InP* (Science and Encyclopedia, Vilnius, 1994), p. 163.

Translated by M. Skorikov

Semiconductors, Vol. 37, No. 2, 2003, pp. 220–223. Translated from Fizika i Tekhnika Poluprovodnikov, Vol. 37, No. 2, 2003, pp. 230–234.
Original Russian Text Copyright © 2003 by Faizrakhmanov, Bazarov, Kurbatova, Khaibullin, Stepanov.

Synthesis of New Carbon–Nitrogen Nanoclusters by Annealing Diamond-Like Carbon Films in Nitrogen

I. A. Faizrakhmanov[1], V. V. Bazarov[1], N. V. Kurbatova[1], I. B. Khaibullin[1], and A. L. Stepanov[1, 2]

[1] Physicotechnical Institute, Russian Academy of Sciences, Kazan, 420029 Russia

[2] Physikalisches Institut IA der RWTH; 52056 Aachen, Germany

e-mail: stepanov@physik.rwth-aachen.de

Submitted May 22, 2002; accepted for publication June 3, 2002

Abstract—Diamond-like carbon (DLC) films were prepared by ion-beam sputtering of a graphite target and annealed at a temperature of 400°C in vacuum and nitrogen with oxygen admixture (about 1–2%). The Raman and optical absorption spectra of these films were studied. Anomalous changes in the DLC films annealed in nitrogen were detected. The optical absorptance of films in the visible range of the spectrum decreased by approximately two orders of magnitude; the *D* and *G* lines of graphene nanoclusters disappeared in the Raman spectra, while new narrow lines at 928, 968, and 2324 cm^{-1}, as well as a broad line at 2200–2400 cm^{-1}, arose. These changes were found to be reversible. Subsequent annealing of the films in vacuum (400°C) restored the optical properties and Raman spectra of the samples. The results obtained are indicative of the formation of new carbon–nitrogen nanoclusters under certain conditions of annealing of a DLC film. © *2003 MAIK "Nauka/Interperiodica".*

1. INTRODUCTION

The properties of nanostructures and nanocluster systems significantly differ from those of bulk materials. In recent years, these objects have attracted considerable interest from the standpoint of their application in nanoelectronics and optoelectronics. Basic research gave rise to a new line of inquiry, i.e., the physics of nanostructures. Carbon-based nanostructures, including diamond-like carbon (DLC) films, are of particular interest in this context (see [1]). The role of nanometer particles in DLC films is played by graphene nanoclusters, from 0.5 to 5 nm in size, incorporated into a diamond-like amorphous host. Size quantization gives rise to a gap in the electron spectrum of graphene nanoclusters, which controls the optical absorption edge in these materials. Therefore, the electronic properties of carbon films can be varied over a wide range by controlling the sizes and concentrations of nanoclusters. This may be attained either by varying the conditions of film deposition or by subsequent energy-beam treatment. A characteristic property of these materials is metastability. Annealing at temperatures of ~300°C and above results in graphitization of the diamond-like host due to graphene nanocluster growth, which narrows the optical bandgap, increases the film conductivity by a few orders of magnitude, and causes characteristic changes in the Raman spectra [2]. A similar effect is also observed during ion implantation of diamond-like films [3]. However, an inverse process can be observed when bombarding with heavy ions such as xenon [4]. Radiation defects also have a significant effect. For example, the optical gap E_{gT}, determined from the Tauc dependence, becomes negative, which is caused by a large contribution of the band-gap electronic states (caused by nanocluster structure defects) to optical absorptance [4].

The incorporation of impurity atoms presents another possibility for controlling the electronic structure of graphene nanoclusters. Most of the studies in this line of inquiry are concerned with doping diamond-like films with nitrogen. It has been established that nitrogen impurity narrows the optical band gap and activates Raman vibrational modes in infrared absorption [5]. A similar effect was also observed when doping carbon film with copper [6]. However, in contrast to the incorporation of nitrogen into the nanocluster structure, copper atoms interact with nanoclusters in accordance with the intercalation mechanism. As a result of charge transfer from a copper atom to a nanocluster, the electron density becomes significantly redistributed and nanoclusters gain metal properties.

When studying DLC films, anomalous behavior of their optical properties in the course of annealing in nitrogen was detected. The optical absorptance in the visible region of the spectrum decreased by a few orders of magnitude, and the films became virtually transparent. Since nitrogen is almost inert under the annealing temperatures used in experiment (T = 400°C and lower), the result obtained was absolutely incomprehensible but intriguing. Thus, this new effect called for detailed studies.

2. EXPERIMENTAL

Diamond-like *a*-C films with a thickness of $d \approx$ 300 nm were deposited via ion-beam sputtering of graphite (xenon was used as the working gas; the ion energy was 1 keV) [7]. Fused quartz and single-crystal silicon wafers were used as substrates. The optical gap and the refractive index of the initial samples were ~0.8 eV and $n \approx 1.95$, respectively. We studied the optical properties and the Raman spectra (the excitation wavelength was $\lambda = 488$ nm) of the initial samples and samples annealed at a temperature $T = 400°C$ in vacuum (the residual pressure was $\sim 10^{-3}$ Pa) and in a nitrogen flow. The latter was initiated by the evaporation of liquid nitrogen containing 1–2% oxygen. The film thickness was determined by ellipsometry. The spectral dependence of the film absorptance in the visible and near ultraviolet regions was determined from film reflection and transmission spectra. Using these data, the Tauc dependence was derived,

$$(\alpha E)^{1/2} = B^{1/2}(E - E_{gT}), \qquad (1)$$

where α is the film absorptance; E is the photon energy; E_{gT} is the Tauc optical gap, defined by the average size of graphene nanoclusters in the film; and B is the Tauc dependence parameter, which is proportional to the graphene nanocluster concentration in the sample [3].

The Raman spectra of carbon films contain characteristic G (graphitic, 1575 cm^{-1}) and D (disordered, 1360 cm^{-1}) lines. Both bands are related to the vibrational modes of carbon atoms in graphene nanoclusters. The ratio between the intensities of these lines is defined by the nanocluster size; therefore, Raman spectroscopy allows for the determination of the average size of graphene nanoclusters.

3. EXPERIMENTAL DATA AND DISCUSSION

Figure 1 shows the Tauc dependences for carbon films annealed under various conditions. Annealing in vacuum results in the known changes in optical absorption (narrowing of the optical gap E_{gT}; see Fig. 1, curve *2*), which is caused by an increase in the size of nanoclusters. This conclusion is confirmed by the Raman spectroscopy data. Figure 2 shows the Raman spectra of an initial sample (curve *1*) and a sample annealed in vacuum (curve *2*). One can see that the spectrum of the initial sample is typical of diamond-like films. Annealing the films in vacuum causes the ratio of the D and G peak intensities to increase, which is also indicative of an increase in the size of nanoclusters. As the ellipsometry measurements show, the film thickness remained unchanged, while the refractive index slightly increased ($n \approx 2.1$ at the wavelength $\lambda = 632.8$ nm).

Annealing in nitrogen proceeds in two stages. A nanopore film arises at the first stage, which is indicated by a significant decrease in the refractive index (from 1.92 to 1.5). In addition, the film thickness decreases (from 300 to 210 nm). The decrease in the film thickness and density is caused by chemical interaction between oxygen (contained as an admixture in the working gas during annealing) and carbon; as a result, carbon dioxide is produced. At this stage, annealing also causes an increase in the size of nanoclusters, which is indicated by the optical measurement data (Fig. 1, curve *3*) and the Raman spectrum (Fig. 3, spectrum *1*). In this respect, this annealing does not differ from annealing in vacuum. A slight difference lies in the fact that a peak from the silicon substrate emerges

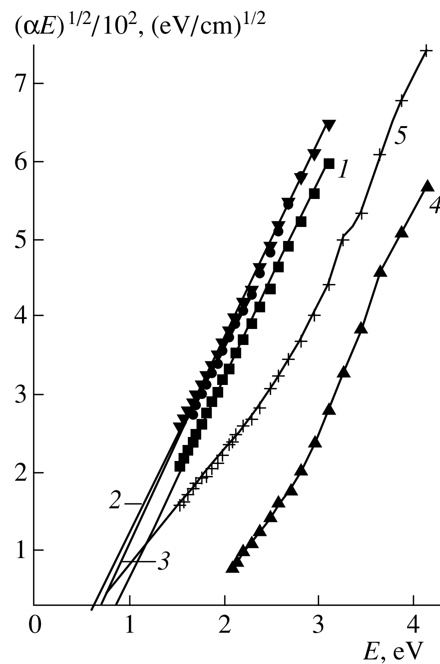

Fig. 1. Tauc dependence for the *a*-C films under various annealing conditions at $T = 400°C$: (*1*) initial sample, (*2*) 1-h annealing in vacuum, (*3*) 10-min annealing in N_2, (*4*) 35-min annealing in N_2, (*5*) (35-min annealing in N_2) + (1-h annealing in vacuum).

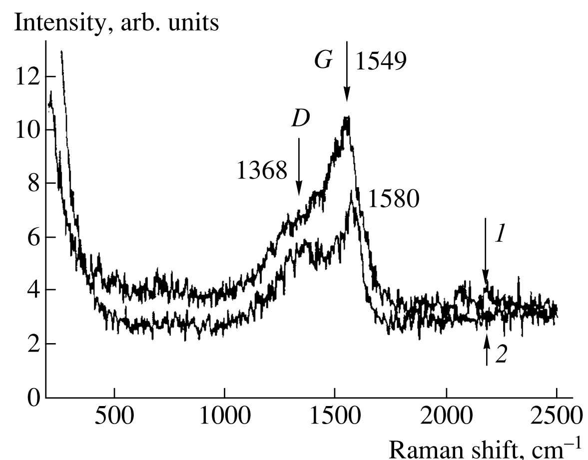

Fig. 2. Raman spectra of the initial sample (*1*) and after 1-h annealing in vacuum (*2*).

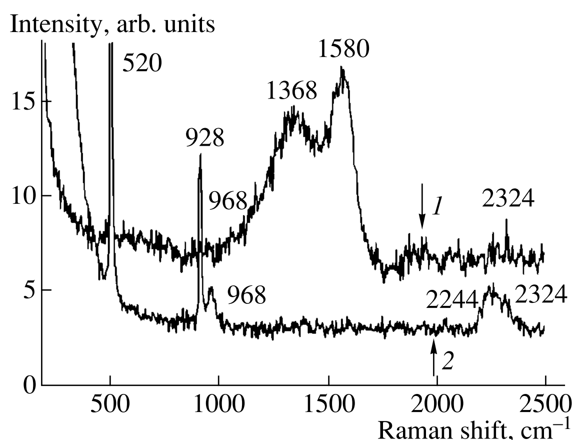

Fig. 3. Raman spectra of the samples after (*1*) 10-min and (*2*) 35-min annealing in nitrogen.

in the Raman spectrum at a frequency of 520 cm^{-1}, which is caused by a decrease in the refractive index and the carbon film thickness.

At the second stage, the film becomes translucent (see Fig. 1, curve *4*) and the Raman spectrum changes significantly (Fig. 3, spectrum *2*). The *G* and *D* lines disappear; however, several new lines arise, including one related to nitrogen molecules. At this stage, the spectral dependence of absorptance is no longer described by the Tauc dependence, which is indicative of a significant change in the electronic structure of the nanoclusters. Ellipsometry measurements showed that the film thickness remains unchanged ($d \approx 210$ nm), while the refractive index decreases to $n \approx 1.4$. The absence of the *G* and *D* lines and the significant change in the optical properties of the film suggest that the graphene nanoclusters disappear. However, this is not the case. If annealing is repeated at the same temperature but in vacuum, the optical absorption (Fig. 1, curve *5*) and Raman (Fig. 4) spectra are partially restored. It is worth noting that the spectral dependence of absorptance is again described by the Tauc law and the optical gap becomes the same as that after 10-min annealing in nitrogen (the first annealing stage). However, the slope of the dependence is appreciably smaller. This means that the electronic structure of some of the nanoclusters (approximately 2/3) is completely restored. The optical properties are completely restored if repeated annealing in vacuum is carried out at a temperature of ~500°C. The activation energy of this process is ~0.064 eV.

The low-temperature and reversible character of the observed changes in the electronic and vibrational structure of nanoclusters with a low activation energy of restoration indicate that the changes are related to adsorption of nitrogen molecules at graphene nanoclusters. This process requires nitrogen molecule transport to the nanocluster surface, which is attained owing to nanopores formed at the first annealing stage, during which nitrogen penetrates into the sample bulk. Therefore, an oxygen admixture in the nitrogen flow is a necessary condition.

As was mentioned above, molecular nitrogen is chemically inert at the annealing temperatures used and, thus, cannot form a chemical bond with carbon atoms. Therefore, the interaction between molecular nitrogen and a nanocluster must proceed according to the intercalation mechanism by means of electron transport to a cluster or, conversely, from a cluster. The direction of electron transport is controlled by the relative positions of the ground and excited levels of the nanocluster and adsorbed molecule, as in the case of adsorption, e.g., of NO_2 and NH_3 molecules at the diamond film surface [8]. The ground state of a nanocluster is lower than the vacuum level by approximately 1.5–2 eV [9]. The ionization and excitation energies of a nitrogen molecule are 15.5 and 6.1 eV, respectively; i.e., the first excited state is lower than the vacuum level by 9.4 eV. Therefore, we may assume that the electronic systems of the nanocluster and the adsorbed nitrogen molecule arrive at equilibrium due to electron transfer

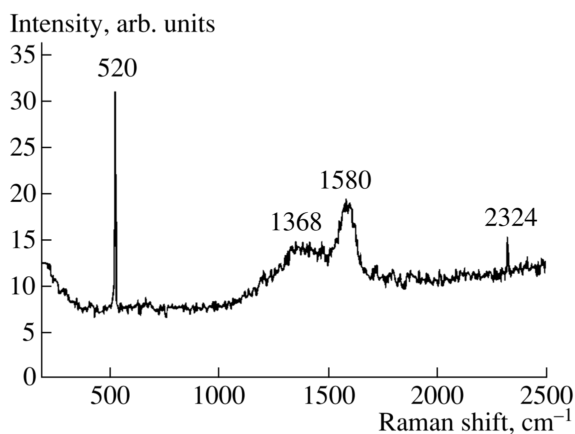

Fig. 4. Raman spectrum of the sample after 35-min annealing in nitrogen and subsequent 1-h annealing in vacuum.

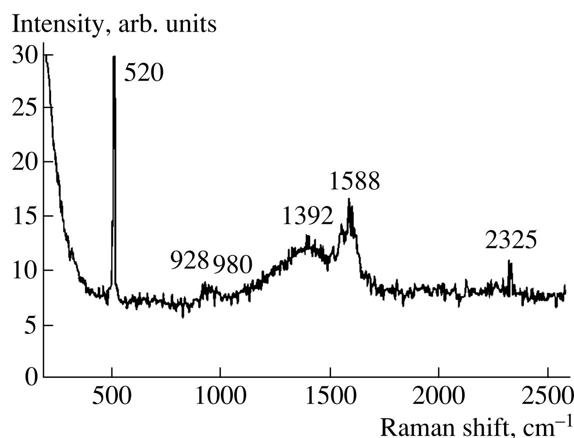

Fig. 5. Raman spectrum of the sample after 35-min annealing in nitrogen and subsequent 5-min annealing in vacuum.

from the nanocluster to the nitrogen molecule. As a result, the optical gap of the nanocluster widens significantly.

As in the case of intercalation by copper atoms [6], a single adsorbed nitrogen molecule is sufficient to change the electronic structure of a nanocluster. When the number of such molecules becomes large; i.e., the cluster becomes coated with nitrogen molecules, its vibration spectrum is shifted to higher frequencies (a band in the range of 2100–2300 cm^{-1}) and an additional vibrational mode appears (a band at 900–1000 cm^{-1}) due to weak bonding of nitrogen molecules with the nanocluster. The drastic change of the vibration spectrum indicates the formation of a new type of carbon–nitrogen nanoclusters. On the basis of this model, the two well-resolved peaks in the region of 900–1000 cm^{-1} can be explained by two types of nanoclusters; these are most likely nanoclusters with even and odd numbers of carbon atoms.

Figure 5 shows the intermediate Raman spectrum observed for the samples subjected to short-term (~5 min) repeated annealing in vacuum. One can see that these spectra contain bands characteristic of graphene and carbon–nitrogen nanoclusters. Similar spectra were observed previously in at least two studies [10, 11]. In the former study, DLCs doped with nitrogen were produced using a plasma beam source (PBS). Anomalous behavior of the optical and electrical properties of the films was detected as the nitrogen impurity concentration increased. Schwan *et. al.* [10] concluded that the film deposited using the PBS technique contains a substantially fewer number of graphene nanoclusters. The results obtained in this study show that this is not the case. The cause for this is that the electronic structure of at least a fraction of the nanoclusters is significantly modified due to intercalation by molecular nitrogen. In [11], a similar Raman spectrum was observed for DLC films produced by filtered vacuum cathodic arc evaporation and the band in the region of 950 cm^{-1} was attributed to the second-order Raman spectrum of the silicon substrate.

4. CONCLUSIONS

Anomalous changes in the vibrational spectrum and the optical properties of carbon films were detected in the course of annealing ($T = 400°C$) in nitrogen with an oxygen admixture. These changes were found to be reversible. Film modification was found to proceed in two stages. A nanopore carbon film is formed at the first stage. At the second stage, nitrogen molecules diffuse into nanopores. We suggested a qualitative model which attributed the observed changes to interaction between nitrogen molecules and graphene nanoclusters according to the intercalation mechanism with the formation of a new type of carbon–nitrogen nanoclusters.

ACKNOWLEDGMENTS

This study was supported by the federal program "Support for Leading Scientific Schools," project no. 00-15-96615.

REFERENCES

1. J. Robertson, Adv. Phys. **35**, 317 (1986).
2. R. O. Dillon, J. A. Woollam, and V. Katkanant, Phys. Rev. B **29**, 3482 (1984).
3. I. A. Faĭzrakhmanov, V. V. Bazarov, V. A. Zhikharev, and I. B. Khaĭbullin, Fiz. Tekh. Poluprovodn. (St. Petersburg) **35**, 612 (2001) [Semiconductors **35**, 591 (2001)].
4. I. A. Faizrakhmanov, V. V. Bazarov, V. A. Zhikharev, *et al.*, Vacuum **62**, 15 (2001).
5. J. H. Kaufman, S. Metin, and D. D. Saperstein, Phys. Rev. B **39**, 13053 (1989).
6. V. I. Ivanov-Omskiĭ and É. A. Smorgonskaya, Fiz. Tekh. Poluprovodn. (St. Petersburg) **32**, 931 (1998) [Semiconductors **32**, 831 (1998)].
7. I. A. Faĭzrakhmanov and I. B. Khaĭbullin, Poverkhnost **5**, 88 (1996).
8. Ri Sung Gi, K. Tashiro, S. Tanaka, *et al.*, Jpn. J. Appl. Phys. **38**, 3492 (1999).
9. K. Lmimouni, C. Legrand, C. Dufour, *et al.*, Appl. Phys. Lett. **78** (17), 2437 (2001).
10. J. Schwan, V. Batori, S. Ulrich, *et al.*, J. Appl. Phys. **84**, 2071 (1998).
11. J. Ullmann, Nucl. Instrum. Methods Phys. Res. B **127/128**, 910 (1997).

Translated by A. Kazantsev

Semiconductors, Vol. 37, No. 2, 2003, pp. 224–226. Translated from Fizika i Tekhnika Poluprovodnikov, Vol. 37, No. 2, 2003, pp. 235–237.
Original Russian Text Copyright © 2003 by Kazanskiĭ, Mell, Forsh.

AMORPHOUS, VITREOUS, AND POROUS SEMICONDUCTORS

Effect of Thermal Annealing on Optical and Photoelectric Properties of Microcrystalline Hydrogenated Silicon Films

A. G. Kazanskiĭ*, H. Mell, and P. A. Forsh***

** Moscow State University, Moscow, 119899 Russia*

*** Philipps-Universität Marburg, Fachbereich Physik, D-35032, Marburg, Germany*

Submitted June 6, 2002; accepted for publication June 14, 2002

Abstract—The effect of thermal annealing in the temperature range T_a = 300–600°C of films of microcrystalline hydrogenated silicon (μ*c*-Si:H) lightly doped with boron on the spectral dependences of the absorption coefficient (α) at photon energies $h\nu$ = 0.8–2.0 eV, dark conductivity (σ_d), and photoconductivity ($\Delta\sigma_{ph}$) was studied at room temperature. With increasing annealing temperature, a nonmonotonic variation of α (at $h\nu$ < 1.2 eV), σ_d, and $\Delta\sigma_{ph}$ was observed. The data obtained are attributed to a change in the concentration of electrically active impurities and formation of defects, caused by hydrogen effusion and bond restructuring at high annealing temperatures. © *2003 MAIK "Nauka/Interperiodica".*

Recently, microcrystalline hydrogenated silicon (μ*c*-Si:H) has been widely used to design electronic and optoelectronic devices [1, 2]. At the same time, carrier generation, transport, and recombination processes, governing the parameters of μ*c*-Si:H optoelectronic devices, are not yet fully understood. This is due to the complex structure of μ*c*-Si:H, which includes microcrystals and their boundaries, an amorphous phase, and voids. The multiphase structure of μ*c*-Si:H leads to a complex space and energy distribution of localized states, related to microcrystal boundaries and defects, which govern the behavior of nonequilibrium carriers. The available published data indicate that high-temperature annealing of μ*c*-Si:H affects both the structure of the material [3] and the concentrations of hydrogen [4] and defects [5] in μ*c*-Si:H. Therefore, our study was concerned with the effect of thermal annealing on the optical, electrical, and photoelectric properties of microcrystalline hydrogenated silicon lightly doped with boron. Films were annealed in order to change the structure and defect concentration of μ*c*-Si:H and to reveal their effect on the above-mentioned properties of μ*c*-Si:H.

We deposited the μ*c*-Si:H films under study, with a thickness of 0.7–0.8 μm, onto quartz substrates via decomposition of a mixture of monosilane (SiH_4) and hydrogen in an RF glow discharge. The substrate temperature was 250°C. To improve the photosensitivity of the films, they were lightly doped with boron in the course of deposition [6]. Doping was carried out by introducing diborane (B_2H_6) into the reaction chamber at a volume ratio $[B_2H_6]/[SiH_4]$ of 4×10^{-6}. The resulting films were of the *p*-type. According to electron microscopy, the unannealed films were composed of columns 30–100 nm in diameter that contained crystals 3–30 nm in size. The crystalline component of the films was 85% according to Raman spectra. μ*c*-Si:H samples obtained in a single growth run were then annealed in vacuum at a residual pressure $P = 2 \times 10^{-4}$ Pa at various temperatures in the range T_a = 300–600°C. Ohmic contacts (Au) were deposited onto the surface of the annealed films. The contact spacing was 0.6 mm. We carried out all measurements in a vacuum at a residual pressure of $P = 10^{-3}$ Pa after annealing the films at 180°C for 30 min.

Figure 1a shows spectral dependences of the absorption coefficient (α), which were obtained by the constant photocurrent method for an unannealed μ*c*-Si:H film and μ*c*-Si:H films annealed at different temperatures. Spectral dependences of the relative change in absorption, which is caused by high-temperature annealing ($\alpha_{an}/\alpha_{unan}$), are shown in Fig. 1b. Here, α_{an} and α_{unan} are the coefficients of absorption of annealed and unannealed films, respectively. As seen from Fig. 1b, the most pronounced changes in absorption are caused by high-temperature annealing at photon energies $h\nu$ < 1.2 eV. According to [7], the absorption at these photon energies is due to defect states in the band gap of μ*c*-Si:H. With the annealing temperature increasing to T_a = 500°C, the absorption at $h\nu$ < 1.2 eV grows, with the most pronounced rise in absorption observed at T_a ranging from 400 to 500°C. With T_a increasing further, the absorption at $h\nu$ < 1.2 eV decreases somewhat. It is noteworthy that raising the annealing temperature from 400 to 500°C also results in a minor increase in absorption at photon energies $h\nu$ > 1.2 eV.

The effect of the annealing temperature on the dark conductivity (σ_d) and photoconductivity ($\Delta\sigma_{ph}$) measured at $h\nu$ = 1.3 eV (intensity $I = 4 \times 10^{15}$ cm^{-2} s^{-1}) and 1.8 eV (intensity $I = 6 \times 10^{14}$ cm^{-2} s^{-1}) is shown in Fig. 2. It can be seen that σ_d grows with the annealing temperature T_a increasing to 450°C. With the annealing temperature increasing further, σ_d starts to decrease. This

1063-7826/03/3702-0224$24.00 © 2003 MAIK "Nauka/Interperiodica"

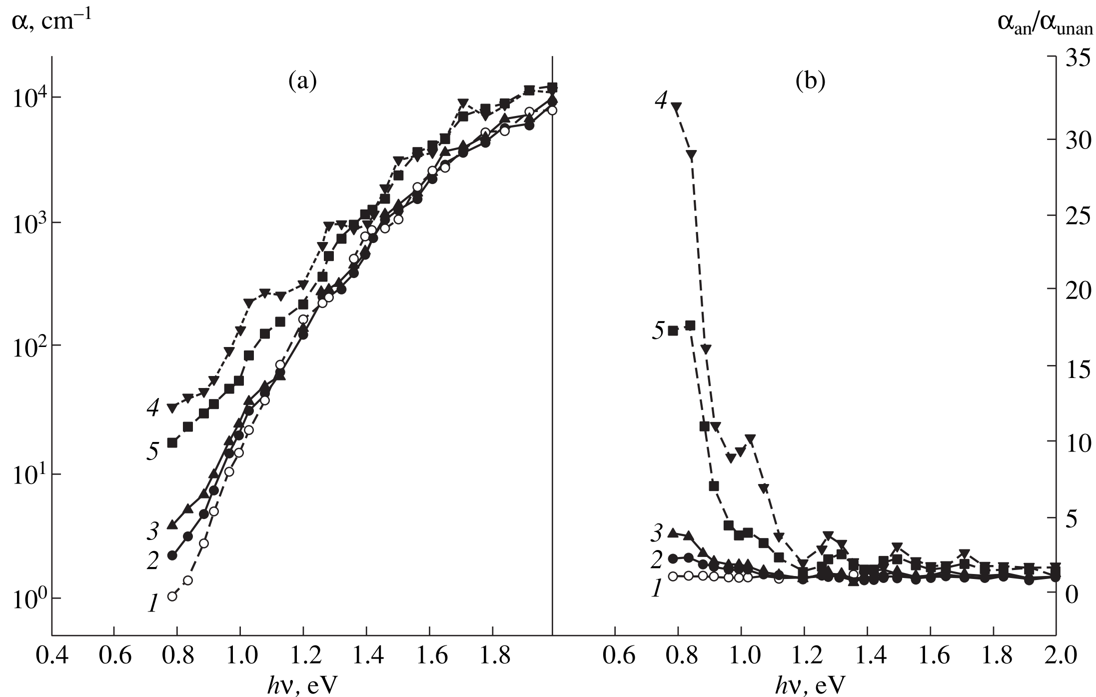

Fig. 1. Effect of μ*c*-Si:H film annealing temperature on (a) spectral dependences of the absorption coefficient measured by the constant photoconductivity method, and (b) spectral dependences of the relative change in the absorption coefficient caused by annealing. (*1*) Unannealed film; T_a: (*2*) 300, (*3*) 400, (*4*) 500, and (*5*) 600°C.

decrease is most pronounced in the temperature range from 500 to 550°C. Annealing at $T_a = 600$°C makes σ_d somewhat higher. The behavior of $\Delta\sigma_{ph}$ with the annealing temperature is similar to that of $\sigma_d(T_a)$, except in the high-temperature range, where $\Delta\sigma_{ph}(600°C) < \Delta\sigma_{ph}(500°C)$.

Let us consider the results obtained. As already mentioned, the absorption at $h\nu < 1.2$ eV is, in the opinion of Beck *et al.* [7], determined by the defect states in μ*c*-Si:H. Therefore, the observed change in the absorption in this range of photon energies may characterize the change in the defect concentration upon annealing μ*c*-Si:H. In particular, the rise in absorption upon annealing μ*c*-Si:H at temperatures up to 500°C may be due to an increase in the concentration of defects associated with dangling bonds both (mainly) at the surface and (to a lesser extent) within the columns, which appear as a result of hydrogen effusion during μ*c*-Si:H annealing. The temperature range in which the most pronounced increase in absorption is observed (400–500°C) corresponds to the temperatures at which the rate of hydrogen effusion from μ*c*-Si:H is at a maximum [8]. The decrease in absorption at $T_a = 600$°C may be due to bond restructuring at the column surface, which lowers the concentration of dangling bonds. The observed nonmonotonic variation of absorption in the range $h\nu < 1.2$ eV with the annealing temperature is in agreement with the nonmonotonic variation of the electron spin resonance (ESR) signal from dangling bonds for undoped μ*c*-Si:H films annealed at different temperatures.

It is noteworthy that a certain contribution to the absorption of μ*c*-Si:H may come from optical transitions involving states that belong to the amorphous phase and the exponential tails of the density of states, which appear as a result of the structural disorder and presence of microcrystal boundaries in μ*c*-Si:H. Variation of the density of these states with annealing temperature may also affect the manner in which the spectral dependence of absorption is changed.

It is known that high-temperature annealing of amorphous hydrogenated silicon increases the concentration of electrically active impurities [9]. If we assume that a similar process occurs in μ*c*-Si:H, then, presumably, the rise in conductivity with increasing T_a at $T_a \leq 450$°C (Fig. 2) is also due to an increase in the concentration of electrically active boron atoms and the corresponding shift of the Fermi level toward the valence band edge. The decrease in σ_d within the range $T_a = 450$–550°C may be due to an increase in the density of defect states within the columns (these states lie at the midgap of μ*c*-Si:H) and the corresponding shift of the Fermi level toward the midgap. For μ*c*-Si:H films annealed at $T_a \geq 550$°C, a change of the carrier transport mechanism is also possible. This is indicated by the results of our studies of the influence exerted by T_a on the temperature dependences of σ_d of μ*c*-Si:H films. It is noteworthy that a dramatic decrease in σ_d of undoped μ*c*-Si:H films annealed at $T_a = 470$–570°C was also

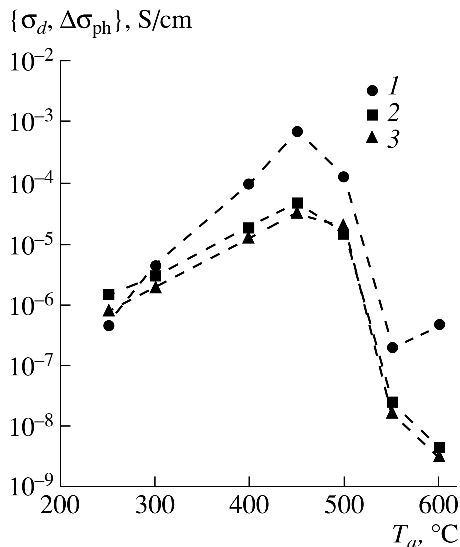

Fig. 2. (*1*) Dark conductivity σ_d and (*2*, *3*) photoconductivity $\Delta\sigma_{ph}$, measured at photon energies (*2*) $h\nu$ = 1.8 eV and (*3*) $h\nu$ = 1.3 eV, vs. annealing temperature. The values at T_a = 250°C correspond to an unannealed sample.

observed in [3, 5]. Lips *et al.* [5] considered this decrease in σ_d in terms of the barrier model of carrier transport in μ*c*-Si:H and attributed it to the expansion of the carrier-depleted layer to the entire column volume, which occurs when the concentration of dangling bonds at the column boundary exceeds a certain critical value. The increase in σ_d observed at T_a > 570°C, which correlates with the decrease in the ESR signal, was attributed to bond reconstruction and/or recrystallization.

In our opinion, the dependence $\Delta\sigma_{ph}(T_a)$ shown in Fig. 2 is accounted for by a change, upon annealing, in the Fermi level position and defect concentration, which affect the lifetime of nonequilibrium carriers in μ*c*-Si:H [5, 11]. At T_a < 450°C, the rise in $\Delta\sigma_{ph}$ with increasing T_a is presumably due to a shift of the Fermi level toward the valence band edge. At the same time, at T_a > 450°C, the decrease in σ_d with increasing T_a is associated both with a shift of the Fermi level toward the midgap and with an increase in the concentration of defects acting as recombination centers upon annealing.

Thus, our study demonstrated that thermal annealing of μ*c*-Si:H films weakly doped with boron leads to nonmonotonic variation of the absorption coefficient (at $h\nu$ < 1.2 eV), dark conductivity, and photoconductivity. In our opinion, this variation is due to changes in the concentration of electrically active impurities, the formation of defects at column boundaries and within the columns, and bond restructuring at high annealing temperatures.

REFERENCES

1. H. Stiebig, T. Brammer, J. Zimmer, *et al.*, J. Non-Cryst. Solids **266–269**, 1104 (2000).
2. Y. Uchida, T. Ichimura, M. Ufno, and H. Haruki, Jpn. J. Appl. Phys. **21**, L586 (1982).
3. D. Will, C. Lerner, W. Fuhs, and K. Lips, Mater. Res. Soc. Symp. Proc. **467**, 361 (1997).
4. M. Kondo, S. Yamasaki, and A. Matsuda, J. Non-Cryst. Solids **266–269**, 544 (2000).
5. K. Lips, P. Kanschat, D. Will, *et al.*, J. Non-Cryst. Solids **227–230**, 1021 (1998).
6. R. Fluckiger, J. Meier, M. Goetz, and A. Shah, J. Appl. Phys. **77**, 712 (1995).
7. N. Beck, J. Meier, J. Fric, *et al.*, J. Non-Cryst. Solids **198–200**, 903 (1996).
8. T. Itoh, K. Yamamoto, K. Ushikoshi, *et al.*, J. Non-Cryst. Solids **266–269**, 201 (2000).
9. I. A. Kurova, A. N. Lupacheva, N. V. Meleshko, and É. V. Larina, Fiz. Tekh. Poluprovodn. (St. Petersburg) **28**, 1092 (1994) [Semiconductors **28**, 628 (1994)].
10. J. W. Orton and M. J. Powell, Rep. Prog. Phys. **43**, 81 (1980).
11. A. G. Kazanskiĭ, Kh. Mell, E. I. Terukov, and P. A. Forsh, Fiz. Tekh. Poluprovodn. (St. Petersburg) **36**, 41 (2002) [Semiconductors **36**, 38 (2002)].

Translated by M. Tagirdzhanov

Semiconductors, Vol. 37, No. 2, 2003, pp. 227–232. Translated from Fizika i Tekhnika Poluprovodnikov, Vol. 37, No. 2, 2003, pp. 238–242.
Original Russian Text Copyright © 2003 by Kosyachenko, Rarenko, Zakharchuk, V. Sklyarchuk, E. Sklyarchuk, Solonchuk, Kabanova, Maslyanchuk.

Electrical Properties of Surface-Barrier Diodes Based on CdZnTe

L. A. Kosyachenko, I. M. Rarenko, Z. I. Zakharchuk, V. M. Sklyarchuk, E. F. Sklyarchuk, I. V. Solonchuk, I. S. Kabanova, and E. L. Maslyanchuk

Chernovtsy National University, Chernovtsy, 58012 Ukraine

Submitted February 27, 2002; accepted for publication April 25, 2002

Abstract—Diode structures obtained by vacuum sputtering deposition of Al onto the surface of p-$Cd_{1-x}Zn_xTe$ ($x = 0.05$) single crystals were studied. In the context of the Sah–Noyce–Shockley model for generation and recombination of charge carriers, a quantitative description of the diodes' electrical characteristics is attained.
© 2003 MAIK "Nauka/Interperiodica".

1. INTRODUCTION

A bright outlook for the use of CdTe in detectors of X-ray and radioactive radiation was substantiated and experimentally verified as early as the mid-1960s [1, 2]. The use of CdTe makes it possible to widen the sensitivity range of a detector to higher photon energies (up to several hundred electronvolts) compared to Si-based detectors, while the wider band gap of CdTe ensures operation at room temperature. By the early 1980s, as a result of subsequent research efforts, CdTe detectors had found application in industry and medicine, dosimetry and radiology, space studies, radioastronomy, and other fields [3, 4]. Notwithstanding the fact that a bright outlook for CdTe detectors had been repeatedly confirmed in further studies, technological problems have hindered the wide use of these detectors [5–9]. Only the careful control of the material and detector itself at all stages of growth and fabrication can ensure that the parameters which satisfy the specified requirements are attained. As a result, we have a low yield and, consequently, high cost of devices.

It was ascertained in the early 1990s in the course of the development of substrate material for $Hg_{1-x}Cd_xTe$ epitaxial layers that single crystals of $Cd_{1-x}Zn_xTe$ solid solution with $x = 0.05$–0.1 have a higher structural quality than CdTe crystals [10–12]. A lower concentration of defects and wider band gap of $Cd_{1-x}Zn_xTe$ make it possible to obtain single crystals with stoichiometric composition and a resistivity of about 10^{11} Ω cm at room temperature; this resistivity is about two orders of magnitude higher than that of CdTe (without compensation with chlorine) [12]. However, leakage currents in $Cd_{1-x}Zn_xTe$ detectors obtained by deposition of Au or Pt (metals with a high work function) were found to be lower than those of CdTe detectors only by several times. The origin of these currents is unclear; this is also true of the main mechanism of charge transport that controls the characteristics of $Cd_{1-x}Zn_xTe$ detectors. The possibility of decreasing the leakage currents by forming a rectifying contact between p-$Cd_{1-x}Zn_xTe$ and a metal with a low work function has not been realized.

In this paper, we report the results of studying the charge-transport mechanisms in Al–$Cd_{1-x}Zn_xTe$ surface-barrier structures with $x = 0.05$. The characteristics of these structures are interpreted in terms of a generation–recombination model in the space-charge region (SCR) of the diode structure.

2. SINGLE CRYSTALS OF $Cd_{1-x}Zn_xTe$

In order to fabricate the diodes, we used $Cd_{1-x}Zn_xTe$ single crystals ($x = 0.05$) grown by a modified Bridgman–Stockbarger method in quartz graphitized containers. Plates cut from cylindrical ingots were ground and thoroughly polished using diamond paste with a successively decreasing grain size (this size was less than 1 μm at the final stage). The band-gap width was determined from optical-absorption curves. In experiments, we used plane-parallel plates with thicknesses d in the range from 1 mm to 50–70 μm. It was found that, in the transparency region ($h\nu < E_g$), the values of the absorption coefficient α determined taking into account multiple reflections increase appreciably as the sample thickness decreases. For the samples with $d > 50$ μm, interference effects are not important. Therefore, the effect observed in many samples can be attributed to the fact that the absorption coefficient of the surface layer is larger than that of the crystal bulk [13, 14]. As the sample is thinned, the influence of this layer on sample transmission increases, which manifests itself in the observed dependence of the absorption coefficient. Comparison of the transmission spectra for samples differing in thickness shows that the thickness of the

1063-7826/03/3702-0227$24.00 © 2003 MAIK "Nauka/Interperiodica"

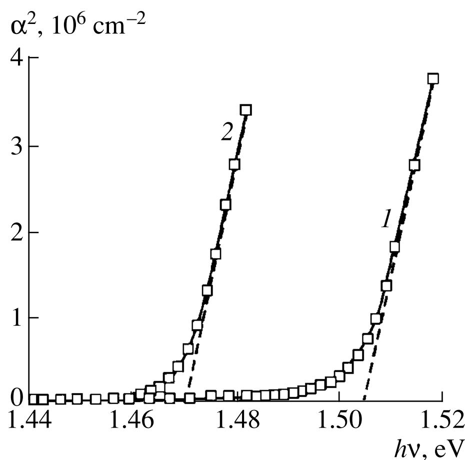

Fig. 1. Spectral dependences of absorption in the (*1*) $Cd_{0.95}Zn_{0.05}Te$ and (*2*) CdTe single crystals in the region of large absorption coefficients at 300 K.

surface layer with a larger absorption coefficient is no less than 30–50 μm.

Apparently, an increase in the absorption coefficient in the surface layer with a thickness of several tens of micrometers cannot be caused by mechanical damage in the ordinary sense when the damaged-layer thickness is governed by the grain size of the used abrasive agent. Additional absorption of light in the transparency region of $Cd_{1-x}Zn_xTe$ single crystals can be caused by dislocations and strain-related distortions of the crystal lattice, which arise as a result of mechanical treatment of the crystal surface, much the same as that which occurs in CdTe single crystals [15]. Dislocations act as sinks for impurities and defects, which may manifest itself not only in additional absorption but also in the appearance of a selective photoconductivity band in the region of $h\nu < E_g$. As has been shown [15], the effects of a locally stressed layer on the photoconductivity and crystal transparency are eliminated as a result of the chemical etching off of surface layers which are about 20 μm and 100 μm thick, respectively. It is not inconceivable that damage to the crystal lattice as a result of mechanical treatment of the surface can give rise to amorphization of the surface layer in a $Cd_{1-x}Zn_xTe$ crystal. Electron-diffraction studies of CdTe crystals [16] indicated that such a layer with a thickness larger than 20 μm and an absorption coefficient much larger than that in the crystal bulk can be formed.

The presence of a damaged layer at the mechanically polished surface distorts the fundamental-absorption edge, which is typically determined from the transmittance curves for the thinnest possible samples. Therefore, thin samples should be produced by chemical treatment rather than by mechanical polishing. Taking this into account, in Fig. 1 we show the curves of optical absorption in $Cd_{1-x}Zn_xTe$ in the region of large values of α; for the sake of comparison, the corresponding values of α for CdTe are also shown. The curves are plotted in coordinates that imply the allowed band-to-band transitions, in which case we have $\alpha \propto (h\nu - E_g)^{1/2}$.

As can be seen, extrapolation of the linear portion to the intersection with the abscissa axis yields the values E_g = 1.505 and 1.47 eV for $Cd_{0.95}Zn_{0.05}Te$ and CdTe, respectively (at 300 K). Expansion of the $Cd_{1-x}Zn_xTe$ band gap by 0.035 eV in comparison with CdTe is consistent with the almost linear increase in E_g from 1.47 eV for CdTe to 2.26 eV for ZnTe. It is worth noting that the absorption coefficient α is no larger than 1 cm^{-1} for thick samples (i.e., with the least pronounced effect of the surface layer) in the transparency range. This circumstance indicates that the single crystals used have fairly high quality [16, 17].

The presence of a damaged layer at the surface of $Cd_{1-x}Zn_xTe$ crystals also affects the results of electrical measurements. The resistance between two point-contact nonrectifying probes formed at opposite sides of the wafer depends on the wafer area; specifically, this resistance decreases appreciably as the wafer size decreases. This established fact is indicative of the comparatively low resistivity of the damaged layer at the crystal surface. This means that a surface layer with relatively low resistivity shunts the resistance of the crystal bulk.

The charge-carrier concentration in the single crystals under investigation was determined from the temperature dependence of the resistance. In order to minimize the effect of the surface layer, these temperature dependences were measured using large-area (0.5–1 cm^2) wafers subjected to chemical etching. The distance between the Fermi level and the valence-band top Δμ was determined from the slope of the dependence of resistance R between two nonrectifying contacts on temperature T (as a plot of ln$R$ vs. 1/T) and was found to be equal to 0.19 eV. Hence, it follows that the hole concentration $p = N_v\exp(-\Delta\mu/kT)$ is equal to 8×10^{15} cm^{-3} at room temperature (N_v is the effective density of states in the valence band). For such a material, the SCR width

$$W = \left[\frac{2\varepsilon\varepsilon_0(\varphi_0 - eV)}{e^2 p}\right]^{1/2}$$

(here, φ_0 is the barrier height, which can be estimated at 1 eV; ε is the relative dielectric constant of the semiconductor and is equal to 10.2 for CdTe; and ε_0 is the dielectric constant of free space) is equal to 4×10^{-15} cm under the conditions of zero bias. A surface-barrier diode with this active-region thickness can be used to detect X-ray photons with energies as high as 50 keV. However, the results reported below are also applicable to diodes fabricated from a material with a lower concentration of charge carriers (with a higher resistivity).

3. DIODES AND THEIR ELECTRICAL CHARACTERISTICS

The diode structures were obtained by evaporation of Al (in a vacuum chamber with a pressure of 10^{-4} Torr) onto the chemically etched surface of p-$Cd_{1-x}Zn_xTe$ single crystals at a temperature of about 100°C. A nonrectifying contact to the substrate was formed by chemical deposition of Cu from an aqueous $CuSO_4$ solution in the presence of In.

In Fig. 2, we show the current–voltage (I–V) characteristics of an Al–$Cd_{1-x}Zn_xTe$ structure measured at various temperatures in the range of 293–373 K.

Special attention should be given to the fairly high quality of the diode. At voltages of ±1 V, the forward current exceeds the reverse current by a factor larger than 10^4 at room temperature and by an even larger factor at lower temperatures. The forward portion of the I–V characteristic at $V < 0.6$–0.8 V (depending on temperature) follows the dependence $I \propto \exp(eV/2kT)$ as the current changes by more than four orders of magnitude, which is indicative of the generation–recombination origin of current in the samples under consideration. This is also shown by a sublinear increase in the reverse current, which is especially pronounced at elevated temperatures.

In the region of large forward currents (currents higher than 30–100 μA), the deviation of the curve $I(V)$ from the exponential law is caused by a voltage drop across the series resistance R_s in the diode structure. The value of R_s can be determined from the dependence of the diode's differential resistance R_{dif} on voltage. A portion with a tendency towards leveling off at $R_{dif} \approx R_s$ is observed at large biases in the $I(V)$ dependence measured at 373 K (see Fig. 3a); thus, we obtain R_{dif} = 420–480 Ω. The current I depends linearly on V in the same region of bias voltages (Fig 3b). The cutoff voltage on the horizontal axis in this dependence yields the value of limiting voltage across the barrier; in the case under consideration, this voltage is equal to about 0.7 V. As a result, we may conclude that the barrier height in the diode under consideration is no lower than 0.7 eV.

4. CALCULATION OF THE CURRENT–VOLTAGE CHARACTERISTIC

According to the Sah–Noyce–Shockley model [18], the generation–recombination rate in a depletion layer is given by

$$U(x, V) = \frac{n(x, V)p(x, V) - n_i^2}{\tau_{p0}[n(x, V) + n_1] + \tau_{n0}[p(x, V) + p_1]}, \quad (1)$$

where $n(x, V)$ and $p(x, V)$ are the concentrations of free charge carriers in the conduction and valence bands, respectively; and τ_{n0} and τ_{p0} are the effective lifetimes of electrons and holes, respectively, in the SCR. The

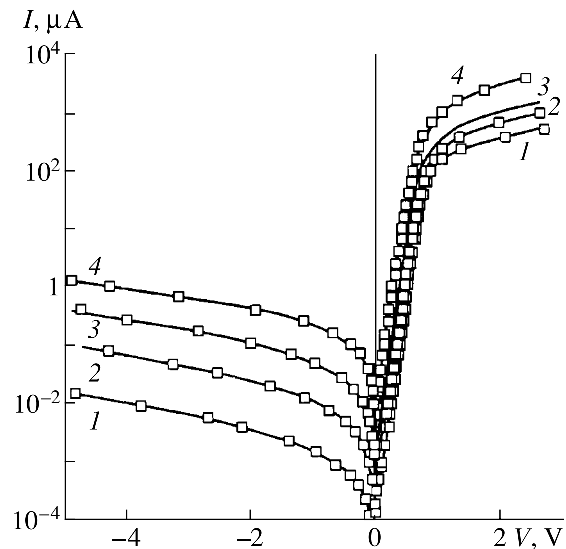

Fig. 2. Current–voltage characteristics of an Al–$Cd_{1-x}Zn_xTe$ diode at temperatures T = (1) 293, (2) 313, (3) 340, and (4) 373 K.

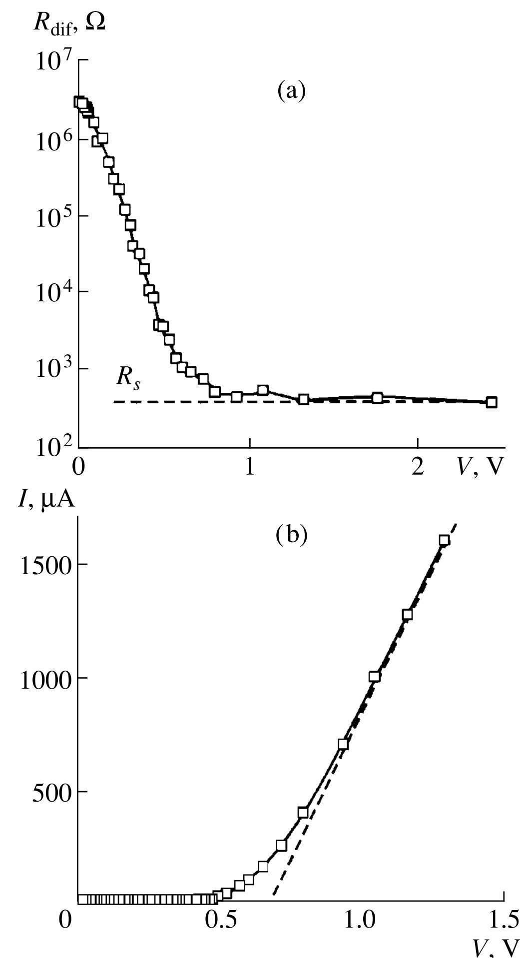

Fig. 3. Dependences of (a) differential resistance and (b) forward current for an Al–$Cd_{1-x}Zn_xTe$ diode on the bias voltage at T = 373 K.

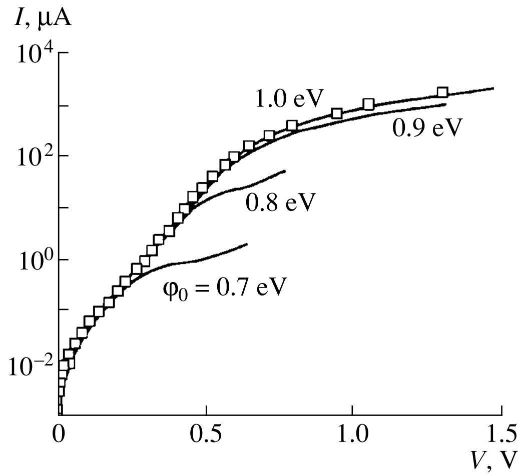

Fig. 4. Forward portions of the current–voltage characteristics calculated for several values of the barrier height φ_0 indicated at the curves. $T = 373$ K and $R_s = 440\ \Omega$.

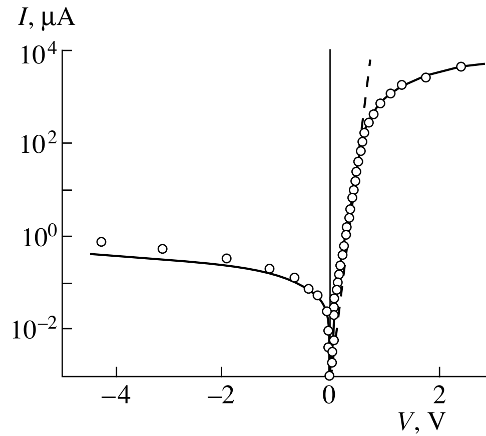

Fig. 5. The measured (circles) and calculated (solid line) current–voltage characteristics of an Al–CdZnTe diode at 373 K. The dashed line represents the dependence $I(V)$ without taking into account the voltage drop across the series resistance of the diode structure (440 Ω).

quantities n_1 and p_1 are equal to equilibrium concentrations of electrons and holes when the Fermi level coincides with the recombination-center level; i.e.,

$$n_1 = \frac{N_c}{\exp\left(\frac{E_t}{kT}\right) + 1}, \quad (2)$$

$$p_1 = \frac{N_v}{\exp\left(\frac{E_g - E_t}{kT}\right) + 1}, \quad (3)$$

where N_c is the effective density of states in the conduction band, E_t is the energy spacing between the recombination-center level and the valence-band top, and E_g is the band gap. The density of the generation–recombination current is obtained by integrating $U(x, V)$ over the entire SCR; i.e.,

$$I = Ae\int_0^W U(x, V)dx, \quad (4)$$

where A is the diode area and e is the elementary charge.

If the energy is reckoned from the valence-band top in the crystal bulk, the electron and hole concentrations in the SCR are given by [19]

$$n(x, V) = N_c \exp\left[-\frac{E_g - \Delta\mu - \varphi(x, V) - eV}{kT}\right], \quad (5)$$

$$p(x, V) = N_v \exp\left[-\frac{\Delta\mu + \varphi(x, V)}{kT}\right], \quad (6)$$

where $\varphi(x, V)$ is the potential-energy profile in the SCR:

$$\varphi(x, V) = (\varphi_0 - eV)\left(1 - \frac{x}{W}\right)^2. \quad (7)$$

In Fig. 4, we show the diode's I–V characteristics calculated using formula (4) and taking into account (1)–(3) and (5)–(7) for several barrier heights φ_0 at 373 K.

In calculations, we assumed that the effective masses of electrons and holes were equal to $0.11m_0$ and $0.35m_0$, respectively; we also took into account the narrowing of the band gap (as the temperature increased) with the coefficient -4×10^{-4} eV/K, set the series resistance R_s equal to 440 Ω, and assumed that $\Delta\mu = 0.19$ eV.

As might be expected, the best fit of the results of calculations to the experimental data is attained if we assume that the recombination-center level is located at the midgap, i.e., if we set $E_t = 0.75$ eV. According to the Shockley–Read statistics, the level at $E_t \approx 0.75$ eV corresponds to the most efficient recombination centers; as this level recedes from the midgap, the lifetime of charge carriers increases rapidly.

In order to attain the best fit of the calculated value of forward current to the corresponding experimental data, we assumed that the lifetimes of charge carriers τ_{n0} and τ_{p0} were equal to 2×10^{-10} s. These lifetimes are controlled by the capture cross section and the concentration of impurity (defect) levels in the semiconductor band gap [18]. The value of τ_{n0} coincides with the electron lifetime if all traps are empty; in contrast, the value of τ_{p0} coincides with the hole lifetime if all traps are filled with electrons.

Figure 4 illustrates variations in the dependence $I(V)$ as the barrier height φ_0 is varied. The best fit of the

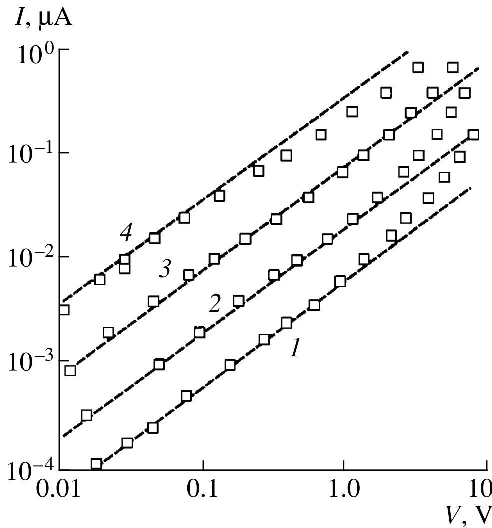

Fig. 6. Reverse portions of current–voltage characteristics at temperatures T = (*1*) 293, (*2*) 313, (*3*) 340, and (*4*) 373 K. Dashed lines represent the linear dependences.

results of calculations to the experimental data is attained if we assume that $\varphi_0 \approx 1$ eV.

Knowing all the necessary parameters, we can calculate not only the forward current but also the reverse current; the latter is shown in Fig. 5 for a temperature of 373 K. As can be seen, good agreement between the results of calculations and the experimental data is observed not only for forward biases but also for low reverse-bias voltages (with magnitudes smaller than ~1 V). As the magnitude of the reverse-bias voltage increases, experimental points deviate upward from the calculated dependence. At lower temperatures, the discrepancy between the results of calculations and measurements increases, so that the reverse current measured at 293 K exceeds the calculated generation current by more than an order of magnitude. As the temperature is lowered, the shape of the I–V characteristic also changes. This is readily illustrated in Fig. 6, where we show the reverse portions of the I–V characteristics of the same diode at several temperatures.

It follows from theory that, in the range of low reverse-bias voltages ($kT \ll |eV| \ll E_g - E_t$), the generation current depends linearly on the applied voltage, whereas this dependence is sublinear at higher voltages [19]. In fact, such behavior of $I(V)$ is observed for the dependence measured at 373 K (Fig. 6, curve *4*). However, a linear increase in current with voltage changes to a superlinear dependence at lower temperatures (Fig. 6, curves *1*, *2*). Apparently, such evolution of the $I(V)$ dependence can be attributed to the increasing role of tunneling, which is dominant in the charge transport at low temperatures.

The barrier width in the diodes under investigation is equal to 10^{-4} cm at the magnitudes of reverse-bias voltages equal to about 5 V. It seems unlikely that there is any appreciable tunneling through such a wide barrier over the entire diode surface. However, tunneling is quite probable at the sites where the electric field is concentrated, in particular, at the periphery of the metal contact. Leakage currents of such an origin are always observed unless special precautions are taken (passivation of the surface, formation of a guard ring, and so on).

5. CONCLUSIONS

The results of optical and electrical measurements indicate that there is a layer with a thickness of 30–50 nm at the surface of $Cd_{1-x}Zn_xTe$ single crystals; this layer has a much higher absorptance and electrical conductivity than those in the bulk of the crystal.

The Al–CdZnTe contact features a clearly pronounced diode characteristic with a rectification factor exceeding 10^4 at room temperature. The height of the barrier formed as a result of vacuum evaporation of Al onto the p-CdZnTe surface amounts to $\varphi_0 \approx 1$ eV.

The dominant mechanism of charge transport in the Al-CdZnTe diodes under investigation is the generation–recombination of charge carriers in the space-charge region. The current–voltage characteristic of the diodes is quantitatively described in terms of the Sah–Noyce–Shockley model for generation and recombination. Leakage currents (apparently, of tunneling origin) are involved in the formation of reverse current at low temperatures.

REFERENCES

1. E. N. Arkad'eva, O. A. Matveev, S. M. Ryvkin, and Yu. V. Rud', Zh. Tekh. Fiz. **36**, 1146 (1966) [Sov. Phys. Tech. Phys. **11**, 846 (1966)].
2. E. N. Arkad'eva, O. A. Matveev, S. M. Ryvkin, and Yu. V. Rud', Fiz. Tekh. Poluprovodn. (Leningrad) **1**, 805 (1967) [Sov. Phys. Semicond. **1**, 669 (1967)].
3. P. Siffert, Nucl. Instrum. Methods **150**, 1 (1978).
4. Eiji Sakai, Nucl. Instrum. Methods Phys. Res. **196**, 121 (1982).
5. K. Mochizuki, T. Yoshida, K. Igaki, *et al.*, Mater. Lett. **3**, 219 (1985).
6. M. R. Squillante, G. Entine, E. Frederick, *et al.*, Nucl. Instrum. Methods Phys. Res. A **283**, 323 (1989).
7. G. Entine, P. Waer, T. Triernan, and M. R. Squillante, Nucl. Instrum. Methods Phys. Res. A **283**, 282 (1989).
8. M. Richter and P. Siffert, Nucl. Instrum. Methods Phys. Res. A **322**, 529 (1992).
9. Y. Eisen, Nucl. Instrum. Methods Phys. Res. A **322**, 596 (1992).

10. J. F. Butler, C. L. Lingren, and F. P. Doty, IEEE Trans. Nucl. Sci. **39**, 605 (1992).
11. R. Hess, P. DeAntonis, E. J. Morton, and W. B. Gilboy, Nucl. Instrum. Methods Phys. Res. A **353**, 76 (1994).
12. Y. Eisen and A. Shor, J. Cryst. Growth **184/185**, 1302 (1998).
13. M. P. Lisitsa, B. N. Malynko, E. V. Pidlisnyi, and G. G. Tsebulya, Surf. Sci. **11**, 411 (1968).
14. M. P. Lisitsa, V. N. Malinko, E. V. Podlisnyĭ, and G. G. Tsebulya, Ukr. Fiz. Zh. **14**, 1297 (1969).
15. A. Baĭdullaeva, A. I. Vlasenko, and P. E. Mozol', Fiz. Tekh. Poluprovodn. (St. Petersburg) **31**, 1428 (1997) [Semiconductors **31**, 1234 (1997)].
16. D. T. F. Marple, Phys. Rev. **150**, 728 (1966).
17. R. O. Bell, Rev. Phys. Appl. **12**, 391 (1977).
18. C. Sah, R. Noyce, and W. Shockley, Proc. IRE **45**, 1228 (1957).
19. L. A. Kosyachenko, V. P. Makhniĭ, and I. V. Potykevich, Ukr. Fiz. Zh. **23**, 279 (1978).

Translated by A. Spitsyn

Semiconductors, Vol. 37, No. 2, 2003, pp. 233–238. Translated from Fizika i Tekhnika Poluprovodnikov, Vol. 37, No. 2, 2003, pp. 243–248.
Original Russian Text Copyright © 2003 by Skrynnikov, Zegrya, Pikhtin, Slipchenko, Shamakhov, Tarasov.

PHYSICS OF SEMICONDUCTOR DEVICES

Internal Quantum Efficiency of Stimulated Emission of (λ = 1.55 μm) InGaAsP/InP Laser Diodes

G. V. Skrynnikov, G. G. Zegrya, N. A. Pikhtin*, S. O. Slipchenko, V. V. Shamakhov, and I. S. Tarasov

Ioffe Physicotechnical Institute, Russian Academy of Sciences, Politekhnicheskaya ul. 26, St. Petersburg, 194021 Russia

**e-mail: nike@hpld.ioffe.rssi.ru*

Submitted June 17, 2002; accepted for publication June 19, 2002

Abstract—The stimulated emission (η_i^{st}) of InGaAsP/InP separate-confinement double heterostructure lasers operating at λ = 1.5–1.6 μm has been studied experimentally and theoretically. Laser heterostructures with a varied design of the waveguide layer were grown by MOCVD. The maximum internal quantum efficiency $\eta_i^{st} \approx 97\%$ was obtained in a structure with a double-step waveguide characterized by minimum leakage into the *p*-emitter above the generation threshold. The high value of η_i^{st} is provided by low threshold and nonequilibrium carrier concentrations at the interface between the waveguide and *p*-emitter. The calculation yields η_i^{st} values correlating well with the experimental data. © *2003 MAIK "Nauka/Interperiodica"*.

1. INTRODUCTION

The emission power is one of the most important characteristics of a semiconductor laser. The internal quantum efficiency of stimulated emission, η_i^{st}, is the principal factor defining the efficiency of semiconductor laser operation and, finally, the optical output power. Typical η_i^{st} values of separate confinement (SC) heterostructure lasers with a lasing wavelength λ = 1.3–1.55 μm are 65–75% [1]. The cause for low η_i^{st} values are additional losses, such as current losses above the generation threshold [2]. Since similar lasers emitting at $\lambda \approx 0.98$ μm have an η_i^{st} close to 100% [3], a detailed study of the loss mechanisms in lasers with λ = 1.3–1.55 μm seems urgent. An analysis of η_i^{st} for heterostructures differing in the waveguide design can provide structure optimization and substantially raise the emission power.

The goal of the present study is the experimental and theoretical investigation of the internal quantum efficiency of stimulated emission of InGaAsP/InP separate-confinement double heterostructure (SC DH) lasers (λ = 1.5–1.6 μm) with varying design of the waveguide layer.

2. SAMPLES

Figure 1 shows three SC heterostructures with two strained quantum wells (QW) selected as basic samples for study; they differ in the configuration and energy parameters of the waveguide "steps" (*A* is a simple, *B* a double-step, and *C* a single-step waveguide). The QW thickness is varied in the range d_a = 50–64 Å. The parameters of the heterostructures are listed in the table. All samples were grown on *n*-InP substrates by MOCVD. The composition of the solid solution in InGaAs strained QWs and emitters was the same. A structure was divided into laser diodes whose cavity length varied in the range L = 200–2500 μm. The cavity faces were coated by Si/SiO_2 mirrors with a reflectance $R > 0.95$ and an antireflection coating with $R < 0.04$. The diodes were mounted onto copper heat sinks using indium solder.

3. EXPERIMENT

The light–current characteristics were recorded for laser diodes of differing cavity length, from which the external differential quantum efficiency and threshold current density were determined. Figure 2 presents thus-obtained dependences of the inverse external differential quantum efficiency η_d on the laser cavity length. Using the experimental $\eta_d(L)$ dependences and the well-known relation

$$\eta_d = \eta_i \frac{\alpha_{ext}}{\alpha_{int} + \alpha_{ext}}, \quad (1)$$

we determined the internal optical loss α_{int} and the internal quantum efficiency of stimulated emission,

Table

Structure type	E_{g1}, eV	E_{g2}, eV	E_{g3}, eV	W_1, μm	W_2, μm	W_3, μm	α_i^{exp}, cm^{-1}	η_i^{exp}, %	η_i^{calc}, %	Γ_{WG}^{Σ}, %	Γ_{ac}, %
A	1.13	–	–	1.0	–	–	4.5	67	73	13	1.03
B	1.24	1.13	1.03	0.86	0.36	0.12	3.6	85	90	16	1.45
C	1.181	0.992	–	0.672	0.232	–	9	95	97	20	2

η_i^{st}, for all the structures studied. The obtained values of α_{int} and η_i are listed in the table.

4. THEORETICAL MODEL

First of all, it is necessary to note that the definitions of the internal quantum efficiency above and below the lasing threshold are strongly different. Below the threshold, the internal quantum efficiency is expressed via the ratio of the rates of radiative and nonradiative recombination processes, R_{ph} and R_{nr} [5]:

$$\eta_i = \frac{R_{ph}}{R_{ph} + R_{nr}}. \quad (2)$$

Above the lasing threshold, the internal quantum efficiency of stimulated emission, η_i^{st}, is defined as the ratio of the stimulated emission current I_{st} to total current I above the generation threshold [6]:

$$\eta_i^{st} = \frac{I_{st}}{I - I_{th}}. \quad (3)$$

It is necessary to note that, at high (close to 100%) internal quantum efficiency of spontaneous emission, the internal quantum efficiency of stimulated emission may strongly differ from 100%. This is related to the existence of various current leaks. Above the generation threshold, the total current through the laser structure can be defined as the stimulated emission current summed with all the other components:

$$I = I_{st} + I_L + I_{th}. \quad (4)$$

Here, I_L is the leakage current above the generation threshold, and I_{th} is the threshold current which will be calculated in terms of the model [7], which demonstrated good correlation with an experiment for $\lambda \approx 1.55$ μm lasers [8]. Then, with account of Eq. (4), the relation for η_i^{st} becomes

$$\eta_i^{st} = 1 - \frac{I_L}{I - I_{th}}. \quad (5)$$

This expression shows that the magnitude of η_i^{st} is affected only by those currents which continue growing even above the generation threshold; in our case, these are the leakage currents.

As a rule, above the generation threshold, the electron and hole densities n_{th}, p_{th}, and, correspondingly, the position of quasi-Fermi levels in the active region are stable, or vary only slightly [6]. Then, all the currents which depend monotonically on these densities do not affect the η_i^{st} value. However, the carrier density in the waveguide, N_{SCH}, keeps on growing above the generation threshold [9]. In the experiment, this process is accompanied by the increasing intensity of the photolu-

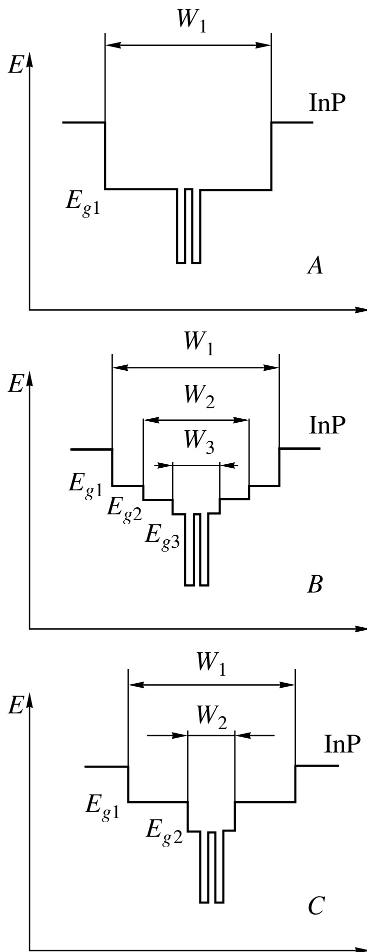

Fig. 1. Band diagrams of the laser structures under study. (*A*) simple waveguide, (*B*) double-step waveguide, (*C*) single-step waveguide; (W_1, W_2, W_3) and (E_{g1}, E_{g2}, E_{g3}) are the waveguide thickness and band gap, respectively.

minescence (PL) bands related to optical transitions within the waveguide or those from the waveguide layer to QW levels. Increasing spontaneous emission from the waveguide above the generation threshold, which is indicative of increasing carrier density in this layer, was observed in [2]. This experiment showed that the reduction of η_i^{st} cannot be accounted for only by recombination in the waveguide. The leakage of carriers to a contact also contributes to the magnitude of η_i^{st}, and the leakage current increases as the current of majority carriers rises, since the drift component of the current leakage to the emitter increases. The rise of spontaneous emission from the waveguide was also observed in [10], and the increasing PL from the waveguide above the generation threshold was attributed to the finite time of the carrier trapping by a QW. In this situation, the injected carriers are accumulated in the waveguide, which indirectly raises the intraband absorption losses and reduces the differential quantum efficiency of a laser.

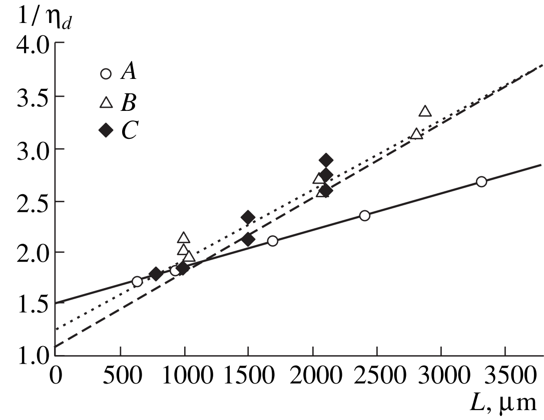

Fig. 2. The inverse external differential quantum efficiency η_d vs. the laser cavity length L: (A) simple, (B) double-step, (C) single-step waveguide.

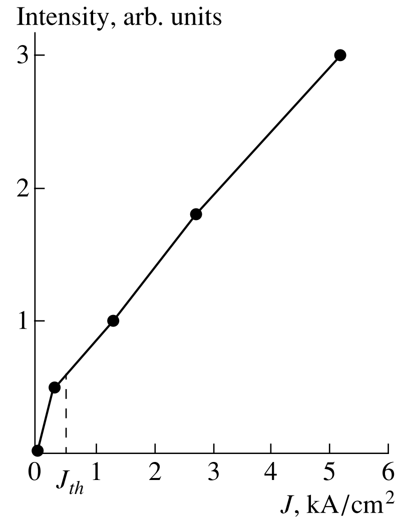

Fig. 3. The intensity of PL from the waveguide layer I vs. the driving current density J (below and above the threshold).

In all the structures under study, we observed an increase in the intensity of spontaneous emission related to radiative transitions from the waveguide layer with the narrowest band gap to the levels in the QW and to the waveguide itself (Fig. 3) [9]. This fact, which indicates that the carrier density in the waveguide layers increases above the generation threshold, can be explained as follows. The rise of carrier density in the waveguide N_{SCH} is caused by carrier emission from QWs [7]. A part of the injected carriers is emitted from QWs and contributes to N_{SCH}, with this concentration increasing linearly with the driving current. Some carriers entering the waveguide recombine radiatively or nonradiatively, and others form leak currents from the waveguide to the emitter via drift and diffusion. The magnitude of these leak currents, which varies in direct proportion to the density N^* of minority carriers (electrons) at the interface with the p-type layer, grows with an increase in the total current density J flowing through the heterostructure. In the general case, the total leakage current J_L is defined by three components (recombination, drift, and diffusion) and takes the form

$$J_L = \frac{eN_{SCH}L_{SCH}}{\tau_n} + N^*D_n^e e(J^*_{drift} + J^*_{diff}). \qquad (6)$$

Here, L_{SCH} is the waveguide thickness; N_{SCH}, the carrier density in the waveguide; τ_n, the lifetime of minority carriers in the waveguide region, defined by all the recombination processes occurring therein; D_n^e, the diffusion constant of minority carriers in the emitter; J^*_{drift} and J^*_{diff}, the dimensionless diffusion and drift components of the density of leakage current from the waveguide to the emitter. The total leakage current J_L (6) for the studied structures was calculated by the method derived in [2] with the self-consistent determination of leakage J_L and recombination currents in the active region. It was assumed that

(1) all the layers in a heterostructure are quasi-neutral, and the quasi-Fermi levels of majority and minority carriers are continuous at all the interfaces;

(2) the space charge layers in the waveguide, formed at the interface and providing quasi-neutrality, occupy a small fraction of the total waveguide thickness, and the recombination there is negligible;

(3) Auger recombination occurs only in the active region;

(4) heating processes in the active region are negligible;

(5) above the generation threshold, the electron and hole densities and, correspondingly, the quasi-Fermi

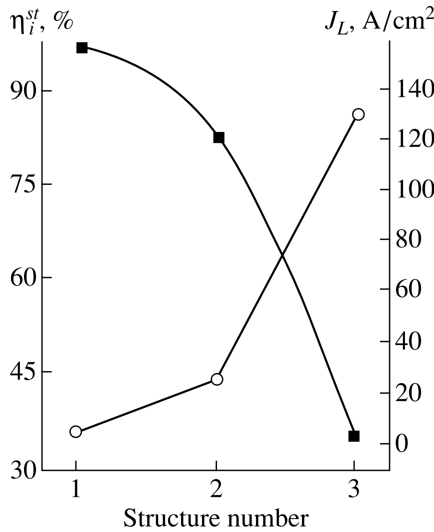

Fig. 4. Calculated η_i^{st} and J_L for SC DH with (*1*) single-step waveguide *C*; (*2*) $E_g^{WG} = 0.992$ eV; (*3*) $E_g^{WG} = 1.18$ eV.

levels do not change across the active region and the interface between the active region and the waveguide;

(6) in a heterostructure with a step waveguide, the threshold density at the interface with the *p*-emitter is calculated in terms of the Boltzmann approximation successively for each of the waveguides.

The increase in the hole density Δp in the portion of the waveguide between the active region and the *p*-type emitter is expressed in terms of the recombination current in the active region (which includes spontaneous and stimulated recombination) as follows [2]:

$$J_p = D_p \frac{\Delta p}{(d_w/2)} \frac{(n_0 + 2p_1)}{(n_0 + \gamma p_1)} e, \quad (7)$$

where D_p is the diffusion coefficient of holes; d_w, the waveguide size; n_0, the equilibrium density of electrons in the waveguide; p_1, the hole density at the interface between the waveguide and QW; and

$$\gamma = 1 - J_n/J_p \frac{\mu_p^w}{\mu_n^w}, \quad (8)$$

where μ_p^w and μ_n^w are the hole and electron mobilities in the waveguide. The expression for γ includes the density of the electron leakage current J_n, which is composed of the diffusion and drift components of the total leakage current (6). The current J_n itself is dependent on Δp and defined as

$$J_n = eD_n^e n_e (1/L_S \coth(SL_S) + 0.5z), \quad (9)$$

where D_n^e is the diffusion coefficient of electrons in the *p*-emitter; *S*, the thickness of the *p*-emitter,

$$L_S = \sqrt{(1/L_n^2 + 1/4z^2)}; \quad (10)$$

L_n, the diffusion length of electrons in the emitter,

$$z = kT/eE; \quad (11)$$

and *E*, the electric field in the emitter, equal to

$$E = \frac{I_p}{e\mu_p^e N_a}. \quad (12)$$

Here, μ_p^e and N_a are the hole mobility and the doping level in the emitter, respectively; and n_e is the density of nonequilibrium electrons at the interface between the emitter and waveguide.

The recombination and leakage currents were calculated until self-consistent solutions with the initial Δp, J_n values at the generation threshold were obtained.

The recombination current in the waveguide was calculated assuming that the radiative recombination constant B_w is independent of the total current in the structure, because the contribution from the recombination in the waveguide to the total leakage current is small as compared with other J_L components.

Using the calculated J_L and the determined threshold current density J_{th}, we can find η_i^{st} by determining the internal quantum efficiency above the generation threshold (5). The calculated η_i^{st} values for the studied structures are listed in the table.

5. DISCUSSION

Structures differing in the design of their waveguide layer show wide variation (from 67 to 97%) in their values of internal quantum efficiency of stimulated emission (see the Table). This result can be explained as follows. As stated above, the strongest influence on current leakages (6) is exerted by the density N^* of minority carriers (electrons) at the interface with the *p*-layer, which is determined by the threshold density and the design of the waveguide layer. Increasing the threshold density raises the density of "delocalized" carriers above the well, which, in turn, determines the density at the interface between the well and waveguide and the density of minority carriers at the interface with the *p*-emitter. Additional energy steps in the waveguide reduce the density of minority carriers at the emitter interface and, correspondingly, leakage currents.

Next in importance is carrier accumulation and recombination in the waveguide layer with the narrowest band gap above the generation threshold, which is due to carrier emission from QWs. This factor makes no significant contribution to the total leakage current,

but it clearly illustrates an increase in density in the waveguide layers above the threshold.

In the laser structures under study that have the same design and composition of the active layer, the threshold density is determined by the optical confinement factor and internal optical losses. In other words, the material gain in these structures is virtually the same (lasers of the same cavity length), and the modal gain is determined by the optical confinement factor, which, combined with internal optical losses, determines the threshold density in the active region.

The optical confinement factor in the active region was calculated for the fundamental TE mode and was found to be different in single-step waveguide (*C*) and separate-confinement (*A*) structures: 2 and 1.05%, respectively. The threshold density n_{th} in the structures was determined in terms of the model [7] from the known relation of balance between the gain and losses at the generation threshold:

$$N_{QW}\Gamma g(n) = \alpha_{int} + \alpha_{ext}, \tag{13}$$

where N_{QW} is the number of QWs; Γ, the optical confinement factor for a QW; $g(n)$, the carrier density–dependent gain per QW; α_{int}, the internal losses at the generation threshold; $\alpha_{ext} = \frac{1}{L}\ln\frac{1}{R}$, the mirror losses; and L, the cavity length.

As a result, the threshold density in a type-*A* structure appeared to be nearly 1.4 times that in a type-*C* structure.

Owing to additional energy steps, the laser diodes based on a heterostructure with a stepwise type-*C* waveguide show a density of minority carriers at the interface with the *p*-layer which is almost an order of magnitude lower than type-*A* structures (the calculated N^* densities are 10^{14} and 10^{15} cm^{-3}, respectively). The calculations were performed using the Boltzmann approximation in each of the waveguides successively. The density of the leakage current into the emitter decreased in direct proportion to the minority carrier density at the interface between the waveguide and the *p*-emitter. The band related to recombination in the wide-bandgap waveguide layer is not observed in the PL spectra of type-*C* structures, which also indirectly indicates a decrease in the minority carrier density at the interface between the waveguide and *p*-emitter.

Thus, compared with a type-*A* structure, a type-*C* structure with a single-step waveguide has twice as high an optical confinement factor in the active region and an order-of-magnitude lower density of minority carriers at the interface between the waveguide and *p*-emitter. These two factors provide high (close to 100%) η_i^{st} values in the laser diodes based on type-*C* structures.

To perform a more detailed comparison of different structure designs, we selected a type-*C* structure with the maximum internal quantum efficiency of emission and two standard structures with a simple waveguide, in which the E_g of the waveguide layer corresponded to the band gaps of the first (0.992 eV) and second (1.18 eV) waveguides in the type-*C* structure (see the Table). The waveguide thickness in standard structures corresponded to the thickness of the wide-bandgap waveguide of the type-*C* structure. For these structures, we calculated the minority carrier densities at the interface with the *p*-emitter and total leakage currents into the *p*-emitter, optical confinement factors in the active region, and the internal quantum efficiencies of stimulated emission. Figure 4 summarizes the calculation results. The type-*C* structure is characterized by minimum leakage currents J_L and a maximum η_i^{st} value. Hence, it follows that only the combination of two factors, low threshold density of carriers and low density of minority carriers at the interface between the waveguide and *p*-emitter, can provide a maximum value of the internal quantum efficiency of stimulated emission in laser diodes.

The calculated η_i^{st} values for the studied structures are listed in the table; they are somewhat higher than the measured ones. This may be due to the fact that additional mechanisms of losses, such as, e.g., active region heating, were disregarded in calculations. On the whole, the calculated values obtained correlate well with the experiment, thus leading to a conclusion on the applicability of this model for the calculation of the internal quantum efficiency of stimulated emission in laser heterostructures above the generation threshold.

6. CONCLUSIONS

The internal quantum efficiency of stimulated emission of SC InGaAsP/InP DH lasers of various waveguide design has been studied experimentally and analyzed theoretically.

The theory predicts that lasers (λ = 1.5–1.6 μm) with an internal quantum efficiency of stimulated emission η_i^{st} close to 100% can be developed.

As shown, the experimental η_i^{st} values have a large scatter (67–96%), depending on the design of the laser heterostructure. The internal quantum efficiency of stimulated emission is lowered by leakage currents existing above the generation threshold. The leakage can be minimized by reducing the threshold density of injected carriers in the active region and the density of nonequilibrium carriers at the interface between the waveguide and *p*-emitter. By raising the optical confinement factor in the active region and including additional energy steps in the waveguide, we have succeeded in obtaining an internal quantum efficiency of stimulated emission $\eta_i^{st} \approx 96\%$ in SC heterostructure lasers operating at λ = 1.5–1.6 μm.

ACKNOWLEDGMENTS

We are grateful to E.G. Golikova and Yu.A. Ryaboshtan for the structures used in experiment; and to A.Yu. Leshko, A.V. Lyutetskiĭ, and N.V. Fetisova for assistance with sample preparation and conducting experiments.

This study was supported in part by the Russian Foundation for Basic Research (project nos. 01-02-17851, 01-07-90299, 01-07-903000) and by the Ministry of Industry and Science of the Russian Federation program "Physics of Solid-State Nanostructures."

REFERENCES

1. A. Yu. Leshko, E. G. Golikova, V. A. Gorbylev, *et al.*, Pis'ma Zh. Tekh. Fiz. **26** (6), 5 (2000) [Tech. Phys. Lett. **26**, 295 (2000)].
2. D. Z. Garbuzov, A. V. Ovchinnikov, N. A. Pikhtin, *et al.*, Fiz. Tekh. Poluprovodn. (Leningrad) **25**, 928 (1991) [Sov. Phys. Semicond. **25**, 560 (1991)].
3. D. A. Livshits, I. V. Kochnev, V. M. Lantratov, *et al.*, Electron. Lett. **36**, 1848 (2000).
4. E. G. Golikova, V. A. Kureshov, A. Yu. Leshko, *et al.*, Pis'ma Zh. Tekh. Fiz. **26** (20), 40 (2000) [Tech. Phys. Lett. **26**, 913 (2000)].
5. N. C. Casey, Jr. and M. B. Panish, *Heterostructure Lasers* (Academic, New York, 1978; Mir, Moscow, 1981), Parts A and B.
6. L. A. Coldren and S. W. Corzine, *Diode Lasers and Photonic Integrated Circuits* (Wiley, New York, 1995).
7. L. V. Asryan, N. A. Gun'ko, A. S. Polkovnikov, *et al.*, Semicond. Sci. Technol. **15**, 1131 (2000).
8. G. G. Zegrya, N. A. Pikhtin, G. V. Skrynnikov, *et al.*, Fiz. Tekh. Poluprovodn. (St. Petersburg) **35**, 8 (2001) [Semiconductors **35**, 962 (2001)].
9. A. Yu. Leshko, A. V. Lyutetskiĭ, N. A. Pikhtin, and G. V. Skrynnikov, Fiz. Tekh. Poluprovodn. (St. Petersburg) **34**, 1457 (2000) [Semiconductors **34**, 1397 (2000)].
10. H. Hirayama, J. Yoshida, Y. Miyake, and M. Asada, Appl. Phys. Lett. **61**, 2398 (1992).

Translated by D. Mashovets